Stress-diffusion coupling. From interstitial problems to the gas nitriding of steel.

Lisa Germain

HESAM UNIVERSITÉ

Arts et Métiers Sciences et Technologies

ÉCOLE DOCTORALE SCIENCES ET INGÉNIERIE
[Laboratoire MSMP - campus Aix-en-Provence]

Thèse de doctorat

presentée par : **Lisa GERMAIN**
pour obtenir le grade de : **Docteur de l'Université HESAM**

preparé à : **École Nationale Supérieure d'Arts et Métiers**

Stress-diffusion coupling.
From interstitial problems to the gas nitriding of steel

Thèse de doctorat dirigée par :
Pr. BARRALLIER Laurent

et co-supervisée par:
Dr. JÉGOU Sébastien

Jury

Pr. Luc PICHON	Professeur, CNRS-Institut Pprime	Président
Pr. Benoit PANICAUD	Professeur, Université de Technologie de Troyes (UTT)	Rapporteur
Dr. Julien TEIXEIRA	Chercheur CNRS, Institut Jean Lamour (IJL)	Rapporteur
Pr. Laurent BARRALLIER	Professeur, Laboratoire MSMP, Arts et Métiers	Examinateur
Dr. Sébastien JÉGOU	Maître de Conférence, Laboratoire MSMP, Arts et Métiers	Examinateur

THÈSE

Acknowledgments

J'ai effectué ma thèse au sein du laboratoire Mécanique, Surface, Matériaux et Procédés (MSMP) d'Arts Métiers, au campus d'Aix-en-Provence. Elle a été financée par le Ministère de l'enseignement supérieur et de la recherche (MESR). Je remercie l'école doctorale pour m'avoir accepté sur ce sujet de thèse.

Je tiens à remercier Monsieur Laurent Barrallier, Professeur au campus des arts-et-métiers d'Aix-en-Provence, directeur de cette thèse, qui a su tout au long de ces trois années me faire confiance et me permettre de prendre confiance en mes capacités. Ses réponses à mes nombreuses questions et son partage d'expérience m'ont été précieux, je lui en suis reconnaissante.

Je tiens à remercier Monsieur Sébastien Jégou, Maître de Conférence au laboratoire MSMP, co-encadrant de cette thèse, pour la rigueur de son expertise lors des expériences et son exigence sur la qualité exigée lors de la réalisation de l'écrit de mes travaux.

Je tiens à remercier Monsieur Luc Pichon, Professeur à l'Université de Poitiers, qui m'a fait l'honneur de présider mon jury de thèse, ainsi que pour sa gentillesse et sa bienveillance.

Je tiens à remercier Monsieur Benoit Panicaud, Professeur à l'Université de Troyes, qui a accepté d'être l'un des rapporteurs de ma thèse. Je le remercie également d'avoir accepté de rapporter mon mémoire de première année et pour les échanges que nous avons eus lors des différentes conférences où nous nous sommes rencontrés.

Je tiens à remercier Monsieur Julien Texeira, Chercheur au C.N.R.S. de Nancy, qui a accepté d'être rapporteur de ma thèse.

Je tiens à remercier Monsieur Frédéric Hecht, Professeur emérite au Laboratoire Jacques-Louis Lions à Sorbonne Université de Paris, pour les échanges et l'aide apportée sur leur logiciel FreeFEM++.

Je tiens à remercier toute l'équipe du laboratoire MSMP, ainsi que les doctorants du LISPEN, pour leur accueil chaleureux et leur présence durant ces trois années de thèse. Je suis particulièrement reconnaissante envers Jean-François Mathieu, Fabrice Guittonneau et Agnès Fabre d'avoir pris le temps de me former sur les équipements et pour leur aide précieuse lors de certaines expériences. Et aussi à Laurence Combarieu, qui a toujours le mot juste pour vous faire rire. Je tiens également à la remercier ainsi que Léa Fidone pour leur aide dans l'organisation finale de ma thèse.

Je remercie Hugo, Louise, Flavien, Hassan et Yanxue pour les moments d'évasion le temps d'une soirée ou d'un week-end. Je tiens à remercier Charlotte, qui m'a permis d'être dans un endroit calme et apaisant pendant la période de rédaction. J'aimerais aussi remercier plus personnellement Jean-François Mathieu, avec qui nous avons pu longuement échanger/partager sur nos rêves de vie mêlant voyage et aventure.

Je n'oublie pas ma famille qui a été présente à chaque instant durant ces trois années, même si elle se trouve

à plus de 1000 km d'Aix-en-Provence au bout du monde français : ma chère Bretagne. Je tiens particulièrement à remercier ma mère, ma grand-mère, ma mamie, mon petit-frère qui m'ont apporté leur plus grand soutien, leur réconfort sur les difficultés que nous pouvons rencontrer dans la vie et pour leurs précieux conseils.

Je ne peux conclure sans remercier Rolly, ce petit être à quatre pattes, qui m'a apporté tant de réconfort et sans lequel je n'aurais pas pris le temps de m'occuper de moi tout en profitant de faire ce que j'aime : randonner. Et aussi, merci à mon cher voisin, Loris, pour sa disponibilité et pour nos longues balades éclairées à la frontale (tard ! très tard !), après mes journées de travail.

Contents

List of Tables

List of Figures

Part I

English manuscript

Introduction

For many years, an important field of study has been the coupling phenomena between a mechanical stress field (applied or residual) and a chemical field in a material diffusion process. The improvement of the physical and mechanical properties of material surfaces is a challenge that both academic and industrial researchers are interested in. Industrially, effective depths are used and defined to determine the depth of a nitrided layer. This research therefore focuses mainly on the thickness of the diffusion layer, i.e. the long-range diffusion. Diffusion leads to improvements in surface hardness but also to a local change in the microstructure and thus to a change in local volumes. This strong local strain leads to long-range elastic strain, which results in a residual stress field. This residual field allows for improved mechanical properties such as, for example, the fatigue life of the stressed part [Godet, 2018]. The greater the depth of the diffusion layer, the deeper the corresponding residual stress profile.

Experimentally, many studies focus on the coupling between mechanical pretreatment and thermochemical treatment in order to create diffusion shorts in order to increase the diffused depths. The findings of these studies are based on plastic strain phenomena (e.g. nanocrystallisation). Nanostructured surfaces induce an increase in the volume fraction of the grain boundaries, a high dislocation density which have a significant influence on the diffusion kinetics [Lu and Lu, 2004, Tong et al., 2008, Chemkhi, 2014]. Nanostructures provide faster diffusion paths for interstitial atoms on the material surface. However, mechanical pretreatment also causes residual stress gradients (i.e. elastic strains). The effect of stresses, whether gradient or homogeneous, revealed that it is the sign of the stresses that predominates on the diffusion kinetics: positive stress increases the diffusion kinetics, conversely for negative stresses [Kirchheim, 1986, Araki and Arai, 2010a, Guillot, 2018].

The first question could therefore be: which source of stress (elastic or plastic) dominates the short- and long-range diffusion kinetics? Gas nitriding is the thermochemical treatment studied in this thesis. It consists of placing a steel part in a furnace where the atmosphere, notably ammonia, is controlled. The diffusion of nitrogen significantly improves the mechanical properties of the surface (resistance to fatigue, wear, cracking and corrosion). The development of compressive residual stresses and the increase in surface hardening lead to an increase in mechanical properties. Long range interstitial diffusion leads to large stress gradients associated with phase transformations (short-range diffusion). The formation of residual stresses during nitriding is caused by the type of volume change associated with phase precipitation during diffusion of nitrogen [Barrallier, 1992].

The 33CrMoV12-9 nitrided steel grade studied in this thesis is commonly used in the aerospace, naval and motorsport fields and has non-homogeneous mechanical properties. A nitrided surface zone is significantly harder than the base metal and has high compressive surface stresses. Industrially, the development of parts requires higher and higher mechanical loads, with deeper and deeper nitriding ranges, which leads to longer and longer processing times and thus to resource intensive processing. Research into the effect of stresses on diffusion

kinetics aims to reduce treatment times and/or temperatures while optimising treatment ranges. For example, a study by Tong showed a reduction in temperature from 500 °C to 300 °C in the case of pure iron through a surface mechanical attrition treatment before the thermochemical nitriding treatment [Tong et al., 2003]. Today, numerical methods combined with experimental methods are a cheap and fast way to predict the phenomena.

On the analytical side, a large number of studies have been carried out on the understanding of stress-diffusion coupling phenomena. These studies have mainly focused on the influence of a stress gradient on the diffusion kinetics by assuming an effective diffusion coefficient. In 1996, Voorhees and Larché defined analytical formulations that take into account the effect of stress on mobility [Larché and Voorhees, 1996]. This equation thus includes the coupling of two effects of stress on long-range diffusion phenomena: the effect of the magnitude and sign of the stress on mobility (Fickian term) and the stress gradient as a driving force (Nersntien term). A second question could be: what is the effect of the sign of the stress? A third question would be: which term (Fickian or Nersntian) dominates the long range diffusion kinetics? For many years, the numerical development of thermochemical treatments (i.e. diffusion phenomena of oxygen, hydrogen or, for example, nitrogen) has been known and developed. In the laboratory, a 1D model has been developed, optimised and coupled to the Thermo-calc database in order to predict nitrogen concentration profiles and nitride/carbon contents as a function of the input boundary conditions [Barrallier, 1992, Jegou, 2009, Fallot, 2015]. However, this model does not take into account the stress-diffusion coupling (stress effects at each time t), but only calculates the final residual stress profile from the final concentration profile.

The objective of this thesis is to better understand this coupling, starting with the problems of interstitial diffusion and progressing to the case of gas nitriding of the ferritic steel grade 33CrMoV12-9. The first objective of this research is to understand the effect of elastic stresses (applied/residual stresses) on the diffusion kinetics by combining theoretical and experimental observations. The second objective is to decouple the effects of elastic stresses and incompatible plastic stresses on diffusion kinetics.

The first chapter will therefore focus on a bibliographic synthesis of the gas nitriding treatment, the analytical equations of the stress-diffusion coupling, modelling on existing binary models, and experiments involving the diffusion phenomena by elastic and plastic stresses. A second chapter will be devoted to the numerical study of the stress-diffusion coupling in the case of a binary model without precipitation and without carbon co-diffusion phenomena, with the aim of observing and understanding the impact of a stress gradient and that of mobility stresses on the long-range kinetics. A third chapter will be devoted to the implementation of specific tests to decouple the effect of elastic stresses and incompatible plastic stresses on short- and long-range diffusion. The analysis of the mechanical properties (hardness, residual stresses and microstructure) of the samples will be studied and compared to reference samples. A final chapter will be devoted to the conclusions and perspectives of this work.

Chapter 1

Bibliography

Contents

1.1 Gas nitriding

Nitriding is an old thermochemical treatment where the first industrial applications were made in the 1930s [Fry, 1932]. Nitriding is a thermochemical process in which nitrogen diffuses from the surface to the core material [Ghiglione et al., 1996]. There exist different nitriding processes (salt bath, ionic or gas), each with its own advantages and disadvantages, which make it possible to obtain layers with the desired characteristics. The mechanical, metallurgical and chemical characteristics of the layers are strongly dependent on the processes used to form them. Gas nitriding is the particular treatment used in this study. Indeed, this treatment has been studied for years in the laboratory, within the framework of the understanding of the genesis of residual stresses [Barrallier, 1992], the metallurgical and mechanical characterisation of nitrided layers [Locquet et al., 1997], the influence of alloying elements on the genesis of residual stresses [Jegou, 2009], the role of carbon [Jegou, 2009, Fallot, 2015], the influence of surface preparations before treatment [Guillot, 2018] or the influence of the mechanical behaviour of a nitrided layer [Weil, 2017, Godet, 2018].

The aim of this process is to improve the near-surface mechanical properties of mechanical parts, for all types of steels (conventional structural steels [Barrallier, 1992, Locquet, 1998, Girodin and Moraux, 2002, Jegou, 2009, Weil, 2017, Godet, 2018, Guillot, 2018], tool steels [Ozbaysal et al., 1986], stainless steels [Rizk, 1979, Christiansen and Somers, 2005, Christiansen and Somers, 2010]) as:

— wear resistance [Belahssen et al., 2014],
— fatigue life [Castex et al., 1987, Jack and Winnik, 1979, Li et al., 1999],
— corrosion resistance [Belahssen et al., 2014].

One of the main advantages of this process is the low strain of the part after treatment compared, for example, to carburizing. Indeed, this process ends with a slow cooling (consequence of the low temperature below the allotropic transformation) to avoid thermal shocks that cause cracks and high strains. This treatment is often used on power transmission systems such as bearings and gears. The mechanical properties of the parts after nitriding are thermally stable [Barrallier, 1992]. In the case of highly stressed parts in contact, it is necessary to eliminate the compound layer to reduce the risks of spalling and cracking [Alanou et al., 2004].

This process also has weak points, which is mainly the treatment time (often several hours) due to the low treatment temperatures between 400 and 590°C. The ammonia molecule cracks at 400°C and above [Grabke, 1968]. As the samples are nitrided in the quenched and tempered state, 590°C should not be exceeded in order not to modify the microstructure of the steel. Other weak points are the low diffusion depths reached due to low temperature which leads to longer time (up to 1 mm depending on the material: austenitic steel [Somers et al., 1989, Christiansen et al., 2008], martensitic steel [Barrallier, 1992, Locquet, 1998, Jegou, 2009, Guillot, 2018]), the complexity of finding optimized treatment parameters (time, temperature, nitriding potential), the toxicity and danger of the products used (ammoniac and hydrogen).

All of these enhancements are the result of improved mechanical properties throughout the treatment process. In fact, Fig. 1.1 contains some of the characteristics on which the researcher bases his or her hypotheses on a certain phenomenon or improvement. The fatigue life or corrosion resistance are greatly improved by residual compressive stresses on the surface of the material (see section 1.1.4), and the resistance to wear is greatly improved by a high surface hardness, which can reach a factor of two when compared to the hardness of the base material (see section 1.1.3). Residual stresses and durability are both the result of diffusion and precipitation phenomena that find origins in the nitrogen and carbon in-depth profiles (see section 1.1.2.3).

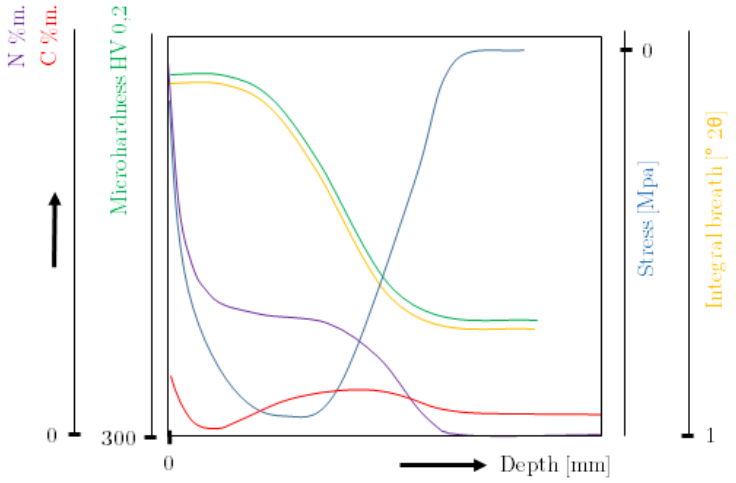

Figure 1.1 – Diagram illustrating the evolution of microstructure characteristic curves and mechanical property gradients in the case of a nitrided layer of a 33CrMoV12-9 steel inspired by [Barrallier, 1992].

1.1.1 Principle

The gas nitriding treatment is defined as a mass transfer of nitrogen atoms from ammonia into the material as a result of the following reaction:

$$NH_3 \rightleftharpoons N + \frac{3}{2}H_2 \tag{1.1}$$

Where NH_3 is the ammonia molecule, N is the nitrogen atoms adsorbed at the surface and H_2 is the hydrogen molecule. A catalytic effect occurs on the samples. Fig. 1.2 shows that during nitriding, nitrogen atoms diffuse from the surface to the core of the part through the cracking of ammonia between 400 and 590°C.

As for any chemical reaction, the law of mass allows us to write the reaction constant K such that:

$$K = \frac{a_N p_{H_2}^{3/2}}{p_{NH3}} \tag{1.2}$$

Where a_N is the nitrogen activity N in the material and p_{H_2} and p_{NH3} are the partial pressure of hydrogen and ammonia respectively in the furnace.

Considering the nitrogen atoms in the ferritic matrix as a dilute solid solution, the concentration of dissolved nitrogen in the matrix takes the following form:

$$[N] = K \frac{p_{NH_3}}{p_{H_2}^{3/2}} \tag{1.3}$$

Where $\frac{p_{NH_3}}{p_{H_2}^{3/2}}$ is the known nitriding potential K_N.

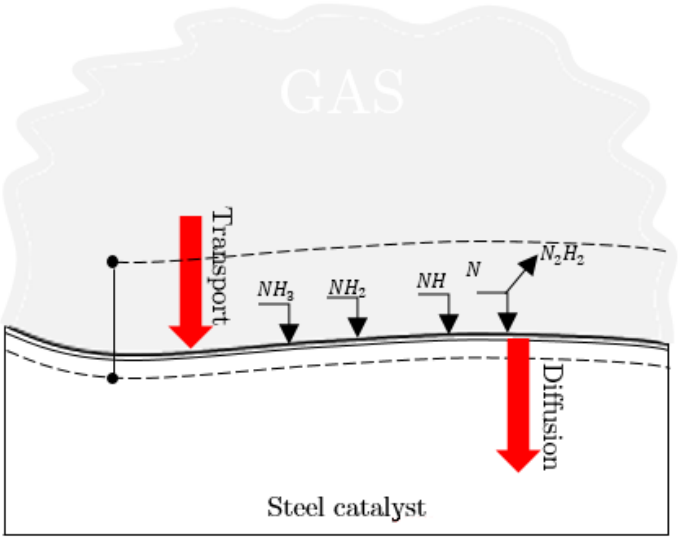

Figure 1.2 – Catalytic effect of nitriding gas on material.

1.1.2 Systems

The diffusion is associated with a local enrichment of the matrix in nitrogen [KlÄumper-Westkamp et al., 1989]. Interstitial atoms have a higher diffusion rate than the atoms of the addition elements that are substituted in the crystal lattice [Jack, 1975]. When the solubility limit of the nitrogen in the ferrite is reached, precipitates form and grow. Schematically, part of the nitrogen is used to precipitate the nitride while the other part diffuses to the core material. The mechanism stops when the system is in thermodynamic equilibrium.

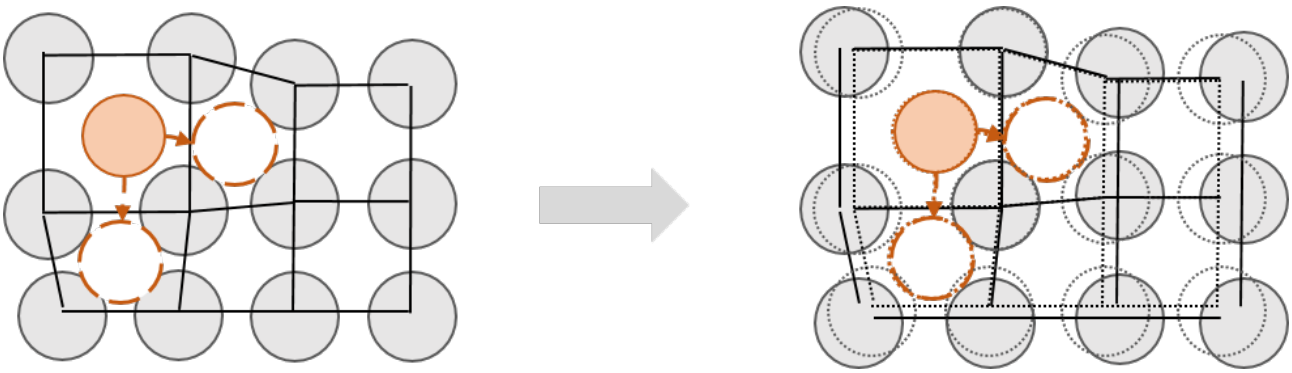

Figure 1.3 – Interstitial diffusion scheme.

The gas nitriding of a ferritic steel (grade 33CrMoV12-9) is the context of this research. A combined phenomenon of diffusion and precipitation will be studied. At the end of the treatment, the obtained layers show distinct nitrogen and carbon profiles that reflect the circumstances of the treatment (time, temperature, nitriding potential, etc.) as well as the impact of the alloying elements contained in the steel. The concept of diffusion is, by definition, the basis for understanding any process that occurs during nitriding. Therefore, several systems will be presented until the one that most closely approximates the conditions of a steel is reached.

1.1.2.1 Pure iron system

Many researchers have investigated the main diffusion-precipitation phenomena during nitriding treatment under simple initial composition conditions (binary systems) as for example on the pure iron [Wriedt et al., 1987]. Fig. 1.4 a) shows a microscopic observation of a nitrided surface distinguishing the different layers (compound layer: γ'-Fe_4N and ϵ-$Fe_{2-3}N$ and diffusion layer). According to the Fe-N phase diagram, the solubility limit of nitrogen in ferrite in the most commonly used nitriding temperature range (400-590°C) is very low (< 0.1 m.%N / < 0.4 at.%N) as shown in Fig. 1.4 b). As soon as this solubility limit is exceeded, iron nitrides formed as a function of the mass fraction of nitrogen. Fig. 1.4 b) shows the relationship between the iron-nitrogen equilibrium diagram and the nitrogen concentration profile in the case of compound layer growth.

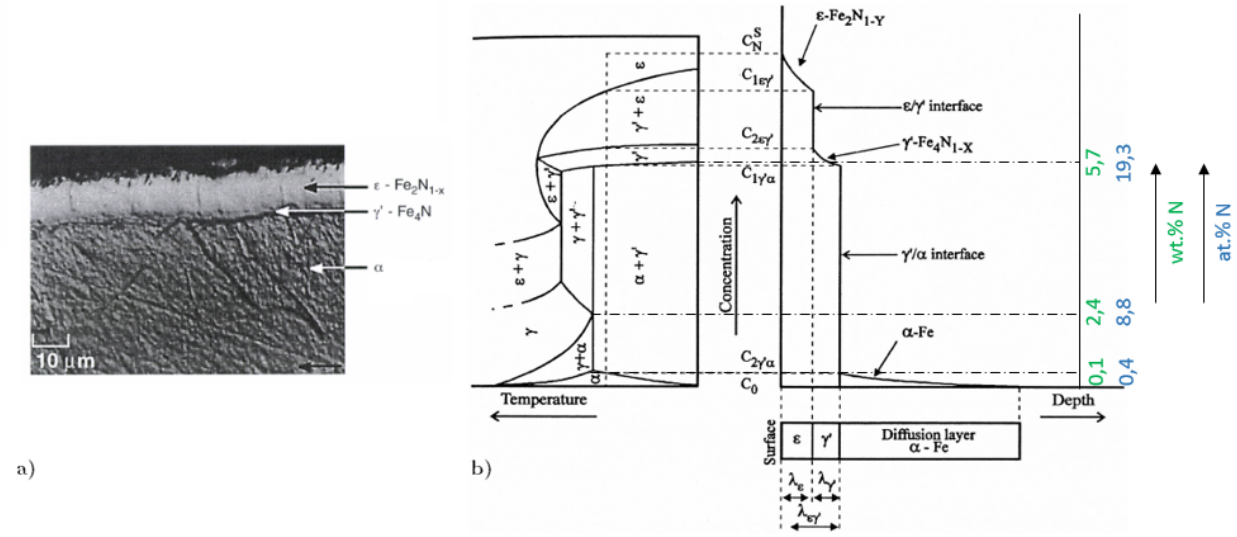

Figure 1.4 – a) Micrographic section of a pure iron rod after 5 hours of treatment [Bockel-Macal, 1997, Bockel et al., 1998]. b) Relationship between the iron-nitrogen equilibrium diagram and the nitrogen concentration profile in the case of the growth of the compound layer [Torchane et al., 1996].

The nitrided layer is characterised by three layers:

— A porous layer called compound layer or white layer which can reach up 0 to 50 μm. It depends directly on the nitrogen potential K_N used and on the treatment time (Lehrer diagram see Fig. 1.5). It is called the white layer because of its metallographic appearance after nital etching. It is composed of iron nitrides γ'-Fe_4N and ϵ-$Fe_{2\text{-}3}N$. γ'-Fe_4N precipitates at low temperatures and is the first to form. Its range of existence is narrow from 19.3 to 20.3 % atomic units of nitrogen. As for the ϵ-$Fe_{2\text{-}3}N$, it has a compositional range between 24.2 and 26.6 % atomic percent of nitrogen, resulting in a large variation of the lattice parameters. The compound layer is known to increase the tribological and corrosion resistance properties of the surface of the steels [Rozendaal et al., 1985, Barralis et al., 1986]. Indeed, iron nitride γ'-Fe_4N improves the resistance to cracking and the nitride ϵ-$Fe_{2\text{-}3}N$ is responsible for the good tribological and wear resistance properties. However, in some industrial applications, the compound layer is removed (machining or etching) in order to reduce the risk of surface cracking in the case of parts subjected to high rolling loads

[Alanou et al., 2004]. The formation of the compound layer sets the nitrogen content at the beginning of the diffusion layer [Gerardin and JP, 1977, Somers and Mittemeijer, 1990, Mittemeijer and Somers, 1997, Somers, 2004]],

— A diffusion layer of up to 1000 μm where the nitrogen is in solid solution in the ferritic matrix,

— A base material (Fe-α).

The Lehrer diagram, as shown in Fig. 1.5, relates the domains of existence of the phases to the percentage of nitrogen, temperature and nitriding potential and expresses the gas (NH3)/solid equilibrium. Figs. 1.4 and 1.5 show that on pure iron it is possible to obtain a single-phase (γ'-Fe_4N), two-phase (γ'-Fe_4N + ϵ-$Fe_{2\text{-}3}N$) or virgin compound layer by controlling the nitriding potential (equivalent to an at.%N) [Michalski et al., 2005, Hosmani et al., 2008].

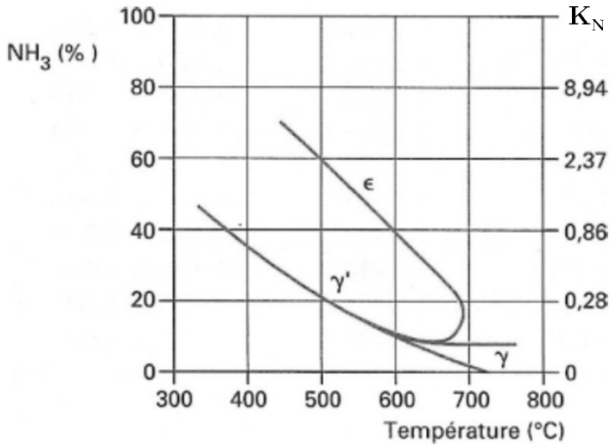

Figure 1.5 – Lehrer diagram [Lehrer, 1930].

1.1.2.2 Fe-M (M = Cr, V, Mo ...) system

Once the studies on a simple system (binary system) were made and understood, it is interesting to approach industrial materials. Indeed, studies have been carried out on more complex, systems containing additional elements (such as chromium, vanadium, molybdenum, etc.) in order to study their influence on the properties of the nitrided layer and their effect on the formation of the nitrides of the "MN" (M = Cr, V ...) type alloying elements.

As previously, the nitrided layer is composed of:

— A compound layer corresponding to the one explained in subsection 1.1.2.1,

— A diffusion layer: nitrogen has a strong affinity for some alloying elements such as chromium, vanadium and molybdenum [Rickerby et al., 1986, Chechenin et al., 2000, Gouné et al., 2003, Sennour et al., 2004, Ginter et al., 2006]. The diffusion layer is responsible for the fatigue strength and wear properties of nitrided parts [Mittemeijer et al., 1981]. Indeed, the precipitation of nitrides of alloying elements leads to a strong increase in hardening as well as a state of compressive residual stresses of the surface (see respectively section 1.1.3 and 1.1.4),

— A base material.

The compound layer was presented in its composition, however, it is interesting to understand the stages of evolution of the compound layer after an incubation period. This evolution was presented by Hosmani and described in six steps [Hosmani et al., 2008, Hosmani et al., 2009]:

1. A preferential diffusion of nitrogen at grain boundaries and nucleation of iron nitrides,
2. A precipitation of alloying element nitrides,
3. The progressive transformation of the ferrite grains from the grain boundaries results in the production of a layer of iron nitrides at the surface,
4. Depending on the processing conditions (usually a high nitriding potential), ϵ-$Fe_{2\text{-}3}N$ nitrides may occur before the complete formation of a γ'-Fe_4N nitride layer,
5. Pore formation if the thermodynamic conditions favour nitrogen atom recombination into N_2 molecules,
6. During relatively long cooling at zero nitrogen flux, a reorganisation of the combination layer is observed. The iron nitride ϵ-$Fe_{2\text{-}3}N$ is consumed in favour of the nitride γ'-Fe4N. The thickness of the relevant layers then lowers and grows [Liapina et al., 2006]. In general, the thickness of the layer γ'-Fe_4N diminishes due to a narrowing stability region as temperature falls, releasing nitrogen atoms prone to diffuse [Somers and Mittemeijer, 1990]. Such effect can also be observed during post-nitriding tempering, and allow to find a lower atomic fraction of substituted iron in the nitrides than after nitriding. This observation is accompanied by a decrease in the surface nitrogen fraction, which can be explained by the loss of iron in substitution within the nitrides [Ginter, 2006].

1.1.2.3 Fe-C-M (M = Cr, V, Mo...) system

After examining the basic iron-nitrogen system, followed by systems including other elements (chromium, vanadium, molybdenum, and so on), it becomes interesting and important to add a last component, which is carbon (to approach the conditions of a steel). Indeed, the experimental work of this PhD is concerned with an aeronautical steel (ferritic steel) composed of several alloying components, including carbon. In recent years, many studies have focused on understanding the role that carbon plays [Jack, 1948b, Jack, 1948a, Jegou, 2009, Christiansen and Somers, 2010, Fallot, 2015]. Indeed, this element brings significant modifications to the microstructure: during heat treatments by the appearance, in this study, of a martensitic tempered structure or during the nitriding treatment by a co-diffusion with nitrogen. Indeed, the stability of the carbon before and during the nitriding treatment is more than important since it will compete with the nitrogen atoms and thus modify the thermodynamics and kinetics of the treatment. The study is placed in the case of gas nitriding of a carbon-based iron alloy containing carbon up to 0.30 wt% (e.g. steel grade 33CrMoV12-9). The carbon concentration profile for this steel has been studied several times [Barrallier, 1992, Jegou, 2009, Fallot, 2015].

The diffusion coefficients of nitrogen and carbon in ferrite are much larger at the nitriding temperature than those of the alloying elements.

In carbon iron-based alloys, the alloying elements are present in two forms: in solid solution in the ferritic matrix, and in substitution within the tempered carbides. However, nitrogen has a greater affinity for the alloying elements than carbon. The diffusion kinetics of the nitrogen atoms then compete with the transformation kinetics of the carbides. Two modes of precipitation of alloying element nitrides coexist and compete. The first

is the precipitation of nano-scale semi-coherent nitrides from the substitutional solid solution. The second mode of precipitation corresponds to the transformation of tempering carbides ($M_{23}C_6$, M_7C_3 or MC; M designating a metal atom, such as $Cr_{23}C_6$) into incoherent M(N,C) carbo-nitrides [Leroy et al., 1986, Locquet et al., 1997]. The carbides serve as nucleation and growth sites for the incoherent nitrides, this is due to the nitrogen affinity of the addition elements. The nitrides are globular intergranular or intragranular, smaller in size than the carbides [Locquet, 1998]. This reduction in size is supposed to result from a loss of iron during the transformation [Leroy et al., 1986]. Incoherent nitrides can precipitate in a particular arrangement known as a "chaplet" as presented by Locquet [Locquet, 1998]. The size of incoherent nitrides increases with depth [Locquet, 1998]. This phenomenon can be explained by the fact that when the nitrided thickness increases, the nitrogen flux decreases, reducing the number of nitride germination sites and thus favouring the growth/coalescence phenomenon. Coalescence phenomena are also observed on the size of incoherent nitrides when the temperature increases. The transformation of the carbides into incoherent nitrides is accompanied by a release of the carbon initially present in the carbides [Leroy et al., 1982, Larsson and Ågren, 2004, Tsujikawa et al., 2005, Hirsch et al., 2004]. The carbon released in the ferritic matrix during the transformation of the carbides into nitrides diffuses either towards the core or towards the surface [Leroy et al., 1982, Dulcy et al., 2002, Nakata et al., 2003, Larsson and Ågren, 2004, Hirsch et al., 2004, Dulcy and Gantois, 2005]. A study by Calliari et *al.* showed the decrease in nitrogen diffusion kinetics of samples whose surface had been previously decarburised [Calliari et al., 2006]. Barrallier carried out (see Fig. 1.6) some simulations schematically representing what happens during gas nitriding as a function of time in terms of nitrogen and carbon concentration as a function of depth [Barrallier, 2014]. Barrallier et *al.* used the thermodynamic software Thermo-Calc® to show the volume fraction of precipitates (CrN , M_3C, $M_{23}C_6$, M_7C_3) in the diffusion layer as a function of depth and time [Barrallier, 2014]. It is important to note that these simulations do not take into account the development of a compound layer during the treatment. This is why the profiles do not show the carbon enrichment, at the steel surface, created by the precipitation of iron nitride ϵ-$Fe_{2\text{-}3}N$ (ϵ-$Fe_{2\text{-}3}N$ has an important solubility of carbon). Indeed, this figure allows to observe the evolution of carbon diffusion in the diffusion layer. Two distinct zones are observed in the diffusion layer:

— A depletion at the interface, between the compound and diffusion layers due to the diffusion of carbon released during the transformation of carbides into nitrides, is observed [Leroy et al., 1982, Dulcy et al., 2002, Dulcy and Gantois, 2005]. There are two possible phenomena: decarburisation near the surface can lead to an enrichment of carbon in the diffusion layer and a sharp decrease in carbon content at the interface with the compound layer; or an overall decrease in carbon content in the diffusion layer [Hirsch et al., 2004]. The term decarburisation is used here in order to simplify the proposal, it is not a question of a classic decarburisation as for example during tempering or austenitisation. Instead, it is a combined migration of carbon to the surface with hydrocarbon formation to the core material,

— A carbon enrichment of the nitrogen diffusion front that corresponds to the precipitation of the M_7C_3 and $M_{23}C_6$ carbides [Jegou, 2009], as shown in Fig. 1.7. Indeed, part of the carbon released during the carbide-nitride transformation diffuses with nitrogen and precipitates with the alloying elements in solid solution at the nitrogen diffusion front to form carbides (M_7C_3 and $M_{23}C_6$) [Dulcy et al., 2002, Dulcy and Gantois, 2012]. Some carbon atoms are precipitated at the grain boundaries of the diffusion layer as M_3C cementite. The distribution of these precipitations depends on the carbon content and becomes maximum near the carbon enrichment. From a thermodynamic point of view, due to the co-diffusion of carbon with nitrogen, carbon migrates to regions where its chemical potential μ_{carbon} is

lower [Lightfoot and Jack, 1975, Leroy et al., 1982]. From a mechanical point of view, some carbides, notably $M_{23}C_6$, precipitate at grain boundaries. They lead to the embrittlement of steel, making it more susceptible to corrosion (due to chromium depletion). This is why carburigenic elements are important, as they capture carbon and thus prevent the formation of carbides with certain elements.

Fig. 1.7 shows that the fraction of nitrides of the alloying elements is maximal at the beginning of the diffusion layer and decreases in a similar way to the profile of the nitrogen up to the base material [Locquet et al., 1997, Sennour et al., 2004]. It is therefore interesting to note that the level of the diffusion layer is a function of the amount of nitrogen reacting with the alloying elements.

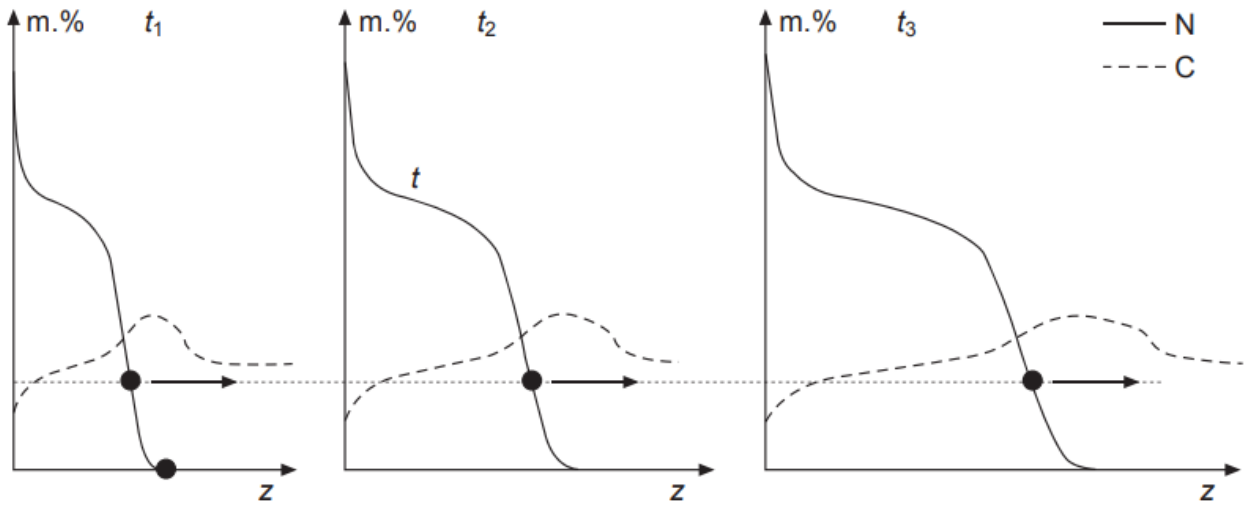

Figure 1.6 – Schematic evolution of nitrogen and carbon concentration in low-alloy steels during nitriding at 560°C. [Barrallier, 2014]

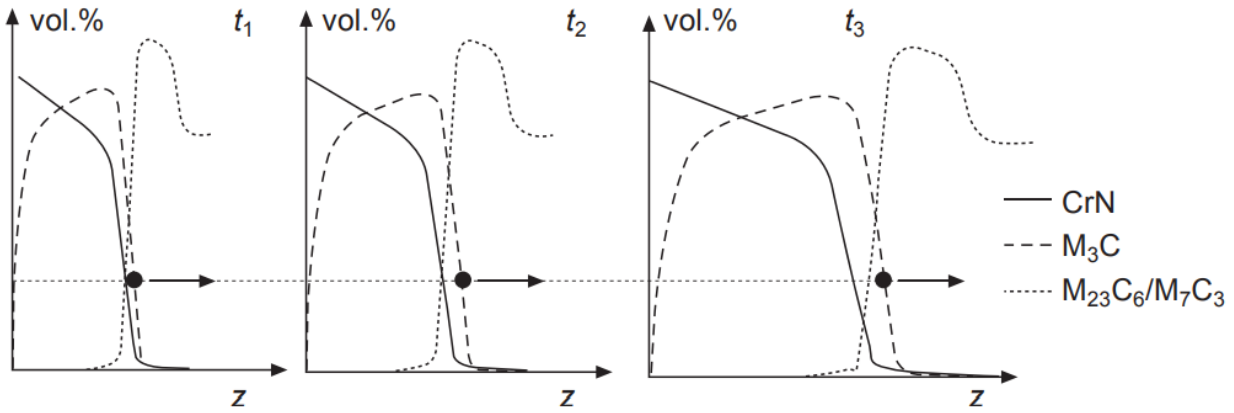

Figure 1.7 – Schematic evolution of the volume fraction of nitrides and carbides in low-alloy steels during nitriding at 560°C. [Barrallier, 2014]

The Lehrer binary diagram has proved to be insufficient in the case of steels because of the element carbon. These diagrams show the influence of carbon on the composition of the compound layer. Indeed, Fig. 1.8 shows two equilibrium diagrams of the iron-carbon-nitrogen system at two temperatures 500°C and 565°C. They reveal that the iron nitrides γ'-Fe_4N and ϵ-$Fe_{2\text{-}3}N$ have important equilibrium domains depending on the nitrogen and carbon content, but also a greater or lesser solubility of these elements in each of these phases. The first observation is that the compound layer can be presented in the form of a single-phase layer, e.g. γ'-Fe4N or ϵ-$Fe_{2\text{-}3}N$, a two-phase layer (γ'-Fe_4N + ϵ-$Fe_{2\text{-}3}N$) or without. It is known that the γ'-Fe_4N has a very low affinity with carbon (0.2 %)m. [Gerardin and JP, 1977, Colijn et al., 1983]. The comparison of these two diagrams allows us to observe that:

— The solubility of carbon in ferrite remains almost zero and shows no effect of temperature [Dupuy, 1930],

— There are domains of equilibrium that include the presence of Fe_3C (cementite) and of γ'-Fe_4N and/or ϵ-$Fe_{2\text{-}3}N$ (iron nitrides). The temperature does not seem to have an impact on the α+Fe_3C+γ'-Fe_4N domain. However, temperature has a strong influence on the Fe_3C+γ'-Fe4N+ϵ-$Fe_{2\text{-}3}N$ domain. As a reminder, the iron nitride γ'-Fe_4N improves the wear resistance and the nitride ϵ-$Fe_{2\text{-}3}N$ is responsible for the good tribological and wear resistance properties. As for cementite, it is a so-called brittle compound, resistant to wear, and very hard,

— The solubility of nitrogen in cementite is the order of 0.05% m.,

— The solubility of carbon in iron nitride γ'-Fe_4N ($< 0.2\%$ m) is low,

— The domain of existence of the nitrides γ'-Fe_4N + ϵ-$Fe_{2\text{-}3}N$ decreases when the temperature increases,

— The domain of existence of the carbo-nitride ϵ-$Fe_{2\text{-}3}N$ increases with temperature.

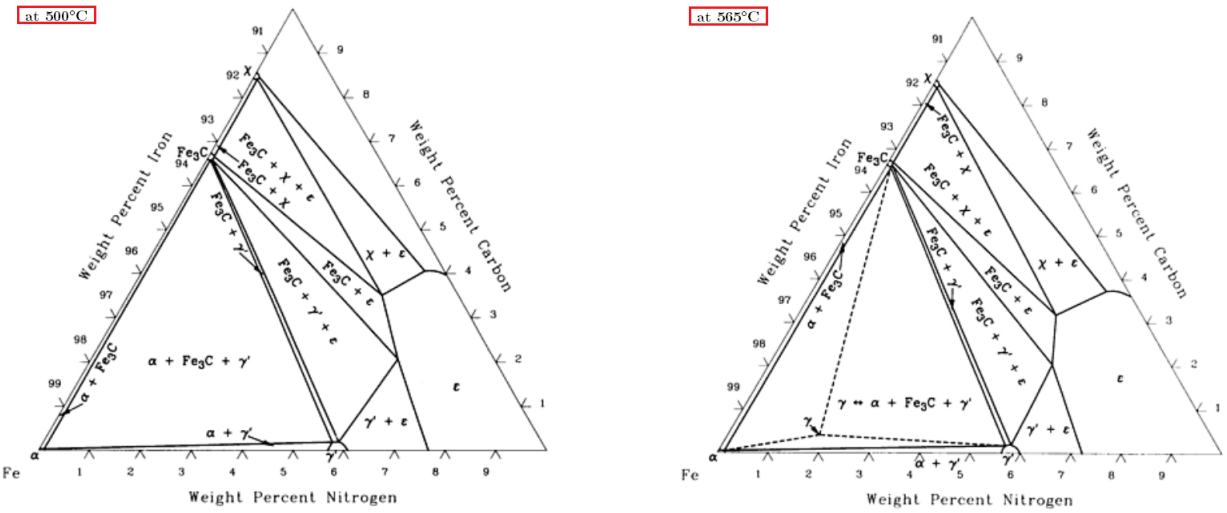

Figure 1.8 – Ternary Phase Diagrams of C-Fe-N (Carbon - Iron - Nitrogen) at 500°C and at 565°C [Raghavan, 1987, Swartzendruber, 1998].

The Lehrer diagram is still a reference on the understanding and evolution of phases as a function of K_N and temperature. Researchers often aim to create a Lehrer diagram applied to the material under study or simply add a few points to it in order to understand the phenomena. For the material used in this study (32CDV13

steel), Dulcy modified the Lehrer diagram due to the alloying elements and carbon diffusion. Indeed, in Fig. 1.9, the dotted line corresponds to the boundary between the γ'-Fe_4N and ϵ-$Fe_{2\text{-}3}N$ zones found by Dulcy and *al.* on steel grade 33CrMoV12-9.

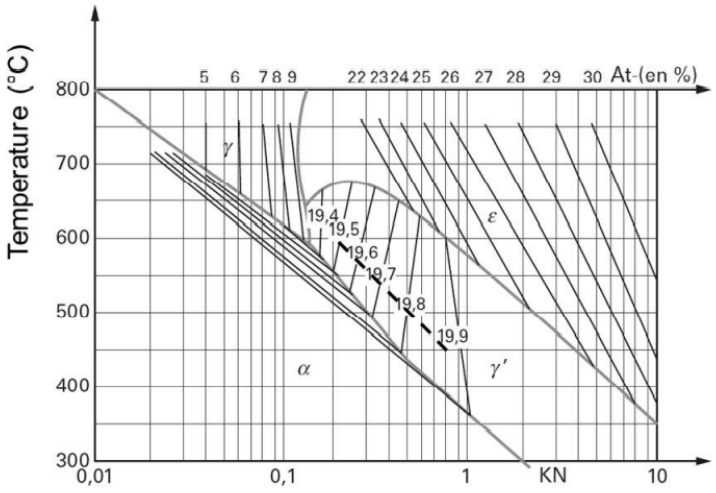

Figure 1.9 – Lehrer diagram of the iron-nitrogen system, the dotted line corresponds to the boundary between the ϵ and γ' zones analysed by Dulcy et *al.* on steel grade 33CrMoV12-9. [Lehrer, 1930, Dulcy et al., 2002]

In a simple case, here pure iron, it has been shown that a local equilibrium at the interfaces ϵ-$Fe_{2\text{-}3}N$/γ'-Fe_4N and γ'-Fe4N/α-Fe) is considered [Somers and Mittemeijer, 1995, Appolaire and Gouné, 2006]. In the case of steels (i.e. presence of carbon and alloys elements), the compositions evolve during the treatment [Rozendaal et al., 1985, Mittemeijer et al., 1981, Somers, 1989, Ratajski, 2009]. Intermingling of the layers in relation to each other is observed, implying that the interfaces of the nitride layers γ'-Fe_4N et ϵ-$Fe_{2\text{-}3}N$ are no longer as clear. In the case of a steel, the more the carbon content, the more it will be important in the near surface and will favour nitride ϵ-$Fe_{2\text{-}3}N$. The latter has a high carbon solubility.

The transformation of carbides into nitrides appears to be a synergistic process including nitride precipitation and ferrite dissolution [Leroy et al., 1986, Locquet et al., 1997, Ginter et al., 2006]. Indeed, the amount of iron present in the nitrides in substitution of the alloying elements is less than that initially contained in the carbides. The crystalline similarities between cementite and $Fe_{2-3}N$ cause the transformation. Cementite is formed when carbides are converted into nitrides during the initial stages of nitriding.

After looking at the ternary diagrams, it may be interesting to understand the order in which precipitates are created:

— Precipitation of the carbides from the alloying elements of the solid solution,

— Precipitation of the semi-coherent MN nitrides from the alloying elements of the solid solution,

— Transformation of carbides into nitrides and precipitation of cementite at grain boundaries.

Many studies have shown that the surface nitrogen fraction after treatment is higher than the theoretical fraction in the case where all alloying elements are assumed to have reacted to form nitrides and the solid solution fraction in the matrix is taken into account (as shown in Fig. 1.6) [Somers et al., 1989, Mittemeijer and Somers, 1988, Schacherl et al., 2004, Ginter et al., 2006, Hosmani, 2005, HOSMANI, 2006, Hosmani et al., 2007, Hosmani et al., 2008,

Clauss et al., 2008, Meka et al., 2014, Jung et al., 2011]. Two theories, explaining this "excess", have been announced. The first, proposed by Mittemeijer et *al.*, involves distinguishing between mobile nitrogen atoms, which have interacted with the alloying elements to create MN nitrides and are adsorbed at the matrix/precipitate contact, and immobile nitrogen atoms, which are in solid solution in the ferritic matrix. The volumetric variations produced by the precipitation distort the crystal lattice of the ferrite, causing an increase of the solid solution around the precipitates [HOSMANI, 2006, Hosmani et al., 2007]. The second, postulated by Ginter, is that beyond a certain nitrogen proportion, there occurs a substitution of alloying elements by iron atoms within MN nitrides. [Ginter, 2006, Ginter et al., 2006, Jessner et al., 2009]. This replacement, which may reach up to 30%, would allow for a rise in the molar fraction of nitrides and, as a result, the amount of nitrogen on the surface.

1.1.3 Hardening

In the industry, effective nitriding depths are used and defined to determine the depth of a nitrided layer. It is defined as the thickness of the nitrided layer with a hardness difference between the core material and the surface layer that is (HV_{core} + 100 HV0.2). It is important to recognize that the depth of a nitrided layer may be most simply investigated using chemical analysis to determine the mass percentage of nitrogen as a function of depth. Both analyses are merged in the case of a simple geometry. Chemical analysis is typically not possible in the case of complex geometry and may also be time consuming, hence micro-hardness testing is essential to determine the nitrided zones.

The initial effect of nitriding is a considerable increase in the surface hardness of the part. Fig. 1.10 shows a schematic representation of the evolution of hardness as a function of thickness in the case of nitrided steel, where it can be seen that the surface hardness is significantly improved compared to the base material.

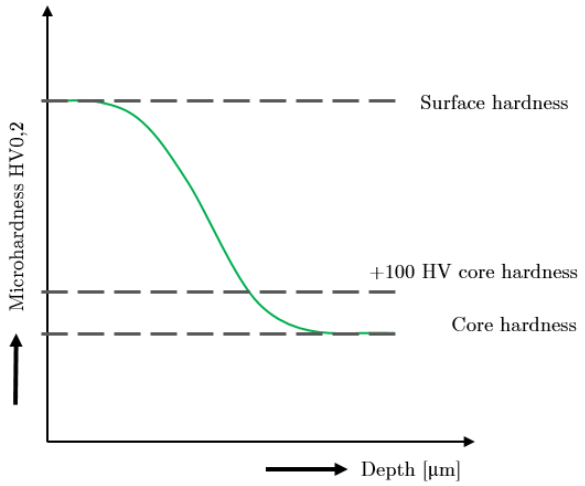

Figure 1.10 – Schematic representation of the evolution of hardness as a function of thickness in the case of nitrided steel.

Hardening mechanisms consist of introducing discontinuities in the crystal lattice within a material that hinder the movement of dislocations in their sliding planes [Pickering, 1978]. Depending on the scale of observation,

these obstacles are obtained by:

— Other dislocations (strain hardening),

— Solid solutions of atoms in insertion or substitution,

— Precipitates of second phases,

— The interfaces or grain boundary,

— The transformations, the previous effects being more or less accentuated according to the transformation temperature.

It is known that the primary process of plastic strain is dislocation motion. To harden the material, the action of dislocations must be slowed down but not blocked. Other dislocations, inserting or replacing foreign atoms, grain boundaries or second phase precipitates can all impede dislocation movement. Nitriding occurs in the case of structural hardening caused by second phase precipitation, namely by the small size of the nitrides in the MN alloy. Precipitates are the primary cause of hardness in the case of nitriding (precipitates discussed in Section 1.1.2.3). In other words, dislocation braking is caused by the crossing of precipitates. More precisely, the crossing of incoherent precipitates involves an Orowan-type bypass mechanism with the formation of dislocation loops resulting from a Frank-Read process [Locquet, 1998]. The shearing process of the precipitates is involved in the crossing of the semi-coherent MN precipitates [Locquet, 1998].

As illustrated schematically in Fig. 1.1, the hardness profiles of a nitrided layer generally show a hardness maximum near the surface which decreases with distance from the surface, falling to the value of the base material hardness approximately near the diffusion front zone.

The researchers concluded that hardening is produced by the precipitation of nano-sized alloy components after comparing different alloys. The experiments revealed that hardening is significant when the volume fraction of nitrides and the percentage of alloying elements in solid solution in the matrix are high. Nitrogen enrichment is particularly significant when the concentration of the additive elements is high [Locquet, 1998, Sennour, 2002, Ginter, 2006]. Consequently, the hardness increases but the effective depth of nitriding decreases. As with nitrogen enrichment, the type of alloyed elements is critical [Seybolt, 1969, Lightfoot and Jack, 1975]. In general, hardness increases with the volume fraction of nitrides and the extent of precipitation.

1.1.4 Residual stresses

Residual stresses are defined as stresses that exist in a sample without external solicitation [Totten et al., 2002]. To correctly design the parts, engineering offices must understand and quantify the fields of stresses generated by mechanical forces in order to counterbalance them with residual stresses, often compressive. Indeed, they have evolved into a complete optimization parameter in the design of mechanical systems, and are no longer limited to a result of manufacturing processes (elaboration, shaping, surface treatments). In general, under external loading, they can be sources of stress concentration, hastening the deterioration and leading to the failure of a component.

For example, tensile residual stresses will have a negative impact on corrosion resistance under stresses. On the contrary, residual compressive stresses will work against the opening of cracks, increasing the tensile strength and fatigue resistance. The methods for introducing residual stresses might be mechanical (eg. shot-peening), thermal (eg. superficial quenching), or thermochimical (eg. nitriding, carburizing, carbonitriding).

It is also worth noting that a machining operation such as grinding generates tensile or compressive stresses depending on the operation's parameters and the balance between thermal and mechanical effects. Nitriding induced compressive stresses were firstly evaluated by R.B. Waterhouse by comparison with compressive stress obtained in sulphidized coatings from the deflection of the specimen [Waterhouse, 1965]. In this thermochemical treatment, the residual stresses have a chemical origin. The development of residual stresses during nitriding is known to follow the kinetics of phase transformation. The limiting rate of nitrogen supersaturation of the ferritic matrix and carbon diffusion is the transformation of carbides into nitrides. Indeed, nitrogen diffusion causes the precipitation of nitrides, whereas carbon diffusion causes the precipitation of carbides (more details in the section 1.1.2.3). This precipitation, like those of nitrides, generates a change in volume, which results in stress-free volumetric strains. As a result, residual stresses are induced by volumetric strains as depth below the surface increases. The lower the carbide transformation kinetics, the lower the decarburisation during nitriding and the higher the residual stresses. The kinetics are governed by temperature and nitriding potential. Furthermore, as previously stated, the alloying elements are definitely important. The higher the additional element content, the larger the volume percentage of MN nitrides. As a result, the volume strains and residual stresses will be greater [Djeghlal and Barrallier, 2003]. Because of nitrogen's affinity for these elements, the stress field extent decreases and the stress minimum moves towards the material surface [Barrallier, 2014].

The nitrogen being in solid solution of insertion, there is thus a modification of the molar volume of the ferrite; the formation of nitrides or carbonitrides have a different molar volume from that of the ferrite (see Tab. 2.4) [Barrallier, 1992]. In further depth, the volume change is caused by several factors:

— Different densities between the precipitates and the matrix (see Fig. 1.11 and Tab. 2.4) [Goldschmidt, 1967]. These changes in molar volume are commonly referred to as "specific volume variation" $\frac{\Delta V}{V}$,

— Differents coefficients of thermal expansion of $6.10^{-6}K^{-1}$ for precipitates and $12.10^{-6}K^{-1}$ for ferritic matrix [Goldschmidt, 1967]. Because of its low cooling, gas nitriding treatment is often regarded as a non-thermal shrinking treatment. However, it's interesting to understand that thermal expansion coefficients influence the growth of residual stresses. According to the studies, cooling during processing has little effect on the residual stresses, due to the small differences between the thermal expansion coefficients of the diffusion layer and the base material. Moreover, the thermal expansion coefficient of ϵ-$Fe_{2-3}N$ nitride evolves as a function of the nitrogen concentration (as shown in the table) [Somers, 1989, Somers and Mittemeijer, 1990, Gressmann et al., 2008]. During processing, volume stresses occur in this layer [Kreft et al., 1992, Kreft et al., 1995, Gunther et al., 2004]. In the early stages of treatment, the compressive residual stresses are low. They then increase before becoming rather stable. Barrallier demonstrated the very minimal role of cooling in creating residual stresses in the diffusion layer using a self-consistent micromechanical model [Barrallier, 1992],

— Different lattice parameters are used, resulting in crystal incompatibilities at the precipitate/matrix interface.

Residual stresses are found throughout the multiscale in-depth incompatibility of stress-free strain. In other ways, the residual stress field and associated elastic strain exists to make the total strain compatible and satisfy the Saint-Venant compatibility equations (see in Eq. 1.14 section 1.2.2.1). The stress-free strain ε_{ij}^{F} is directly related to the microstructure transformations that occur during nitriding. In fact, Fig. 1.11 presented by S. Jegou [Jegou, 2009] shows this scaling problem. The origin of the residual stresses in the case of nitriding is due to precipitation and phase transformation induced by nitrogen diffusion (order II stresses) and the resulting

microstructure gradient (order I stresses see Fig. 1.11). From a macroscopic point of view, the nitrided surface expands and the base material opposes it. The state of compressive stress is therefore due to the positive values of volume change of the nitrided layer. From a microscopic point of view, the nitrided layer can be divided into sub-layers according to depth, each of which is distinguished by volumetric strains specific to its microstructure. The chemical gradient linked to the diffusion of nitrogen atoms generates a microstructure gradient and therefore a volume strain gradient along the diffusion axis. In the case of nitriding a single geometry specimen, the strain gradient can be assumed to lead to incompatible strains in the direction of the gradient [Mittemeijer, 1984, Somers and Mittemeijer, 1990, Barrallier and Barralis, 1994]. As these strains are incompatible, additional accommodating strains will be created between the different depths, which, by equilibrium, leads to a planar state of compressive residual stresses at the surface. The macroscopic mechanical equilibrium is expressed by the divergence of the stress tensor (see Eq. 1.15 in section 1.2.2.1).

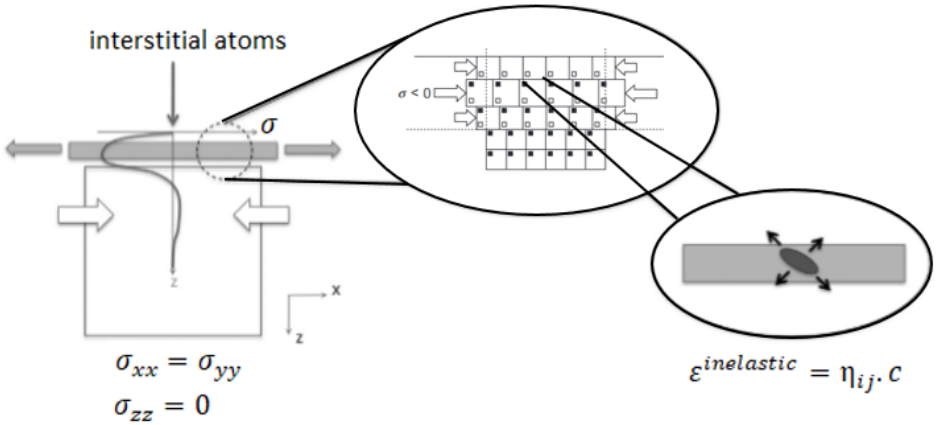

Figure 1.11 – Representation of the 3 orders of magnitude of residual stress [Jegou, 2009].

Stress analyses on previously decarburised nitrided surfaces, performed by X-ray diffraction, revealed that the lower the original carbon concentration, the higher the residual compressive stresses in ferrite [Barrallier, 1992, Barrallier and Barralis, 1994, Jegou, 2009, Jégou et al., 2011, Barrallier and Jégou, 2015, Barrallier and Jégou, 2016, Jegou et al., 2016, Jegou et al., 2018]. Again, it is shown that the distribution of additional elements between the solid solution of the ferritic matrix substitution and the tempered carbides is important.

Studies have shown the influence of carbon diffusion during processing on residual stresses, showing that any changes in the microstructure gradient will generate strong changes in residual stresses. [Barrallier, 1992, Jegou, 2009].

1.1.5 Influence of nitriding parameters

A gas nitriding treatment can be defined using three main parameters that are the nitrogen potential K_N, the treatment temperature T and the treatment time t. The influence of process parameters on residual stresses and hardening has been the subject of several studies [Dulcy and Gantois, 2012, Ginter, 2006, Guillot, 2018]. Their conclusions are as follows:

— Nitriding potential K_N: its increase causes the stress maximum to move towards the core and the stress field to expand, but has no effect on the residual stress maximum or the surface stress. Barralis observed

an increase in maximum surface hardness with nitriding potential [Barralis et al., 1986]. However, Ginter showed that if a white layer is present on the surface, K_N has no effect on the hardening of the nitrided layers [Ginter, 2006]. Figure 1.12 illustrates the evolution of nitrogen and carbon content as a function of nitriding potential, demonstrating that nitrogen enrichment and decarburisation are strongly limited by nitriding conditions,

— Nitriding time t: As previously shown in Figs. 1.6 and 1.7, the nitrogen profile and the nitride fraction of the alloying elements are highest at the beginning of the diffusion layer and decrease in a similar way to the base material [Locquet et al., 1997, Sennour et al., 2004] (see section 1.1.2.3). Figures 1.6 and 1.13 b) indicate that carbon exhibits a typical co-diffusion defined, on the one hand, by enrichment towards the nitrogen diffusion front and, on the other hand, by decarburisation at the gas/solid interface followed by enrichment of the compound layers during long nitriding. A 100-hour carbon profile may be separated into five main zones [Jegou, 2009, Jegou et al., 2010]:

  — zone 1: a surface overcarburization corresponding to the compound layer (note : this overcarburization is not observed in every case, as for example in figures 1.12 and 1.13 it is observed only in the case of figure 1.13b) for a treatment of 30 h.),

  — zone 2: a decarburised zone at the interface between the compound layer and the diffusion layer,

  — zone 3: a zone where the quantity of carbon increases from 0.2%m. to 0.4%m,

  — zone 4: an overcarburization at the nitrogen diffusion front due to carbide precipitation,

  — zone 5: the core material.

  The increase in nitriding time implies an expansion of zones 2 and 3 as well as an increase in overcarburation at the front of nitrogen diffusion. The amount of carbon in zone 3 is lower for 100 hours of nitruration compared to that measured for 10 hours. The nearly complete decarburization of zone 2 corresponds to the transition of cementite into nitride γ'-Fe_4N. The decrease in carbon content in zone 3 corresponds to the dissolution of cementite. These phase transitions help to explain the evolution of residual stresses observed with increasing nitruration time.

  — Surface compressive is caused by the transformation of cementite to nitride γ'-Fe_4N,

  — A reduction in the cementite fraction causes a reduction in specific volume and volume fraction of precipitate, resulting in a reduction in residual stresses,

  — An increase in over-carburation at the nitrogen diffusion front causes an increase in the carbide fraction. This precipitation of carbides causes a decrease of alloying elements in solid solution, resulting in a decrease in the precipitation of semi-coherent MN nitrides from the ferritic solid solution over time,

  — An increase in over carburisation at the diffusion front causes a decrease in the volume change with time, resulting in a decrease in the stress maximum.

— Nitriding temperature T: is recognised as a key parameter with a considerable impact on residual stresses as well as on hardening, involving the activation of stress relaxation events during processing (restoration, coalescence). The evolution of the nitrogen and carbon profiles as a function of three temperatures (480°C, 520°C and 550°C) is shown in Fig. 1.14. The temperature activates the diffusion of nitrogen, which leads to an increase in the effective depth and, consequently, to an increase in depth hardening. It is also known that increasing temperature causes a decrease in the maximum compressive stress, as

well as a loss of surface and core hardness (if the temperature is too close to the quenching temperature or if the treatment time is too long) due to coalescence of globular nitrides and hardened carbides. The surface hardness decreases with temperature because the size of the semi-coherent nitrides increases with temperature.

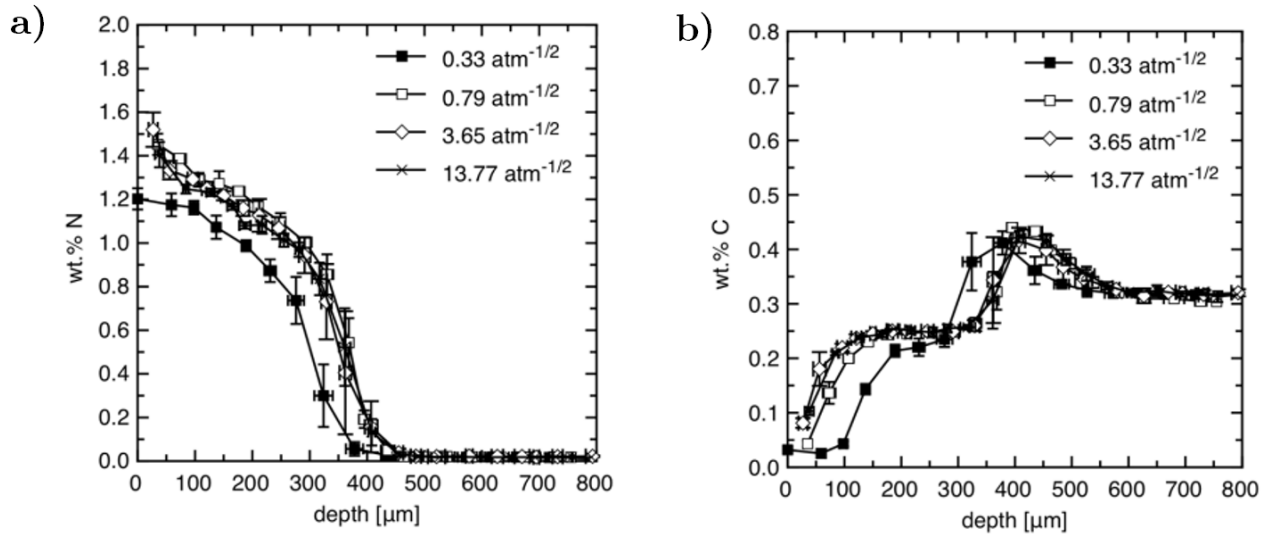

Figure 1.12 – Content in-depth profiles from OES analyses of a 33CrMoV12-9 steel nitrided at 550 °C during 30 h. a) Carbon content. b) Nitrogen content. [Fallot, 2015, Jegou et al., 2016]

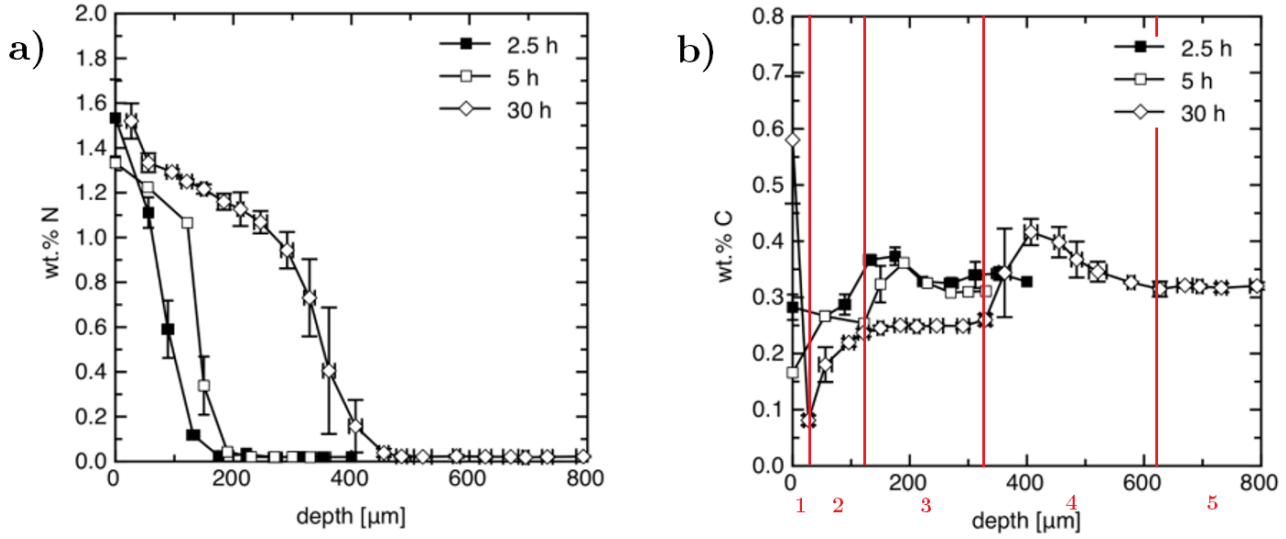

Figure 1.13 – Content in-depth profiles from OES analyses of a 33CrMoV12-9 steel nitrided at 550 °C with K_N 3.65 $atm^{-1/2}$. a) Nitrogen content. b) Carbon content. [Fallot, 2015, Jegou et al., 2016]

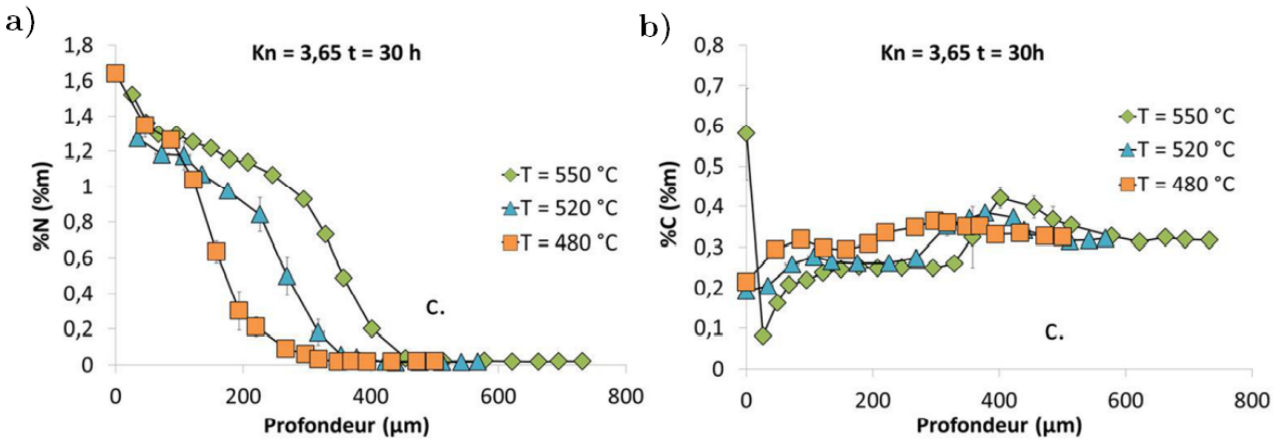

Figure 1.14 – Content in-depth profiles from OES analyses of a 33CrMoV12-9 steel nitrided during 30 h with K_N 3.65 $atm^{-1/2}$. a) Nitrogen content. b) Carbon content. [Fallot, 2015]

Studies have shown that, as the treatment temperature increases and the fraction of alloying elements decreases, the diffusion kinetics are accelerated compared to those of precipitation [Ginter, 2006]. This implies that nitrogen is likely to diffuse deeper into the material. Conversely, the higher the quantity of additions, the more the nitrogen atoms react with the additions in solid solution at the near surface, the more the diffusion and transformation kinetics are balanced [Leroy et al., 1986, Locquet et al., 1997, Ginter et al., 2006].

1.2 Coupling stress-diffusion

The description of the microstructure of a nitrided surface enabled the inclusion of several thermochemical concerns. As a result, nitriding treatment is a complex subject according to physical phenomena in competition. The main concern of the treatment is the diffusion of nitrogen. Diffusion in nitrided steels is driven by physical processes short-range diffusion (precipitation), long range diffusion (nitrogen diffusion) and co-diffusion (carbon). Section 1.1.2.3 demonstrated that nitrogen diffusion occurs in a forced regime, with a constant flux or concentration at the material surface. The key factor in diffusion is the chemical potential gradient with depth. Mechanical factors (stresses, plastic strains, etc.) caused by metallurgical phenomena (precipitation) can affect the diffusion mechanisms involved in precipitation processes (microscopic diffusion). The well-known Fick's laws can describe the diffusion of nitrogen [Fick, 1855] (see section 1.2.1). The first Fick's law only considers long-range diffusion, or diffusion without precipitation. This law, in the case where the diffusion coefficient D is considered constant, is therefore not representative of diffusion phenomena because it does not take into account stress coupling (stress-free strains ε^F). Several researchers have explored the diffusion-precipitation model; however, the link with stress has not been considered [Fallot, 2015]. Diffusion problems are vector problems, while stresses are tensor problems. This means that solving the stress-diffusion coupling equations is a spatial problem. For this reason, some researchers have focused on the coupling between diffusion and stress, concentrating only on volume diffusion (i.e. long range diffusion). Diffusion is a matter of scale, both local and global. Only the long-range diffusion (i.e. the global effect) is taken into account. In industry, effective diffusion depths are constantly being improved by increasing their thickness. Consequently, the analysis of the stress-diffusion coupling in this study will focus on the case of a binary system in infinitely dilute solid solution

(no precipitation). Several researchers have been interested in the coupling equations between diffusion and stress (both from the point of view of the coupling of mechanics to diffusion and diffusion to mechanics) since the middle of the 20 th century. Indeed, the objective has been to build physical models capable of managing the mechanical and chemical equilibrium of an open system (such as thermochemical surface treatments) by means of elastic coefficients. The purpose was then to review the methods needed to develop analytical formulations for stress-diffusion coupling using irreversible thermodynamics. Cahn et Larché proposed a model based on the Li's equation to study the influence of local stresses on diffusion in a solid medium with compositional inhomogeneities [Chen-Min Li, 1978]. They developed a model based on the thermodynamics of a multicomponent solid which finds equilibrium under stress (non-hydrostatic) [Larché and Cahn, 1973, Larche and Cahn, 1978a, Larché and Cahn, 1982, Larché and Cahn, 1985]. They placed themselves in a purely elastic case, in order to estimate that equilibrium is possible since any relative movement of atoms, either by sliding or by diffusion, is ignored. They assume that the solid is composed of a lattice embedded in the solid which allows them to define the displacement and thus the strain, but they place themselves in a scenario where all variables create a set of state variables (strain, compositional variables and entropy density). Since infinitesimal strain is assumed, the thermodynamic fields expressed in densities will correspond either to the current state of the crystal (Eulerian description) or to the appropriate reference state (Lagrangian description).

1.2.1 Fick's theory

In 1855, Fick proposed two equations in analogy with Fourier's heat equation [Fourier and Darboux, 1822]. The first Fick's law (given in Eq. 1.4) in the case of the diffusion of a binary (without precipitation) is [Fick, 1855]:

$$\left(J_I^\phi\right)_z = -D_I^\phi \frac{\mathrm{d}c_I^\phi}{\mathrm{d}z} \tag{1.4}$$

Where $\left(J_I^\phi\right)_z$ is the flux in z direction , c_I^ϕ is the concentration of the element I, $\frac{\partial c_I^\phi}{\partial z}$ is the gradient of concentration as a function of z direction and D_I^ϕ is the coefficient of diffusion of element I in the phase ϕ_I described by an Arrhenius law [Arrhenius, 1889, Logan, 1982].

The second Fick's law (Eq. 1.5), is known as the law of mass conservation in a non-permanent equation. This equation applies only to strictly conservative species (or particles) [Philibert, 1990]. Eq. 1.5 predicts changes in concentration with respect to time in the form of a partial differential equation:

$$\frac{\partial c_I^\phi}{\partial t} = -\frac{\partial \left(J_I^\phi\right)_z}{\partial z} \qquad \text{on} \qquad \mathrm{V} \tag{1.5}$$

Where $\frac{\partial c_I^\phi}{\partial t}$ is the gradient of concentration as a function of time, $\frac{\partial c_I^\phi}{\partial z}$ is the gradient of flux as a function of z direction and Eq. 1.6 is the boundary condition:

$$J_I^\phi = \left(J_I^\phi\right)_z n_z \qquad \text{on} \qquad \partial\mathrm{V} \tag{1.6}$$

Where n_z is the z normal and ∂V is the surface of the volume V.

Eq.1.4 describes the diffusion of matter in a binary medium assuming that the diffusion is isotropic in the steady state assumption but can also describe that in the anisotropic case if c_I^ϕ depends only on z. Diffusion occurs then from regions of high concentration to regions of low concentration, with a magnitude proportional to the concentration gradient (spatial derivative).

The diffusion coefficient can be defined as a linear function of the inverse of the absolute temperature [Philibert, 1990]:

$$D_I^\phi = D_0^\phi \exp\left(-\frac{\Delta H}{k_B T}\right) = D_0^\phi \exp\left(-\frac{E_A}{RT}\right) \tag{1.7}$$

Where D_0^ϕ is the pre-exponential factor of the specie [$m^2.s^{-1}$], E_A is the activation energy [$J.mol^{-1}$], T is the temperature [K, R is the universal gas constant [$J.mol^{-1}.K^{-1}$], k_B is the Bolztmann's constant [$J.K^{-1}$] and ΔH is the enthalpy [J]. If D_I is considered independent of c_I, given the following initial and boundary conditions: $t = 0$, $c_I(z, 0) = 0$ and $c_I(0, t) = c_0$ for all t, the solution of Eq.1.5, in the case of a semi-infinite medium, is:

$$c_I(x, t) = c_0 \text{erfc}\left(\frac{z}{2\sqrt{D_I t}}\right) \tag{1.8}$$

where erfc is the complement error function, c_0 is the nitrogen concentration at the surface and c_I^∞ $(= 0)$ is the nitrogen concentration to infinity. If D_I varies with nitrogen concentration, Eq. 1.8 is insufficient to correctly describe the actual nitrogen concentration curve.

For a given temperature and limit concentration, from Eq. 1.8, the effective depth of nitriding, should follow a law in $\sqrt{t}$. The actual values of binary systems (e.g. Fe-N, Zr-O, Pd-H) are lower than those predicted by Fick's laws. This is due to the explanation given by Curie later reported in an article from 1984, on the non-validity of Fick's laws [Revel et al., 1984]. The presence of residual strains due to nitriding suggests that the shape of the curve is not perfectly under a Fick's law. In the case of long distance inhomogeneity, Fick's law was proved to be invalid. So, the classical diffusion laws are not sufficient to describe the evolution of the nitrogen distribution in the nitrided layer. This invalidity includes the fact that, it will be shown in the next sections, many authors employed the effective diffusion coefficient for a long period.

1.2.2 Elements of continuum mechanics and thermodynamics

The formalism of continuous mechanics and thermodynamics involves state variables (observable variables): the temperature T and the total strain ε (assuming small strains).

1.2.2.1 Fundamental statements of mechanics

1.2.2.2 Strain equations

In the present work, the infinitesimal transformations theory is taken into account, i.e. the hypothesis of small perturbations. This implies that in the case of small perturbations, the state of strain is represented by the linearized strain tensor ε_{ij} from v_i displacement, where:

$$\varepsilon_{ij}^{\text{tot}} = \frac{1}{2}\left(v_{i,j} + v_{j,i}\right) \tag{1.9}$$

The total strain is the sum between elastic strains ε^{e}, which are compatible strains and the stress-free strains (eigenstrains) ε^{F}, which are incompatible strains [Mura, 1987].

$$\varepsilon_{ij}^{\text{tot}} = \varepsilon_{ij}^{\text{e}} + \varepsilon_{ij}^{\text{F}} \tag{1.10}$$

In the case of small strains, isotropic material, an initially unstressed material and by a homogeneous approach with strictly constant coefficients (depending neither on t nor on T), the elastic strains $\varepsilon_{ij}^{\text{e}}$ are described as:

$$\varepsilon_{ij}^{\text{e}} = \frac{1+\nu}{E}\sigma_{ij} - \frac{\nu}{E}\,\sigma_{kk}.\delta_{ij} \tag{1.11}$$

Where ν is the Poisson's coefficient, E is the Young's modulus and δ_{ij} is the Kronecker's symbol.

Stress-free strains, $\varepsilon_{ij}^{\text{F}}$, are the sum of the plastic, thermal, volumetric strains and transformation strains. In the present work, thermal and plastic strains are neglected because no post-mortem plastic strain heterogeneity is observed, and temperature effects are negligible, especially during cooling. Only the volumetric strains that are associated with the phase transformations and the solid solution during the diffusion process are taken into account [Cahn, 1961].

In a case where a crystal lattice is in a homogeneous medium with anisotropic elastic properties, the stress-free strains $\varepsilon_{ij}^{\text{F}}$ function of c_I^{ϕ} are defined by [Larché and Cahn, 1973, Larché and Cahn, 1982, Cahn, 1961]:

$$\varepsilon_{ij}^{\text{F}}\left(c_I^{\phi}\right) = \left(\eta_I^{\phi}\right)_{ij} c_I^{\phi} \tag{1.12}$$

where c_I^{ϕ} is the concentration [mol/m^3] of the element I of the phase ϕ_I and $\left(\eta_I^{\phi}\right)_{ij}$ is the chemical expansion tensor defined as $\left(\eta_I^{\phi}\right)_{ij} = \frac{\partial \varepsilon_{ij}^{F}}{\partial c_I^{\phi}}$. In isotropic case, the compositional strain tensor takes the form:

$$\left(\eta_I^{\phi}\right)_{ij} = \eta_I^{\phi}\delta_{ij} = \frac{\triangle V_I}{3V_a}\delta_{ij} \tag{1.13}$$

Where $\triangle V_I$ is the partial molar volume of the element I and V_a is the molar volume of the host lattice.

In continuum mechanics, a tensor field of compatible strain in a plate is a unique tensor field that is obtained when the body is subjected to a single-valued continuous displacement field in order to guarantee the uniqueness of the solution [de Saint and de Saint-Venant, 1864]. Indeed, the residual stress field is statically admissible, the total strains $\varepsilon_{ij}^{\text{tot}}$ must satisfy the six compatibility equations:

$$\varepsilon_{ik,jl}^{\text{tot}} - \varepsilon_{jk,il}^{\text{tot}} - \varepsilon_{il,jk}^{\text{tot}} + \varepsilon_{jl,ik}^{\text{tot}} = 0 \tag{1.14}$$

1.2.2.3 Mechanical equilibrium

The equations of continuum mechanics Eq. 1.15, describe the variation of stresses in the absence of body forces ($f_i = 0$) on the solid and without taking into account of dynamical effects (inertia times acceleration), and

must be satisfied at every point within the body if the body is at static equilibrium. If the stress distribution is homogeneous, Eq. 1.15 is automatically satisfied since each derivative with respect to distance is identically equal to zero.

$$\sigma_{ij,j} = 0 \qquad \text{on} \qquad \text{V} \tag{1.15}$$

Where the σ_{ij} is the Cauchy's stress tensor. Eq. 1.16 describes the boundary conditions of the stress distribution existing in the material necessary for equilibrium, in the case where the volume element has a surface boundary, so that any surface force will also contribute to the forces equilibirium:

$$\sigma_{ij} n_j = g_i \qquad \text{on} \qquad \partial\text{V} \tag{1.16}$$

Where n_j is the unit vector in the direction $\vec{j}$ on the boundary and g_i is the applied force in the direction $\vec{i}$, in other words, is the surface force density in ∂V.

Constitutive equations are described by the generalized Hooke's law relating stresses to strains as follows:

$$\sigma_{ij} = \mathcal{C}_{ijkl} \left(\varepsilon_{kl}^{\text{tot}} - \varepsilon_{kl}^{\text{F}} \right) \tag{1.17}$$

Where $\mathcal{C}_{ijkl}$ is the stiffness tensor and the alternative form of the stress-strain relationship in the form:

$$\varepsilon_{ij}^{\text{tot}} = \varepsilon_{ij}^{\text{F}} + \mathcal{S}_{ijkl} \sigma_{kl} \tag{1.18}$$

Where $\mathcal{S}_{ijkl} = {\mathcal{C}_{ijkl}}^{-1}$ is the compliance tensor. Eq. 1.17, in the isotropic and elastic case, takes the form:

$$\sigma_{ij} = 2\mu \varepsilon_{ij}^{\text{e}} + \lambda \varepsilon_{kk}^{\text{e}} \delta_{ij} \tag{1.19}$$

Where λ and μ are the Lamé's coefficients.

1.2.2.4 Definition of chemical potential applied to interstitial diffusion

In 1923, Gilbert Newton Lewis introduced the concept of chemical activity a_I in the definition of chemical potential [Lewis and Randall, 1923]. This notion made it possible to study the cases of solids. For a solution at constant temperature and pressure, the chemical potential μ_I of the element I is equal to:

$$\mu_I \left(T, P, c_I^{\phi} \right) = \mu_I^0 \left(T \right) + RT \ln \left(a_I \right) \tag{1.20}$$

Where $a_I = \gamma_I c_I^{\phi}$, T is the temperature, γ_I is the activity coefficient, P is the pressure of a fluid around the medium [Pa], R is the universal gas constant [J.mol^{-1}.K^{-1}]. So in case of $\gamma_I = 1$, corresponding to an ideal solution (i.e. molecules of different species interact with molecules of other species in the same manner that molecules of the same species interact in the pure form), then $\mu_I \left(T, P, c_I^{\phi} \right) = \mu_I^0 \left(T \right) + RT \ln \left(c_I^{\phi} \right)$.

Cahn and Larché defined a new potential called "diffusion potential" on the thermochemical equilibrium of multiphase solids under stress [Larche and Cahn, 1978a]. Far from equilibrium, this potential is not constant throughout the solid and further diffusion can only occur in directions determined by gradients [Larché and Cahn, 1982,

Larché and Cahn, 1985]. They showed that the chemical potentials of interstitials μ_I^ϕ are constant and equal to the chemical potentials M_I^ϕ of the corresponding species (Eq. 1.21) the chemical potentials are assumed known at a fluid pressure P around the medium, stress σ_{ij} and composition c_I^ϕ:

$$M_I^\phi\left(P,\sigma_{ij},c_I^\phi\right)=\mu_I^\phi\left(P,\sigma_{ij},c_I^\phi\right) \tag{1.21}$$

It is important to understand that in the case of nitrogen diffusion, the main force is the chemical potential gradient $\frac{\partial\mu_N\left(P,\sigma_{ij},c_N^\phi\right)}{\partial c_N^\phi}$ of the nitrogen N in the ferritic matrix, where the diffusion occurs. The further away from the surface, the lower the chemical potential of the nitrogen.

Thanks to Eqs. 1.20 and 1.21, the gradient of the potential diffusion is equal to:

$$\frac{\partial M_I^\phi}{\partial c_I^\phi}=RT\frac{\partial\ln\left(a_I\right)}{\partial c_I^\phi}=RT\frac{\partial\ln\left(\gamma_I c_I^\phi\right)}{\partial c_I^\phi}=\frac{RT}{c_I^\phi}\left[1+\frac{\partial\ln\left(\gamma_I\right)}{\partial\ln\left(c_I^\phi\right)}\right] \tag{1.22}$$

Where $\phi=\left[1+\frac{\partial\ln(\gamma_I)}{\partial\ln\left(c_I^\phi\right)}\right]$ is the thermodynamic coefficient.

The compositional derivatives of the strain at constant temperature and stress, from 1.18, become:

$$\left(\frac{\partial\varepsilon_{mn}}{\partial c_I^\phi}\right)_{T,\sigma_{ij}}=\left(\frac{\partial\varepsilon_{mn}^{\mathrm{F}}}{\partial c_I^\phi}\right)_{T,\sigma_{ij}}+\left(\frac{\partial\mathcal{S}_{mnij}}{\partial c_I^\phi}\right)_{T,\sigma_{ij}}\sigma_{ij} \tag{1.23}$$

Thanks to the Maxwell's equation given by [Larché and Cahn, 1973]:

$$V_a\left(\frac{\partial\varepsilon_{ij}}{\partial c_I^\phi}\right)_{T,\sigma_{mn}}=-\left(\frac{\partial M_I^\phi}{\partial\sigma_{ij}}\right)_{T,c_I^\phi,\sigma_{mn\neq i,j}} \tag{1.24}$$

Eq. 1.23 becomes:

$$\rho_a\left(\frac{\partial M_I^\phi}{\partial\sigma_{ij}}\right)_{T,c_I^\phi,\sigma_{mn\neq i,j}}=-\left(\frac{\partial\varepsilon_{ij}^{\mathrm{F}}}{\partial c_I^\phi}\right)_{T,\sigma_{mn}}-\left(\frac{\partial\mathcal{S}_{ijkl}}{\partial c_I^\phi}\right)_{T,\sigma_{mn}}\sigma_{kl} \tag{1.25}$$

Where $\rho_a=\frac{1}{V_a}$ is the molar density of the host lattice.

The diffusion potential on the volume under stress σ_{ij}, at the same composition and temperature, is obtained by integrating Eq. 1.25 as:

$$\int_{M_I^\phi\left(T,P,c_I^\phi\right)}^{M_I^\phi\left(T,\sigma_{ij},c_I^\phi\right)}\rho_a\mathrm{d}M_I^\phi=-\int_{-P\delta_{ij}}^{\sigma_{ij}}\left(\frac{\partial\varepsilon_{ij}^{\mathrm{F}}}{\partial c_I^\phi}\right)\mathrm{d}\sigma_{ij}-\int_{-P\delta_{ij}}^{\sigma_{ij}}\left(\frac{\partial\mathcal{S}_{ijkl}}{\partial c_I^\phi}\right)\sigma_{kl}\mathrm{d}\sigma_{ij} \tag{1.26}$$

Where $M_I^\phi\left(T,P,c_I^\phi\right)$ is the diffusion potential of an unstressed volume element at temperature T, pressure P, and composition c_I^ϕ [Larché and Cahn, 1985]. If the composition derivative is independent of the stress state, the potential of diffusion becomes:

$$M_I^\phi\left(T,\sigma_{ij},c_I^\phi\right)=M_I^\phi\left(T,P,c_I^\phi\right)-V_a\left(\frac{\partial\varepsilon_{ij}^{\mathrm{F}}}{\partial c_I^\phi}\right)(\sigma_{ij}+P\delta_{ij})-\frac{V_a}{2}\left(\frac{\partial\mathcal{S}_{ijkl}}{\partial c_I^\phi}\right)\left(\sigma_{ij}\sigma_{kl}-P^2\delta_{ij}\delta_{kl}\right) \tag{1.27}$$

Eq. 1.27 gives the stress dependence of the diffusion potential when the small strain approximation is valid. As a reminder, the stress σ_{ij} is only a function of the real composition c_I^ϕ and the real strain ε_{ij}, regardless of the path chosen to reach that state. As explained before, the stress-free strains ε_{ij}^F are produced by a change of composition from 0 to c_I^ϕ at zero stress ($\sigma_{ij}=0$). Also, with the small strain assumption taken into account, a change in stress from 0 to σ_{ij} at constant composition c_I^ϕ implies that in the reference state, the pressure around the system is null $P=0$. So, Eq. 1.27 is simplified [Larché and Cahn, 1973, Larché and Cahn, 1982]:

$$M_I^\phi\left(T,\sigma_{ij},c_I^\phi\right)=M_I^\phi\left(T,0,c_I^\phi\right)-V_a\left(\frac{\partial\varepsilon_{ij}^{\mathrm{F}}}{\partial c_I^\phi}\right)\sigma_{ij}-\frac{V_a}{2}\left(\frac{\partial\mathcal{S}_{ijkl}}{\partial c_I^\phi}\right)\sigma_{ij}\sigma_{kl} \tag{1.28}$$

Where $M_I^\phi\left(T,0,c_I^\phi\right)=\mu_I\left(T,0,c_I^\phi\right)$ is the diffusion potential at zero stress.

If the elastic constants are independent of composition, Eq. 1.28 simplifies to:

$$M_I^\phi\left(T,\sigma_{ij},c_I^\phi\right)=M_I^\phi\left(T,0,c_I^\phi\right)-V_a\left(\frac{\partial\varepsilon_{ij}^{\mathrm{F}}}{\partial c_I^\phi}\right)\sigma_{ij} \tag{1.29}$$

The dependency of the chemical potential with the stress state was firstly developed from both Gibbs and Helmholtz free energies using a variational approach [Larche and Cahn, 1978a, Larché and Cahn, 1978]. Li et *al.* have developed the definition of the chemical potential of a moving component in a stressed solid based on the Gibbs equation [Li et al., 1966]. For a moving component, the chemical potential can only be defined at the surface. Even in a homogeneous chemically stressed body, the chemical potential of the stationary component may be different at different surfaces. If the crystal is isotropic or has cubic symmetry, the compositional strain is given by Eq. 1.13. Based on thermodynamic theory, when a mobile solute in an ideal and dilute solid solution is subjected to stresses, the diffusion potential becomes:

$$M_I^\phi\left(T,\sigma_{ij},c_I^\phi\right)=M_I^\phi\left(T,0,c_I^\phi\right)-V_a\eta_I^\phi\sigma_{kk} \tag{1.30}$$

In case of dilute solution i.e. $c<<1$ and isotropic material, the diffusion potential gradient becomes [Larché and Cahn, 1985]:

$$\frac{\partial M_I^\phi}{\partial x_i}=\frac{RT}{c_I^\phi}\frac{\partial c_I^\phi}{\partial x_i}-V_a\eta_I^\phi\frac{\partial\sigma_{kk}}{\partial x_i} \tag{1.31}$$

Eq. 1.31 was confirmed by Kirchheim [Kirchheim, 1986]. In fact, he showed that under applied tensile stress, the change in chemical potential (here equal to the potential of diffusion) is proportional to the stress and the partial molar volume V_a.

R. Kirchheim studied the effect of a torsion stress on wires, these experiments showed that the pure shear stress produced by torsional stress had no impact on diffusion kinetics relative to tensile stress and concluded on no change of the chemical potential. In addition, it was observed that torsion leads to a reorientation of point defects [Kirchheim, 1986, Hwang and Perng, 1994].

In the case of interstitial diffusion η is positive, i.e. an increase in the concentration of the constituent increases the volume of the crystal. For a given composition, it follows that a compressive hydrostatic stress ($\sigma_{kk} < 0$) increases the diffusion potential, while a tensile stress reduces it. Since the diffusion potential is constant at equilibrium, either the stress is uniform, in which case the composition is uniform, or the stress is not uniform and correlatively the composition is not uniform.

1.2.3 Stress-diffusion coupling

Cahn and Larché have defined a very rigorous method based on the thermodynamics of irreversible processes. Cahn and Larché used the equation developed by Li to study the dependence of local diffusion stresses in a solid medium, where the stresses developed from inhomogeneities of composition [Chen-Min Li, 1978, Larche and Cahn, 1978a, Larché and Cahn, 1982].

1.2.3.1 Coupling via diffusion equations

As presented before, the Fick's law were showed non-validated in case of the inhomogeneity at a long distance [Revel et al., 1984]. If not considered, one experimentally determined a so-called effective diffusion coefficient rather than an intrinsic one as it will be defined below. The stress-diffusion coupling shows the combined effect of a concentration gradient and a mechanically-induced driving force. More generally, when a force is applied, a concentration gradient is created involving diffusion which opposes "forced" diffusion [Philibert, 1990].

$$\left(J_I^\phi\right)_i = -\left(D_I^\phi\right)_{ij} \frac{\partial c_I^\phi}{\partial x_i} + \langle\left(v_I^\phi\right)_i\rangle c_I^\phi \tag{1.32}$$

Where $\langle\left(v_I^\phi\right)_i\rangle$ is the average speed where the Nernst-Einstein relationship gives $\langle\left(v_I^\phi\right)_i\rangle = \frac{F_j\left(D_I^\phi\right)_{ij} N_a}{RT}$ with F_j is the driving force (as the electrotransport, the thermotransport, the centrifugal force, the stress gradient,...) and N_a is the Avogrado's number. In the absence of force, defects migrate randomly by jumping from one site to another by thermal agitation.

$\langle\left(v_I^\phi\right)_i\rangle c_I^\phi$ corresponds to the Nernstian term i.e. the action of an external force, or driving force, under the effect of which the particles move with a certain average speed giving rise to a flow. In this work, $F_j = \frac{d\sigma_{ij}}{dx_i}$ is focused on a driving force due to a stress gradient [Kirchheim, 1986]. It follows that Eq. 1.32 takes the form:

$$\left(J_I^\phi\right)_i = -\left(D_I^\phi\right)_{ij}^{\text{eff}} \frac{\partial c_I^\phi}{\partial x_i} = -\left(D_I^\phi\right)_{ij} \left(1 + \frac{c_I^\phi}{k_B T} \frac{\partial \sigma_{ij}}{\partial c_I^\phi}\right) \frac{\partial c_I^\phi}{\partial x_i} \tag{1.33}$$

The presence of a gradient of stress induced by the composition is equivalent to an additional driving force. This term is a function of the state of stress and composition. It represents the stress-induced diffusion forces during diffusion of the species directly influencing the diffusion velocity of the mechanically diffusing atom undergone by the structure [Volkl, 1965, Wipf, 1976, Lewis et al., 1993]. Moreover, some studies show that the diffusion could be affected by external stresses. In fact, stresses can be decomposed as:

$$\sigma_{ij}^{\text{totale}} = \sigma_{ij}^{\text{residual}} + \sigma_{ij}^{\text{external}} \tag{1.34}$$

Where $\sigma_{ij}^{\text{residual}}$ is the residual stress tensor (presented in section 1.1.4) and $\sigma_{ij}^{\text{external}}$ is the external stress tensor. In fact, studies showed that the diffusion processes are affected by mechanical stresses, more precisely by crystal strains that cause them, through two possible origins [Beck et al., 1966, Li et al., 2017]:

— residual, corresponding to a state of self-equilibrated stress, i.e. they occur in a volume of material without being mechanically stressed [Noyan and Cohen, 1987, Macherauch, 1987, Barralis et al., 1999];

— external, corresponding to a state of mechanical stress applied to the limits of the volume of material.

Due to volume strains, i.e. stress-free strains (Eq. 1.12), interstitial diffusion causes the development of compressive surface stresses during mechanical equilibration (Eq. 1.14). Fig. 1.15 shows how various thickness samples can produce the same diffusion profile with distinct residual stress $\sigma_{ij}^{\text{residual}}$ profiles. The flux at instant t causes a concentration field, which induces a stress state and the flux kinetics. In other words, nitrogen diffusion may be represented as a closed loop in which the concentration creates a stress-free strains gradient $\frac{\partial \varepsilon_{ij}^{\text{F}}}{\partial x_i}$, which leads to a local stress gradient $\frac{\partial \sigma_{ij}^{\text{local}}}{\partial x_i}$, which leads to a global stress gradient $\frac{\partial \sigma_{ij}^{\text{global}}}{\partial x_i}$, which leads to the diffusion kinetics. Local stresses $\sigma_{ij}^{\text{local}}$ correspond to stresses at the mesoscopic scale, i.e. at the scale of individual small layers. The global stresses $\sigma_{ij}^{\text{global}}$ correspond to the stresses on a macroscopic scale, i.e. on the scale of the sample.

Richmond established, by analogy with thermoelasticity, the concept of residual strains owing to chemical concentration gradients. His study seeks to visualise the effect of nitriding time on the residual stress field (σ_θ, σ_r et σ_z in polar coordinates) for a nitrided bar of pure iron at 500°C. These findings show that as time passes, the surface stress lowers, stresses increase, and mechanical rebalancing leads in increased tensile stresses in the core [Richmond et al., 1964].

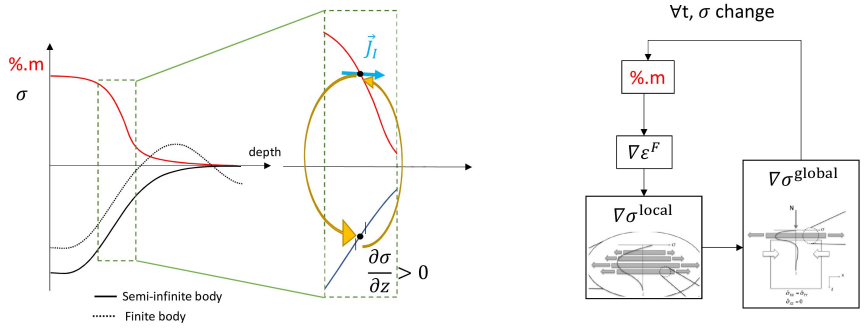

Figure 1.15 – (left) Schematic evolution of residual stresses for two sample thicknesses (semi-infinite and finite body) with the same diffusion profile of insertion atoms. (right) Evolution over time of residual stresses at local and global scales.

According to the physical description of atomic transport in a solid, the diffusion process must be detailed using the Thermodynamics of Irreversible Processes (TIP) theory. From the Helmholtz free energy F, it is possible to determine the useful work that can be provided by a closed thermodynamic system, at constant temperature T, during a reversible transformation:

$$F = U - TS \tag{1.35}$$

Where U is the internal energy and S is the entropy. It is then possible to introduce a new variable named the free energy density, in the case of elastic and isothermal study [Lemaitre and Chaboche, 1990]:

$$f_v\left(\varepsilon^e, c_I^\phi\right) = u_v - Ts_v \tag{1.36}$$

Where $s_v = \frac{S}{V}$ and $u_v = \frac{U}{V}$ are respectively the entropy and the internal energy densities per unit volume of the reference configuration (or per atom or lattice site). In case of an isothermal study, the total derivative of f_v is given by:

$$\dot{f}_v\left(\varepsilon^e, c_I^\phi\right) = \dot{u_v} - \dot{s_v}T \tag{1.37}$$

The internal energy and entropy can be defined according to thermodynamic laws [Voorhees and Johnson, 2004, Honig, 2007, Kozeschnik, 2007]. In continuum mechanics, the Clausius-Duhem inequality is often used to express the second law of thermodynamics to determine whether the constitutive relationship of a material is thermodynamically permissible. This inequality makes it possible to assert the irreversibility of natural processes, particularly with regard to energy dissipation. The objective is now to determine the Clausius-Duhem inequality in terms of the entropy. In fact, the entropy balance describes how the entropy of a body changes as a result of any modification of the system. The thermodynamic state of a crystal is by definition heterogeneous since composition, strain and entropy are functions of position and time. This implies that the entropy S or the internal energy U of the system must be expressed as the integral of their density over the volume of the system. By keeping with the equilibrium principle, the perturbation in the local entropy density must be accomplished holding the total entropy of the crystal, S, fixed:

$$\delta S = \int_{\mathcal{V}} \dot{\delta s_v} \quad \mathrm{d}\mathcal{V} = 0 \tag{1.38}$$

$$S = \int_{\mathcal{V}} \frac{ds_v}{dt} \quad \mathrm{d}\mathcal{V} \tag{1.39}$$

From equilibrium thermodynamics of homogeneous systems it is known that the entropy flux is the quotient of the diffusion flux $\vec{j}$ in the case of an open system and a similar relationship is postulated between the specific heat production r and the entropy production. With these assumptions, the global formulation of the Clausius-Duhem inequality is derived from the second law of thermodynamics [François et al., 2012a]:

$$\frac{d}{dt}\int_{\mathcal{V}} s_v d\mathcal{V} \geq \int_{\mathcal{S}} \frac{r}{T}\rho d\mathcal{S} - \int_{\mathcal{S}} \frac{M_I^\Phi\left(J_I^\phi\right)_i}{T} n_i d\mathcal{S} \tag{1.40}$$

Where t is the time, the integration is over the volume $\mathcal{V}$ of the body, $\mathcal{S}$ is the surface of the body, ρ is the mass density of the body, $\vec{n}$ is the unit normal to the surface. All the variables are functions of a material point at x at time.

The total entropy density $s_v\left(e, c_I^\phi\right)$ is known as the difference between the bulk entropy and the surface entropy where e is the internal energy density per unit volume. In our case, the system is adiabatic $r = 0$ i.e. the surface entropy will be not taken into account. From the hypotheses, the derivative of the total entropy density is:

$$\frac{ds_v}{dt} \geq -\text{div}J_s \tag{1.41}$$

where J_s is the entropy flux due to mass and energy diffusion (see Eq. 1.42).Eq. 1.41 shows that the local entropy production is positive if J_s is defined as [Garcke et al., 2004]:

$$J_s = -\frac{1}{T}\left(\sum_{I=1}^{n} M_I^\phi \left(J_I^\phi\right)_i\right) \tag{1.42}$$

So Eq. 1.41 combined with Eq. 1.42 take the form of an inequality as:

$$T\frac{\partial s_v}{\partial t} - \frac{\partial\left(M_I^\phi\left(J_I^\phi\right)_i\right)}{\partial x_i} \geq 0 \tag{1.43}$$

Through the same development as entropy S, the first principle of thermodynamic, in the case where $r = 0$, in terms of density, is given as:

$$\frac{\partial u_v}{\partial t} = \sigma_{ij}\frac{\partial \varepsilon_{ij}^{\text{tot}}}{\partial t} \tag{1.44}$$

The volumic dissipation takes the form:

$$\mathcal{D}_v = \frac{\partial u_v}{\partial t} - T\frac{\partial s_v}{\partial t} - \frac{\partial f_v}{\partial t} = \sigma_{ij}\frac{\partial \varepsilon_{ij}^{\text{tot}}}{\partial t} - \frac{\partial\left(M_I^\phi\left(J_I^\phi\right)_i\right)}{\partial x_i} - \frac{\partial f_v}{\partial t} \geq 0 \tag{1.45}$$

From Eq. 1.36, the free energy density is considered to have a mechanical part and a chemical part [Villani et al., 2014]:

$$f_v\left(\varepsilon_{ij}^e, c_I^\phi\right) = f_v^{\text{mech}}\left(\varepsilon_{ij}^{\text{e}}, c_I^\phi\right) + f_v^{\text{chem}}\left(c_I^\phi\right) \tag{1.46}$$

Where

$$f_v^{\text{mech}}\left(\varepsilon_{ij}^{\text{e}}, c_I^\phi\right) = \frac{1}{2}\varepsilon_{ij}^{\text{e}}\mathcal{C}_{ijkl}\left(c_I^\phi\right)\varepsilon_{ij}^{\text{e}} \tag{1.47}$$

and

$$f_v^{\text{chem}}\left(c_I^\phi\right) = E^f c_I^\phi + RTW \tag{1.48}$$

Where W is the number of possible paths for an interstitial atom. It is written in the form of a binomial coefficient. In a case of an ideal solution and for a monoatomic crystal i.e. an infinite and regular stack of identical atoms for interstitial atoms $W = c_I^\phi \ln\left(c_I^\phi\right) + \left(1 - c_I^\phi\right)\ln\left(1 - c_I^\phi\right)$ and in a infinite solution $W = c_I^\phi \ln\left(c_I^\phi\right)$, E^f is the enthalpy of formation of one mole for the species considered.

Thanks to Eq. 1.10 and Eqs. 1.45 to 1.48, the volumic dissipation $\mathcal{D}_v$ becomes [Lemaitre and Chaboche, 1990, Villani et al., 2014]:

$$\mathcal{D}_v = \left(\sigma_{ij} - \frac{\partial f_v}{\partial \varepsilon^{\mathrm{e}}_{ij}}\right)\frac{\partial \varepsilon^{\mathrm{tot}}_{ij}}{\partial t} + \left(M^{\phi}_I + \sigma_{ij}\frac{\partial \varepsilon^{\mathrm{tot}}_{ij}}{\partial c^{\phi}_I} - \frac{\partial f_v}{\partial c^{\phi}_I}\right)\frac{c^{\phi}_I}{\partial t} - \left(J^{\phi}_I\right)_i \frac{\partial M^{\phi}_I}{\partial x_i} \geq 0 \quad (1.49)$$

Since the Clausius-Duhem inequality holds regardless of any particular $\dot{\varepsilon}^{e}_{ij}$ and according to Coleman-Noll's argument, the state laws for stress σ_{ij} and diffusion potential M^{ϕ}_I are [Noll, 1974]:

$$\sigma_{ij} = \frac{\partial f_v}{\partial \varepsilon^{\mathrm{e}}_{ij}} \quad (1.50)$$

$$M^{\phi}_I = \frac{\partial f_v}{\partial c^{\phi}_I} - V_a \sigma_{ij}\left(\eta^{\phi}_I\right)_{ij} \quad (1.51)$$

From Eqs. 1.49 to 1.51, the inequality dissipation is simplified:

$$\mathcal{D}_v = -\left(J^{\phi}_I\right)_i \frac{\partial M^{\phi}_I}{\partial x_i} \geq 0 \quad (1.52)$$

To ensure positivity of $\mathcal{D}_v$, the existence of a convex dissipation potential $\Omega\left(\nabla M^{\phi}_I\right)$ is used [Lemaitre and Chaboche, 1990]

$$\left(J^{\phi}_I\right)_i = -\frac{\partial \Omega^{\mathrm{chem}}}{\partial\left(\frac{\partial M^{\phi}_I}{\partial x_i}\right)} \quad (1.53)$$

$$\Omega^{\mathrm{chem}} = \frac{1}{2} B_{ij}\frac{\partial M^{\phi}_I}{\partial x_i}\frac{\partial M^{\phi}_I}{\partial x_i} \quad (1.54)$$

These two equations allowed to understand the meaning of the Cahn and Larché formalism. Indeed, they used a formalism based on the equation defined by [Einstein, 1905] and Darken [Sridhar, 2010], showing that the flux is proportional to the gradient of the diffusion potential as presented in Eq. 1.55 [Larché and Cahn, 1973, Larche and Cahn, 1978a, Larché and Cahn, 1982].

$$\left(J^{\phi}_I\right)_i = -B^{\phi}_{ij}\frac{\partial M^{\phi}_I}{\partial x_i} \quad (1.55)$$

Cahn et Larché proposed a development regarding the coefficient B, which is also known as the Onsager matrix [Larché and Cahn, 1985]. It is a function of local temperature T, stress σ and composition c^{ϕ}_I. Voorhees et Larché defined the coefficient B_{ij} as a function of composition and stress, for isotropic material, in the case of a first-order stress [Larché and Voorhees, 1996]:

$$B_{ij} = \frac{c^{\phi}_I}{\Phi RT}\left(B^0_{ij} + B^1_{ijkl}\sigma_{kl}\right) \quad (1.56)$$

Where:

$$B^0_{ij} = D^{\phi}_I \delta_{ij} \quad (1.57)$$

$$B^1_{ijkl} = \beta\delta_{ij}\delta_{kl} + \gamma_I\left(\delta_{ik}\delta_{jl} + \delta_{il}\delta_{jk}\right) \quad (1.58)$$

Where $\Phi\left(=1+\left(\frac{\partial \ln \gamma_I}{\partial \ln c_I^\phi}\right)\right)$ is the thermodynamic factor. Larché and Voorhees proposed that the coefficients β and γ_I are simple scalars [Larché and Voorhees, 1996]. γ_I is defined as the thermodynamic activity coefficient, by Philibert [Philibert, 1996b], which also intervenes in the chemical activity factor (see Eq. 1.20) and the coefficient β is a measure of the activation volume.

Thanks to simplications, Eq. 1.56 becomes:

$$B_{ij} = \frac{c_I^\phi}{\Phi RT}\left(D_I^\phi.\delta_{ij} + \beta\sigma_{kk}\delta_{ij} + 2\gamma_I\sigma_{ij}\right) \tag{1.59}$$

The addition of the terms $(\beta\sigma_{kk}\delta_{ij} + 2\gamma_I\sigma_{ij})$ shows the influence of the stresses on the mobility by means of the hydrostatic stresses σ_{kk} and the normal stresses σ_{ij}. The authors suggest and show, through experiments, that the term $2\gamma_I\sigma_{ij}$ equivalent to the effect of shear does not seem to have any influence on the mobility [Larché and Voorhees, 1996, Philibert, 1996b, Kirchheim, 1986]. Furthermore, if the three components σ_{kk} are equal, the well-known effect of hydrostatic pressure is present [Mehrer, 1996]. Finally, it it noticed that $\beta\sigma_{kk}\delta_{ij}$ and $2\gamma\sigma_{ij}$ are homogeneous to a diffusion coefficient, β and γ_I are in [$\mathrm{cm}^2.\mathrm{s}^{-1}.\mathrm{MPa}^{-1}$]. Through the study of the unit of the two coefficients, it is possible to conclude that neither of them has a unit homogeneous to the given definition. At present, it is not possible to really define these two coefficients β and γ_I. They will therefore be used without giving them a physical meaning.

J.M-C. Li studied chemical stresses in elastic media of simple geometries [Li, 1981]. J.L. Chu, used the formalism of J.M-C. Li, and conducted an analysis of the effects of chemical stresses on diffusion [Chu and Lee, 1994]. They found that chemical stresses improve mass transfer and that the effective diffusivity resulting from chemical stresses is proportional to the concentration.

Using Eqs. 1.22, 1.30 and 1.59, and assuming no dependence of elastic properties with the composition change, the flux (Eq. 1.55) in general case is equal to:

$$\left(J_I^\phi\right)_i = -\frac{c_I^\phi}{\Phi RT}\left(D_I^\phi\delta_{ij} + \beta\sigma_{kk}\delta_{ij} + 2\gamma_I\sigma_{ij}\right)\left(\frac{RT\Phi}{c_I^\phi}\frac{\partial c_I^\phi}{\partial x_i} - V_a\eta_{kl}\frac{\partial\sigma_{kl}}{\partial x_i}\right) \tag{1.60}$$

From the definition of the thermodynamic factor given in Eq. 1.22, in case of infinitely diluted solution $c << 1$, it is possible to write:

$$\frac{\partial \ln\gamma_I}{\partial c_I^\phi}\frac{\partial c_I^\phi}{\partial \ln c_I^\phi} = \frac{\frac{\partial\gamma}{I}}{\partial t}\gamma_I c_I^\phi \tag{1.61}$$

So the thermodynamic factor Φ:

$$\lim_{c_I^\phi\to 0^+}\Phi = \lim_{c_I^\phi\to 0^+}\left[1 + \frac{\partial \ln\gamma_I}{\partial \ln c_I^\phi}\right] = 1 \tag{1.62}$$

In case of isotropic material, it follows:

$$\left(J_I^\phi\right)_i = -\frac{c_I^\phi}{RT}\left(D_I^\phi\delta_{ij} + \beta\sigma_{kk}\delta_{ij} + 2\gamma_I\sigma_{ij}\right)\left(\frac{RT}{c_I^\phi}\frac{\partial c_I^\phi}{\partial x_i} - V_a\eta\frac{\partial\sigma_{kk}}{\partial x_i}\right) \tag{1.63}$$

If Eq. 1.63 is written as Eq. 1.33, an effective diffusion coefficient can be defined as:

$$\left(D_I^\phi\right)^{\text{eff}} = \left(D_I^\phi \delta_{ij} + \beta\sigma_{kk}\delta_{ij} + 2\gamma\sigma_{ij}\right)\left(1 - \frac{V_a\eta}{RT}c_I^\phi\frac{\partial\sigma_{kk}}{\partial c_I^\phi}\right) \tag{1.64}$$

In case of dilute solution and when the tensor B_{ij} is independent of the stresses, Eq. 1.59 takes the form defined by [Larché and Cahn, 1982] (Eq. 1.65):

$$B_{ij} = \frac{D_I^\phi \delta_{ij} c_I^\phi}{RT} \tag{1.65}$$

Where the tensor ${D_I^\phi}_{ij}$ is the diffusion coefficient of the tracer in dilute solution. So the flux equation is finally equal to:

$$\left(J_I^\phi\right)_i = -D_I^\phi\delta_{ij}\frac{\partial c_I^\phi}{\partial x_i} + \left(\frac{D_I^\phi\delta_{ij}V_a}{RT}c_I^\phi\eta\frac{\partial\sigma_{kk}}{\partial x_i}\right) \tag{1.66}$$

1.2.3.2 Coupling via composition fields

It is necessary to determine the coupling from a mechanical point of view as a function of the composition fields. As explained previously, at equilibrium, the diffusion potential M is constant and satisfies the mass balance equation (Eqs. 1.5 and 1.6). The expression of the chemical equilibrium concentration is obtained as a function of the corresponding diffusion potential, $\left(M_I^\Phi\right)_{eq}$, from Eq. 1.51, assuming that $c_I^\phi \ll 1$.

$$\left(c_I^\Phi\right)_{eq} = \exp\left(\frac{V_a}{RT}\left(M_I^\Phi\right)_{eq} - \frac{E_f}{RT}\right)\exp\left(\frac{V_a}{RT}\left(\eta_I^\Phi\right)_{ij}\sigma_{ij}\right) \tag{1.67}$$

In the case of an open-system elastic constant system, Cahn and Larché introduced a notion χ_I^ϕ as [Larché and Cahn, 1985]:

$$\frac{1}{\chi_I^\phi} = \rho\left(\frac{\partial M_I^\Phi}{\partial c_I^\Phi}\right)_{\sigma_{ij}=0} \tag{1.68}$$

Eqs. 1.51 and 1.68, allow to simplify the chemical equilibrium concentration, as:

$$\left(c_I^\Phi\right)_{eq} = \left(c_I^\Phi\right)_0 + \chi_I^\phi\left(\eta_I^\Phi\right)_{ij}\sigma_{ij} \qquad \text{avec} \qquad \chi_I^\phi = \frac{V_a}{RT}c_I^\phi \tag{1.69}$$

Where $\left(c_I^\Phi\right)_0 = \exp\left(\frac{V_a}{RT}\left(M_I^\Phi\right)_{eq} - \frac{E_f}{RT}\right)$

At equilibrium, where χ_I^ϕ is taken as a function of $c_I^\phi = \left(c_I^\Phi\right)_0$:

$$\varepsilon_{ij}^F\left(c_I^\phi\right) = \left(\eta_I^\Phi\right)_{ij}c_I^\phi + \chi_I^\phi\left(\eta_I^\Phi\right)_{ij}\left(\eta_I^\Phi\right)_{kl}\sigma_{kl} \tag{1.70}$$

According to Hooke's law (Eq. 1.17) , the total strain tensor is written as:

$$\varepsilon_{ij}^{tot} = \left(\mathcal{S}_{ijkl} + \chi_I^\phi\left(\eta_I^\Phi\right)_{ij}\left(\eta_I^\Phi\right)_{kl}\right)\sigma_{kl} + \left(\eta_I^\Phi\right)_{ij}c_I^\phi \tag{1.71}$$

According to Cahn and Larché, [Larché and Cahn, 1985], the compliance tensor for isotropic material is of the form:

$$\mathcal{S}^0_{ijkl} = \mathcal{S}_{ijkl} + \chi^\phi_I \left(\eta^\Phi_I\right)_{ij} \left(\eta^\Phi_I\right)_{kl} \tag{1.72}$$

$$\mathcal{S}^0_{ijkl} = \left(-\frac{\nu}{E} + \chi^\phi_I \left(\eta^\Phi_I\right)^2\right) \delta_{kl} + \frac{1}{2G} \left(\delta_{ik}\delta_{jl} + \delta_{il}\delta_{jk}\right) \tag{1.73}$$

The equation of mechanical equilibrium Eq. 1.5, without force at long distance thus becomes:

$$\mathrm{div}\left[{\mathcal{S}^0_{ijkl}}^{-1} \left(\varepsilon^{tot}_{kl} - \left(\eta^\Phi_I\right)_{kl} c^\phi_I\right)\right] = 0 \tag{1.74}$$

This equation (Eq. 1.75) shows that the problem of diffusion/mechanical equilibrium is equivalent to solving the purely elastic problem for a "fictitious" coefficient $\mathcal{S}^0_{ijkl}$ known. The elasticity constants for an open system are defined as follows:

$$\nu_0 = \frac{\nu - \chi^\phi_I \left(\eta^\Phi_I\right)^2 E}{1 + \chi^\phi_I \left(\eta^\Phi_I\right)^2 E} \quad ; \quad E_0 = \frac{E}{1 + \chi^\phi_I \left(\eta^\Phi_I\right)^2 E} \quad ; \quad G_0 = G \tag{1.75}$$

Where ν_0 is the "fictitious" Poisson's coefficient, E_0 is the "fictitious" Young's modulus and $G = \frac{E}{2(1+\nu)}$ is the shear modulus. The fictitious tensor of compliance, for isotropic material, then becomes:

$$\mathcal{S}^0_{ijkl} = -\frac{\nu_0}{E_0}\delta_{ij}\delta_{kl} + \frac{1}{2G_0} \left(\delta_{ik}\delta_{jl} + \delta_{il}\delta_{jk}\right) \tag{1.76}$$

Eqs. 1.75 to 1.76 show that if the concentration, c^ϕ_I, or the coupling parameter, η, are small; then, the open system constants reduce to the standard elastic constants.

This same study, in the case of isotropy, can be carried out by means of the generalised Hooke's law Eq. 1.10 and Eqs. 1.11 to 1.12:

$$\varepsilon^{\mathrm{tot}}_{ij} = \frac{1+\nu}{E}\sigma_{ij} - \frac{\nu}{E}\sigma_{kk}\delta_{ij} + c^\phi_I \eta^\Phi_I \delta_{ij} \tag{1.77}$$

So:

$$\varepsilon^{\mathrm{tot}}_{ij} - \eta^\Phi_I \delta_{ij} c^\phi_I = \frac{1+\nu}{E}\sigma_{ij} - \frac{\nu}{E}\sigma_{kk}.\delta_{ij} \tag{1.78}$$

The previous equation becomes as a function of the strain:

$$\sigma_{ij} = 2\mu \left(\varepsilon^{\mathrm{tot}}_{ij} - c^\phi_I \eta^\Phi_I \delta_{ij}\right) + \lambda \left[\varepsilon^{\mathrm{tot}}_{kk} - c^\phi_I 3\eta^\Phi_I\right] \delta_{ij} \tag{1.79}$$

However, in the isotropic case the Lamé coefficients μ et λ are a function of E_0 et ν_0 (elasticity constants for an open system):

$$\lambda = \frac{E_0 \left(\nu_0 + \chi_I^{\Phi} \left(\eta_I^{\Phi} \right)^2 E_0 \right)}{(1+\nu_0) \left(1 - 2\nu_0 - 3\chi_I^{\Phi} \left(\eta_I^{\Phi} \right)^2 E_0 \right)} \tag{1.80}$$

$$\mu = \frac{E_0}{2\left(1+\nu_0\right)} \tag{1.81}$$

The equation of mechanical equilibrium Eq. 1.15 thus becomes in the case of an isotropic material:

$$\mathrm{div}\left[2\mu \left(\varepsilon_{ij}^{\mathrm{tot}} - c_I^{\phi} \eta_I^{\Phi} \delta_{ij} \right) + \lambda \left[\varepsilon_{kk}^{\mathrm{tot}} - c_I^{\phi} 3 \eta_I^{\Phi} \right] \delta_{ij} \right] = 0 \tag{1.82}$$

1.2.4 Numericals simulations carried out on the coupling stress-diffusion

As analytical solutions are listed under certain study hypotheses, it is worthwhile to enumerate several simulations that have been performed in various domains leading to the diffusion phenomena in a metallic material.

1.2.4.1 Without stress coupling

Some research have focused on modelling diffusion in the case of a binary system, taking precipitation events into consideration but ignoring the coupling with stresses [Somers and Mittemeijer, 1995, Torchane et al., 1996, Keddam et al., 2004a, Keddam et al., 2005, Brossard et al., 2007, Torchane, 2014]. Their goals were to use a model based on the Fick equations to investigate the growth dynamics of the various phases shown on the Lehrer diagram, notably the ϵ-$Fe_{2-3}N$ and γ'-Fe_4N phases in the case of pure iron. The models were created to simulate the formation of monolayers and bilayers on a substrate in which solute diffusion determines growth kinetics as a function of the gas nitriding process parameters (t, T, K_N). The condition of pure iron is acquired directly from the experimental nitrogen profile (shown in Fig. 1.4). The numerical simulations were then compared to experimental data. The kinetics of layer development and microstructure evolution were studied using mass sampling equipment, layer thickness measurements and optical microscopy. Torchane demonstrates the consistency of the thickness values of the separated phases, and finds that the analytical predictions are in agreement with the actual results [Torchane et al., 1994].

Identification of the experiment, i	1	2	3	4	5
Time of treatment, t (min)	30	60	120	180	240
Surface nitrogen concentration,	8,50	8,47	8,52	8,53	8,48
C_N^S (Wt.%)	**8,50**	**8,50**	**8,50**	**8,50**	**8,50**
($\varepsilon + \gamma'$) total layer thickness,	6,00	8,50	12,20	14,80	17,10
$\lambda_{\gamma'\alpha}$ (µm)	**6,15**	**8,70**	**12,30**	**15,07**	**17,40**
ε layer thickness,	2,65	3,65	5,40	6,50	7,75
$\lambda_{\varepsilon\gamma'}$ (µm)	**2,69**	**3,81**	**5,39**	**6,60**	**7,62**
γ' layer thickness,	3,35	4,85	6,80	8,30	9,35
$\lambda_{\gamma'} = (\lambda_{\gamma'\alpha} - \lambda_{\varepsilon\gamma'})$ (µm)	**3,46**	**4,89**	**6,91**	**8,47**	**9,78**

Figure 1.16 – Experimental and theoretical thicknesses (in bold) of ϵ and γ' and surface nitrogen concentrations determined at 570°C during a gas nitriding treatment on pure iron. [Torchane et al., 1994]

In the applied case of gas nitriding, models have been developed on: pure iron [Somers and Mittemeijer, 1995, Du and Ägren, 1995, Du and Ågren, 1996, Torchane et al., 1996, Mittemeijer and Somers, 1997, Sun and Bell, 1997, Belmonte et al., 2001, Somers, 2004, Keddam et al., 2004b], pure iron for industrial steels [Cavaliere et al., 2009], binary systems like Fe-V, Fe-Cr or Fe-Mo [Sun and Bell, 1997, Gouné et al., 2000, Schacherl et al., 2004, Hosmani et al., 2007] or even on the steel grade 33CrMoV12-9 (grades used during this thesis work) [Locquet, 1998, Ginter, 2006, Jegou, 2009, Depouhon et al., 2014]. The modelling of nitriding is complex because many physico-chemical phenomena (diffusion, precipitation, phase transformation, interface movement, and carbon diffusion) take place during the treatment. Several points have to be taken into consideration for the modelling of this thermochemical treatment:

— The determination of the initial nitrogen surface condition, following the Dirichlet or Neumann conditions as explained in subsection 1.2.3,

— Modelling the growth of the compound layer. The modelling of the compound layer necessitates the creation of a multi-layer system γ'-Fe4N/ ϵ-$Fe_{2-3}N$/ α-Fe with nitrogen diffusion in each of these layers. Because these layers expand during treatment, an interface displacement model is required,

— MN nitrides precipitate from the alloying elements in solid solution, modifying the nitrogen diffusion kinetics,

— The simulation of the co-diffusion of carbon with nitrogen [Barrallier, 1992, Locquet, 1998, Chaussumier, 1999, Goret, 2006, Jegou, 2009].

A model has been developed, in the laboratory, in the ADA95 language since the 90s [Barrallier, 1992, Locquet, 1998, Chaussumier, 1999, Goret, 2006, Jegou, 2009, Fallot, 2015]. This model is coupled to a thermodynamic database [AB, 2012] via the Thermo-Calc software [Andersson et al., 2002]. The model currently works for the industrial grade 33CrMoV12-9 but can work for any steel grade. It allows the determination of the effective nitriding depth, the phase distribution within the diffusion layer and the extent of the residual stress field. In fact, the nitriding model is divided into three distinct modules:

— n°1: Diffusion,

— n°2: Simulating the precipitation of nitrided layers taking into account carbon diffusion,

— n°3: Residual stress simulation (i.e. micro-mechanical model allowing the determination of residual stresses in the diffusion layer),

The module n°2 follows different steps as presented in Fig 1.17. The first step corresponds to the initialization of the system (nitriding conditions). Only nitrogen and carbon in solid solution are susceptible to diffusion. Boundary conditions were chosen, in terms of nitrogen and carbon surface concentration, in order to treat them simultaneously: compound layer, $C_N(0,t) = 2\%$ m. and $C_C(0,t) = 0.2\%$ m and no compound layer, $C_N(0,t) = 1.2\%$ m. and $C_C(0,t) = 0.03\%$ m. At each time step, the total nitrogen and carbon concentration is calculated to determine the new equilibrium phases. As explained previously (see section 1.1.2.3) the diffusion of nitrogen in the material leads to the transformation of carbides into nitrides, causing a redistribution of carbon.

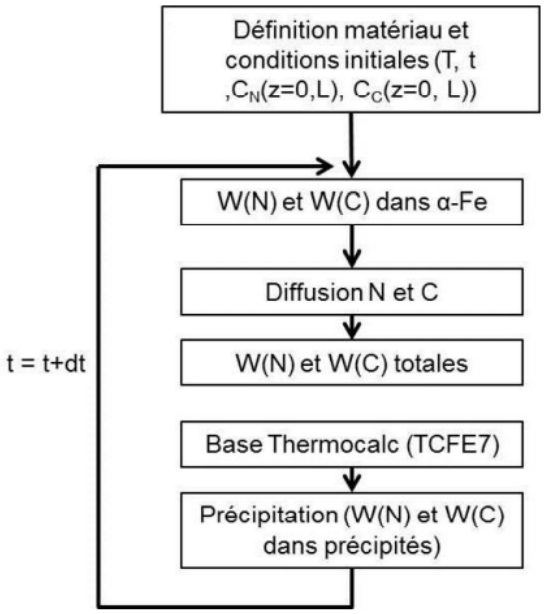

Figure 1.17 – The algorithm of the diffusion-precipitation programme (module n°2) programmed at the MSMP laboratory [Fallot, 2015].

The model made it possible to highlight several things such as the evolution of the mass fraction of M_7C_3 carbides, the mass fraction of $M_{23}C_6$ carbides or that of cementite (see [Barrallier, 1992, Jegou, 2009, Fallot, 2015] for more details).

The model showed some differences in the residual stress profiles between the simulation and the experiment. This might be attributable to a variety of factors, as for example:

— an underestimate of the precipitate fraction,

— no distinction between nitride volumes (e.g., semi-coherent nitride precipitation volume variation > volume variation of incoherent nitride from the transformation of tempering carbides),

— The volume change is determined immediately, not gradually (difference between t initial and t final),

— The mechanical model is calculated directly without taking into consideration the change of the load during treatment.

Although this model estimates the stresses at the end, it is not regarded as a model that takes the stresses into consideration throughout diffusion. To account for the coupling with stresses, a computation at each time increment is required to see the influence of diffusion-induced stresses on diffusion kinetics as well as the effect of external stresses on diffusion kinetics.

1.2.4.2 With stress coupling

The models presented correspond to the case without stress couplings. However, as previously stated, researchers have proved the failure of Fick's law for solid-state diffusion by employing Pierre Curie's work, which established that long distance elastic interactions caused by compositional inhomogeneities result in non-local contributions [Revel et al., 1984]. In other words, self-induced stress fields originate the phenomena of stress-induced diffusion. This is why research have been carried out on coupling. The goal of this numerical research is to predict cracks, for example, in hydrogen or oxygen diffusion issues, in order to enhance diffusion kinetics and therefore create thicker diffusion layers. However, it is also interesting to minimise treatment duration or temperature.

Rozendaal demonstrated, in a study of a nitrided pure iron plate (taking precipitation events into consideration), that the residual stresses at the surface are small, -142 MPa (as shown in Fig. 1.18).

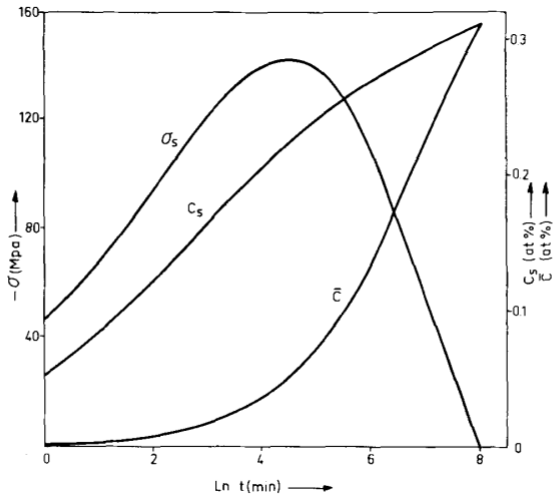

Figure 1.18 – Surface Sress σ_S, nitrogen surface concentration C_S and average concentration $\overline{C}$ of a specimen of thickness 2mm as a function of nitriding time t at 833 K. [Rozendaal et al., 1983]

However, much research has focused on the formation of surface layers (for example, the compound layer in the case of nitriding) or the diffusion layer. Indeed, as mentioned earlier, the interest of each layer is determined by the subsequent use of the part. In the case of gas nitriding, it is often important to have the thickest diffusion layer possible without a compound layer or with a removal of the compound layer after the nitriding treatment.

Tab. 1.1 presents a non-exhaustive list of articles published in the literature on numericals simulations of the coupling between stress and diffusion. The study focuses on the stress-diffusion coupling applied to interstitial diffusion, as stated earlier in the assumptions of the analytical formulations. The study has focused mainly on it. Other papers, on the other hand, have focused on the diffusion of atoms in substitution with vacancies (short list). The first column of the table summarises the general analytical formulations of interstitial and substitutional

diffusion. The table shows five examples of interstitial diffusion applications: nitrogen $N_2\,(N^+)$, hydrogen $H_2\,(H^+)$, oxygen $O_2\,(O^-)$, carbon C and lithium (Li^+). The table shows the results of three mechanical behaviour assumptions: elastic, elasto-plastic, and visco-elastoplastic.

Behaviour material	General considerations	Interstitial					Vacancies/ Substitution
		$N_2\,(N^+)$	$H_2\,(H^+)$	$O_2\,(O^-)$	C	Li (Li^+)	
Elastic	[Larché and Cahn, 1973] [Larche and Cahn, 1978b] [Larche and Cahn, 1978a] [Li, 1981] [Larché and Cahn, 1982] [Larché and Cahn, 1985] [Larche, 1988] [Larché and Voorhees, 1996] [Philibert, 1996a] [Voorhees and Johnson, 2004] [Nazarov and Mikheev, 2005] [Ko et al., 2007] [Gururajan and Lahiri, 2016]	[Galdikas and Moskaliovienе, 2010] [Christiansen and Somers, 2010] [Moskaliovienе and Galdikas, 2019] [Galdikas and Moskaliovienе, 2020]	[Simon and Grzywna, 1992] [Xuan et al., 2009] [Hafftharadaran et al., 2011] [Dejardin et al., 2013] [Creton et al., 2014] [li Lin et al., 2017]	[Sallès-Desvignes et al., 2000] [Araki and Arai, 2010b] [Araki and Arai, 2010a] [Dong et al., 2013] [Zhang et al., 2014] [Liu and Shen, 2018] [Ramsay et al., 2019]	[Li et al., 2017]	[Gao et al., 2015] [Zuo and Zhao, 2014] [Baker et al., 2016] [Li et al., 2016]	
Elasto-plastic		[Jespersen et al., 2016] [Kütükyildiz et al., 2020]	[Panicaud et al., 2012] [Di Leo and Anand, 2013] [Barrera et al., 2016]	[Creton et al., 2009] [Wang et al., 2015]		[Zhao et al., 2011]	
Visco-elasto-plastic		[Depouhon et al., 2014]	[Anand, 2011] [Saliya et al., 2019]	[Loeffel and Anand, 2011]			[Villani et al., 2014]

Table 1.1 – Non-exhaustive list of numerical simulations of stress-diffusion coupling.

1.2.5 Experiments carried out by coupling a pre-treatment and thermochemical treatment

The effects of self-induced strains on diffusion have been recognised and investigated quantitatively for some years [Larché and Cahn, 1973, Larche and Cahn, 1978a, Li, 1981, Larché and Cahn, 1982, Larché and Cahn, 1985, Larché and Voorhees, 1996, Li et al., 1966, Philibert, 1996b]. The effects of stresses (applied/residual) are now being studied in a variety of research applications in order to improve the mechanical properties of materials or minimise processing time. This section focuses on the impacts of observable stresses on diffusion, such as the influence of elastic or plastic strains (applied or residual), as well as the effect of residual pre-stresses or differing plastic strain rates experienced by the material prior to processing. Because of their distinctive physical and mechanical qualities, metals are frequently employed as structural materials in modern industry. Interstitial diffusion occurs in a variety of applications, including gas nitriding (diffusion of nitrogen atoms), metal oxidation (diffusion of oxygen atoms), structural hydrogen embrittlement (diffusion of hydrogen atoms), and so on. Gas nitriding is a thermochemical process that improves the surface properties of a material, such as resistance to wear, fatigue, and corrosion [Barrallier and Jégou, 2017]. In the case of gas nitriding, the goal is to discover a way to reduce the process and lower the temperature as much as feasible. Long periods and high temperatures have typically been employed, resulting in high manufacturing costs. These lengthy treatments and high temperatures caused by low temperature (and thus the low nitrogen diffusivity) and the limited mass transfer between the gas reaction and the steel.

The effect of stresses on diffusion kinetics is known from a variety of perspectives, including a homogeneous stress, a stress gradient (often measured by bending), a plastic strain (via creep and fatigue mechanisms), a residual stress state (elastic strain) previously experienced by the material, and a plastic strain rate (dislocation density, diffusion short-circuits).

Tab. 1.2 is a two-entry table showing the relationship between the physical experiment (Applied stress or residual stress) and the physical phenomenon (as phase transformation (ϕ), grains boundaries (GB), density dislocation (ρ_D), vacancies $\overline{V}$). Tabs. 1.3 and 1.4 represent a list of references coinciding between the pre-treatment presented in table 1.2 and the diffusion systems (interstitial or substitution/vacancies). Tab. 1.2 also includes a column that describes how a homogeneous stress affects mobility. In fact, the coefficients are included in the work of Voorhees in 1996 (see Eq. 1.59). Tabs. 1.3 and 1.4 present a non-exhaustive list of articles published in the literature on the coupling between stress and diffusion.

From these tables, it was observed that a very large number of studies coupling mechanical pre-treatment before thermochemical treatment have been carried out for many years. These studies show real scientific improvements on the diffusion kinetics. However, this literature search has allowed us to observe that these metallurgical improvements are the coupling between several phenomena and do not really seem to demonstrate the individual impact of these phenomena. Indeed, as shown in Fig. 1.19 , in the case of SMAT mechanical pretreatment, for example, this leads, through the impact of a ball-like medium, to a near-surface plasticity phenomenon and thus to a compressive residual stress field. More precisely, this leads to a microstructure gradient, which generates a residual stress gradient. These two phenomena thus lead to the coupling of plastic and elastic strain phenomena.

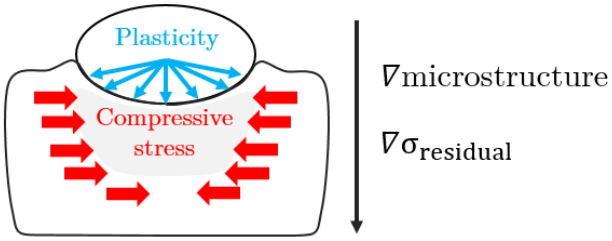

Figure 1.19 – Schematic representation of the effect of a mechanical pre-treatment such as SMAT on a steel material.

Fig. 1.20 represents schematically, from papers on molecular dynamics [Araki and Arai, 2010a], how potential energies are affected under homogeneous stresses. At the atomic scale, tensile stress results in a larger lattice distance, leading to a larger atomic jump, and vice versa in the case of homogeneous compressive stress. Although this lattice distance difference seems to be more favourable in the case of compressive stress (higher jump statistics), this diffusion enhancement in the case of tensile stress has been explained by potential energy differences through higher energy gradients on the tensile stress side. But it is also attributed to the elastic recovery force, i.e. the elastic strain energy, caused by the tensile stress, and not to the lattice strain itself. In other words, the recovery forces caused by the tensile stress would attract the inserted atom to another free position, while the repulsive force caused by the compressive stress could inhibit the migration of the atom.

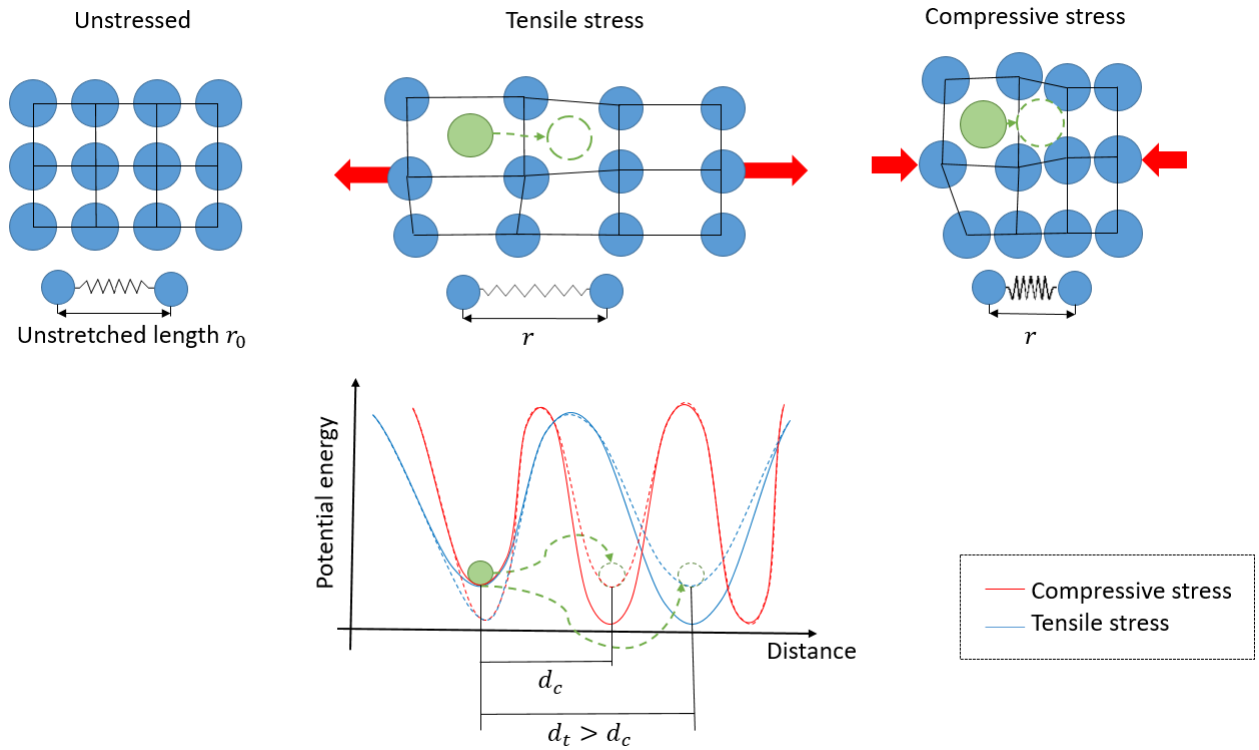

Figure 1.20 – Schematic representation of the effect of homogeneous stresses (tensile/compressive) on jump distances and potential energies.

		Diffusion coefficient D				σ		$\partial\sigma$
		ϕ	GB	ρ_D	$\overline{V}$	β	γ	
Applied stress σ	without σ	Kirkendall effect	Grains size					
	$\sigma < \sigma_E$		Creep	Creep	Creep	*Tensile test*	*Shear test*	Bending test Polishing Sand Blasting
	$\sigma > \sigma_E$		Creep Cold Rolling Tensile test	Creep Cold Rolling Tensile	Creep			
Residual stress σ_R from space gradient	Thermal $\partial\varepsilon_{th}$							
	Plasticity $\partial\varepsilon_p$	Ball Milling LHT [1]	SMAT [2] SANCT [3] USP [4] UCFT IB	SMAT SANCT UCFT Creep SP [5]	SANCT			
	Phase transf. $\partial\varepsilon_T$	HPT [6] Ball Milling Heat treatment LHT		HPT				Bending test Sand blasting
	Vacancies $\partial\varepsilon\overline{V}$				IB			

Table 1.2 – List of physical phenomena obtained by mechanical treatments.

1. Laser Heat treatment.
2. Mechanical surface attrition treatment -> formation of nanocrystallites in the surface layer (nanostructuration) = improved mechanical properties of metallic materials.
3. Surface-Alternating Current Nanocrystalline Treatment -> breaking and reforming of chemical bonds due to ionic transgression = refined grain.
4. Ultrasonic shot peening -> surface treatment by cold working via a medium that impacts the surface of a mechanical part: significant plastic strain on the surface of the part (nanocrystallisation) + compressive residual stress layer = improved mechanical properties of the material.
5. Shot peening -> (similar to USP process) surface treatment by cold working via a medium that impacts the surface of a mechanical part: significant plastic strain on the surface of the part (nanocrystallisation) + compressive residual stress layer = improved mechanical properties of the material.
6. Cold high pressure torsion -> transformation de phase (e.g. austenite in martensite).

Treatments	Interstitial			Vacancies / Substitution	Observations	
	$N_2\,(N^+)$	$H_2\,(H^+)$	$O_2\,(O^-)$		Surface layer (e.g. compound layer, oxide layer)	Diffusion layer
Kirkendall effect				[Smigelskas and Kirkendall, 1947]		
Grain size						(larger grains) ↙
Creep	[Limarga and Wilkinson, 2006]		[Moulin et al., 1996] [Krupp et al., 2008]		tensile ↗ compressive ↙	tensile ↗ compressive ↙
Tensile or Compressive test	[Guillot et al., 2016]	[Beck et al., 1966] [Bockris et al., 1971] [Kirchheim, 1986] [Hwang and Perng, 1994] [Frappart et al., 2012]	[Calvarin et al., 2000] [Yen and Hwu, 2000] [Calvarin-Amiri et al., 2001] [Gauthier et al., 2009] [Araki and Arai, 2010b] [Araki and Arai, 2010a] [Zhou et al., 2010] [Ramsay et al., 2019]	[Li et al., 2017]	tensile ↗ compressive ↙	tensile ↗ compressive ↙
Shear test		[Kirchheim, 1986]			no effect	no effect
Bending test	[Hirsch et al., 2004] [Guillot, 2018]				tensile ↗ compressive ↙	tensile ↗ compressive ↙
Polishing	[Hirsch et al., 2004]					↗
Sand blasting	[Hirsch et al., 2004]					↗
Cold rolling	[Lecis et al., 2012] [Lu et al., 2021] [Biehler et al., 2017]				↙	↙
Ball Milling	[Cemin et al., 2010]				↗	↗
Heat treatment	[Manova et al., 2007] [Kochmanski and Nowacki, 2008]	[Vizcaíno et al., 2014]				$T_{annealing}$ increases -> larger grains: ↙
Laser heat treatment	[Panfil et al., 2017]					

Table 1.3 – List of references for mechanical treatments (included in Tab. 1.2), classified according to their type of diffusion (insterstitial, vacancies or substitutions), and description of the observations made on the behaviour of the diffusion kinetics in coupling with a thermochemical treatment. (part n°1)

Treatments	Interstitial			Vacancies / Substitution	Observations	
	$N_2\,(N^+)$	$H_2\,(H^+)$	$O_2\,(O^-)$		Surface layer (e.g. compound layer, oxide layer)	Diffusion layer
SMAT	[Tong et al., 2003] [Tong et al., 2006] [Lin et al., 2006] [Tong et al., 2007] [Chemkhi et al., 2013] [Balusamy et al., 2013] [Samih et al., 2014] [Sun et al., 2016] [Chemkhi et al., 2017]			[Wang et al., 2003] [Wang et al., 2005] [Lu et al., 2010]	↗	↗
SANCT	[Wang et al., 2006]				↗	
USP	[Gu et al., 2002] [Thiriet et al., 2012]					↗
SP	[Kikuchi et al., 2010] [Jayalakshmi et al., 2016] [Biehler et al., 2017]				↗	↗
UCFT	[She et al., 2013]				↗	↗
IB: Ion bombardment	[Ochoa et al., 2006] [Abrasonis et al., 2006]					↗
Carbon diffusion	[Stewart et al., 1994]					compressive ↙
HPT	[Ferkel et al., 2002] [Ferkel et al., 2003b] [Ferkel et al., 2003a] [Shabashov et al., 2009] [Ramazanov et al., 2016]				↗	↗
Atomic attrition (argon plasma)	[Cemin et al., 2010]					↗

Table 1.4 – List of references for mechanical treatments (included in Tab. 1.2), classified according to their type of diffusion (insterstitial, vacancies or substitutions), and description of the observations made on the behaviour of the diffusion kinetics in coupling with a thermochemical treatment. (part n°2)

1.3 Conclusion

This bibliography chapter allowed to:

— Define the analytical formulations of the stress-diffusion coupling in the situation of interstitial diffusion, beginning with the general formulation and progressing to the simplified formulation. These simulations allow for macroscopic simulations that are near to the real-world settings of the experiments, although they do not yet include all of the active systems,

— List the articles that group numerical simulations of elastic, elastoplastic, and viscoelastoplastic materials,

— List the articles that contain investigations on the influence of stress on diffusion kinetics. The influence of stresses was mostly seen by applied stresses (tensile/compressive/shear test, creep test) and residual stress involving strain gradients: thermal, plastic, phase transformations, or vacancies.

These studies made it possible to understand the interest of pretreatments on the diffusion kinetics via different mechanisms which are those playing on the diffusion coefficient, i.e. phase transformations, grain boundaries, dislocation densities, the effect of homogeneous stresses, then on driving forces via a stress gradient. The effect of applied stresses, whether gradient or homogeneous, revealed that tensile stress enhances diffusion kinetics while compressive stress decreases it. Torsional stress appears to have little effect on diffusion; nonetheless, few tests appear to have been conducted. Bending load testing produces the same results as basic tensile/compressive tests, with the thickness of the treated surface rising on the tensile side and decreasing on the compressive side. They can absorb residual stresses and enhance the depth of the nitriding process, according to tests including fatigue and creep mechanisms. The external stress gradient has a considerable impact on the development of chemical stress as the diffusion time increases. Treatments involving nanostructured surfaces that increase the volume fraction of grain boundaries have a significant influence on the diffusion kinetics. This is due to the fact that these nanostructures provide interstitial atoms on the material surface with fast diffusion paths. Nanostructured materials with a high dislocation density have a significant influence on diffusion dynamics. In some situations, however, a surface pollution layer caused by pre-treatment has been identified, which significantly slows or even stops the nitrogen diffusion process.

This literature review has shown that numerical simulation and experimental studies mainly focus on the definition of an effective diffusion coefficient by considering only the Nernstian term (driving force, or stress gradient), and ignoring the impact of stress on mobility. However, many mechanical treatments have demonstrated the relationship between residual stress and microstructure phenomena. The first key work of this thesis will be to study by numerical simulations the predominance between the driving force and the effect of stress on mobility. The second key work of this thesis will be to set up experiments based on the experimental observations and to try to correlate the numerical and experimental results.

This literature review has also shown that many studies investigate the coupling between mechanical pretreatment and thermochemical treatment. They based their results on incompatible plastic strain aspects (grain boundary density, dislocation density, etc.) while forgetting the elastic strain aspects through e.g. the residual stress. The third key work of this thesis will therefore be to decouple the effects of compatible elastic strains and incompatible plastic strains through experiments.

Chapter 2

Experimental/Numerical methods and preliminary studies

Contents

2.1 Experimental methods

In the first part of this chapter, the experimental and numerical methods implemented in the framework of the thesis work are detailed. Then, a description of the base material and a study to identify its material parameters are presented.

2.1.1 Nitriding

2.1.1.1 Thermogravimeter

A SETARAM Instrumentation SETSYS Evolution 18/16 ATG-ATD/DSC thermogravimeter is used for nitriding treatments. Fig. 2.1a) shows the schematic of the nitriding platform. The gas manifold at the inlet determines the composition and total flow rate of the gas mixture; the gas is then passed through the thermogravimeter, which acts as a nitriding furnace; and a portion of the gas mixture (NH_3+H_2+N_2: diluted according to the selected nitriding potential K_N) is taken from the thermogravimeter furnace for analysis by the mass spectrometer to determine the nitriding potential at the outlet. Before the gas mixture is vented to the outside, most of it is passed through a bubbler to neutralise ammonia. The thermogravimeter has the advantage that the sample mass change can be assessed as a function of time. Fig. 2.1.b) shows a cross-section of the thermogravimeter. It consists of a beam balance with platinum hooks to which a sample is suspended. Counterweights are used to balance the initial weight of the sample. During the treatment, the mass gain of the sample is measured. A maximum mass gain variation of 400 mg with a measurement accuracy of 0.03 mg can be measured. The tube furnace is 18 mm diameter made of alumina, which is neutral toward the dissociation of ammonia. A thermocouple located 20 mm below the sample allows controling temperatures up to 1200°C with an homogenous temperature area of approximatively 30 mm long.

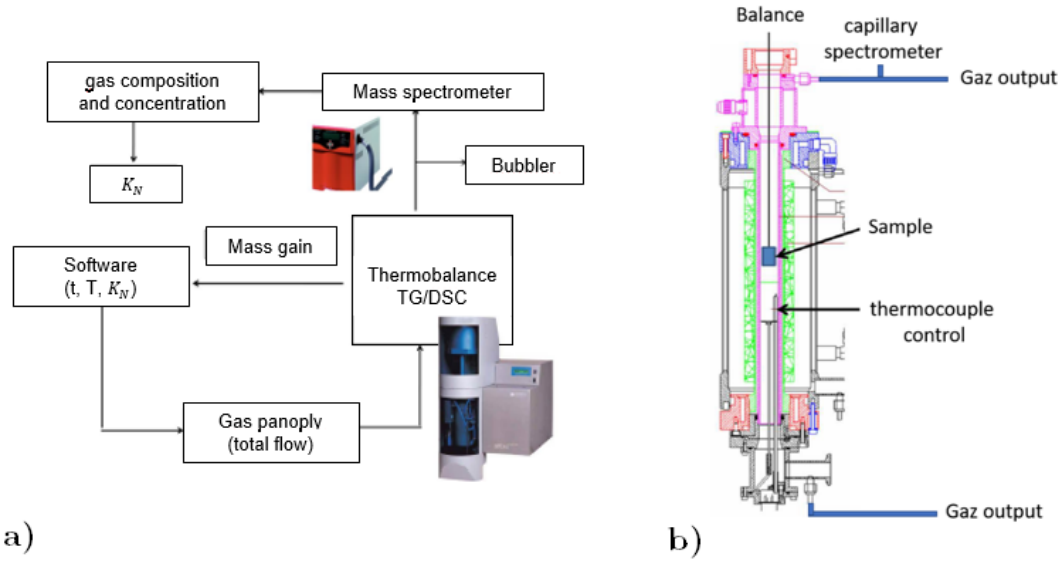

Figure 2.1 – a). Diagram of the thermogravimeter from the programming on the computer, to the gas management, and the gas outlet. b). Cross-sectional drawing of the thermogravimeter.

2.1.1.2 Preparation of the specimens

The gas nitriding process is extremely sensitive to surface contamination [Guillot, 2018]. Therefore, it is essential that each sample is prepared in an equivalent manner. Several steps are taken to achieve this:

— Polishing of each surface to P1200 grain size,

— Degreasing (industrial degreaser) + ethanol drying (3 times).

After a thorough cleaning, the sample is weighed and placed on the thermogravimeter hook to counterbalance the beam balance before being lowered into the alumina tube. After sealing the thermogravimeter, the purging process is repeated twice:

— Vacuum cycle:

  — Purge until 3000 Pa,

  — Vacuum until 20 Pa.

— Gas flowing in an inert N_2 gas with a flow of 200 mL/min for about 20 min.

The total mass flow rate is based on the assumption that the decomposition kinetics of ammonia on the surface of the iron is minor compared to the atmospheric turnover kinetics. In other words, the nitriding potential K_N can be considered constant during the treatment. Furthermore, in order to prevent the parts of the balance from reacting with the active gas in the furnace, the balance placed at the top of the gravimeter is subjected to a He flow equal to the total mass flow of active gas (mix of ammonia NH_3, nitrogen N_2 and hydrogen H_2) in the furnace.

During gaseous nitriding, the gas mixture is composed of ammonia NH_3, nitrogen N_2 and hydrogen H_2 with a total mass flow rate of 200 mL/min. The exact composition of the gas atmosphere is set up according to the desired nitriding potential.

The evolution of mass and temperature is tracked and graphically plotted on a graph during the treatment. Fig. 2.2a) is an example of a final curve obtained after a 5 h treatment on a 500 μm thick sample with a K_N = 3.711 $atm^{-\frac{1}{2}}$. Then, as illustrated in Fig. 2.2b), a processing software is used to cut the signal from the mass sample of interest in order to determine the mass change of the sample and its time derivative. Figs. 2.2 a) and b) show that the mass is not linear in time. In fact, the kinetics demonstrate a peak in mass increase that is related to the beginning of compound layer growth. Indeed, as mentioned in previous chapter in section 1.1.2.1, γ'-Fe_4N precipitates at low temperatures and is the first of the iron nitrides to form, with an existence range of 19.3 to 20.3 % atomic units of nitrogen.

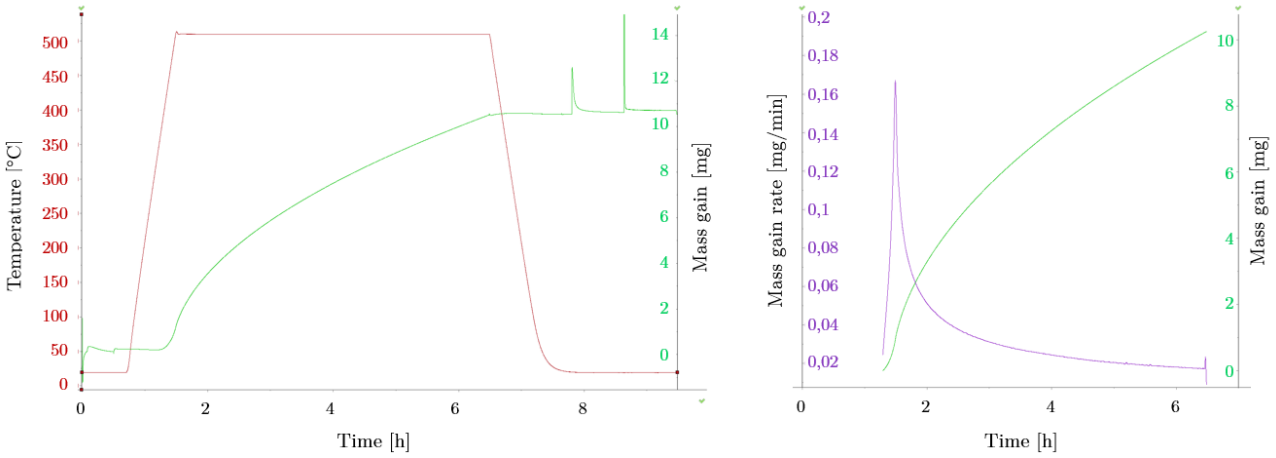

Figure 2.2 – a) Final curve of the evolution of temperature and mass gain as a function of time, b) Evolution of mass gain and mass kinetics as a function of time, obtained after a 5 h gas nitriding treatment on a 500 μm thick sample with a $K_N = 3.711$ atm$^{-\frac{1}{2}}$ at 520 °C.

2.1.2 Sample preparation

An abrasive saw is used to cut a cross-section of the samples, obtaining a sample thickness of 4-5 mm. The samples are mounted in a single-use support. The advantage is that many samples can be placed in the support at the same time to maintain a consistent surface finish between each set of samples. First, an abrasive polish on silicon carbide paper is applied, ranging from P180 to P1200. The polishing is then carried out on 3 and 1 μm felt discs, followed by a final polishing step using a 0.05 μm alumina solution (pH 7). The sample is cleaned with water and dried with ethanol between polishing steps. The sample is then immersed in ethanol and placed in an ultrasonic bath to remove any polishing residue, for several minutes.

2.1.3 Scanning electron microscope (SEM)

A JEOL JSM 7001F scanning electron microscope (SEM) is used at the MSMP laboratory.

Firstly, the electron backscatter imaging (BSE) technique is used to immediately observe, for example, martensite laths, nitrides (ϵ-$Fe_{2-3}N$ and γ'-Fe_4N), cementite Fe_3C, etc. It is a scanning electron microscopy method for detecting atomic number changes on the surface of the sample. Essentially, SEM involves the use of high-energy electrons to produce high-resolution images that indicate the distribution of different components in a sample. Digital image micrographs can have a spatial resolution of less than one nm per pixel. The SEM is equipped with an Oxford Instrument X-max energy dispersive spectrometer (EDS) with a 20 mm detector. Throughout this work, the conditions for BSE imaging are:

— Electron acceleration voltage: 12 kV,

— BSE detector (COMPO),

— Magnification: ×700 and ×2500.

Crystallographic analysis by electron backscatter diffraction (EBSD) was performed to identify and examine the phase fractions, for example, in the case of the compound layer between ϵ-$Fe_{2-3}N$ and γ'-Fe_4N or to observe

crystal orientations. All the diffraction planes create a band, which finally produces a diffraction pattern. The aim here is to estimate the position of a succession of Kikuchi bands using image analysis and a Hough transform, and then to index the bands using the Miller indices of the diffracting crystal plane. Diffraction is very sensitive to sample preparation. The depth of the electrons is shallow (10 to 20 nm), so any surface contamination and topography must be avoided. To improve the contrast of the backscattered electron image, the flat, polished polycrystalline sample towards the diffraction camera is tilted at an angle of 60-70° from the horizontal. The EBSD maps are plotted thanks to a Nordlys hkl camera and are analysed by Inca software. The conditions for the analysis of EBSD analysis are:

— Electron acceleration voltage: 15 kV,
— Tilt angle of the specimen: 60°,
— Image size: 700×1400 pixels,
— Step size: 0.06 μm,
— Colour's phase on the map:
  — Iron α-Fe -> red,
  — Cementite Fe_3C -> yellow,
  — Nitride Fe_3N -> green,
  — Nitride Fe_4N -> blue.

The samples were prepared in the same way as described in Section 2.1.2 (mirror without etching).

2.1.4 Optical microscope

Microstructure observations are made with an Olympus BX41M optical microscope equipped with a PixelLink camera resolution. The images are analysed by ImageJ software.

The samples are prepared as described above in Section 2.1.2. They will then be etched for a few seconds with a 3 % nitric acid solution (3 mL nitric acid + 97 mL ethanol) to reveal the microstructure.

2.1.5 Hardness

Hardness measurements were used to characterise the surface hardness and determine the effective depth of nitriding. The Vickers microhardness test was performed using a QNESS Q10A+ automated microdurometer. To establish a hardness profile of the nitrided surface, three filiations were made in a staggered pattern, with an indentation every 30 μm at different locations and a distance of three times the diagonal between each indentation. The hardness filiations start at z = 20 μm from the surface to avoid taking the compound layer (7-8 µm in general in the present work) into account and continue until the base material is reached (depth defined using microscopic observations). The effective depth is defined as the depth at which the hardness of the diffusion zone is equal to the hardness of the core to which is added 100 Vickers (as described in Section 1.1.3). Positions and measurements of the indentations were determined using the Qpix Control2 program in conjunction with the microdurometer. The HV0.1 microhardness filiation tests were performed in accordance with NF EN ISO 6507-1 standard [6507-1:2018, 2018]. The holding period was set to 15 seconds.

The samples were prepared in the same way as described in Section 2.1.2 (mirror without etching).

2.1.6 X-ray diffraction

The technique of X-ray diffraction (XRD) is used to characterise crystalline materials, whether they are massives samples, powders, or deposits. X-ray diffraction is based on the recording of a diffractogram and the analysis of the peaks of this diagram, which permits the characterisation of crystallites existing in the sample from the elements listed below:

— Peak position: qualitative investigation, identification of crystalline phases present, stress measurements,

— Peak width: indicator of the heterogeneity of a microstructure crystallite size and form, internal tensions,

— Peak intensity: chemical composition calculation, quantitative phase analysis, preferred orientation.

Phase and stress analysis on nitrided samples will be performed in this work.

2.1.6.1 Phase analysis

X-ray diffraction is a non-destructive technique for the qualitative and quantitative study of polycrystalline materials which allows the nature of the phases present to be recognised from the crystal structure. The phase is found by analysing the spectrum and comparing it with conventional diagrams. The method is based on the interaction of the crystal structure of a sample with shortwave radiation. Indeed, the analysis of the distribution of the positions of the diffraction peaks by the sinus method makes it possible to identify the crystal structures. X-ray diffraction can be used to study phases with a volume fraction of at least 3 to 5 % [Castex et al., 1981].

Using X-rays to investigate matter has various advantages, one of which is that their wavelengths are of the same order of magnitude as interatomic distances. When X-rays reach the lattice planes of crystal lattices, they either interact with the electron clouds of the atoms that make up that plane, or they do not interact and can proceed to the next plane. These planes are separated by typical distances that vary depending on the nature being examined (lattice distances). Bragg's law may then be used to find the directions in which the interference is constructive, known as diffraction peaks:

$$2d_{\{hkl\}}.\sin(\theta) = \lambda \tag{2.1}$$

Where d is the interreticular distance, $\{hkl\}$ are the Millers' indice, θ is the angle of incidence of the X-rays and λ is the wavelength of the X-rays.

A quantitative and index study of the diffraction peaks can be performed to determine which phase is present.

2.1.6.1.1 Quantitative method Quantitative XRD analysis identifies the crystallographic forms of any crystalline structure present in a material. The amount of phase present is proportional to the area of the diffraction peak in the $(2\theta, I_{\{hkl\}})$ diagram. In fact, this method is based on the measurement of the integrated intensity of the diffraction peaks and the application of a theoretical relationship between these intensities and the volume percentage of the phases composing the sample. In the presence of a mixture of phases, the area under the peak increases with the fraction of a phase present. It is required to assume that the breadth of the peaks is consistent from one sample to the next when the approach considers peak height, although this is only true

under certain conditions (absence of microstresses, identical crystallite size from one sample to another and without crystallographic texture (isotropic), homogeneous).

A peak is considered as the scheme in Fig. 2.3. Indeed, the width of a peak is characterised by its full width at half maximum (FWHM), i.e. the width of the peak at 50 % I max.

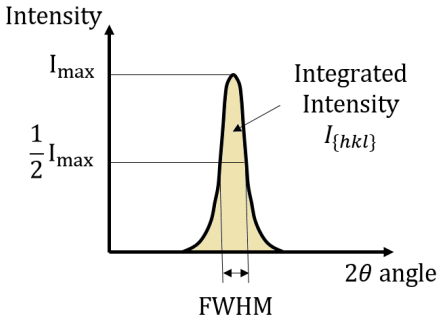

Figure 2.3 – Schematic representation of a diffraction peak.

The quantitative study used in this study is based on ASTM E975-13 [ASTM International, 2013]. Indeed, the interest is to calculate for each diffracted angle, the ratio:

$$\frac{I_{\{hkl\}}}{R_{\text{theoretical}}} \tag{2.2}$$

Where $I_{\{hkl\}}$ is the measured diffracted peak area and $R_{\text{theoretical}}$ is the theoretical diffraction peak area taking into account the structure factor F (extinction conditions depending on the nature of the atoms, wavelength, and crystallographic structure of the phase considered), the Debye factor (influence of temperature on the X-ray scattering phenomenon in the considered phase), the Lorentz-Polarisation factor (diffractometric set-up, here Bragg-Brentano θ-2θ), the multiplicity factor of the considered plane family and the volume of the elementary lattice of the considered phase. Tab. 2.1 summarises the $R_{\text{theoretical}}$ of the phases obtained in this study using equivalent diffraction angles.

The studies carried out in this work were mainly performed at the interface between the compound and diffusion layers in order to characterise the iron nitride gradients observed in this area. However, it is essential to recognise that the small amount of cementite or the small size of the alloying element nitrides cannot be defined in terms of volume fraction and residual stress state.

2.1.6.1.2 Peak indexing method Another method consists in indexing the diffraction peaks. Indeed, each peak (marked by Miller indices $\{hkl\}$) is linked with an atomic plane according to Bragg's law (see Eq. 2.1). It is interesting to understand that, according to Bragg's law, the interreticular distance $d_{\{hkl\}}$ will be the greatest for a small θ. In fact, the interreticular distance is written as follows in case of cubic system:

$$d_{\{hkl\}} = \frac{a}{\left(h^2 + k^2 + l^2\right)^{1/2}} \tag{2.3}$$

Where a is the lattice parameter.

h	k	l	Phase	2θ	$R_{\text{theoretical}}$
1	0	1	Fe_3N	44,85	1,2046E+45
1	1	0	Fe_4N	50,51	6,1919E+44
1	1	0	Fe_3N	58,03	8,9719E+45
1	1	1	Fe_3N	66,72	5,0619E+46
1	1	0	Fe	68,78	6,7473E+46
2	0	0	Fe_4N	74,22	2,8187E+46
2	1	0	Fe_4N	84,84	2,1196E+44
1	1	2	Fe_3N	90,43	1,0242E+46
2	1	1	Fe_4N	95,28	1,5987E+44
2	2	0	CrN	102,92	3,8174E+46
2	0	0	Fe	106,03	1,4559E+46
3	0	0	Fe_3N	114,30	1,5288E+46
2	2	0	Fe_4N	117,14	3,0559E+46
3	0	0	Fe_4N	129,65	3,7174E+43
1	1	3	Fe_3N	132,75	2,4939E+46

Table 2.1 – List of the $R_{\text{theoretical}}$ according to the $\{hkl\}$ indices corresponding to a specific phase and a specific angle 2θ.

2.1.6.2 Stress analysis

2.1.6.2.1 Principle Stress analysis by X-ray diffraction is the most widely used method for surface treatments. It is used to measure strains and to calculate stresses. Due to the multiphased characteristic of material (nitrides and carbides in ferritic matrix), the residual stresses calculated correspond to the average stresses σ_{xx} - σ_{zz} of the ferritic matrix [Macherauch and Hauk, 1987]. The determination of stresses requires a number of assumptions [Castex et al., 1981]:

— linear elastic behaviour of the crystallites which constitute the material,

— isotropic material assuming a sufficiently small crystallite size and random orientation,

— a homogeneous state of stress and strain in the analysed zone.

Various methods, including hole, magnetic and ultrasonic approaches, can be used to calculate residual stresses. X-ray diffraction is the most widely used method for characterising surface treatments [Barrallier, 1992, Locquet, 1998]. In crystalline materials, by using the crystal lattice as a strain gauge, the residual stresses in the different phases of a material can be determined. The elastic strains in the crystal lattice are related to these stresses. Changes in the lattice spacing caused by macroscopic stresses result in a shift of the diffraction peaks, while microstresses manifest themselves in a broadening of the lines, according to the Bragg equation (see Eq. 2.1).

The diffractometer's features allow for extremely accurate and fast intensity measurements, as well as the ability to fully automate the instrument's operation and calculations. The main problem, in this study, is that only a small part of the X-ray diffraction cone is examined.

The stress gauge in X-ray diffraction analysis is the interplanar distance $d_{\{hkl\}}$ of a family of crystal planes. This distance varies as a function of stress. Bragg's law (previously given in Eq. 2.1) is used to calculate the variations of $d_{\{hkl\}}$. Indeed, when the crystal planes are stressed, the distance $d_{\{hkl\}}$ varies and can go from d_0 to d. The strain is represented by the expression $\varepsilon = \frac{d-d_0}{d_0} = \frac{\Delta d}{d_0}$. When, the Bragg's law is differentiated, two

equations are obtained assuming monochromatic beam with a representative diagram of the θ angle in Fig. 2.4:

$$\frac{\Delta d}{d} = -\text{cotg}\theta.\Delta\theta \tag{2.4}$$

$$\Delta 2\theta = -\frac{2}{\text{cotg}\theta}\frac{\Delta d}{d} \tag{2.5}$$

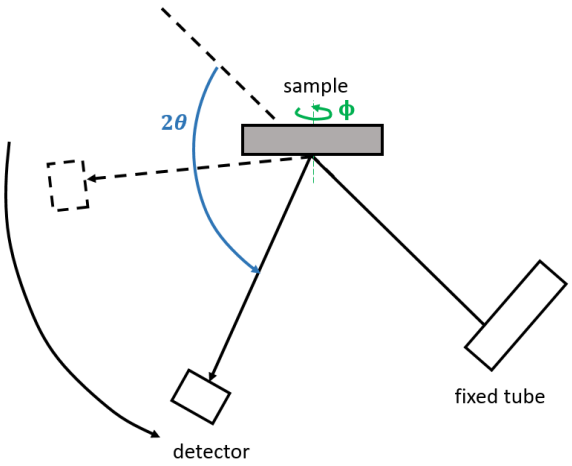

Figure 2.4 – θ-2θ setup type, with ϕ angle, used for X-ray diffraction.

A system of planar stresses is assumed to exist at the surface of a material $\sigma_{xx} \neq 0$ and $\sigma_{yy} \neq 0$ ($\sigma_{zz} = 0$). Because X-rays do not penetrate the material very far (aroung 7 μm), it is presumed that this is the case for X-ray diffraction stress analysis. The law of $\sin^2(\psi)$, which is the fundamental equation relating elastic strain and stress in the stress measurement method, is stated as follows assuming no triaxial stress state:

$$\varepsilon_{\phi\psi} = \frac{1+\nu}{E}\sigma_\phi \sin^2(\psi) - \frac{\nu}{E}(\sigma_1 + \sigma_2) \tag{2.6}$$

The elastic coefficients used in the XRD stress measurements are radiocrystallographic. They depend on the choice of the family of diffracting planes and the material studied. In this study, it is the {211} plane, E = 210 GPa and ν = 0,29.

2.1.6.3 Equipments

In this work, two diffractometers were used. A Siemens D500 diffractometer with a chromium wavelenght (λ = 0, 228975 nm) using a linear detector was used to study parallelepipedic samples. The collected spectra were analysed using Siemens PROFILE software. The residual stresses are calculated using the Siemens STRESS program. The DACO-MP controller used a θ-2θ type setup, with the tube remaining fixed and the sample and detector moving by a θ angle and a 2θ angle, respectively.

A Seifert XRD3000 with a chromium wavelenght (λ = 0, 228975 nm) using a linear detector, a vanadium back filter is placed in front of the linear detector and employing Cr-Kα radiation was used to study the open

ring sample (see section 4.2.3) according to sample geometrical constraints.

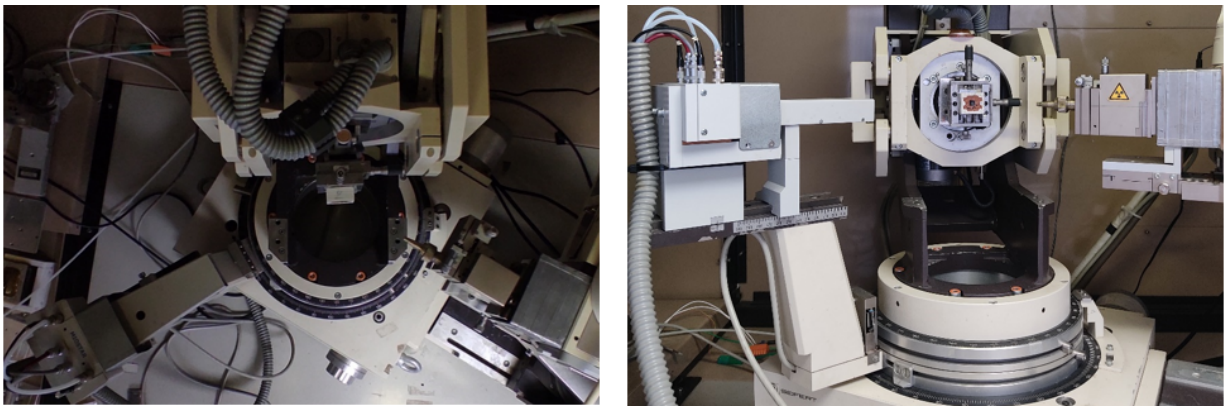

Figure 2.5 – Seifert XRD3000 used for X-ray diffraction.

2.1.6.4 In-depth stress measurement

An electrochemical ecthing method is used to remove the material using a STRUERS LectroPol-5 polisher and a Struers electrolyte A2. Unlike mechanical polishing, this procedure does not create any additional stress.

Thin samples (500 μm thickness) are used in the present work, so a specific support was set up. Indeed, as shown in Fig. 2.6a), the removal of material produces a mechanical rebalancing of the sample, resulting in a curvature. As depths are reached, the curvature varies, resulting in depth measurement errors as well as residual stress calculations errors. Indeed, an error of the order of 50-60 μm in measured depth for a total depth of 250 μm was observed. As a result, the samples were cold mounted in a copper-based resin (see Fig. 2.6b)). Usually the depths are measured with a digital comparator, but due to the expected small influences on the experiments, a Surfascan 3D roughness meter (Fig. 2.7a)) with a resolution of 1 nm was used. It is a SOMICRONIC inductive contact probe roughness metre with 4 mm stroke length and 4 nm vertical resolution. Measurements are taken using a 4 μm acquisition step in x. The results are then processed using a software program. Depth measurements were made using three 14 mm long lines spaced 0.5 mm apart across the crater, as shown in Fig. 2.7b).

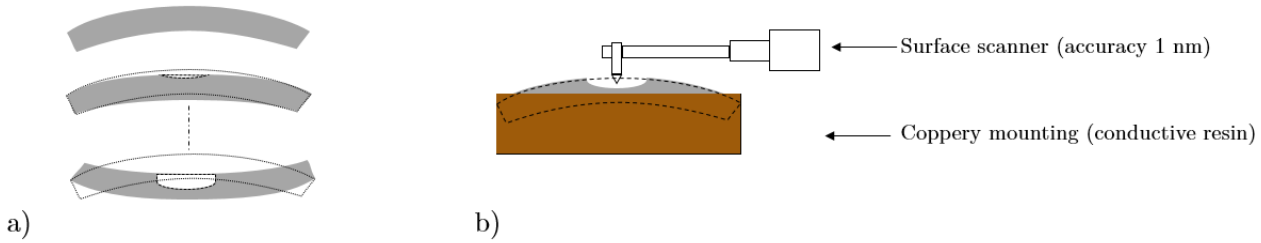

Figure 2.6 – Assembly of thin samples for stress residual and phase analysis.

Due to the small size of the samples, the loss of material produced by electrochemical polishing alters the mechanical balance of the component. The experimentally observed stress levels must then be adjusted to their

a) 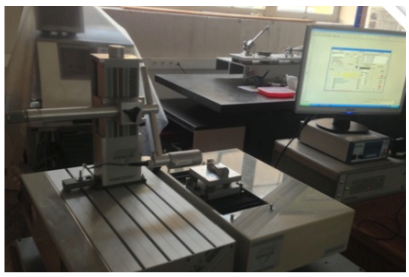

b) 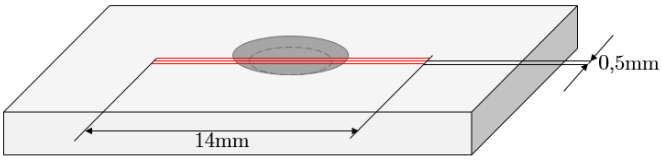

Figure 2.7 – a) Surfascan 3D roughness meter. b) Depth measurements by three 14 mm long lines spaced 0.5 mm apart across the crater.

pre-polishing levels. Moore and Evans developed the principle of calculation [Moore and Evans, 1958]. Castex improved it by taking into account the geometry of the polished zone [Castex, 1984].

Tab. 2.2 shows the experimental parameters for the residual stress evaluations. The generator is set to 20-30 kV and 30 mA.

	Parameters	Case of α-Fe
Material	Young's modulus E (GPa) Poisson's coefficient ν Anisotropic factor	210 0.29 1.39
Diffraction	Goniometer position Wavelength (nm) Diffraction's plane Detector position	ω (i.e. $\theta - 2\theta$ setup) 0.228975 {2 1 1} 156 °
Acquisition	Acquisition step Calculation Acquisition time (s) Φ angle Ψ angle	0.032 ° elliptical 300 (phases analysis) 100 (stress analysis) 0 9 angles with $\pm 3^{\circ}$ oscillations
Data treatment	Treatment zone Profile fitting	40° to 156° Pseudo-Voigt 2

Table 2.2 – Experimental X-ray diffraction parameters for residual stress analysis in steel grade 33CrMoV12-9, ferritic steel, α-Fe matrix.

Real materials have discontinuities (grain boundaries, dislocations, precipitates, etc.) and can no longer be considered as continuous according to the scale of observation. The same analysis area of the sample surface must be studied for all samples. Therefore, analyses and calculations are performed on a representative elementary volume (REV). Here a 2-mm-diameter mask is used. Residual stress measurements were done every 10 μm in depth for the first 50 μm below the surface, then every 25 μm until the diffusion layer was no longer present.

2.1.7 Chemical gradient analysis

2.1.7.1 Equipment

The thermochemical treatment, gas nitriding, causes gradients in the nitrogen and carbon chemical compositions of 33CrMoV12-9 steels. An Ametek SpectroMAXx® BT MX5M spark optical spectroscope (spark-OES) is used to measure these compositions. A plasma is produced near the surface of the material by a voltage differential between an anode and a cathode a few millimetres distant. This plasma eliminates a thin layer of material in the shape of a 6 mm diameter crater. A UV source is sent into the plasma, and the resulting optical spectrum is fed through an optical fibre to a diffraction crystal. The optical lines strength and location are connected to the atomic species and its rate. A calibration (also known as an icalisation) is carried out using a RH 18/34 reference sample (rich in W, Co, Cr and Mo). The depth profile in the nitrided layer is obtained by successive manual removal of material by mechanically polishing the surface with P120 carbide discs. The depths are measured with a digital comparator. Depths are measured at the true positions of each crater. Analyses are carried out every 20-30 μm depth for the first 100 microns, then every 40-50 μm.

Figure 2.8 – Ametek SpectroMAXx® BT MX5M spark optical spectroscope (spark-OES).

2.1.7.2 Preparation of the specimens

The analysis with the spark spectrometer is carried out last, as it is destructive. The following is the analysis procedure:

— measuring the depth of crater positions,

— carrying out the zone analysis using the spectrometer,

— mechanical polishing with silicon carbide paper grade P120 to remove the crater,

— determining the height of the analysis zones.

Special support was required due to the small thickness of some samples. Indeed, the samples are mechanically polished after each analysis to remove craters. As can be seen in Fig. 2.6b), these polishings create a mechanical rebalancing of the sample, resulting in a curved sample. This curvature makes depth measurement complicated. The support chosen was to hold the specimen against a thick support with a tapered screw to confirm that the screw head held the specimen after each mechanical polish.

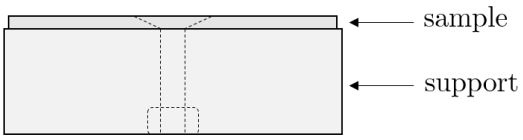

Figure 2.9 – Assembly of thin samples for spark spectrometer analysis.

2.1.8 Copper (de-)plating

Some of nitriding experiments, in Section 4.2.1, will need the use of copper plating. Surtec-prepared solutions will be used, and the Surtec procedures will be followed. Fig. 2.10 shows the setup used composed with a generator, a thermal and magnetic stirrer, a pure copper blank (in orange colour), a solution rich in copper ions, and the copper sample (in grey colour).

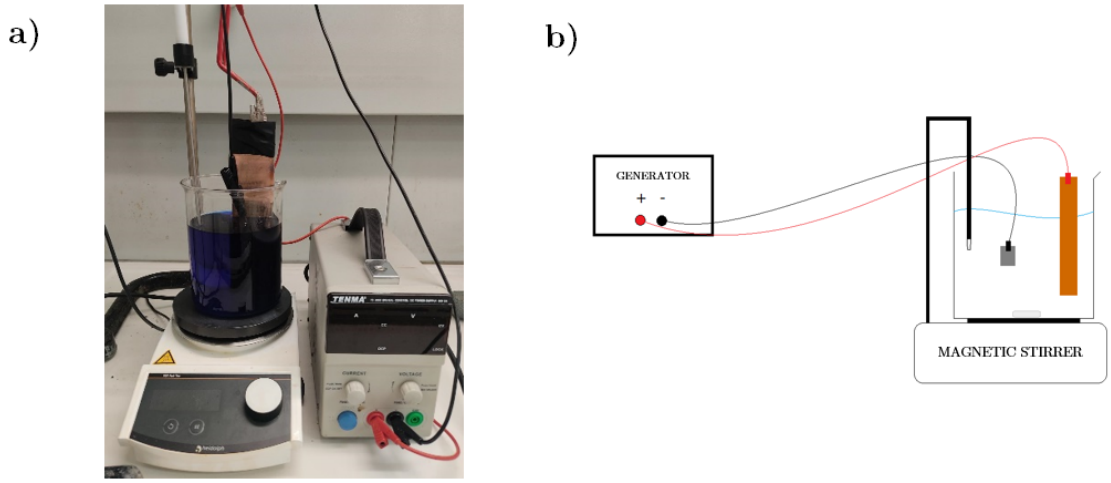

Figure 2.10 – a) Setup for copper deposits. b) Schematic setup for copper deposits.

The protocol is meticulous. Indeed, several steps must be followed:

1. Cleaning of tools:
   - 2 % sodium hypochlorite solution for 24 hours,
   - Rinsing with water,
   - 2 % solution of sulphuric acid, rinsing with water,
   - Solution of 5 % lye of potash.
2. Chemical degreasing: SurTec 196 (alkaline detergent) + SurTec 092 (emulsifying surfactant),

3. Acid stripping: Hydrochloric acid 30 - 50 % (not sold by SurTec) + SurTec 424 attack inhibitor,
4. Electrolytic degreasing: SurTec 196 (alkaline lye),
5. Pre-immersion before copper plating: SurTec 864 IK (1% vol),
6. Electrolytic copper plating: SurTec 864.

The electrolytic copper deposit solution is composed of:

— Fill tank with 1/3 water max (depending on electrolyte (25 to 60 %)),

— Add SurTec 864 l K corrector (2 %),

— Adjust the pH (around 9.5) with potash lye to 45 %,

— Add SurTec 864 electrolyte concentrate,

— Correct the pH again (9.2-9.8),

— Make up to the final volume with water.

The copper deposit bath should heat up at 50-70°C. It is necessary to activate the bath with a current density of 1 - 2 A/dm^2 for 5 min and then in order to obtain a deposit of 0.15 μm/min the cathodic current density is 1.5 A/dm^2. A deposit of 30 μm is required to hold and respond well as a barrier to nitrogen diffusion so the deposit time need to be 200 min. An example of a copper plating is shown in Fig. 2.11.

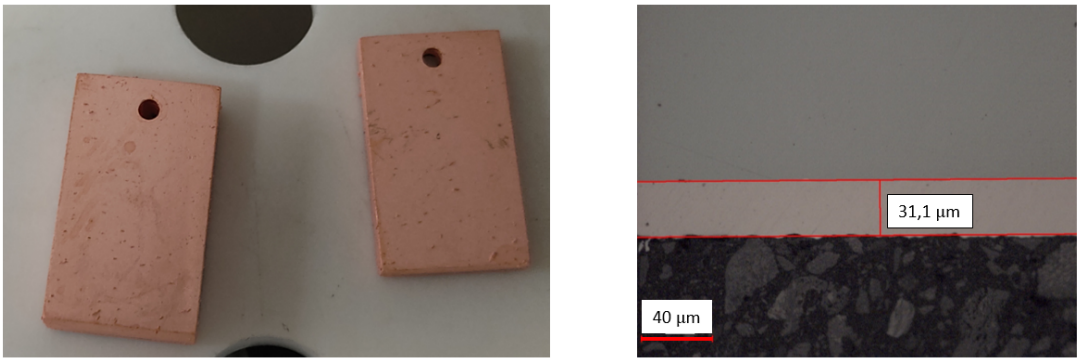

Figure 2.11 – a) Two copper samples after 3.5 hours of copper treatment. b) Optical microscope observation of a cross-sectional deposit of a copper sample after 3.5 hours of copper treatment.

For some parts of the experimental study, it will be necessary to remove the copper deposit chemically, and non-destructively for the steel sample, in order to maintain the mechanical and chemical characteristics of the material. Fig. 2.12 shows the setup used composed with a generator, a magnetic thermal stirrer, a massive piece of steel (in grey colour), a solution rich in copper ions, and the sample to be de-coppered (in orange colour).

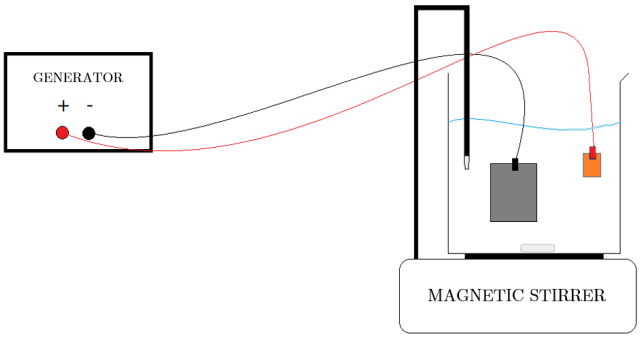

Figure 2.12 – Setup diagram of de-coppery process.

For this purpose, a de-coppery solution (Surtec 991) is used. It is composed of:

— Fill the tank to 80% with water,
— Add the calculated amount of SurTec 991 I (10% vol.),
— Add the calculated amount of SurTec 991 II (2% vol.),
— Heat the bath to 50°C and check the pH (around 6.5).

In order to ensure a safe, i.e. non-destructive, decoppery of the material, it is important to set an adequate current density (here 7 A/dm^2).

2.1.9 Tensile machine

The tensile tests were carried out using an Instron 5800R electromechanical machine equipped with a ± 100 kN load cell and an extensometer. The characteristics of this machine are:

— Minimum tensile speed: 0.1 μm/min,
— Maximum tensile speed: 16 mm/sec,
— Maximum thickness of the specimen in flat jaws: 5 mm,
— Minimum diameter of the test piece in cylindrical jaws: 5 mm,
— Maximum diameter of the test piece in cylindrical jaws: 12 mm.

2.2 Numerical methods

2.2.1 Mechanical modelling using Abaqus

The finite elements software Abaqus from Dassault Systems provides a visualisation and mechanical modelling interface, as well as the ability to perform implicit integration or explicit integration computations (solving dynamic or quasi-static non-linear problems).

Some of the specimens used in this work were designed using Abaqus. The 33CrMoV12-9 material used has been identified using an elasto-plastic law (see section 2.3.2). The designs will include tensile specimens and a split ring. Fig. 2.13 shows the 3D drawings of the final tensile specimen and split ring designed on Abaqus.

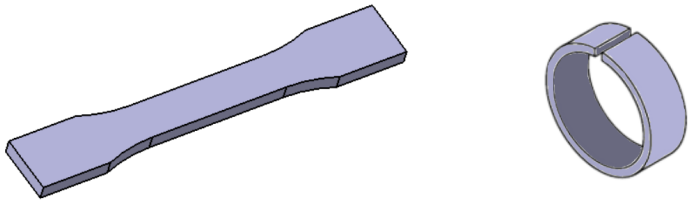

Figure 2.13 – 3D drawings of the tensile specimen and the split ring.

The mesh conditions used throughout these studies are C3D10 i.e. a 10-node quadratic tetrahedron for complex geometries and C3D8R i.e. an 8-node linear brick, reduced integration, hourglass control for simple geometries (e.g. rectangular type).

2.2.2 1D modelling using C language

The C programming language will be used for 1D(-diffusion) and 2D axisymmetric(-stresses) modelling of the stress-diffusion coupling in the applied case of nitrogen interstitial diffusion in iron (α-Fe).

The code was developed within this thesis by writing the coupling by the finite difference method.

The computer used is a DELL PRECISION T3600 and is configured on the open source operating system Linux. It runs on an Intel XEON E5 1620 4 Core 8 Threads 3.6Ghz processor and an 8GB DDR3 ECC (ECC Memory with error correction) RAM.

2.2.3 2D modelling using FreeFEM++

FreeFEM++ is a C++ based partial differential equation solution for 2D and 3D nonlinear multiphysics systems [Hecht, 2020]. From a variational formulation, this language allows to easily solve a linear, nonlinear, time-dependent, or coupled issue.

The influence of a residual stress state prior to the thermochemical treatment will be the focus of the FreeFEM++ simulations (see Section 2.1.2). Indeed, this solver was chosen to model the variational equations of the stress-diffusion coupling in 2D. An example of the implementation of Fick's law (Eq. 1.4), in the case of time discretization by the implicit euler method, is given:

— Variationnal form of Fick's law:

$$0 = \int_V c^* \frac{\partial c}{\partial t} dV + \int_V D\delta_{ij} \frac{\partial c^*}{\partial x_i} dV + \text{BCs} \tag{2.7}$$

— Implementation on FreeFEM++:

```
problem Ficklaw(c1,c2) = int2d(Sh)(c2*c1/dt) - int2d(Sh)(c2*c/dt) // Backward Euler's decomposition
+ int2d(Sh)(D*(dx(c1)*dx(c2)+dy(c1)*dy(c2)))
+ BCs; // Bondaries conditions
```

The goal of these simulations will be to investigate the effect of elastic stresses on diffusion kinetics. Simple geometries (i.e. parallelepipedic samples) will be investigated for this work.

2.3 Base material characterization

It is important to know the initial microstructure of the steel in order to understand the metallurgical phenomena that can occur during a study, treatment (e.g. nitriding) and other processes. The material used in this study is a polycrystalline ferritic steel for industrial use: 33CrMoV12-9. The chemical composition is given in Tab. 2.3.

C	Mn	Si	P	S	Cr	Ni	Mo	V
0,30	0,4-0,7	0,1-0,4	<0,025	<0,025	3,0	<0,3	1,0	0,2

Table 2.3 – Chemical composition of ferritic steel grade 33CrMoV12-9 [AubertDuval,].

It was supplied in non-homogenised form. The homogenisation treatments were then carried out in the laboratory in the quenched and tempered state. The specimens were previously cut by electro-erosion from a 130 mm bar. They were taken at longitudinal iso-radii to limit the probability of carbon segregation. In order to avoid any risk of decarburisation, the parts were carefully wrapped in sheet metal. Indeed, a study by Calliari et *al.* showed that prior decarburisation during a nitriding treatment (see section 1.1.2.3) led to a decrease in the nitrogen diffusion kinetics of the sample [Calliari et al., 2006]. In fact, three successive operations were necessary in order to obtain the expected microstructure and therefore the expected hardening of the material. Firstly, the material is austenitised to bring the precipitates into solution. To do this, the steel is heated to a temperature, in our case 950 °C, such that the iron has acquired its face-centred cubic structure (austenitic - γFe) which can dissolve (in interstitial solution) the carbon present (as opposed to body-centred cubic iron α-Fe in which the carbon is practically insoluble).

The material is then quenched with water or oil (rapid cooling) to avoid precipitation of the carbon (here quenched with water). The quenching process transforms the steel into martensite (a tetragonal phase formed by rapid quenching of F.C.C. (γ)-Fe)), which becomes harder the higher the carbon content (in our case, c%m. = 0.3%). The majority of carbides after quenching are of the $M_{23}C_6$ type, they precipitate at the joints of the martensite laths in the form of ellipses less than one micrometre long and a diameter of about one hundred nanometres [Locquet, 1998, Ginter, 2006]. These carbides also precipitate in the martensite laths in globular form [Locquet, 1998]. The material is then tempered (moderately heated) to precipitate the carbon. This causes the precipitation of fine intra-granular carbides which may be coherent with the α-Fe matrix. The microstructure of the quenched and tempered steel is characterised by a quenched martensite structure [Locquet, 1998]. In this study, the samples were austenitised at 950 °C for 30 minutes, water quenched and tempered at 630 °C for 3 hours, aiming a core hardness of approximatively 400 HV0.2, as shown in Fig. 2.14.

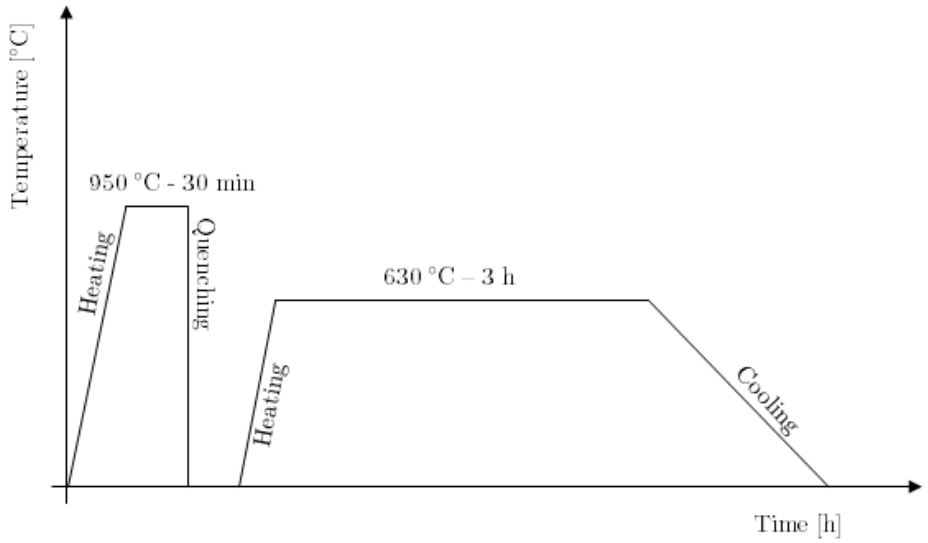

Figure 2.14 – Heat treatments carried out in the laboratory to obtain a hardened and tempered microstructure of the 33CrMoV12-9 steel.

Tempering the steel has preserved the martensite lattice structure while inducing the precipitation of carbides in the form of elongated or globular particles. The initial metallurgical state is characterised by a fine and dispersed precipitation and by the presence of cementite (Fe_3C), molybdenum carbides (Mo_2C), chromium carbides ($Cr_{23}C_6$) and vanadium carbides (VC), which tends to stabilise them [Ginter, 2006]. Tab. 2.4 shows the crystal structure, the lattice parameters and the mass densities of the individual carbides present after treatment of the material.

Phase	crystal structure	Lattice parameters [nm]	Mass density [kg.m^{-3}]
α-Fe	BCC	0.28664	7875
$Cr_{23}C_6$	FCC	1.066	6953
Cr_7C_3	Orthorhombic	a = 0.70149; b = 1.2153; c = 0.4532	6877
VC	FCC	0.41655-0.41310	5259
Fe_3C	Orthorhombic	a = 0.5091; b = 0.67434; c = 0.45260	7675

Table 2.4 – Characteristics of the different carbides present in nitriding steels in the quenched and tempered state [Goldschmidt, 1967].

2.3.1 Microstructure

The experimental characterizations will focus on the 33CrMoV12-9 steel grade. Its properties, physico-chemical and mechanical behaviour have been the subject of numerous studies, allowing to better understand the properties of the material [Guillot, 2018, Godet, 2018].

In order to describe the changes that will be induced by the two surface treatments studied in the present work, it is necessary to characterise the initial microstructure of the steel grade. The metallographic study of the steel was carried out using a scanning electron microscope (SEM) (see Fig. 2.15).

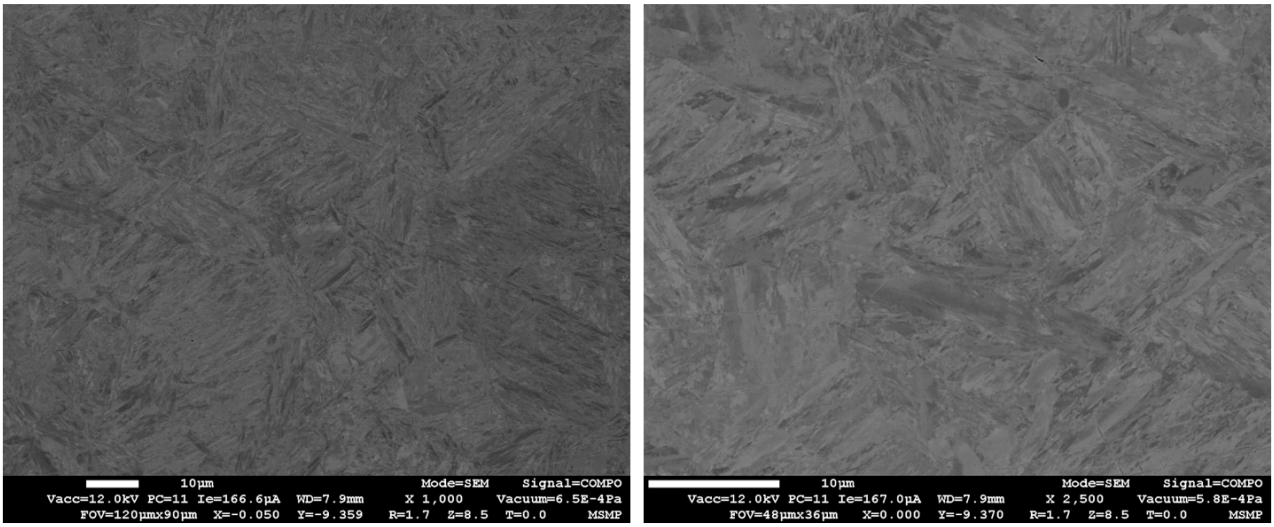

Figure 2.15 – Scanning electron microscope (SEM) images of 33CrMoV12-9 steel before nitriding. a) x1000 b) x2500.

2.3.2 Mechanical material parameters identification

As mentioned above, Abaqus simulations will be performed. In order to model the behaviour of the material, data was identified from an elastoplastic model called Ramberg-Osgood. This model was carried out as part of this thesis and used data from experimental tensile curves extracted by F. Godet [Godet, 2018].

Table 2.5 shows the average mechanical characteristics at 20 °C obtained by reading the curves of F. Godet, where $\sigma_{0.2}$ is the yield strength at 0.2% of strain, σ_m is the tensile strength and A% is the elongation after break.

$\sigma_{0.2}$ [MPa]	σ_m [MPa]	A [%]	E [MPa]
1082	1200	16	202000

Table 2.5 – Mechanical characteristics of the steel grade 33CrMoV12-9 at 20 °C [Godet, 2018].

Ramberg-Osgood's elastoplastic model is presented thanks to Eq. 2.8:

$$\varepsilon = \frac{\sigma}{E} + K\varepsilon_{0.2}^{\mathrm{p}}\left(\frac{\sigma}{\sigma_{0.2}}\right)^{m} \tag{2.8}$$

where K and m are variables, $\varepsilon_{0.2}^{\mathrm{p}}$=0.002[-] is the equivalent total strain at 0.2% of strain.

Les paramètres K et m ont pu être identifiés à partir d'une feuille de calcul EX=cel utilisant le solveur Tab. 2.6 shows the parameters values obtained by identification from the data in Fig. 2.16.

Fig. 2.17 shows the difference between the identified model named Ramberg-Osgood and the experimental curve. The identification fits well with this figure.

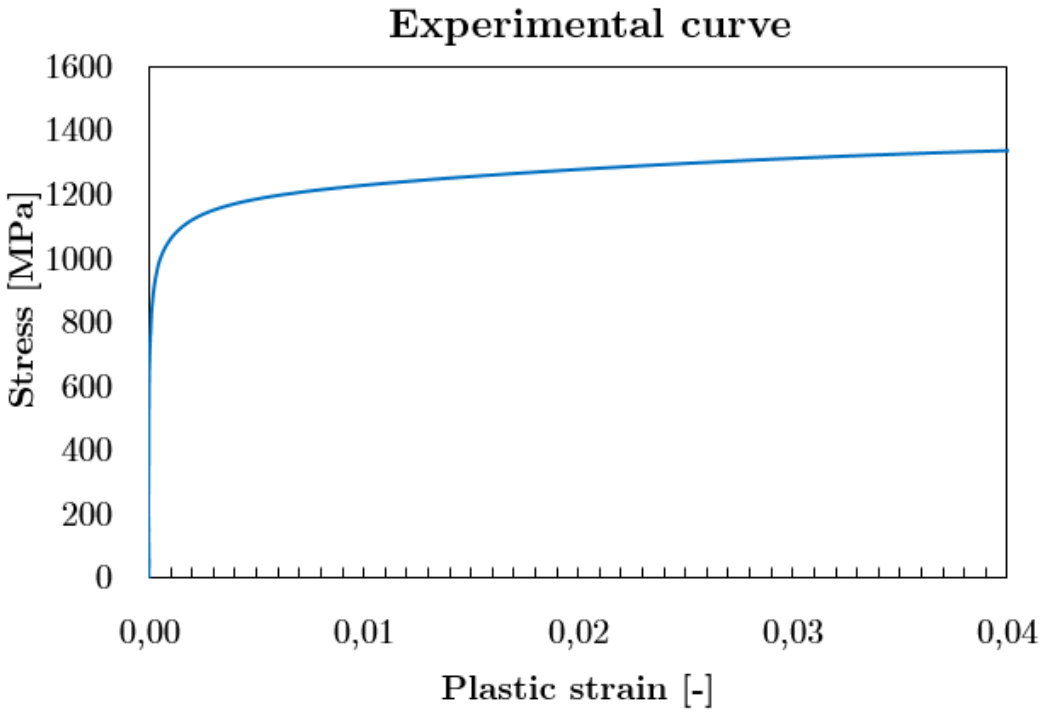

Figure 2.16 – Data from F. Godet on the 33CrMoV12-9 steel [Godet, 2018].

K [-]	m [-]
1.1	14.4

Table 2.6 – Values of K and m obtained, through an identification of the Ramberg-Osgood model, from the data in Fig. 2.16.

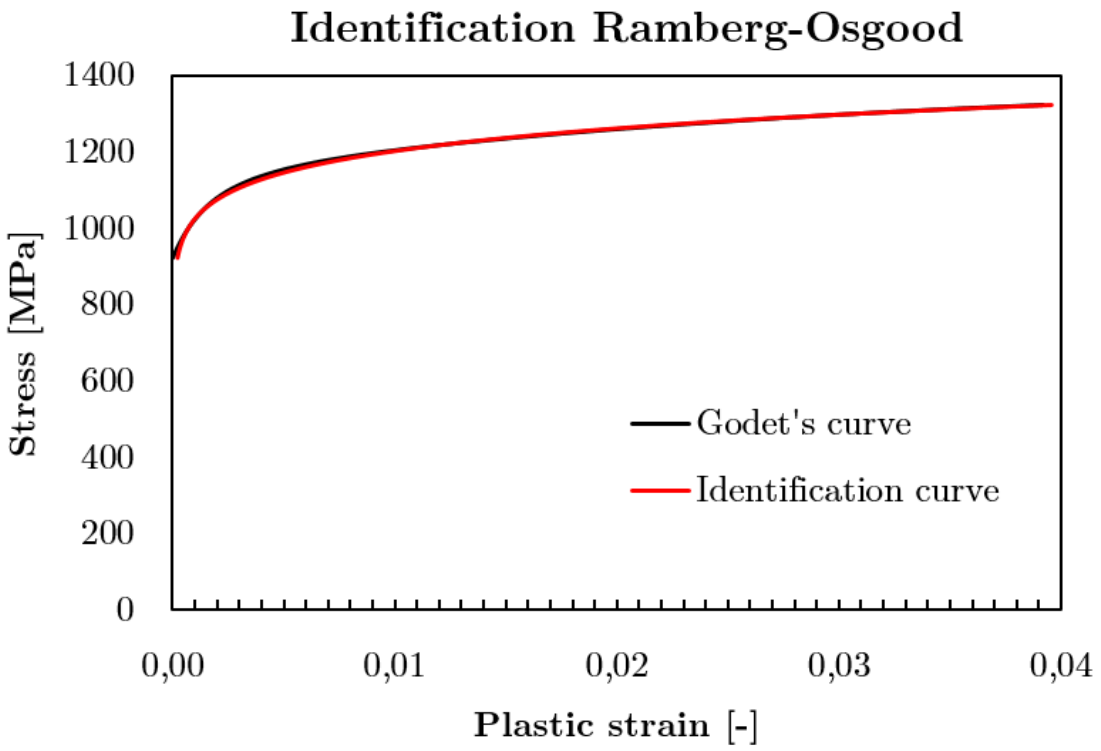

Figure 2.17 – Identification on the 33CrMoV12-9 steel from the Ramberg-Osgood relastionship [Godet, 2018].

Chapter 3

Highlighting of stress-diffusion coupling

Contents

3.1 Stress-diffusion coupling simulations

Many situations today require the use of digital technologies by researchers in order to carry out their studies (which are costly, time-consuming, etc.). As for example, with gas nitriding, which is a long-term thermochemical treatment carried out at high temperature. Thus, the aim of these numerical simulations of stress-diffusion coupling is first to understand the phenomenon by varying factors such as time, sample thickness, boundary conditions, β parameter (defined in Subsection 1.2.3.1) or stress amplitude. The objective is to understand the effect on diffusion kinetics, in particular the long range diffusion of nitrogen. These computational results will represent numerical values of phenomenological parameters, which will then be analysed and interpreted in order to design appropriate studies to try to validate these phenomena and thus conclude on the dominance of stress effects (driving force and mobility). It is important to note that the numerical simulations (carried out in this work) are a mathematical representation of the behaviour of a real system under certain conditions (infinitely diluted solution (c 1), no precipitation phenomena, no co-diffusion, isotropic elastic material and in macroscopic scale study.).

This section will present two models. A first 2D model implemented on the free software FreeFEM++ [Hecht, 2020], with the aim of visualizing and understanding the 2D concentration and stress fields. The coupling equations have highlighted a coupling between a vector aspect by the flux and concentration components and especially a tensor aspect by the strain and stress components. The aim of this model is to highlight the mechanical equilibrium across the cross-section of a sample for different cases of study: symmetrical diffusion, dissymmetrical diffusion, variation of the thickness of the sample. No parametric studies will be presented in this model. A second 1D (2D axisymmetric) model will be presented, this time using a calculation code developed in the laboratory. The aim of this model is to carry out parametric studies on the effect of the stress gradient and stresses on mobility by taking into account, on the one hand, the temporal aspect of the residual stresses and, on the other hand, the constant aspect of the applied stresses (for all neglected creep sources).

3.1.1 Hypotheses

This part deals with numerical simulations based on the FreeFEM++ calculation code, and its main objective is to place itself in a case with strong hypotheses:

— Binary iron-nitrogen (α-Fe-N) layer,

— Case of interstitial diffusion,

— Infinitely diluted medium ($c \ll 1$) with a single diffusing element (without carbon co-diffusion or associated precipitation),

— A supposedly isotropic elastic material,

— Isothermal process.

Throughout these numerical studies, the nitrogen concentration at the surface will be considered as constant, i.e. Dirichlet conditions will be used.

3.1.2 Implementation in FreeFEM++ (2D model)

A 2D model was built using the open-source software FreeFEM++. Starting from a variational formulation, this language allows to easily solve a linear, non-linear, time-dependent or coupled problem. The equations of the stress-diffusion coupling have shown a vector aspect by the aspect of flux and concentration but also a tensor aspect by taking into account strains and stresses. The main interest of this model is to observe from a fine mesh ($\Delta z = 5$ μm), the concentration and hydrostatic stress fields on the cross section of a sample. These fields will be presented as symmetrical images and also as profiles as a function of depth.

The tensor aspect of stress on diffusion kinetics using a 2D stress-diffusion coupling model will then be studied. The assumption of plane stresses is used in this model, allowing a 3D model to be reduced to a 2D model.

3.1.2.1 Variational script

To implement the code in FreeFEM++, it was first necessary to write the equations Eqs. 1.66 and 1.82 based on the principle of the variational approach for solving partial differential equations applied first to the linear elasticity problem and then to the diffusion problem. It is necessary to replace the equation by an equivalent formulation, known as variational, obtained by integrating the equation multiplied by some function, known as a test. In the case of the mechanical problem, the test function will be v_i and for diffusion c^*. They are respectively of the same order as the displacement and the concentration. The approach for both parts will be the same:

— Integration of the equilibrium equation and the mass conservation equation respectively [Lemaitre and Chaboche, 1990],

— Using Green-Ostrogradski's theorem (or divergence theorem) to homogenise integrals,

— Obtaining variational formulations.

The variational aspect of the mechanical problem taking into account stress-free strain of the deviator type, in simplified form, is:

$$\int_V v_i \sigma_{ij,j} dV = \int_{\partial V} v_i \sigma_{ij} n_j dS - \int_V \frac{\partial v_i}{\partial x_i} \sigma_{ij} dV = 0 \tag{3.1}$$

According to Eq.1.82 and Eq.3.1, the variational formulation of the mechanical problem becomes:

$$\int_{\partial V} v_i g_i dS - \int_V \frac{\partial v_i}{\partial x_i} \left(2\mu \left(\varepsilon_{ij}^{tot} - c\eta_{ij} \right) + \lambda \left[\varepsilon_{kk}^{tot} - c\eta_{kk} \right] \delta_{ij} \right) dV = 0 \tag{3.2}$$

In this study, g_i $(= 0)$ term is not taking into account.

The variational aspect of the diffusion problem, in simplified form, is:

$$\int_V c^* \frac{\partial c}{\partial t} dV + \int_V c^* \left(J_I^\Phi \right)_{i,i} dV = 0 \tag{3.3}$$

$$\int_V c^* \left(J_I^\Phi \right)_{i,i} dV = \int_{\partial V} c^* \left(J_I^\Phi \right)_i n_i dS - \int_V \frac{\partial c^*}{\partial x_i} \left(J_I^\Phi \right)_i dV \tag{3.4}$$

According to Eq.1.66 and Eq. 3.3, the variational formulation of the diffusion problem becomes:

$$\int_V c^* \frac{\partial c_I^\Phi}{\partial t} dV + \int_{\partial V} c^* J_I^\Phi dS - \int_V \frac{\partial c^*}{\partial x_i} \left[-D_I^\Phi \delta_{ij} \frac{\partial c_I^\Phi}{\partial x_j} + \frac{1}{3} \frac{D_I^\Phi \delta_{ij} \Delta V}{RT} c_I^\Phi \frac{\partial \left(\sigma_{kk} \delta_{ij} \right)}{\partial x_j} \right] dV = 0 \tag{3.5}$$

Where:

$$\sigma_{kk} \delta_{ij} = (2\mu + 3\lambda) \left[\varepsilon_{kk}^{tot} - c\eta_{kk} \right] \delta_{ij} \tag{3.6}$$

Eqs. 3.2 and 3.5 were then imported into the FreeFEM calculation code [1]. The code presented below is only a part of the code showing the values to be initialized, the diffusion problem corresponding to the variational equation 3.5, the elasticity problem corresponding to the variational equation 3.2 and the loop on the stress-diffusion coupling. Prior to diffusion calculation, a first calculation is used to initialise the elasticity problem. Then, the completed loop first solves one iteration of the diffusion problem and then one iteration of the elasticity problem for every 1000 iterations, i.e. until $t = 1$ s.

```
   // Definition of time value:
dt=0.001 ; // Time increment
iter=1000; // Number increment


   // Definition of source term and initial data:  c= 0 ; // reference concentration
Eo=E; // Open-system Young's modulus
nuo=nu; // Open-system Poisson's coefficient
mu=E/(2.*(1.+nu)); // Open-system μ coefficient i.e.  Lamé's coefficient
lambda=(E*nu)/((1.+nu)*(1.-2.*nu)); // Open-system λ coefficient i.e.  Lamé's coefficient


   // Definition of the system to be solved backward Euler scheme in time:
problem diffusion(c1,c2) = // Variational writing of the diffusion equation coupled with mechan-
ics
int2d(Sh)(c2*c1/dt) //int2d corresponds to a 2D integration formulation, Sh to the type of mesh
chosen, c1 to the c at t and c2 to the c*
- int2d(Sh)(c2*c/dt) // c corresponding to the c at t=t-1
+ int2d(Sh)(D*(dx(c1)*dx(c2)+dy(c1)*dy(c2)))
- int2d(Sh)(D*delta*c1*grad(c2)'*grad(trsig1)) // delta = 1/3 ΔV/RT
+ on(1,c1=C0) // Boundary condition in concentration - Dirichlet conditions
+ on(2,c1=C0)
+ on(3,c1=C0)
+ on(4,c1=C0);
problem elasticite([Vx, Vy],[Ux, Uy]) = // Variational writing of the mechanical equation cou-
pled with diffusion
-int2d(Sh)(2*mu*epsilon(Vx,Vy)'*epsilon(Ux,Uy) + lambda*div(Ux,Uy)*div(Vx,Vy)) // Vx,Vy corre-
spond to the displacement and Ux,Uy to the test function displacement
```

1. Code presented at the Winter Colloquium in Aussois "Contraintes résiduelles : de nouveaux outils pour de nouveaux défis - Élaboration, usage, durée de vie" in January 2020 (see article and poster Appendix A which were the subject of the MECAMAT 2020 Award [Germain et al., 2020]).

```
+ int2d(Sh)((3*lambda+2*mu)*c1*eta*div(Ux,Uy))
+ on(1,Vx=0) // Boundary condition in displacement
+ on(3,Vy=0);

   // Beginning of the computation of the diffusion/stress coupling
elasticite; // Initialization of the mechanical conditions of the sample

   // Loop
for (iter=1;iter< niter+1;iter=iter+1) // Writing the loop "for" by a weak coupling:  first cal-
culation in diffusion then a calculation in mechanics
{
diffusion;
elasticite;
cout ≪ "t = "≪ tt ≪ "/"≪ dt*niter ≪ " -> residu = " < ≪ residu ≪ endl; // Standard C++
output device
// iteration
tt=iter*dt; // total time calculation
c=c1 ; // Backward Euler's method
}
```

3.1.2.2 Numerical solutions

The study conditions related to the diffusion parameters will not correspond to known experimental values (i.e. c_0, D_I^Φ and η), they will be considered as arbitrary in order to have faster calculations, which converge and will only aim at visualising the phenomena.

3.1.2.2.1 Square sample 1×1 mm A preliminary analysis was conducted to validate the 2D model in the situation of Eq. 3.5, i.e. just considering the influence of stress on the driving forces ($\nabla\sigma \neq 0$ and $\beta = 0$). Fig. 3.1 presents the concentration c and hydrostatic stress σ^H ($= \frac{1}{3}\sigma_{kk}$) fields. This diffusion coefficient is much higher than in reality, because FreeFEM++ simulations are long and costly in terms of mesh size. Indeed, the larger D is, the faster the diffusion, and as FreeFEM calculations are long in the case of geometries close to reality for a small time and space step, it is necessary to take a "large" D to reduce the calculation time as much as possible. These simulations therefore only allow us to visualise the effects and influences of stress on the kinetics. Fig. 3.1 shows the 2D concentration and hydrostatic stress fields of a 1×1 mm square sample subjected to a fixed surface concentration of $c_0 = 0.001$ with study parameters presented in Tab. 3.1. A 2D mesh is used, with triangle elements of size 10 μm.

D_I^Φ [cm^2.s^{-1}]	T [°C]	E [GPa]	ν [-]	t [s]	η [-]
5.10^{-5}	520 °C	202	0.29	1	$2{,}4.10^{-3}$

Table 3.1 – Parameters used in terms of the diffusion coefficient D_I^Φ, the temperature of treatment T, the Young's modulus E [Fallot, 2015], the Poisson's coefficient ν [Fallot, 2015] and the time t.

This 2D model aims to understand the tensorial aspects by visualising the symmetry of the fields and also the edge effects. The concentration fields show a maximum concentration at the surface followed by a decay. The hydrostatic stress fields show a negative stress at the surface with an increase in stress to positive stress. The stress calculations are mechanically valid as the mechanical equilibrium is respected immediately from the above mentioned Eq. 3.2.

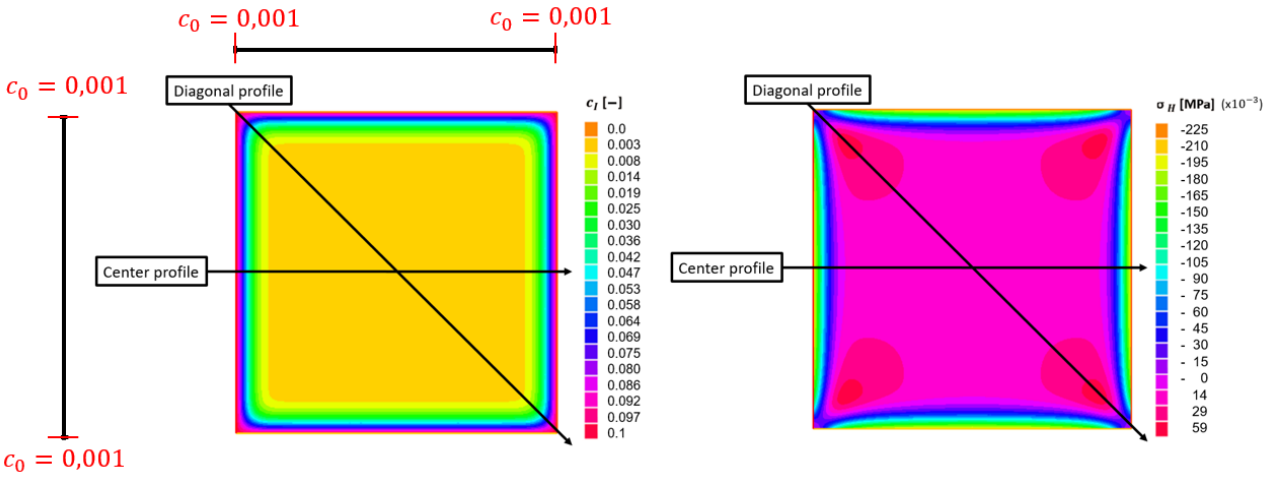

Figure 3.1 – a) Concentration field and b) hydrostatic stress field for a square sample (1×1 mm) in the case of surface concentrations of $c_0 = 0.001$.

The concentration and hydrostatic stress profiles of the central and diagonal profiles (profiles schematised in Fig. 3.1) are, respectively, presented in Figs. 3.2a) and b). The central concentration profile represents the typical evolution of an erfc law observed in diffusion experiments. Similarly, the hydrostatic stress profile represents the well known typical evolution of the mechanical equilibrium associated with diffusion. The diagonal profile shows an evolution that does not follow an erfc law and demonstrates a clear acceleration of the concentration at depth. The diagonal profile in hydrostatic stress shows a distinct profile. The profile follows a zero hydrostatic stress at the surface, a negative gradient with a low compressive stress, a positive gradient with a much higher tensile stress than the central profile, and finally a negative gradient towards the base material. The equation used appears to have an inverse effect on stress acceleration (Eq. 3.5). In hydrostatic stress, the diagonal profile shows a lower stress gradient, very low compressive stresses, and then tensile stresses. The used equation only considers the effect of the stress gradient ($\nabla\sigma \neq 0$) in terms of coupling and thus does not consider the effect of the sign of the stress but only the sign of the stress gradient. The concentration acceleration is simply the product of a double flux effect (the addition of lateral and perpendicular flow) and the gradient effect. This first simulation was validated using Fick's analytical concentration profile. This validation was carried out by calculating the numerical Fick diffusion coefficient $D_{\text{Fick}}^{\text{numerical}}$ and comparing it to the analytical Fick diffusion coefficient $D_{\text{Fick}}^{\text{analytical}}$. The relative error measured from equation : $\left(\frac{D_{\text{Fick}}^{\text{numerical}} - D_{\text{Fick}}^{\text{analytical}}}{D_{\text{Fick}}^{\text{numerical}}}\right) \times 100$, showed that the deviation is of the order of -3%.

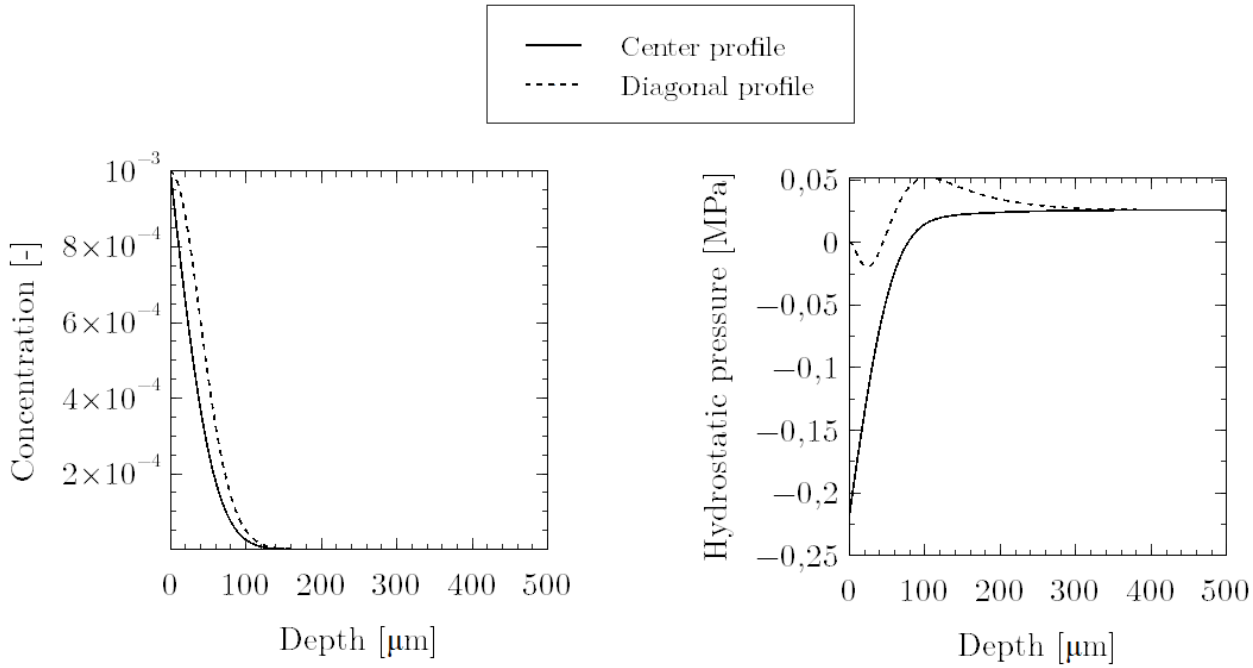

Figure 3.2 – Evolution of concentration and hydrostatic stress as a function of depth for a square sample (1×1 mm) for the diagonal and central profiles.

The triaxiality factor is plotted in Fig. 3.3a) to better understand the tensor aspect on the kinetics. The ratio of the hydrostatic stress (σ^H) to the equivalent von Mises stress σ^{VM} determines the triaxiality Tx of the stresses:

$$Tx = \frac{\sigma^H}{\sigma^{VM}} \tag{3.7}$$

In simple cases, this parameter is equal to:

— Pure shear: $Tx = 0.0$,

— Uniaxial tension: $Tx = 0.33$,

— Equi-bitension: $Tx = 0.66$,

— Uniaxial compression: $Tx = -0.33$,

— Hydrostatic pressure: $Tx \to -\infty$

Fig. 3.3a) shows that the central profile is in uniaxial compression for the first 80 μm, then tends towards equi-bitension stress in the core. The diagonal profile describes a uniaxial compression profile at the surface, followed by a uniaxial tensile state and an equi-bitensile stress state at the core.

Fig. 3.3b) illustrates the evolution of the Young's modulus E_0 defined for an open system, described in Eq. 1.75. This profile shows an inverse evolution of the concentration, the higher the concentration, the lower the Young's modulus E_0. Although thermochemical treatments are intended to improve surface properties such as hardness and fatigue resistance, this graph shows that the sample loses elasticity along the diffusion layer. In

the case here of a binary with a low value concentration field, little difference is observed, however, it shows that in the case of a high concentration, the impact on the Young's modulus could become significant.

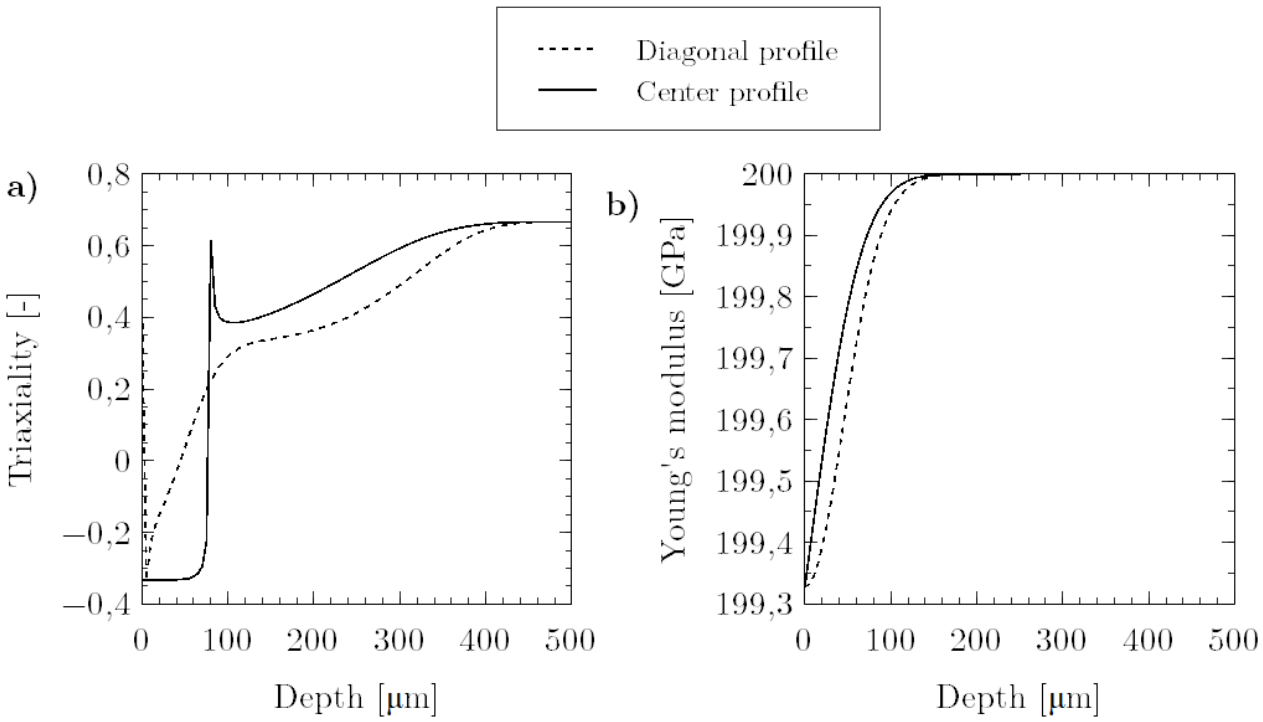

Figure 3.3 – Evolution of triaxiality as a function of depth for a square specimen (1×1 mm) for the diagonal and central profiles.

The central and diagonal profiles of the concentration, hydrostatic stress, triaxiality factor and Young's modulus in an open system were observed. These results made it possible to understand the experimental interest of having samples of sufficiently large dimensions to avoid any edge effect. The observations show that the behaviour in the corners seems to be only a problem caused by a perpendicular double flow, with a very specific hydrostatic stress profile that does not present a standard profile. This observation shows the intention to understand the tensorial aspects in order to observe these phenomena which, in specific industrial cases such as gear teeth, can cause premature failures by modifying the fatigue life characteristics of parts undergoing double flow phenomena.

3.1.2.2.2 Stress gradient effect The previous study demonstrated the importance of avoiding edge effects. The dimensions of this section are therefore based on the samples used in the thermogravimeter treatments, i.e. 17×13×X mm, where X varies between 1 and 5. The three samples were meshed with triangular elements: 1956 (1 mm thick sample), 3752 (2 mm thick sample) and 9313 (5 mm thick sample). The purpose of this search is to visualise the concentration and hydrostatic stress fields as a function of thickness, as well as to plot the equivalent centre profiles of the samples.

Fig. 3.4 presents the three samples that will be compared in this 2D study:

— The 2 sides (S) sample corresponds to a sample that has undergone thermochemical treatment simultaneously on all its faces,

— The 1 side (F1) sample corresponds to a sample that has undergone thermochemical treatment simultaneously on 3 of its sides. In other words, one of its two main faces is blocked to diffusion,

— The 1+1 sides (F2) sample corresponds to a sample that has undergone a first thermochemical treatment simultaneously on 3 of its faces (equivalent to the 1 side (F1) sample) and in a second time has undergone a thermochemical treatment simultaneously on 3 of its faces on the opposite side.

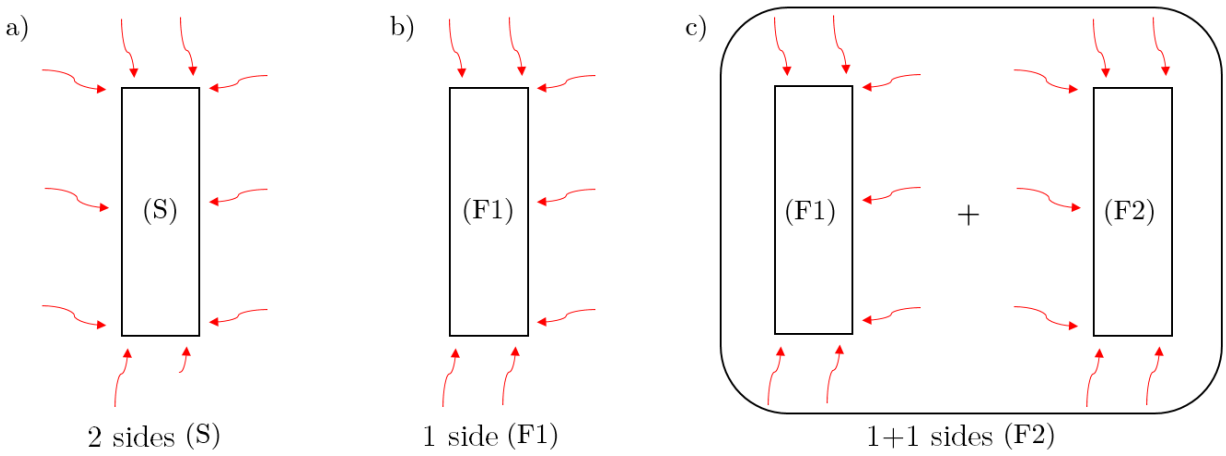

Figure 3.4 – Schematization of the diffusion applied to the samples: 2 sides (S), 1 side (F1) and 1+1 sides (F2).

The aim of this study is to examine the impact of the following factors on the long-range diffusion kinetics:

— the structural influence on asymmetric diffusion at different thicknesses (1 side (F1) sample) compared to a 2 sides (S) sample,

— the impact of a residual stress gradient (1+1 sides (F2) sample),

— the influence of 1+1 sides diffusion versus 2 sides diffusion.

The calculation code in the case of the sample "1+1 sides (F2)" changes with an additional time loop. There are therefore two diffusion problems (diffusion1 and diffusion2) and two mechanics problems (elasticity1 and elasticity2), as written below:

```
   // Definition of time value:
dt=0.001 ; // Time increment
iter=1000; // Number increment
flux=0 ; // flux condition


   // Definition of source term and initial data:  c= 0 ; // reference concentration
Eo=E; // Open-system Young's modulus
nuo=nu; // Open-system Poisson's coefficient
mu=E/(2.*(1.+nu)); // Open-system μ coefficient i.e.  Lamé's coefficient
```

```
lambda=(E*nu)/((1.+nu)*(1.-2.*nu)); // Open-system λ coefficient i.e.  Lamé's coefficient

   // Definition of the system to be solved backward Euler scheme in time:
problem diffusion1(c1,c2) =
int2d(Sh)(c2*c1/dt)
- int2d(Sh)(c2*c/dt)
+ int2d(Sh)(D*(dx(c1)*dx(c2)+dy(c1)*dy(c2)))
- int2d(Sh)(D*delta*c1*grad(c2)'*grad(trsig1))
- int1d(Sh,1)(flux*c2) // Neumann condition, i.e.  flow boundary condition, here flow = 0 to sim-
ulate diffusion blocking
+ on(2,c1=C0);

   problem elasticite1([Vx, Vy],[Ux, Uy]) =
-int2d(Sh)(2*mu*epsilon(Vx,Vy)'*epsilon(Ux,Uy) + lambda*div(Ux,Uy)*div(Vx,Vy))
+ int2d(Sh)((3*lambda+2*mu)*c1*eta*div(Ux,Uy))
+ on(1,Vx=0)
+ on(2,Vy=0);

   problem diffusion2(c3,c4) =
int2d(Sh)(c4*c3/dt)
- int2d(Sh)(c4*c/dt)
+ int2d(Sh)(D*(dx(c1)*dx(c4)+dy(c3)*dy(c4)))
- int2d(Sh)(D*delta*c3*grad(c4)'*grad(trsig2))
+ int1d(Sh, 2)(flux*c4) // here flow = 0 in other words, leading in this case to a phenomenon
called post-diffusion tempering
+ on(1,c3=C0);

   problem elasticite([Vx, Vy],[Ux, Uy]) =
-int2d(Sh)(2*mu*epsilon(Vx,Vy)'*epsilon(Ux,Uy) + lambda*div(Ux,Uy)*div(Vx,Vy))
+ int2d(Sh)((3*lambda+2*mu)*c3*eta*div(Ux,Uy))
+ on(1,Vx=0)
+ on(2,Vy=0);

   // Beginning of the computation of the diffusion/stress coupling
elasticity1;

   // Loop n°1
for (iter=1;iter< niter+1;iter=iter+1)
{
diffusion1;
elasticity1;
```

```
cout ≪ "t = "≪ tt ≪ "/"≪ dt*niter ≪ " -> residu = " < ≪ residu ≪ endl;
// iteration
tt=iter*dt;
c=c1 ;
}

    // Loop n°2
for (iter=1;iter< niter+1;iter=iter+1)
{
diffusion2;
elasticity2;
cout ≪ "t = "≪ tt ≪ "/"≪ dt*niter ≪ " -> residu = " < ≪ residu ≪ endl;
// iteration
tt=iter*dt;
c=c3 ;
}
```

The concentration and stress fields for the three sample types are shown in Fig. 3.5. The asymmetry of the stress field is visible in the sample (F1), with low stress values on the opposite side (F1). Due to the perpendicular double diffusion on the upper side of the sample (F2), tensile stresses due to a biaxial stress state are observed. This demonstrates that performing this type of experiment would lead to preventing diffusion on the upper edges in order to avoid any risk of edge effect. The central profiles have been plotted in Fig. 3.6. The concentration profiles are identical in all three cases. The hydrostatic stress profiles reveal that the (S) and (F2) profiles are identical, but not the (F1) profile. These results lead to the conclusion that for a 5 mm sample, the influence of the gradient is insufficient to detect variations. Furthermore, with these residual stress rates, it can be deduced that the effect of the concentration of a 2 sides sample (S) compared to a 1+1 sides sample (F2) is zero.

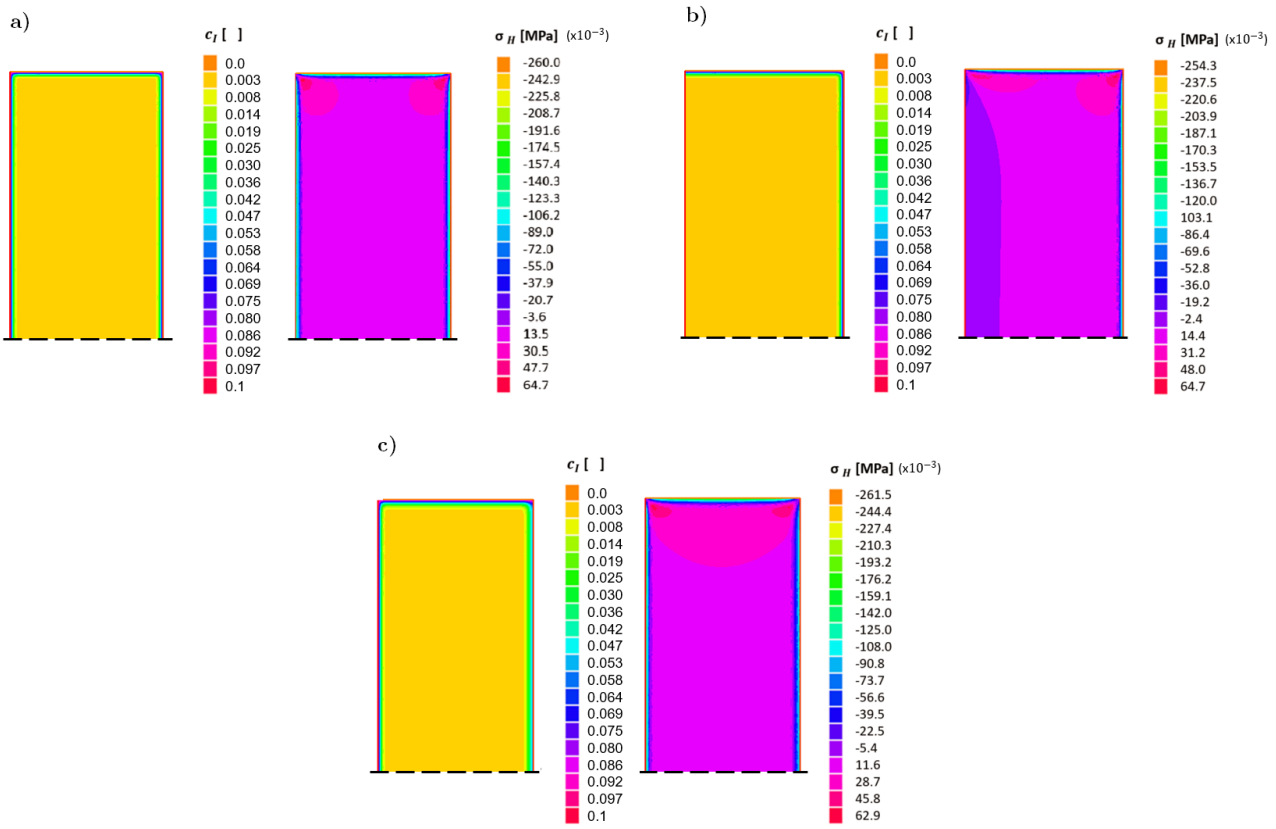

Figure 3.5 – Evolution of the concentration fields and of the hydrostatic stress fields of a cross section of a 5 mm thick sample respectively for a) 2 sides (S) sample, b) 1 side (F1) sample c) 1+1 sides (F2) sample.

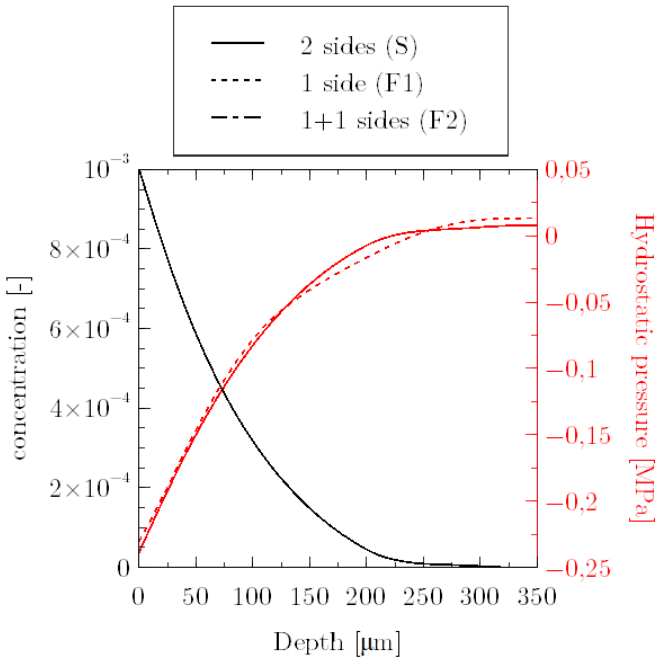

Figure 3.6 – Evolution of concentration and hydrostatic stress profiles of a cross section of a 5 mm thick sample respectively for 2 sides sample (S), 1 side (F1) sample and 1+1 sides (F2) sample.

Figs. 3.7a) and b) show the hydrostatic stress fields for one-sided (F1) diffusion and concentration for 1+1 sides (F2) diffusion respectively.

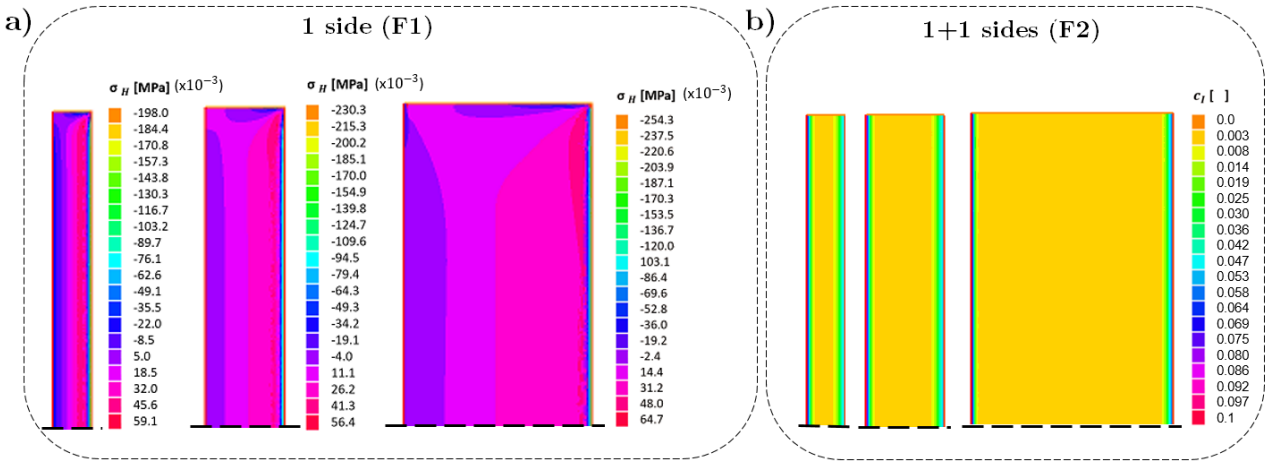

Figure 3.7 – a) Hydrostatic stress field for the case of 1 side (F1) sample, b) Concentration field for the case of 1+1 sides (F2) sample, for three sample thicknesses (1 mm , 2 mm and 5 mm).

Figs. 3.8a) and b) show the stress and hydrostatic stress profiles for the two cases (F1) and (F2), respectively, for the three sample thicknesses (1 mm, 2 mm and 5 mm). Fig. 3.8a) shows that the concentration profiles are identical. The stress profiles (F1) and (F2) corresponding to the three samples are shown in Fig. 3.8b). They show that the surface stress is higher and the stress gradients are larger in the case of the (F2) curves. These differences are due to mechanical equilibrium, as well as the superposition of the stress gradient obtained on the opposite side (F1) and that obtained during diffusion (F2). However, these stress differences have no effect on the diffusion kinetics. This can be explained by the fact that either a positive gradient has no effect on the diffusion kinetics, which contradicts the previous results, or the amplitude of the stress gradient is too small.

Figs. 3.9a) and b) show the concentration and hydrostatic stress profiles between a sample (F1) and a sample (F2) on the opposite side respectively. Fig. 3.9a) shows a clear decrease of 50 % in the surface concentration against a diffusion depth increased by 33 %. These observed phenomena confirm what is known in the literature. Diffusion is a temperature-activated phenomenon, and as demonstrated by Fick's method (see Eg. 1.4), interstitial atoms continue to diffuse towards less concentrated areas in order to reach thermodynamic equilibrium. This is why the profile (F1) shows that diffusion has continued without any new source of diffusion. Fig. 3.9b) shows that the stress values are much lower at the surface after undergoing additional post-diffusion tempering due to reduced concentration.

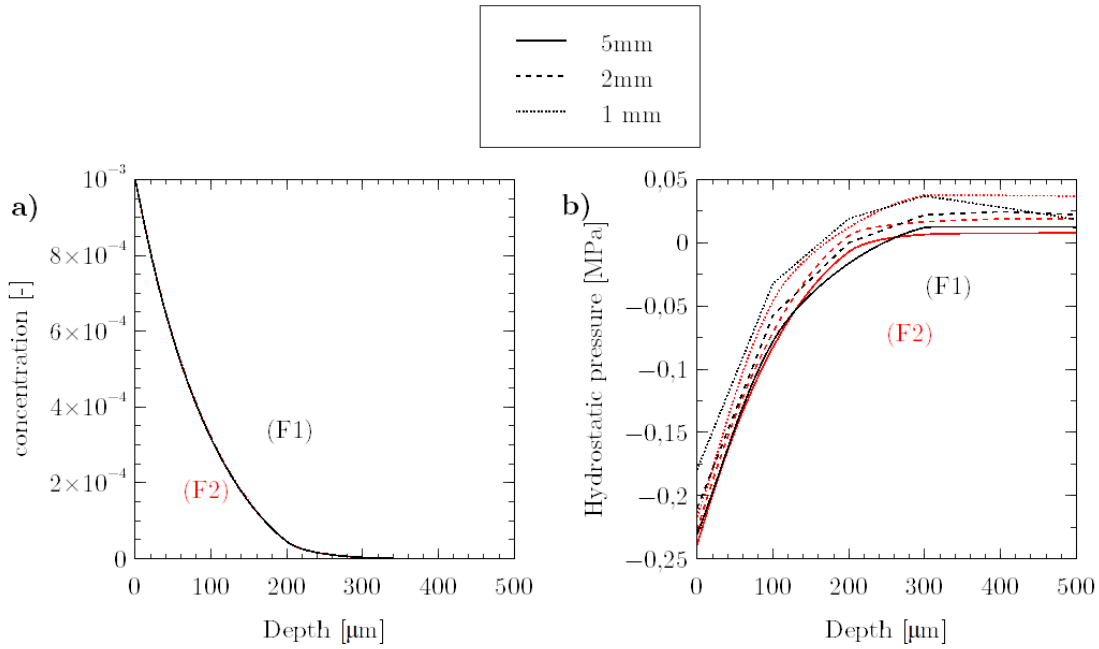

Figure 3.8 – a) Evolution of concentration profiles and b) of hydrostatic stress profiles of the cross-section of three sample thicknesses (1 mm, 2 mm and 5 mm) for a 1 side (F1) sample and a 1+1 sides (F2) sample respectively.

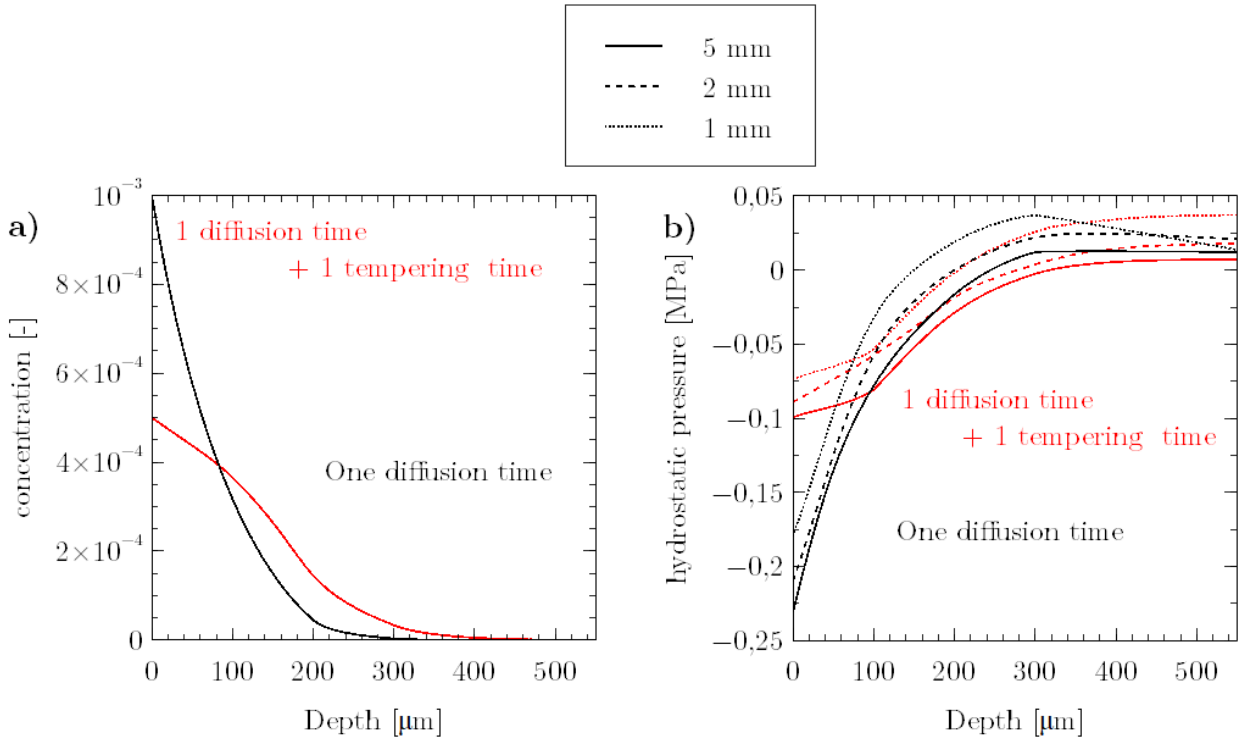

Figure 3.9 – a) Evolution of concentration profiles and b) of hydrostatic stress profiles of the cross-section of three sample thicknesses (1 mm, 2 mm and 5 mm) for a 1 side (F1) sample and the opposite face of a 1+1 sides (F2) sample.

3.1.2.2.3 Stress effect on mobility - β parameter Usually, the coefficients β and γ_I are not taken into account on the effective diffusion coefficient in the mobility part of the stress-diffusion coupling equation. As a result, a large number of papers published on this coupling have used an effective diffusion coefficient $D_{\text{effective}}$ where the mobility is only a function of the stress-independent diffusion coefficient and where the stress only influences the diffusion potential gradient corresponding to the driving force. As presented earlier, Eq. 3.18 shows that mobility could have an effect in the form of a "mobility" stress and in the form of a "mobility" stress gradient.

So the objective is to feed the code with a new notion which is the effect of the stresses on the mobility via a parameter β. In this thesis work, the term $\gamma_I \sigma_{ij}$ is not taken into account. This study focused only on the influence of the hydrostatic stress σ_{kk}. Eq. 3.5 is modified to Eq. 3.8.

$$\int_V c^* \frac{\partial c}{\partial t} dV + \int_{\partial V} c^* \mathrm{j} dS - \int_V \frac{\partial c^*}{\partial x_i} \left[-\left(D + \beta\sigma_{kk}\right) \frac{\partial c}{\partial x_i} + \frac{1}{3} \frac{D\Delta v}{RT} c \frac{\partial \left(\sigma_{kk}\delta_{ij}\right)}{\partial x_i} \right] dV = 0 \tag{3.8}$$

The study is based on a sample cross-section of 1 mm. This study will only consider two cases to observe the concentration and the hydrostatic stress profile:

— Stress gradient effect: $\nabla\sigma \neq 0$ and $\beta = 0$,

— Effect of stress on mobility: $\nabla\sigma = 0$ and $\beta > 0$.

Figures 3.10) and b) show the effect of stress on mobility, via $\beta = 1.3.10^{-5}$ cm^2.MPa^{-1}.s^{-1}, on the concentration and hydrostatic stress profiles, respectively, compared to the case of the effect of a stress gradient. This value of β was retained after several simulations allowing to obtain notable effects on kinetics diffusion. The results show that for the diagonal and central profiles, the effect of mobility leads to a significant slowing down of the diffusion kinetics and a modification of the stress profiles. This observed slowing down is in line with the observations made in the literature where compressive stresses lead to a decrease in diffusion kinetics. The surface stress of the central profile increases from -217×10^{-3} MPa to -230×10^{-3} MPa. These differences are due to mechanical balancing.

Fig. 3.11 shows that taking mobility into account leads to a shift of the profile towards the surface as observed in Fig. 3.10 by a slowing down of the kinetics.

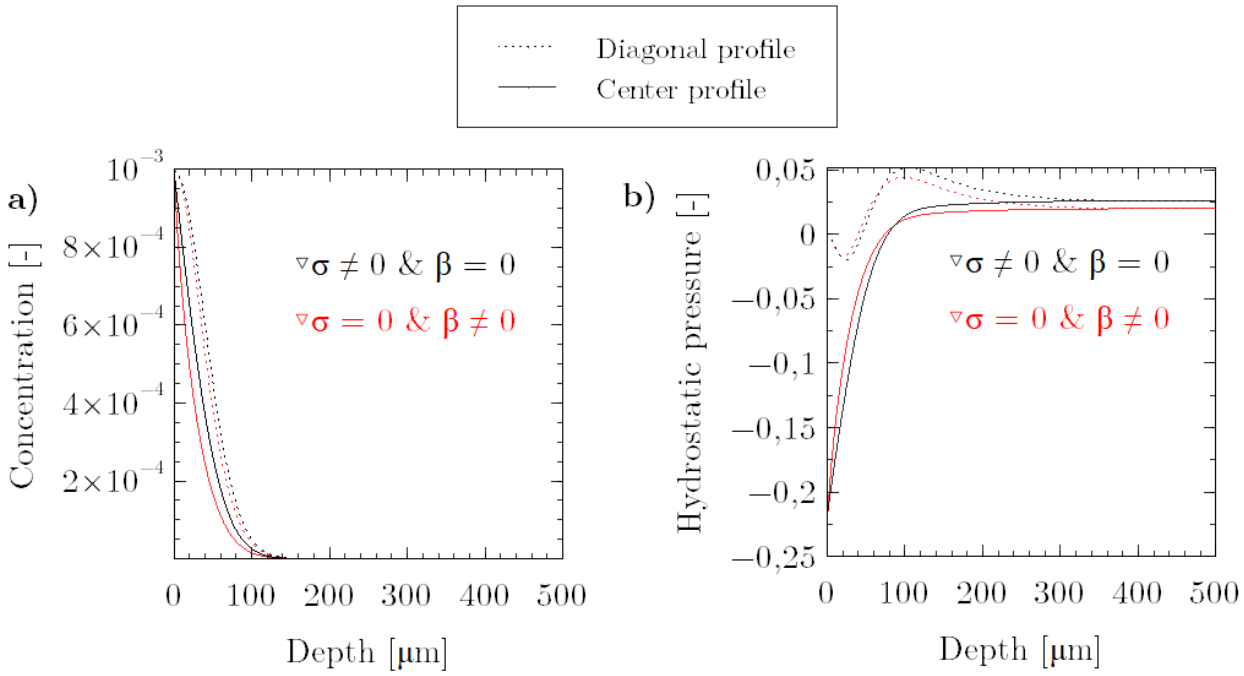

Figure 3.10 – Comparison of diagonal and central profiles of the evolution of a) concentration and b) hydrostatic stress as a function of cross-sectional depth of a square sample 1×1 mm comparing the effect of the stress gradient ($\nabla\sigma \neq 0$ and $\beta = 0$) and the effect of stresses on mobility ($\nabla\sigma = 0$ and $\beta \neq 0$) for one sample (S).

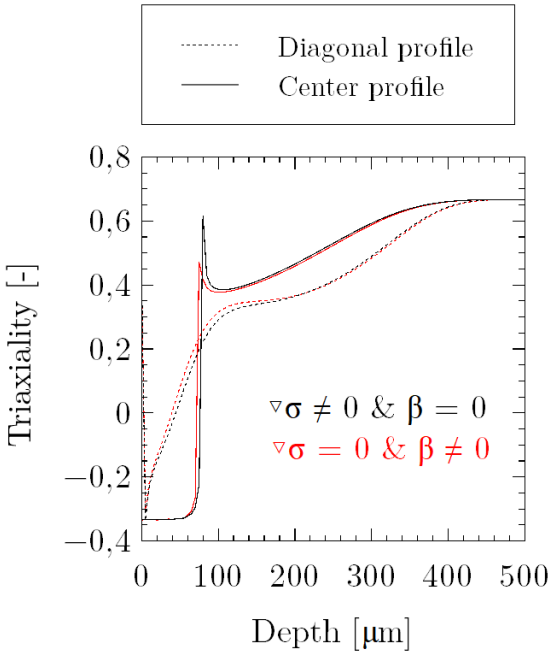

Figure 3.11 – Comparison of the diagonal and central profiles of the evolution of the triaxiality factor Tr as a function of cross-sectional depth of a square sample 1×1 mm comparing the effect of the stress gradient ($\nabla\sigma \neq 0$ and $\beta = 0$) and the effect of stresses on mobility ($\nabla\sigma = 0$ and $\beta \neq 0$) for one sample (S).

3.1.2.3 Conclusion

The flux having a vector dimension and the stresses a tensorial dimension, the interest here was to be able to visualize the evolution of the 2D fields by implementing in a simple way the partial differential equations (PDEs) on the open-source calculation code FreeFEM++. The interest of these simulations, although in 2D, was to quickly implement the calculation by using analogue thermal codes. The implementation aimed to simply write the variational formulations of the PDEs.

Although quick to implement, since this model involves a 2D problem, the computation times associated with the dimensions of the samples are long ($t > 1$ day for real sample sizes, for a fine spatial step and a short time step). Therefore, the numerical simulations presented (t = 1 s and D = 5.10^{-5} $cm^2.s^1$ are not representative of the experimental data and thermochemical treatments. These numerical simulations have, however, provided elements of understanding and visualisation of the concentration and stress fields, more specifically, on the long range diffusion kinetics. This study has allowed to:

— Confirm that the residual stresses in the ferrite are low,

— Observe that a small stress gradient does not influence the kinetics,

— Observe that the influence of stress on mobility has a negative effect when there are compressive stresses in the case of a low stress gradient,

— Observe the resulting stress field distribution,

— Understand the edge effects by observing the impact of double flux and biaxial stress on the diffusion kinetics,

— Observe the tensorial aspects of the stresses with the flux vector aspect,

— Note that the influence of the dimensions of the length of the sample is important to avoid edge effects but the dimensions used experimentally do not present any difficulty,

— Visualise the distribution of a hydrostatic stress field as a function of thickness.

Simulations (2D) would require too much computational time to conduct representative investigations with processing times of the order of 1 h to 3 h and experimental diffusion coefficients. Moreover, the non-linear aspects of the equation when the parameter β is taken into account causes problems when integrating it through divergence problems, for example. Therefore, a 2D axisymmetric model using the finite difference method has been developed.

3.1.3 Implementation C language (2D axisymmetric model)

According to the previous study, the effect of the edge on the size of the laboratory samples had no effect on the central profiles analysed. Therefore, using the finite difference method, a 2D axisymmetric model was implemented (explained in paragraph 3.1.3.2). This method approaches the solution of partial differential equations in two steps: discretisation by finite differences and convergence of the resulting numerical scheme as the distance between points decreases.

Figs. 3.12a) and b) represent, respectively, the 2D axisymmetric model (i.e. 1D-diffusion and 2D-axisymmetric-mechanical) and the boundary conditions in concentration. Where the initial conditions are :

$$\text{at} \qquad t = 0 \qquad z > 0 \qquad c\,(z, 0) = c_0 \tag{3.9}$$

and the limits are:

$$\forall t = 0, \qquad z = 0 \qquad c\,(0, t) = c_s \tag{3.10}$$

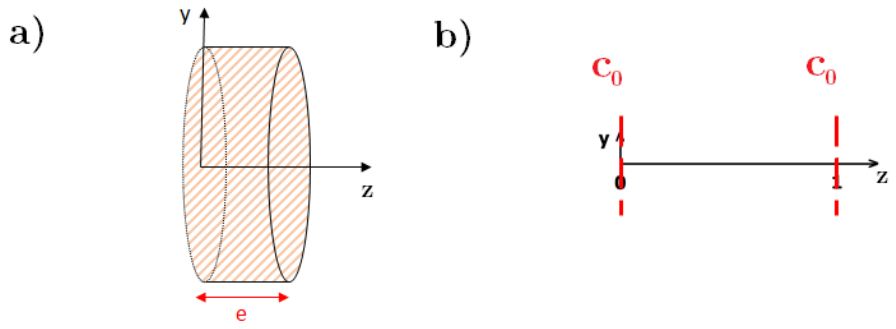

Figure 3.12 – a) 2D axisymmetric model. b) Boundary conditions in concentration.

This study is applied to the case of interstitial diffusion of nitrogen N in α-Fe. Tab. 3.2 shows the parameters used in the simulations corresponding to the mechanical characteristics of the material used, the diffusion data of the case of interstitial diffusion of nitrogen N in α-Fe and programming features.

D_I^{Φ} [$cm^2.s^{-1}$]	T [°C]	E [GPa]	ν [-]	Δz [μm]	Δt [s]	η [-]
$4{,}926.10^{-8}$	520	202 [Fallot, 2015]	0.29 [Fallot, 2015]	10	see Eq. 3.21	$2{,}4.10^{-5}$

Table 3.2 – Parameters, in the case of interstitial diffusion of nitrogen N in α-Fe, used in the simulations. Where Δz is the space step.

3.1.3.1 Equations problems

This 2D axisymmetric model leads to the use of new assumptions. Macroscopic strains and stresses can be expressed using the relations of continuum mechanics. The residual stresses determine a statistically admissible field (S.A.) and satisfy the equilibrium equations Eq. 1.15 and that Eq. 1.16 is for $z = 0$, $\sigma_{ij} n_j = 0$ with $n_j = \begin{pmatrix} 0 \\ 0 \\ 1 \end{pmatrix} : \begin{cases} \sigma_{12} = 0 \\ \sigma_{23} = 0 \\ \sigma_{33} = 0 \end{cases}$.

This leads to a plane state of cylindrical stress:

$$\begin{bmatrix} \sigma_{11} = \sigma & 0 & 0 \\ 0 & \sigma_{22} = \sigma & 0 \\ 0 & 0 & 0 \end{bmatrix} \tag{3.11}$$

$$\begin{bmatrix} 0 & 0 & 0 \\ 0 & 0 & 0 \\ 0 & 0 & \varepsilon_{33} = \varepsilon \end{bmatrix} \tag{3.12}$$

Thanks to Eqs. 3.11 and 3.12, Eqs. 1.78 and 1.81 become:

$$\begin{aligned} \sigma &= -2\mu\eta_I^\phi c_I^\phi + \lambda(\epsilon - 3\eta_I^\phi c_I^\phi) \\ 0 &= 2\mu(\epsilon - \eta_I^\phi c_I^\phi) + \lambda(\epsilon - 3\eta_I^\phi c_I^\phi) \end{aligned} \tag{3.13}$$

$$\begin{aligned} \epsilon &= \frac{2\mu+3}{2\mu+\lambda}\eta_I^\phi c_I^\phi \\ \sigma &= -\frac{2\mu(2\mu+3)}{2\mu+\lambda}\eta_I^\phi c_I^\phi \end{aligned} \tag{3.14}$$

For both cases, the steady-state concentration field and the mechanical equilibrium are determined by solving the coupled problems numerically using a C code solving the explicit method via an axisymmetric 2D model. The analytical solution of the equilibrium is directly adapted to the problem from Eqs. 1.66 and 1.82.

Considering a semi-infinite body implies that $\vec{J_I^\phi} = J_{zz}{}_I^\phi$ and $\gamma_I\sigma_{ij} = 0$ for any value of γ_I (only the flux along z is not equal to zero). It follows, from Eq. 1.60, that the flux is:

$$\begin{aligned} \left(J_I^\phi\right)_{x_3} &= -\frac{c_I^\phi}{\Phi RT}\left(D_I^\phi + \beta\sigma_{kk}\right)\left(\frac{RT\Phi}{c_I^\phi}\frac{\partial c_I^\phi}{\partial x_3} - V_a\eta_I^\phi\frac{\partial\sigma_{kk}}{\partial x_3}\right) \\ &= -\left(D_I^\phi + \beta\sigma_{kk}\right)\frac{\partial c_I^\phi}{\partial x_3} + \frac{V_a\eta_I^\phi}{\Phi RT}\left(D_I^\phi + \beta\sigma_{kk}\right)c_I^\phi\frac{\partial\sigma_{kk}}{\partial x_3} \end{aligned} \tag{3.15}$$

Eq. 3.15 shows that the sum $(D\delta_{ij} + \beta\sigma_{kk}\delta_{ij})$ will slow down the diffusion when $\beta\sigma_{kk}\delta_{ij}$ is negative, where D is independent of the concentration.

During diffusion, the mass conservation must be verified:

$$\frac{\partial c_I^\phi}{\partial t} + \frac{\partial\left(J_I^\phi\right)_{x_3}}{\partial x_3} = 0 \tag{3.16}$$

with

$$\begin{aligned} \frac{\partial\left(J_I^\phi\right)_{x_3}}{\partial x_3} &= \beta\frac{\partial\sigma_{kk}}{\partial x_3}\left(\frac{V_a\eta_I^\phi}{\Phi RT}c_I^\phi\frac{\partial\sigma_{kk}}{\partial x_3} - \frac{\partial c_I^\phi}{\partial x_3}\right) \\ &+ \left(D_I^\phi + \beta\sigma_{kk}\right)\left(\frac{V_a\eta_I^\phi}{\Phi RT}\left(\frac{\partial c_I^\phi}{\partial x_3}\frac{\partial\sigma_{kk}}{\partial x_3} + c_I^\phi\frac{\partial^2\sigma_{kk}}{\partial x_3^2}\right) - \frac{\partial^2 c_I^\phi}{\partial x_3^2}\right) \end{aligned} \tag{3.17}$$

Finally, equation 3.16 can be simplify using $\sigma_{kk} = 2\sigma$ and considering a dilute solution $\Phi = 1$:

$$\begin{aligned} \frac{\partial c_I^\phi}{\partial t} &= 2\beta\frac{\partial\sigma}{\partial x_3}\left(\frac{\partial c_I^\phi}{\partial x_3} - 2\frac{V_a\eta_I^\phi}{RT}c_I^\phi\frac{\partial\sigma}{\partial x_3}\right) \\ &+ \left(D_I^\phi + 2\beta\sigma\right)\left(\frac{\partial^2 c_I^\phi}{\partial z^2} - 2\frac{V_a\eta_I^\phi}{RT}\left(\frac{\partial c_I^\phi}{\partial x_3}\frac{\partial\sigma}{\partial x_3} + c_I^\phi\frac{\partial^2\sigma}{\partial x_3^2}\right)\right) \end{aligned} \tag{3.18}$$

Eq. 3.18 shows that stress affects mobility $\left(D_I^{\phi} + 2\beta\sigma\right)$ and that there is a gradient effect and finally that there is also a mobility/stress coupling term $2\beta\frac{\partial\sigma}{\partial x_3}$.

3.1.3.2 Finite difference equations

Let write one quantity q such as c_I^{ϕ}, σ or ϵ, at t time and at $x_3 = z$ depth as q_z^t. q_{z+1}^{t+1} is then the quantity at time $t+1$ and depth $z+1$.

The numerical solution of equation 3.18 is obtained using a finite difference schema and the explicit scheme (easier convergence for non-linear problems) so that:

$$\begin{aligned}\frac{c_z^t - c_z^{t-1}}{\Delta t} &= 2\beta\frac{\sigma_z^t - \sigma_{z-1}^t}{\Delta z}\left(\frac{c_z^t - c_{z-1}^t}{\Delta z} - 2\frac{V_a\eta_I^{\phi}}{RT}c_z^t\frac{\sigma_z^t - \sigma_{z-1}^t}{\Delta z}\right) \\ + \left(D_I^{\phi} + 2\beta\sigma\right)&\left(\frac{c_{z+1}^t - 2c_z^t + c_{z-1}^t}{\Delta z^2} - 2\frac{V_a\eta_I^{\phi}}{RT}\frac{(c_z^t - c_{z-1}^t)(\sigma_z^t - \sigma_{z-1}^t) + c_z^t(\sigma_{z+1}^t - 2\sigma_z^t + \sigma_{z-1}^t)}{\Delta z^2}\right)\end{aligned} \tag{3.19}$$

where Δz and Δt are respectively spatial and time step.

Equation 3.14 can be written as:

$$\begin{aligned}\epsilon_z^t &= \frac{2\mu+3}{2\mu+\lambda}\eta_I^{\phi}c_z^t \\ \sigma_z^t &= -\frac{2\mu(2\mu+3)}{2\mu+\lambda}\eta_I^{\phi}c_z^t\end{aligned} \tag{3.20}$$

A convergent and stable solution, without the stress effect, is found if the following conditions are verified [Crank, 1979]:

$$\Delta t = \alpha\frac{\Delta z^2}{D_I^{\Phi}} \tag{3.21}$$

Where $\alpha = 0.5$ is the convergence coefficient, (normally $\alpha \leq 0.5$ for the stability).

Fig. 3.13 is the schematic representation of the code used in this work. The coupling is processed using experimentally known input data such as mechanical characteristics (Young's modulus E, Poisson's coefficient ν), concentration data ($c_0 = 0.001$ to 0.0025)), time data (t), data related to the binary system under study (V, V_a, η) and sample thickness. Then, a time loop is performed in which the calculations are made in explicit Euler (see Eq. 3.19). First the diffusion calculation is performed, then the mechanical calculation follows. Indeed, this code is a weak coupling, i.e. the calculations are performed one after the other. At the end of the calculation, several data can be exploited: the concentration and residual stress profiles as a function of depth, as is the case experimentally; but also various data of interest for the understanding of the different terms of the calculation: the first and second derivatives of the concentration and stress profile, the evolution of the Young's modulus E, etc.

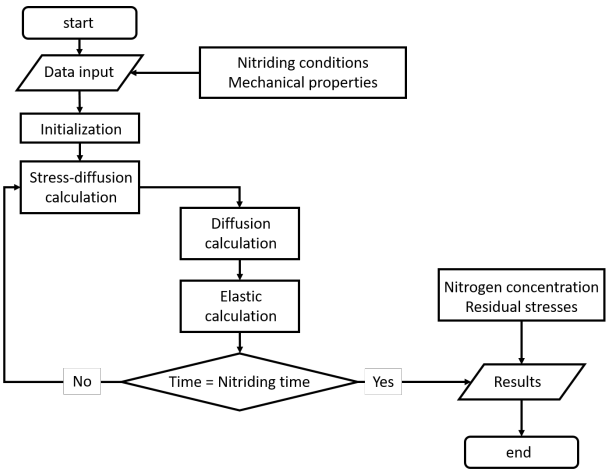

Figure 3.13 – Flowchart of the stress/diffusion coupling used in this work.

3.1.3.3 Time evolution

The 2D axisymmetric model was validated by preliminary simulations. Fig. 3.14a) illustrates the effect of treatment time from 30 to 120 min on the evolution of the concentration as a function of depth for a 10 mm thick sample at 520 °C and a surface concentration of $c_0 = 0.0025$. This concentration value corresponds to the solubility limit, equivalent to the temperature of the study, of nitrogen in α-iron. The Fick equation (Eq. 1.4) (without coupling with stresses) is studied. A comparative analysis of the results under comparable application parameters was used to compare and validate the Fick curves.

The first and second derivatives of the concentration for the three treatment times are shown in 3.14b). These graphs illustrate that the surface kinetics are greater at the beginning of the treatment (i.e. at short times).

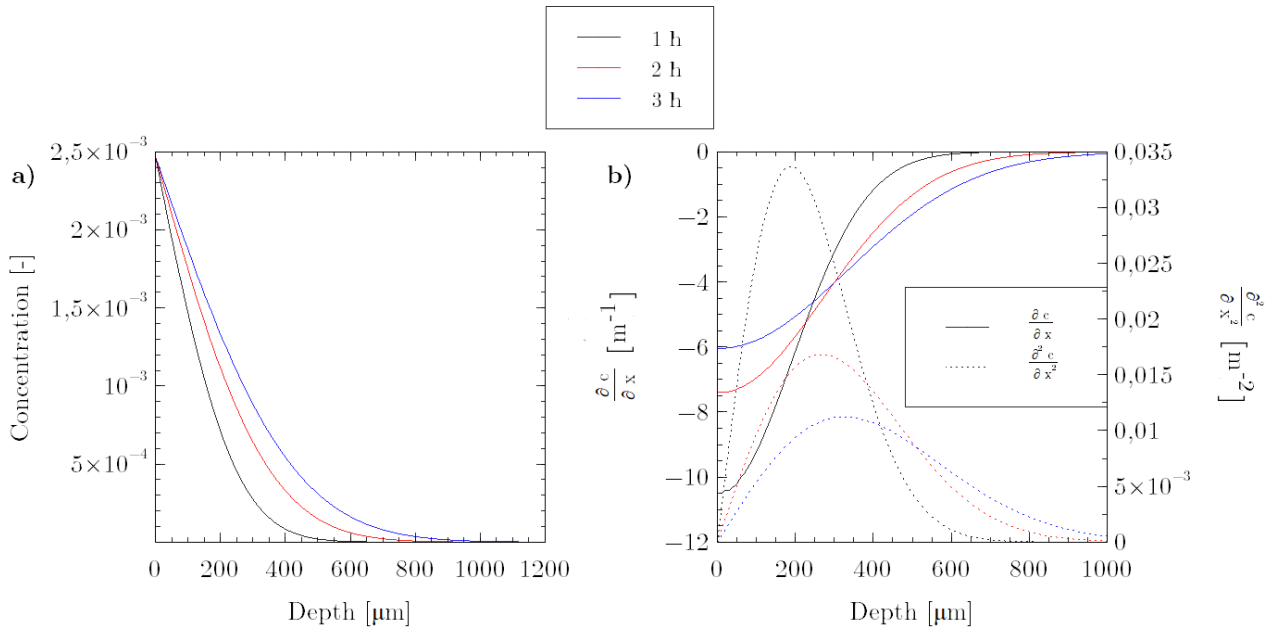

Figure 3.14 – a) Evolution of concentration as a function of depth; b) Evolution of $\frac{\partial c}{\partial x_3}$ and $\frac{\partial^2 c}{\partial {x_3}^2}$ as a function of depth; for a 10 mm thick sample, for 3 treatment times (1h, 2h and 3h).

3.1.3.4 Residual stress study

The effect of chemical stresses on the diffusion of the mass pipe has been extensively studied in the literature, however, the objective is to have information on the predominance between the effect of stresses on the mobility part (see Eq. 3.15) with the $(D\delta_{ij} + \beta.\sigma_{kk}.\delta_{ij})$ and the stress gradient [Larche and Cahn, 1978a, Chen-Min Li, 1978]. Throughout this study, the surface concentration is fixed, the simulations will be interesting to visualize the influence on the depth of the diffusion layer. This first study focuses on the diffusion kinetics by taking into account only the residual stresses induced by the diffusion (see Eq. 3.14) by playing on several parameters: the influence of the coefficient β, the treatment time and the thickness of the sample.

3.1.3.4.1 Influence of β parameter The β parameter established by Voorhees and Larché makes it possible to observe the influence of stress on mobility by varying the amplitude of the stress. The extent of the stresses would imply that they play an important role in the diffusion kinetics from an empirical point of view. Therefore, the first study focuses on the effect of the parameter β on the diffusion kinetics of a semi-infinite plate (10 mm thick) treated for 1 hour at 520 °C with a constant surface concentration. In this study, 3 values of β cm^2.s^{-1}.MPa^{-1} are analyzed: 0, 10^{-11} and 10^{-10} cm^2.s^{-1}.MPa^{-1} all compared to the Fick equation where the diffusion coefficient is equal to $D_I^{\Phi} = 4.9.10^{-8}$ cm^2.s^{-1}. These chosen values of β were defined after several numerical simulations in order to compare only some interesting values.

Fig. 3.15 takes only the effect of a residual stress gradient ($\nabla\sigma \neq 0$) using Eq. 1.63 in the case of $\beta = 0$. It is observe a positive influence thanks to the positive stress gradient.

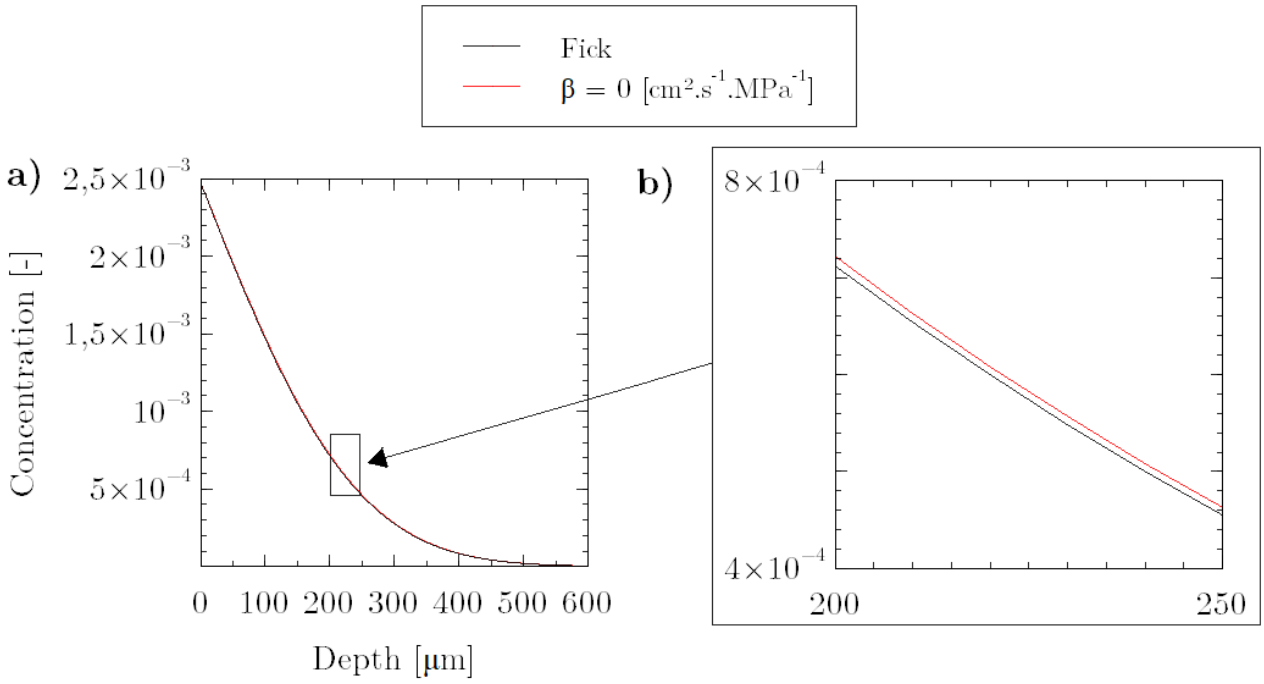

Figure 3.15 – Evolution of concentration profiles as a function of depth for a 10 mm thick sample at 520 °C for 1 h. Comparison of the Fick profile and $\beta = 0$.

Fig. 3.16a) shows that as the value of β increases, the diffusion slows down. More precisely, it is interesting to note that from a certain value of beta the diffusion is slowed down compared to the analytical Fick profile. The curve of $\beta = 10^{-11}\text{cm}^2.\text{s}^{-1}.\text{MPa}^{-1}$ shows a diffusion that remains accelerated compared to the Fick curve but is slowed down compared to the curve taking into account only the stress gradient. The curve of $\beta = 10^{-10}\text{cm}^2.\text{s}^{-1}.\text{MPa}^{-1}$, the diffusion is considerably slowed down compared to the Fick curve. Moreover, it is observed that the stress gradient in MPa/mm increases when β increases, as shown in Tab. 3.3). The positive evolution of the stress gradient leads to a significant decrease in the diffusion kinetics. In general, the study shows the competition between the mobility gradient and the mechanical driving force (stress gradient alone without mobility effect). Fig. 3.16b) corresponds to the zoom shown by a rectangle in Fig. 3.16. It illustrates that when β reaches a particular value, mobility takes over the influence of the stress gradient. Tab. 3.3 also gathers the orders of magnitude F between the Fick diffusion coefficient D_I^{Φ} and the factor $(\sigma_{kk}.\beta)$ where $\left(\sigma_{kk}.\beta = F \times D_I^{\Phi}\right)$. The sign of the residual stresses is at the origin of this negative influence on the kinetics.

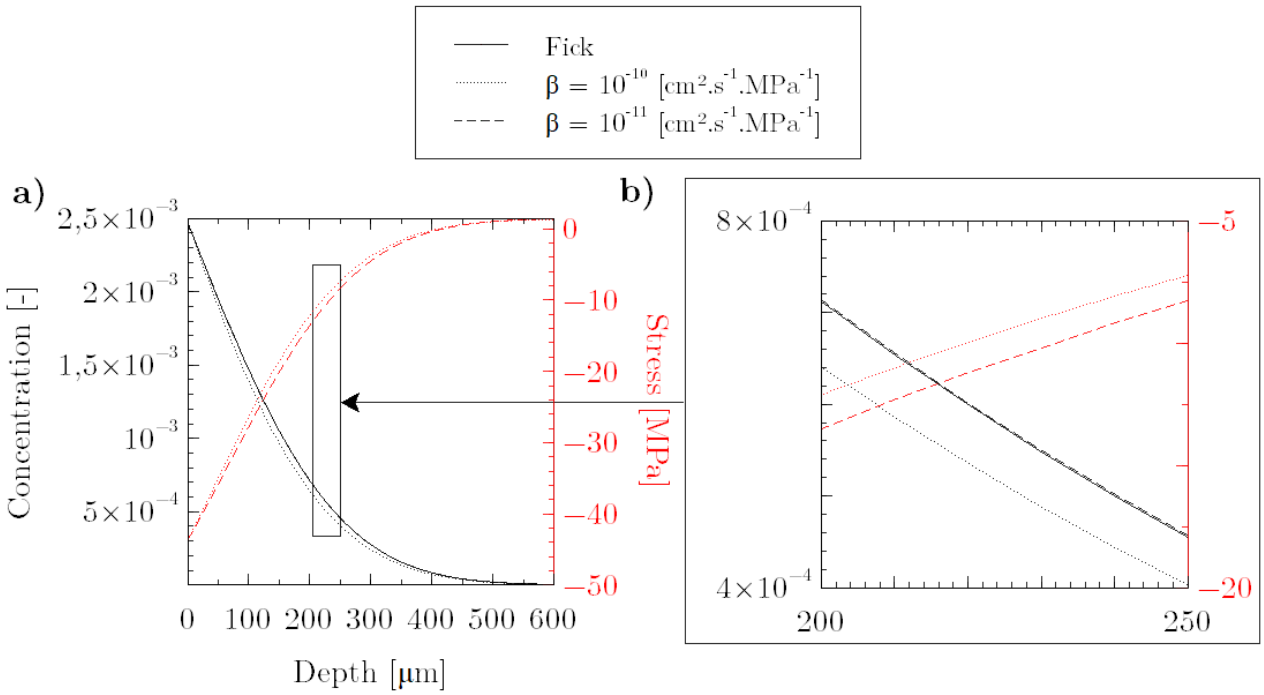

Figure 3.16 – a) Evolution of concentration and residuals stresses profiles as a function of depth for a 10 mm thick sample at 520 °C for 1 h. Comparison of the Fick profile and 2 β values of the coefficient: 10^{-11} and 10^{-10} cm^2.s^{-1}.MPa^{-1}. b) Zoom of Fig.a).

β	$\frac{\partial \sigma}{\partial x_3}$ [MPa/mm]	F [-]
0	139,3	0
10^{-11}	139,5	0,01
10^{-10}	141,2	0,1

Table 3.3 – Evolution of the residual stress gradient and the evolution of the F-factor between the Fick diffusion coefficient D_I^{Φ} and the stress mobility term ($\sigma_{kk}.\beta$) obtained for 3 values of β.

Fig. 3.17b) corroborates the results by observing that, for this case study, the diffusion kinetics are mainly influenced at the beginning of the treatment and are then reflected in the rest of the diffusion layer. The coupling thus presents different effects depending on the depth of the layer.

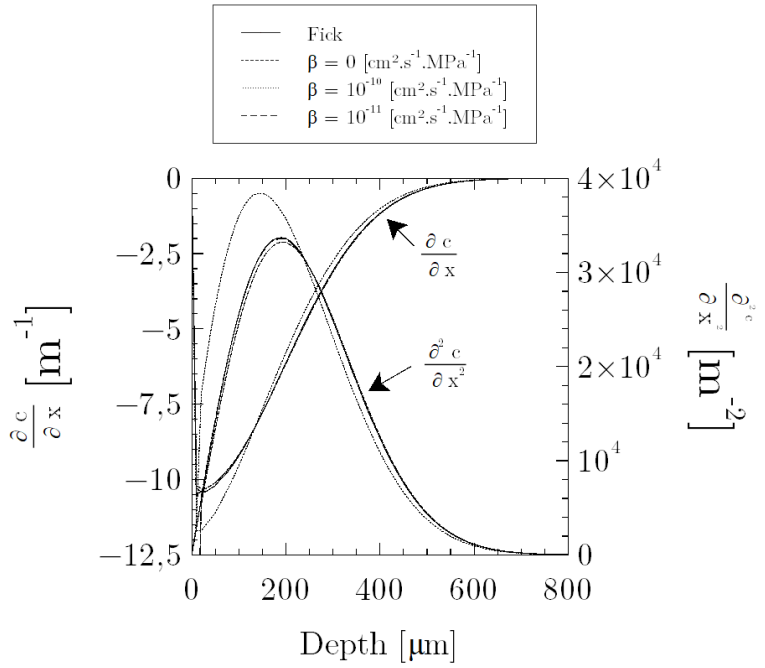

Figure 3.17 – Evolution of $\frac{\partial c}{\partial x_3}$ and $\frac{\partial^2 c}{\partial {x_3}^2}$ as a function of depth for the 4 simulations in Fig. 3.16.

Fig. 3.18 shows the influence of stresses on the mobility ($\beta > 0$ and $\nabla\sigma = 0$). This observation shows that for all values of β the diffusion kinetics are slowed down.

Fig. 3.19 compares the concentration and residual stress profiles as a function of depth for the case ($\beta > 0$ et $\nabla\sigma = 0$) and the case ($\beta > 0$ et $\nabla\sigma \neq 0$) for $\beta = 10^{-10} = \text{cm}^2.\text{s}^{-1}.\text{MPa}^{-1}$. This comparison reveals that the coupling of the stress gradient with mobility results in a slowdown 3 times greater than the profile that only takes mobility into account.

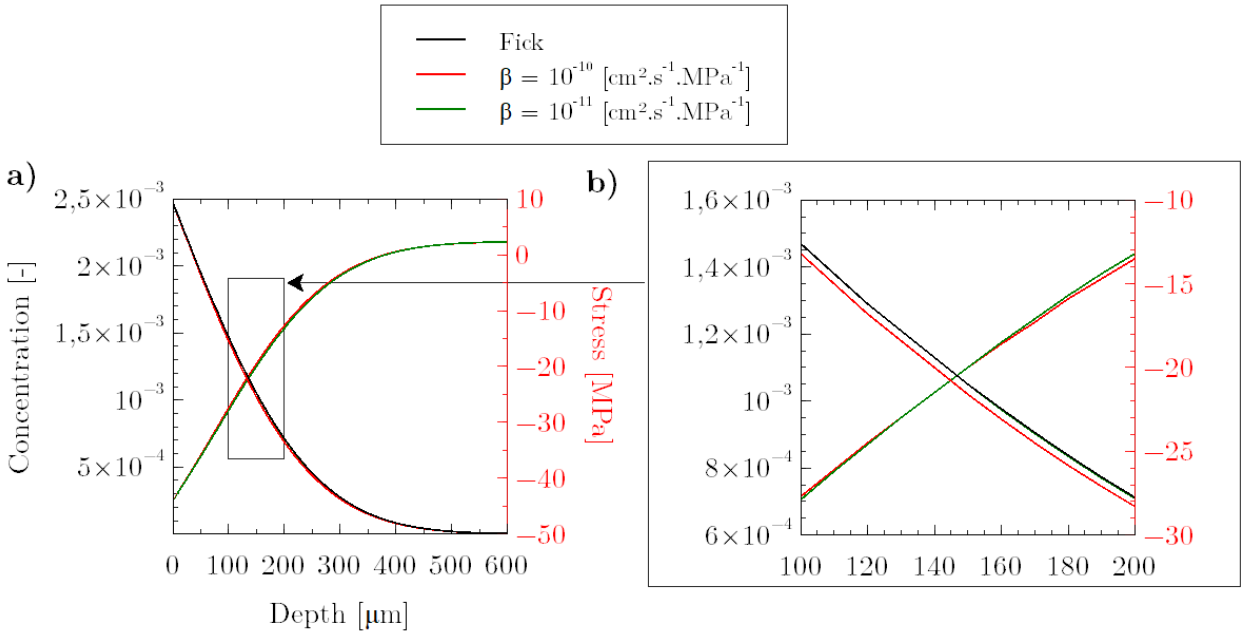

Figure 3.18 – a) Evolution of concentration and residual stress profiles as a function of depth for the case of the effect of stress on mobility ($\beta > 0$ and $\nabla\sigma = 0$) for a 10 mm thick sample at 520 °C for 1 h. Comparison of the Fick profile and 2 values of the coefficient : 10^{-11} and 10^{-10} $cm^2.s^{-1}.MPa^{-1}$. b) Zoom of Fig.a).

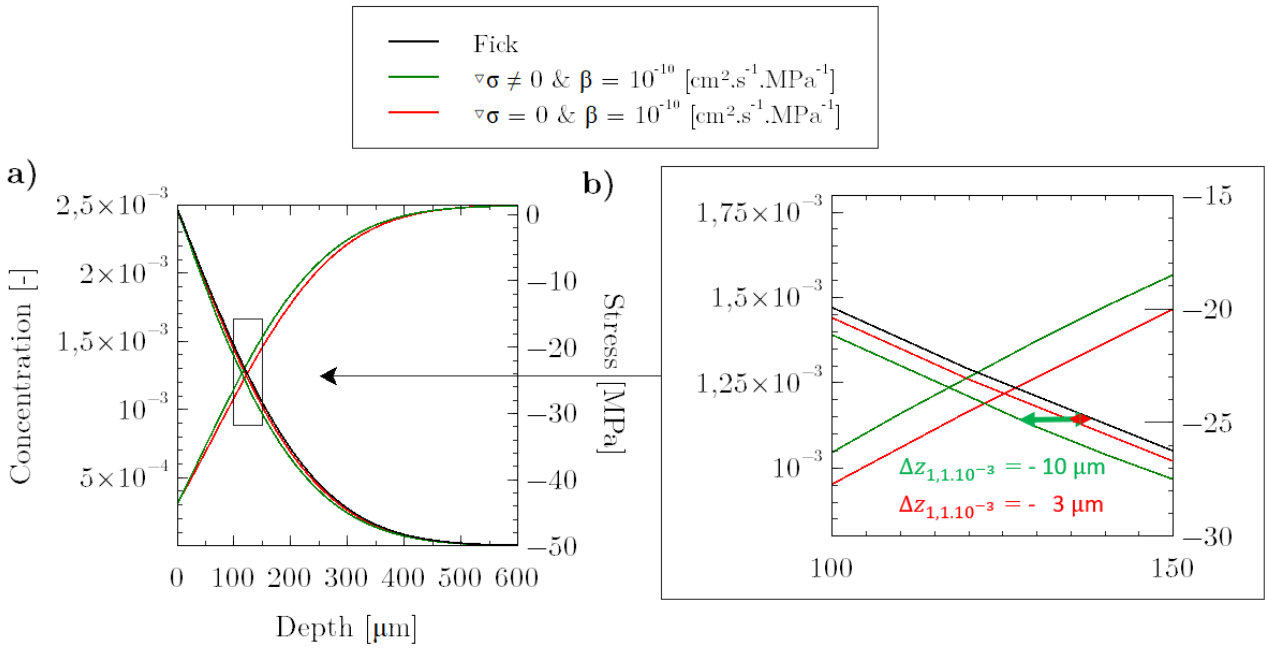

Figure 3.19 – a) Comparison of the concentration profiles (relative to the Fick profile) and residual stress as a function of depth for the case ($\beta > 0$ and $\nabla\sigma = 0$) and the case ($\beta > 0$ and $\nabla\sigma \neq 0$ (Fig. 3.18)) for a 10 mm thick sample at 520 °C for 1 h for $\beta = 10^{-10}$ $cm^2.s^{-1}.MPa^{-1}$. b) Zoom of Fig.a).

This study assumes an indefinitely dilute solution (i.e. a concentration below the solubility limit of the

inserted atom in the host matrix). As shown in Fig. 3.16, this leads to lower residual stresses due to low stress-free strain values associated with extremely modest volume changes. Despite these low values, significant β value in the evolution of the diffusion kinetics can be determined. The next simulations presented in this section "residual stresses" will make comparisons only between two β values: 0 and $\beta = 10^{-10}\text{cm}^2.\text{s}^{-1}.\text{MPa}^{-1}$.

3.1.3.4.2 Time evolution The study focused on the role of time on kinetics, this time taking into account the effect of stress on mobility. The numerical simulations are performed on a semi-infinite plate (10 mm thick) which is subjected to three treatment times (1 h, 2 h, and 3 h) at 520 °C with a constant surface concentration. As the treatment time increases, the concentration increases resulting in more stress-free strain and therefore higher residual stresses. Fig. 3.20 illustrates the beneficial impact of a positive stress gradient and the negative influence when the stresses are included in the mobility. The residual stresses are known to change at each time point (see Fig. 1.15). Tab. 3.4 groups, for the three treatment times, the residual stress gradients, as well as the surface stress values as a function of time and the two values of β. The table shows that the surface stress and the residual stress gradient increase as β increases and decrease as a function of time. Although the increase in surface stress is only of the order of 0.2%, this evolution allows us to define a trend that would be more important for higher stresses. According to the literature review in section 1.1.5, the stress curves show negative stresses with a stronger or weaker gradient over time. Mechanical re-equilibrium shows that as the treatment time increases, the core of the sample is under stress in the centre due to deeper compressive residual stresses.

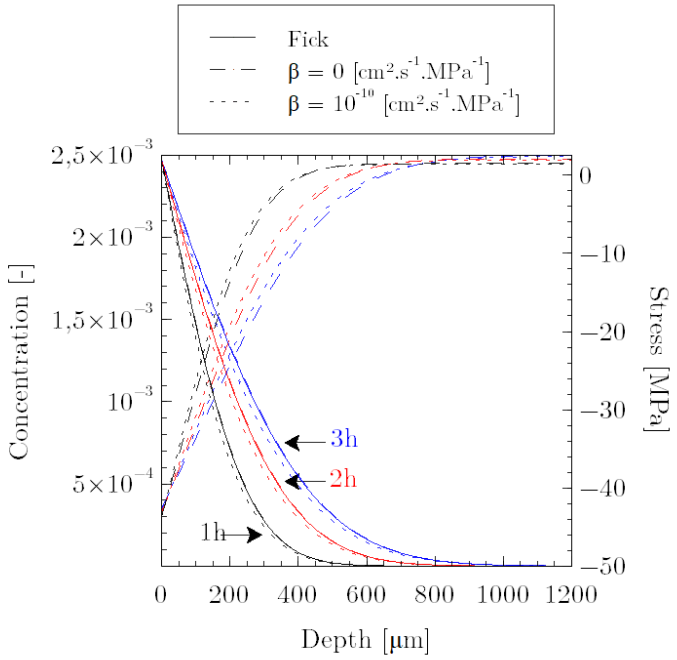

Figure 3.20 – Evolution of concentration and of residual stresses as a function of depth, for a 1 mm sample, for 3 treatment times (1 h, 2 h and 3 h). Comparaison between the Fick's law and two β values: 0 and 10^{-10} $\text{cm}^2.\text{s}^{-1}.\text{MPa}^{-1}$

	β	$\frac{\partial\sigma}{\partial x_3}$ [MPa/mm]	Surface stress [MPa]
1h	0	139,3	-43,6
	10^{-10}	141,2	-43,7
2h	0	108,6	-43,0
	10^{-10}	112,4	-43,1
3h	0	90,7	-42,5
	10^{-10}	96,0	-42,6

Table 3.4 – Stress gradient and surface stress for the β studies shown in Fig. 3.20.

Experimentally, it is known that as the treatment time increases, the stresses in absolute values are initially intense and gradually decrease in intensity and spread out in depth, as shown schematically in Fig. 3.21. Indeed, the surface content is not constant and evolves over time until it reaches a maximum which corresponds to the solubility limit of the system studied. However, it is difficult to understand what happens in the first few seconds of the diffusion. Flow boundary conditions, i.e. Neumann conditions, could be used to observe these phenomena. However, in this work, the surface area is assumed to be constant (Dirichlet boundary conditions) and its value does not exceed the solubility limit (no precipitation).

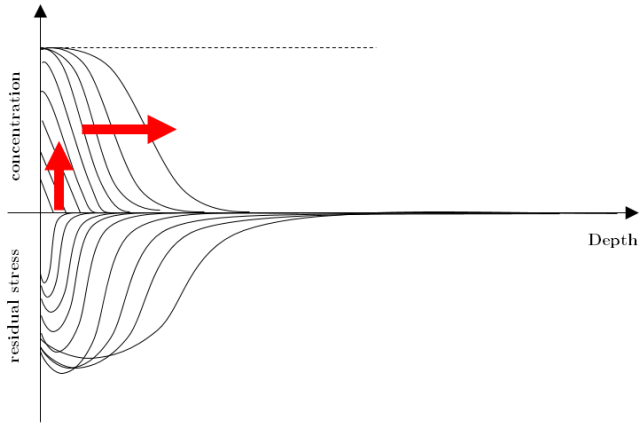

Figure 3.21 – Schematisation of experimental evolution of the concentration and residual stresses over time.

Fig. 3.22 helps explaining the effect of stress on mobility. It can be seen that the first and second derivatives of the stresses, with respect to space and as a function of depth, show a shift towards the surface when $\beta = 10^{-10}$ $cm^2.s^{-1}.MPa^{-1}$. It can be seen that the evolution of the residual stress profiles as a function of time and of β is mainly affected at the beginning of the treatment due to a higher surface stress and a stronger stress gradient as observed in Tab. 3.4. Therefore, the stress gradient is significantly increased at the beginning of the diffusion layer (the first 100-200 μm) and then weakens until $\beta = 0$.

These stress changes are similarly reflected in the evolution of the first and second derivatives of the concentration. In the case $\beta = 10^{-10}$ $cm^2.s^{-1}.MPa^{-1}$, the kinetics are accelerated in the first 100-200 μm of depth (as a function of treatment time). This indicates that the main effect on these first microns comes from the stress gradient and not from mobility. Fig. 3.23 shows that when $\beta = 10^{-10}$ $cm^2.s^{-1}.MPa^{-1}$ the concentration gradient, in comparison with the Fick profile, is higher at the surface and smaller thereafter. This observation is reversed for $\beta = 0$. This would seem to show that the main effect after the first tens of microns comes from

mobility and not from the stress gradient.

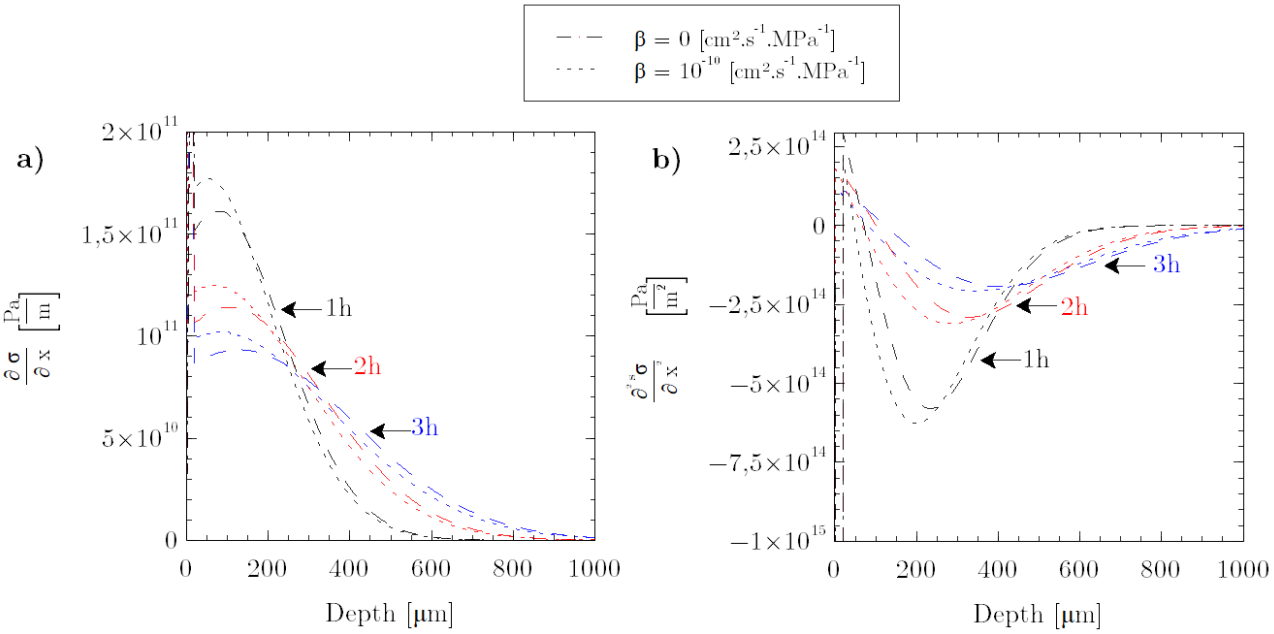

Figure 3.22 – a) Evolution of $\frac{\partial \sigma}{\partial x_3}$; b) $\frac{\partial^2 \sigma}{\partial {x_3}^2}$; as a function of depth for the evolution time simulations presented in Fig. 3.20.

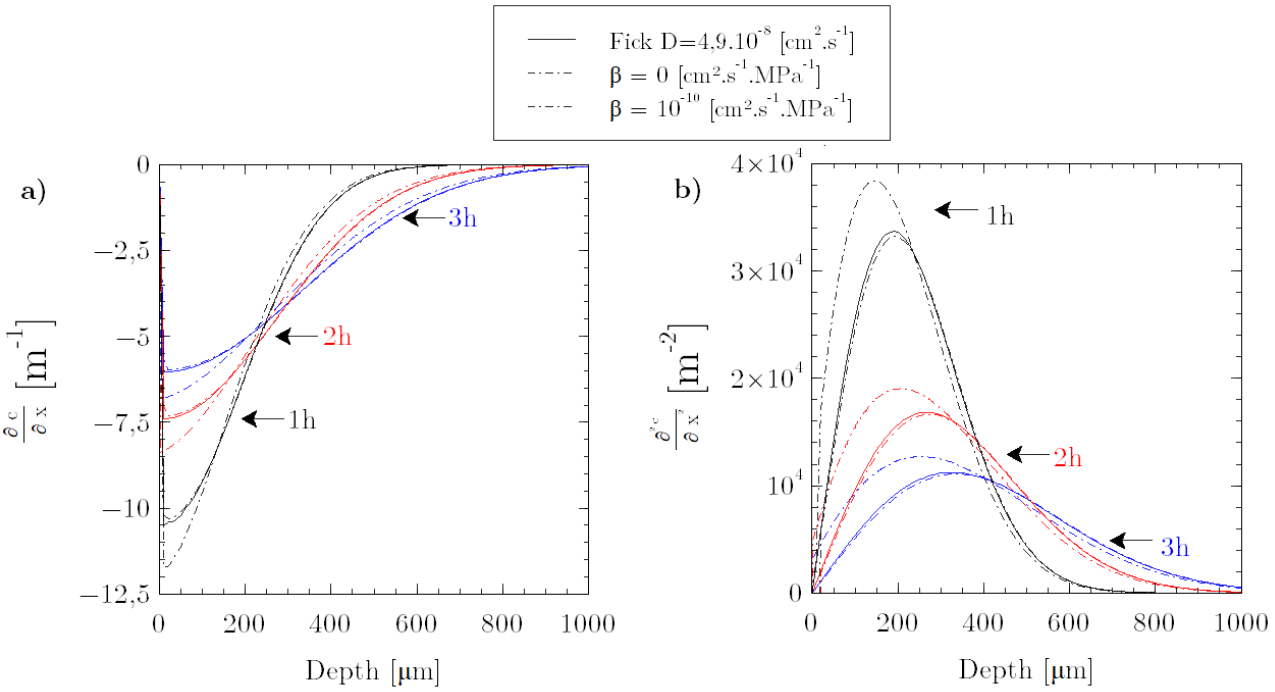

Figure 3.23 – a) Evolution of $\frac{\partial c}{\partial x_3}$; b) $\frac{\partial^2 c}{\partial {x_3}^2}$; as a function of depth for the evolution time simulations presented in Fig. 3.20.

This study confirms that the shorter the time, the higher the residual stress gradient. Furthermore, the observations lead to the conclusion that the effect of the gradient is mainly in the first few microns of depth and the effect of the mobility is mainly in the rest of the diffusion layer.

3.1.3.4.3 Thickness evolution The structural effect is studied in this section. Numerical simulations were carried out for two sample thicknesses (5 mm and 10 mm) after 1 hour of treatment at 520 °C with a constant surface concentration. A first study focuses on the effect of the residual stress gradient ($\nabla\sigma \neq 0$ and $\beta = 0$) on the diffusion kinetics. Two multiplication factors were compared for this effect: CC = 1 and CC = 10. Indeed, the residual stress profiles, observed previously, had low amplitudes resulting from the conditions of simulations which are to be in the case of an infinitely diluted solution (no precipitation phenomenon, i.e. only a nitrogen diffusion phenomenon in the ferric network). However, in nitrided steels, for example, the residual compressive stresses are of the order of hundreds of MPa. This multiplication factor is directly involved in the equations for the components of the elastic strain, in the form of $\varepsilon^{e}_{ij} = \varepsilon^{e}_{ij} * CC$, for each calculation time.

Figure 3.24 shows that the evolution of the concentration profiles per group of CC multiplication factors seems similar. However, the residual stress profiles show a different sharpness. As the thickness of the sample decreases, the surface stress will be lower and the residual stress gradient will be higher as listed in Tab. 3.5. These observations are consistent with the observations reported in the literature (see section 1.1.5).

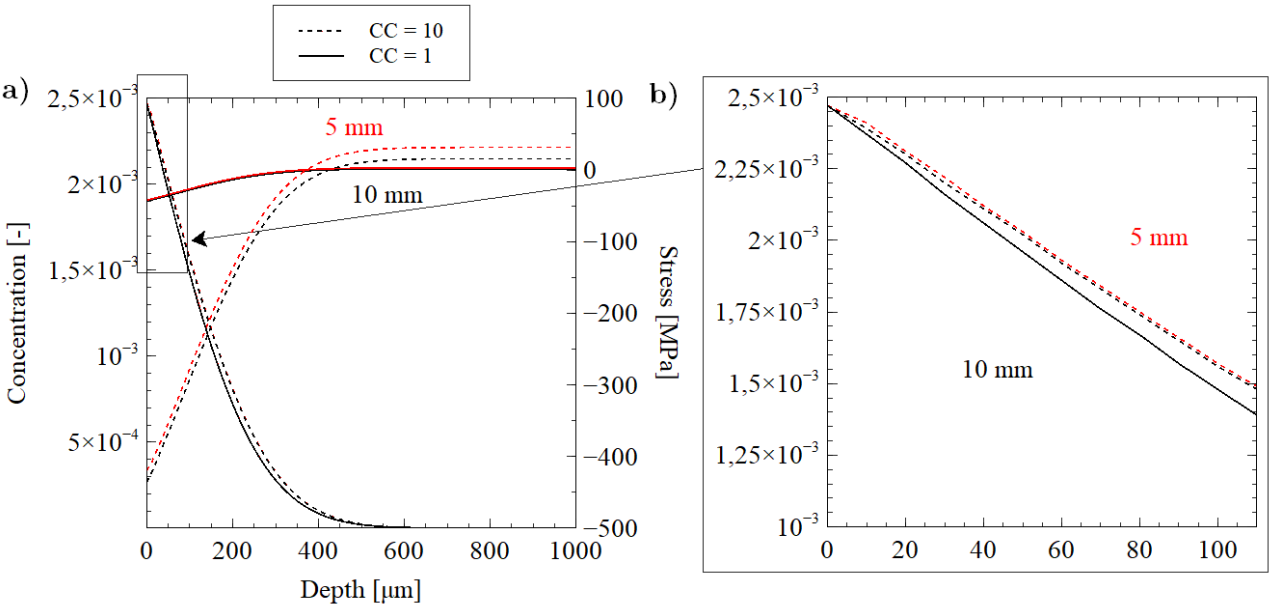

Figure 3.24 – a) Evolution of concentration and residual stress profiles for two thickness sample (5 mm and 10 mm) as a function of two multiplier factors CC (1 and 10). b) zoom of the concentration fields in Fig.a).

	CC = 1		CC = 10	
	5 mm	10 mm	5 mm	10 mm
$\frac{\partial \sigma}{\partial x_3}$ [MPa/mm]	135,08	135,01	1329,6	1324,5
Stress value in surface [MPa]	-42	-44	-419	-435

Table 3.5 – Stress gradient and surface stress for two thickness sample (5 mm and 10 mm) as a function of two multiplier factors CC (1 and 10) shown in Fig. 3.24.

Fig. 3.25 kinetics shows in more detail the evolution of the concentration and stress gradients. Indeed, as seen in the Fig. 3.25, the greater the stress, the greater the stress gradient. In the case of CC = 10, these data reveal a difference (even though it is minor). The graphs show $|\left(\frac{\partial c}{\partial x_3}\right)_{5\text{ mm}}| > |\left(\frac{\partial c}{\partial x_3}\right)_{10\text{ mm}}|$ in the first 180 μm. This is explained by the evolution of the stress gradient, which indicates that in the first 180 μm, $\left(\frac{\partial \sigma}{\partial x_3}\right)_{5\text{ mm}} > \left(\frac{\partial \sigma}{\partial x_3}\right)_{10\text{ mm}}$.

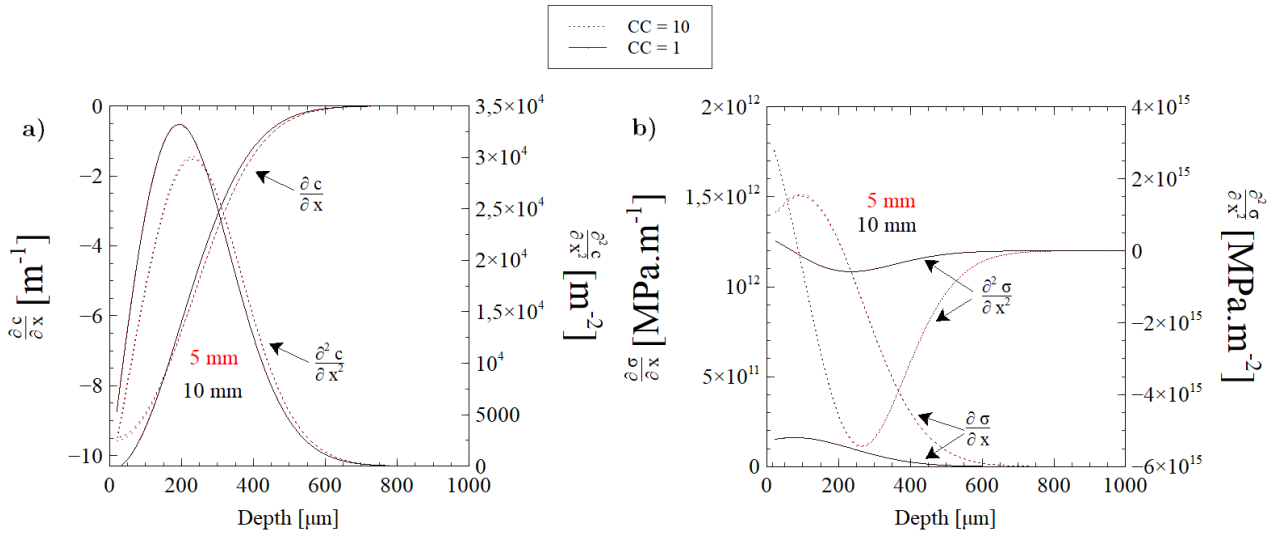

Figure 3.25 – a) Evolution of $\frac{\partial c}{\partial x_3}$ and $\frac{\partial^2 c}{\partial {x_3}^2}$; b) Evolution of $\frac{\partial \sigma}{\partial x_3}$ and $\frac{\partial^2 \sigma}{\partial {x_3}^2}$; for two thickness sample (5 mm and 10 mm) as a function of two multiplier factors CC (1 and 10).

A second study investigates the influence of stress on mobility as a function of thickness (1 mm, 5 mm and 10 mm), while competing with the residual stress gradient. The study focused on a stress multiplier factor CC = 1 and two values of β: 0 and 10^{-10} cm^2.s^{-1}.MPa^{-1}.

The concentration curves have no discernible change for $\beta = 0$, as shown in Fig. 3.26. However, in the case of $\beta = 10^{-10}$ cm^2.s^{-1}.MPa^{-1}, a small positive difference can be noticed as the thickness decreases, despite the fact that the influence on the mobility has a negative effect on the diffusion kinetics. The diffusion is indeed less slowed down for the thinner material (1 mm). This is due to the conflict between the stress value $|\sigma|$ and the stress gradient $\frac{\partial \sigma}{\partial x_3}$. The values of the average stress gradient and the surface stress for each of the six curves are presented in Tab. 3.6. It can be observed that $\left(D_I^\Phi + \beta\sigma_{kk}\right)_{1\text{ mm}} > \left(D_I^\Phi + \beta\sigma_{kk}\right)_{5\text{ mm}} > \left(D_I^\Phi + \beta\sigma_{kk}\right)_{10\text{ mm}}$ and that $\left(\frac{\partial \sigma}{\partial x_3}\right)_{1\text{ mm}} > \left(\frac{\partial \sigma}{\partial x_3}\right)_{5\text{ mm}} > \left(\frac{\partial \sigma}{\partial x_3}\right)_{10\text{ mm}}$.

A particular case here concerns the 1 mm thick sample, which will not be studied further in this paragraph. Indeed, the graph shows the phenomenon of double flow, demonstrating that from a certain depth value, the concentration changes and no longer follows the evolution of the concentration fields of the other thicknesses. This shows the interest of studying samples with similar evolutions in order to deduce which stress effect is predominant.

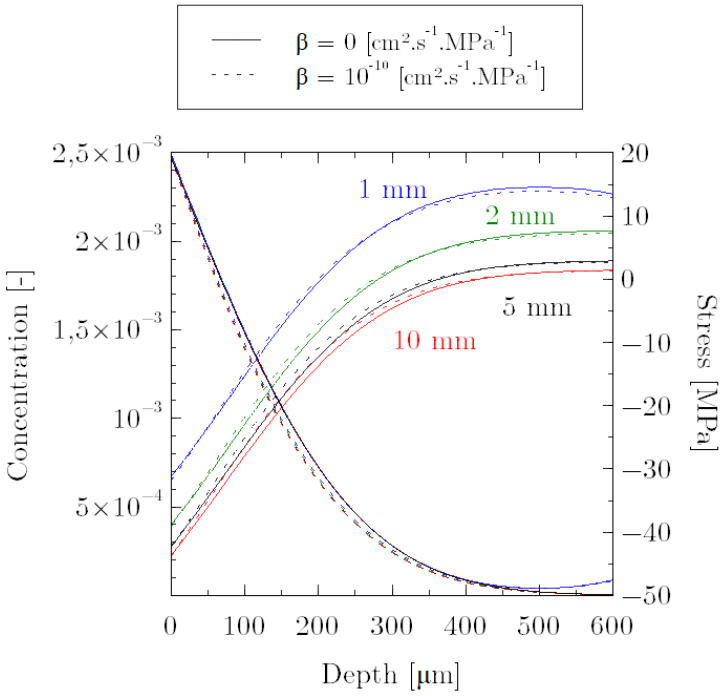

Figure 3.26 – Evolution of concentration and residual stress profiles for four sample thicknesses (1 mm, 2 mm, 5 mm and 10 mm) as a function of two β values (0 and 10^{-10} cm^2.s^{-1}.MPa^{-1}).

	$\beta = 0$			$\beta = 10^{-10}$		
	1 mm	5 mm	10 mm	1 mm	5 mm	10 mm
$\frac{\partial \sigma}{\partial x_3}$ [MPa/mm]	157,6	148,7	139,3	163,7	153,8	141,2
Surface stress [MPa]	-30,8	-42,1	-43,6	-31,5	-42,3	-43,7

Table 3.6 – Stress gradient and surface stress for four sample thicknesses (1 mm, 2 mm, 5 mm and 10 mm) as a function of two β values (0 and 10^{-10} cm^2.s^{-1}.MPa^{-1}).

To better visualise the influence of stresses, the first and second derivatives of the concentration and stress fields are shown only for the 2 mm and 10 mm samples. Initially, by isolating the groups by β value, it is easy to see, as in the previous results (Fig. 3.26), that the evolutions are identical. Indeed, when the thickness of the sample decreases, it can be seen that $\left(\frac{\partial \sigma}{\partial x_3}\right)_{\text{surface}}$ increases, $\left(\frac{\partial \sigma}{\partial x_3}\right)_{\text{in depth}}$ decreases, and $|\frac{\partial c}{\partial x_3}|$ decreases. All these evolutions lead to a decrease of $\left(\frac{\partial c}{\partial x_3}\right)_{\text{surface}}$ and $\left(\frac{\partial c}{\partial x_3}\right)_{\text{in depth}}$. The effect of mobility $\beta = 10^{-10}$ cm^2.s^{-1}.MPa^{-1} compared to the study $\beta = 0$ shows that $\left(\frac{\partial \sigma}{\partial x_3}\right)_{\text{surface}}$ increases and $\left(\frac{\partial \sigma}{\partial x_3}\right)_{\text{in depth}}$ decreases,

which lead to a decrease of $\left(\frac{\partial c}{\partial x_3}\right)_{\text{surface}}$ and an increase of $\left(\frac{\partial c}{\partial x_3}\right)_{\text{in depth}}$. Furthermore, that the local maximum of the stress gradient shifts towards the surface, as observed in Fig. 3.26 where the residual stresses shift towards the surface.

This graph illustrates precisely the effect of mobility, which amplifies a slowdown at the beginning of the concentration profile and an acceleration at the end.

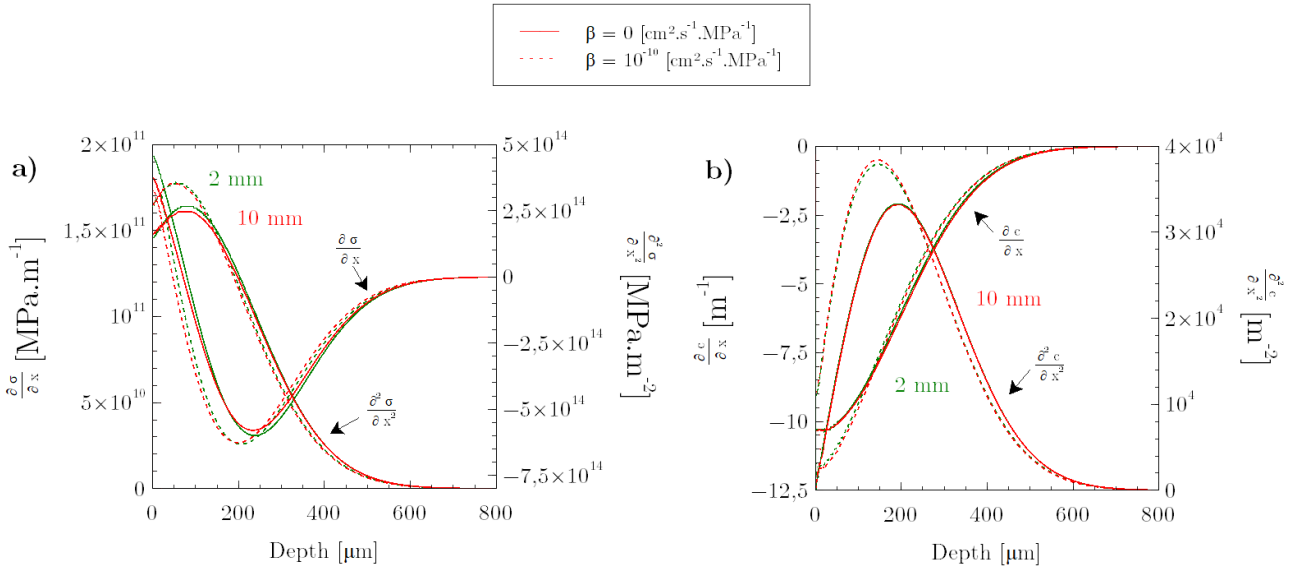

Figure 3.27 – a) Evolution of $\frac{\partial \sigma}{\partial x_3}$ and $\frac{\partial^2 \sigma}{\partial {x_3}^2}$; b) Evolution of $\frac{\partial c}{\partial x_3}$ and $\frac{\partial^2 c}{\partial {x_3}^2}$; for two thickness sample (2 mm and 10 mm) as a function of two β values (0 and 10^{-10} cm^2.s^{-1}.MPa^{-1}).

3.1.3.4.4 Conclusion This investigation on the evolution of kinetics in the case of the temporal evolution of stresses (i.e. residual stresses), made it possible to observe more precisely the effects and to draw conclusions on the predominance between the influence of a stress gradient $\frac{\partial \sigma}{\partial x_3}$ and that of the stress on mobility $\left(D_I^{\Phi} + \beta \sigma_{kk}\right)$. Tab. 3.7 summarises the evolution of surface stresses, stress gradients (surface and in depth) and concentration gradients (surface and in depth) as a function of four factors (time t, sample thickness e, stress amplitude CC and parameter β). For better understanding, Fig. 3.28 schematises the terms used in terms of surface stress, surface gradient and depth gradient.

Parameter evolution		$\lvert\sigma_{\text{surface}}\rvert$	$\frac{\partial \sigma}{\partial x_3}$ surface	$\frac{\partial \sigma}{\partial x_3}$ in depth	$\frac{\partial c}{\partial x_3}$ surface	$\frac{\partial c}{\partial x_3}$ in depth
Time t	↓	↑	↑	↓	↑	↓
Thickness e	↓	↓	↑	↓	↓	↓
Stress amplitude	↑	↑	↑	↑	↑	↑
β	↑	↑	↑	↓	↑	↓

Table 3.7 – Summary table of the evolution observed as a function of four factors (time t, sample thickness e, stress amplitude CC and parameter β).

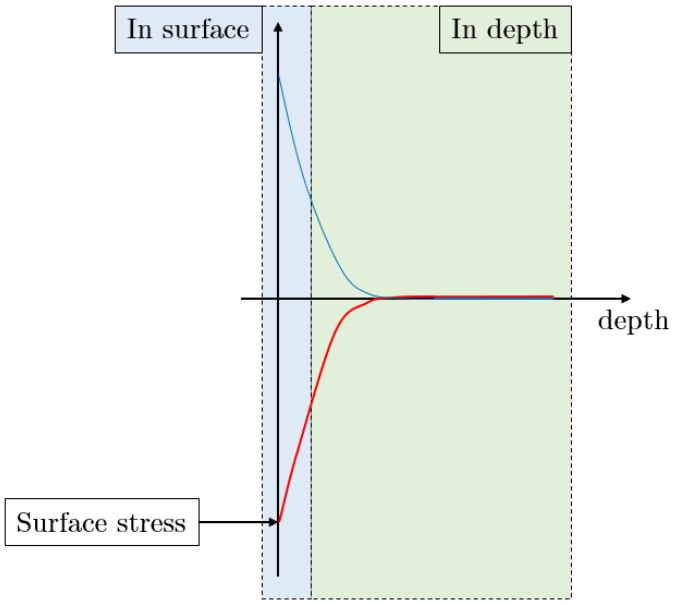

Figure 3.28 – Schematisation of the terms: surface stress, surface gradient and depth gradient.

In addition, some individual observations were made. In the case of:

— the increase in the amplitude of the stresses CC: a shift in depth of the maximum $\frac{\partial \sigma}{\partial x_3}$ and a structural effect due to the increase $\frac{\partial \sigma}{\partial x_3}_{\text{surface}}$ are observed. A general increase of the $\frac{\partial \sigma}{\partial x_3}$ is observed,

— the decrease in thickness e leads to an overall average increase in the stress gradient $\frac{\partial \sigma}{\partial x_3}$,

— and a final known/recognised observation through the observation that an increase in the concentration field at the surface leads to an increase in the concentration field along the entire profile.

3.1.3.5 Specific loading study

The previous study concluded that studies are needed to observe the greatest effect on both driving forces and mobility. Within the framework of this study and the conditions chosen, it was shown that in order to observe a significant influence on the stress gradient (in the case where there are only residual stresses, i.e. a positive gradient and negative stresses), it is necessary to use a thin sample with a short treatment time and a large stress amplitude. It is essential to remember that a nitrided steel results in a much larger residual stress field (through huge volume changes due to precipitation phenomena) than pure iron, with surface stresses ranging from -500 to -1000 MPa. In addition, due to the co-diffusion of carbon and precipitation events, nitrided steel exhibits much slower long-range diffusion where at 520°C $D_{\text{nitrogen}} = 4{,}9.10^{-8}$ cm^2.s^{-1} and $D_{\text{33CrMoV12-9 steel}} = 4{,}7.10^{-9}$ cm^2.s^{-1} [Jegou et al., 2018].

The objective of this study is to fully understand what happens to long-range diffusion under various types of mechanical loading. Therefore, the research focused on the impact of stress fields that can be easily obtained experimentally, such as a tensile/compressive test or a bending test (Fig. 3.29). The influence of residual stresses (effect at each instant) will not be considered in this study in order to draw conclusions on the influence of a so-called homogeneous stress (mobility effect without driving force effect) with/without the influence of β

parameter (mobility effect) and then the influence of a stress gradient (driving force effect) with/without the influence of β parameter (mobility effect).

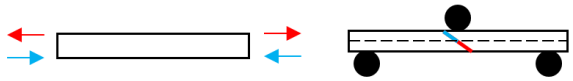

Figure 3.29 – Schematisation of mechanical tests (tensile/compressive and bending test).

In the case of a homogeneous stress shows that, in Eq. 3.18, stress will only have an effect on the diffusivity, the mechanical driving forces being null (stress gradient). Conversely in the case of a stress gradient Eq. 3.18 shows that the stress gradient will have a strong influence.

Throughout this subsection, numerical simulations for a 1 mm thick sample treated for 1 h at 520 °C with a constant surface concentration of $c_0 = 0.001$ will be performed. This surface concentration value is arbitrary because the expansion of the α-iron lattice due to stress-free strains is not taken into account. Only the case of a fixed stress throughout the treatment is taken into account.

3.1.3.5.1 Homogeneous stress The study on homogeneous stress will be divided into two parts. The first is the study of a positive stress of 1 GPa evolving through 5 β values: 0, 10^{-13}, 10^{-12}, 10^{-11} and 10^{-10} $cm^2.s^{-1}.MPa^{-1}$. The second is the study of a positive and negative stress (|1| GPa) for a chosen value of β.

Fig. 3.30a) shows the evolution of the concentration profile for a positive stress of 1 GPa with different values of β. The magnitude of the stress used would actually result in plastic strain fields (plastic strains not considered in this study); however, this value is used to understand the influence and justify (or not) the performance of future experiments. Fig. 3.30a) shows that a positive homogeneous stress accelerates the diffusion kinetics. When $\beta = 10^{-12}$ $cm^2.s^{-1}.MPa^{-1}$, the acceleration becomes considerable and noticeable, i.e. when the orders of magnitude are $\sigma\beta = 0,1 D_I^{\Phi}$. This order of magnitude was previously obtained in the case of studies taking into account residual stresses. These agreements therefore show that whatever the nature of the stresses, the effect of the transport force or mobility stresses is equivalent.

Fig. 3.30b) shows the influence of a positive and negative stress (|1| GPa) for $\beta = 10^{-11}$ $cm^2.s^{-1}.MPa^{-1}$. It shows that a negative stress will have more impact on the diffusion kinetics by strongly slowing down the diffusion. This can be explained, as before, by the sum of these two terms: $\left(D_I^{\phi} + 2\beta\sigma\right)$. The diffusion kinetics is thus accelerated or slowed down according to the sign of the stresses. Fig. 3.30b) shows the depths affected for three concentration values: 4.10^{-4}, 2.10^{-4} and 5.10^{-5}. This diagram illustrates that the same level of stress in tension and compression does not result in symmetrical diffusion. Using the depths of the three concentration points, a negative stress produces 20 % less kinetics than a positive stress. This difference is calculated by comparing the changes in the affected depths represented by Δz_{depth}. This observation is consistent with the known Einstein relation: $z^2 = 2D_I^{\Phi})_{\text{eff}}t$ where $z = x_3$ in this study. It demonstrates that the depth z is propositional to the root of the diffusion coefficient $D_I^{\Phi})_{\text{eff}}$ for a given time t and temperature T. This equation therefore shows an evolution that is not linear. In addition, mobility is considered here to be stress-dependent. In other words, Einstein's equation is modified into the form: $z^2 = 2\left(D_I^{\Phi} + 2\sigma\beta\right)t$. This modification shows a second cause of non-linearity, this time depending on the stress.

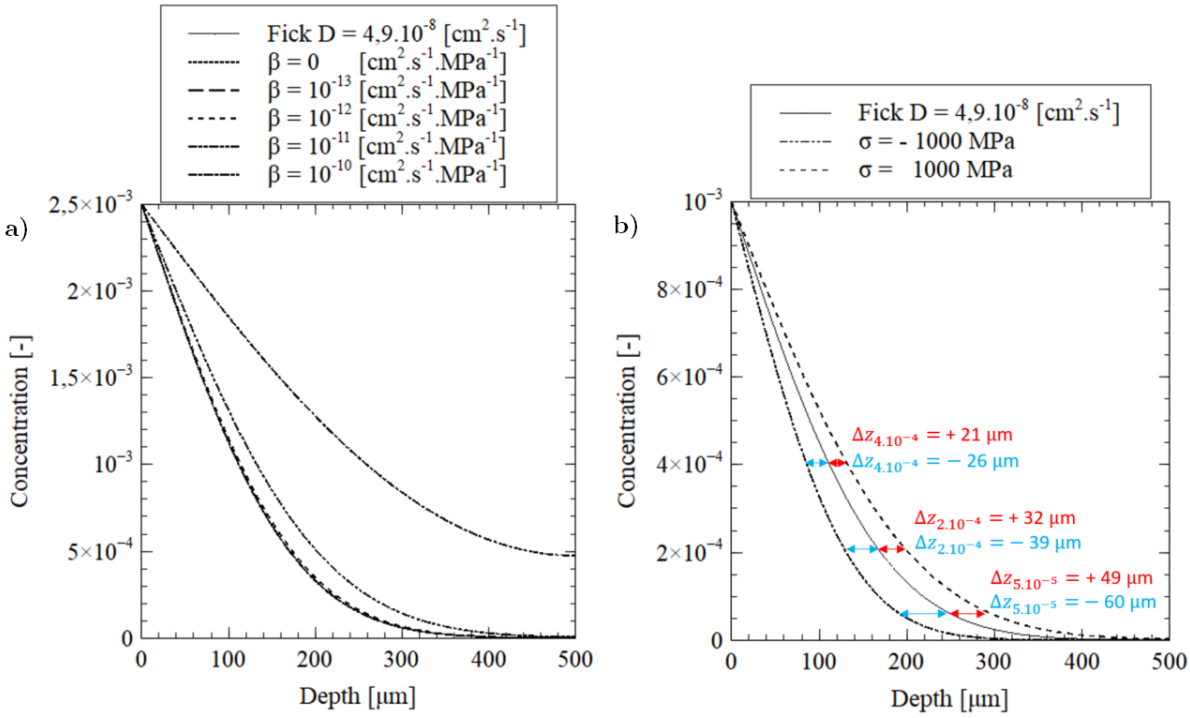

Figure 3.30 – a) Evolution of concentration profiles as a function of five values of β (0, 10^{-13}, 10^{-12}, 10^{-11} and 10^{-10} $cm^2.s^{-1}.MPa^{-1}$) subjected to a homogeneous tensile test (1 GPa); b) Evolution of concentration profiles for two mechanical tests (pure tensile at 1 GPa and pure compressive at -1 GPa as a function of $\beta = 10^{-11}$ $cm^2.s^{-1}.MPa^{-1}$; for a 1 mm thick sample, at 520 °C during a 1 h treatment.

3.1.3.5.2 Stress gradient In order to properly study the effect of the stress gradient combined with the effect of stress on mobility, four cases could be listed:

case number n°X	σ	$\frac{\partial \sigma}{\partial x_3}$	$\frac{\partial^2 \sigma}{\partial {x_3}^2}$
n°1	> 0	> 0	Constant
n°2	< 0	> 0	
n°3	> 0	< 0	
n°4	< 0	< 0	

Table 3.8 – Possible case study for the influence of the stress gradient and stress on mobility.

Only cases n° 2 and n° 3 will be studied, in terms of diffusion, as they are representative of a mechanical bending test. The study will focus on:

— two positive stress gradients of 2 and 4 $GPa.mm^{-1}$ evolving through 2 β values : 0 and 10^{-13} $cm^2.s^{-1}.MPa^{-1}$,

— a positive and negative stress gradient ($|4|$ $GPa.mm^{-1}$) for a chosen value of β.

Fig. 3.31a) concerns the study of two gradient amplitudes: 2 $GPa.mm^{-1}$ and 4 $GPa.mm^{-1}$. These two gradients were studied through 2 β values: 0 and 10^{-13} $cm^2.s^{-1}.MPa^{-1}$.

For case n°2 (see Tab. 3.8), in the left hand side of Fig. 3.31a), it shows that when the parameter $\beta = 0$,

then the greater the positive gradient, the faster the diffusion kinetics are. For a given negative value of stress, a slowing down of the kinetics is observed when β increases. For the case n°3, (see Tab. 3.8), in the right hand side of Fig. 3.31a), it shows that when the parameter $\beta = 0$, then the greater the negative gradient, the slower the diffusion kinetics are. For a given positive value of stress, an acceleration of the kinetics is observed when β increases. These two observations are anomalously justified by the fact that when $\beta > 0$, Eq. 3.18 shows that if the gradient is positive then the terms $\frac{\partial \sigma}{\partial x_3}\left(\frac{\partial c_I^{\phi}}{\partial x_3} - 2\frac{V_a \eta}{RT} c_I^{\phi} \frac{\partial \sigma}{\partial x_3}\right)$ are negative which implies that the diffusion is slowed down. This is reversed in the case of a negative gradient.

Fig. 3.31b) shows the study of a positive and negative stress gradient equal to $|4|$ GPa.mm^{-1} with $\beta = 10^{-13}$ cm^2.s^{-1}.MPa^{-1}. This study is the superposition of cases n°2 and n°3 (see Tab. 3.8) observed in Fig. 3.31a). Fig. 3.31b) shows the depths affected for three concentration values: 4.10^{-4}, 2.10^{-4} and 5.10^{-5}.

This diagram illustrates that the magnitude of the stress gradient in tension and compression does not result in symmetrical diffusion. Using the depths of the three concentration points, a negative stress field with a positive gradient produces a slowing down of the kinetics in the order of 3.3 times greater than the positive impact of a positive stress field with a negative gradient. This result shows a similar trend observed in the case of homogeneous stress. However, this study has shown that for a positive gradient with negative stresses the slowing down effect is accentuated. This is caused by the mobility gradient, i.e. the mobility-stress coupling. Again the modified Einstein relation ($z^2 = 2\left(D_I^{\Phi} + 2\sigma\beta\right)t$) demonstrates that these observations are consistent.

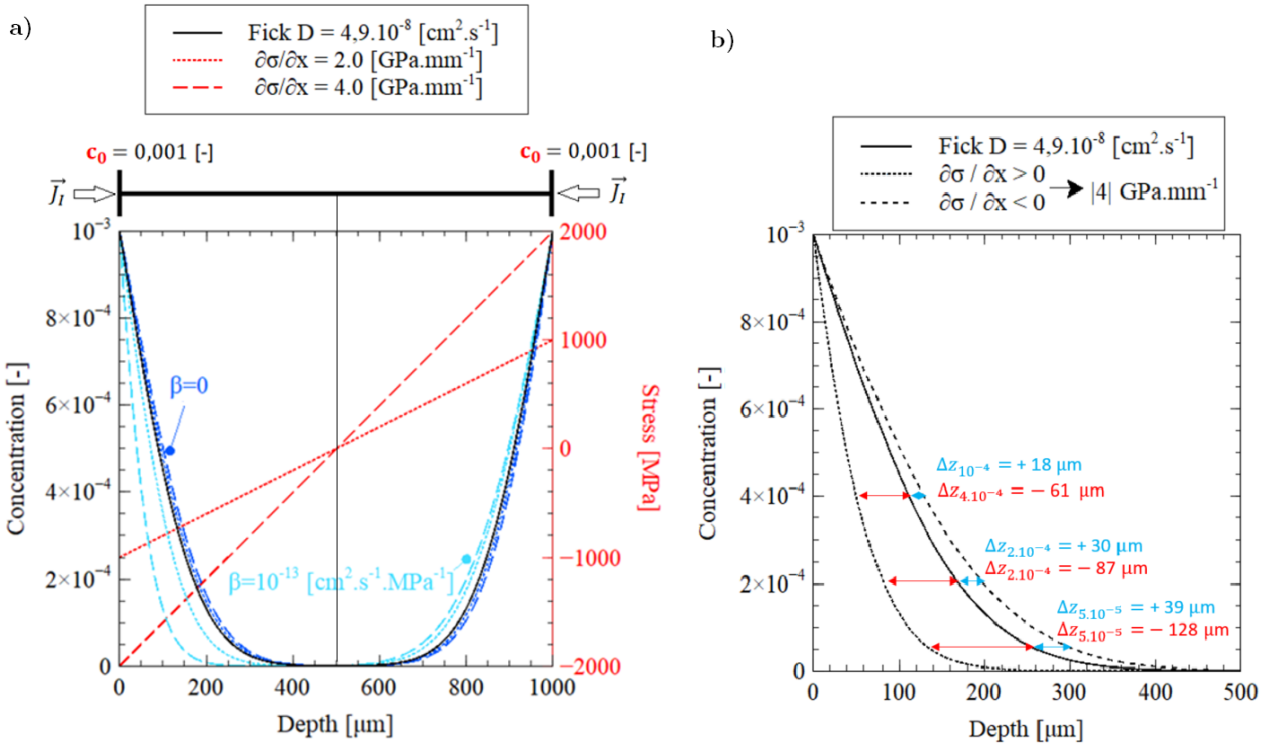

Figure 3.31 – a) Evolution of concentration profiles as a function of two values of β (0 and 10^{-13} cm^2.s^{-1}.MPa^{-1}) subjected to two bending tests (2 GPa.mm^{-1} and 4 GPa.mm^{-1}); b) Evolution of concentration and stress profiles for a bending tests (4 GPa.mm^{-1}) as a function of $\beta = 10^{-13}$ cm^2.s^{-1}.MPa^{-1}; for a 1 mm thick sample, at 520 °C during a 1 h treatment.

3.1.4 Discussion

This study has allowed to investigate the impact of taking into account transport forces (i.e. stress gradient) and/or mobility (i.e. influence of β on the diffusion kinetics). A first 2D study was carried out on the free software FreeFEM++ with the objective of visualizing the tensorial aspects of the stresses. This study made it possible to visualise the concentration and stress fields within a cross section of a sample of equivalent size to the experimental samples. It also allowed to visualize the edge effect and to visualize that the double perpendicular flow leading to a state of biaxial stress plays a major role on the evolution of the concentration by showing an effect that seems to be accelerated. This first study being too costly in terms of simulation time (t > 1 day), a second study in 1D (2D axisymmetric) was carried out using the finite difference method. The objective of this study was to visualise only the central behaviour of the sample. In general, the studies allowed us to observe and confirm the temporal influence of residual stresses on the diffusion kinetics. The shorter the treatment time, the higher the residual stress gradient (via mechanical rebalancing). Furthermore, as the thickness of the sample decreases, the mechanical rebalancing results in an increasing stress gradient, decreasing surface compressive stress and increasing core stress in tensile. However, simulations have shown that the evolution of the concentration profiles are essentially the same. This cannot ensure the influence of the stress gradient due to the small differences and low stress values. However, if the effect of stress on mobility is taken into account, the results show a difference in the concentration profiles by showing that the thinner the sample, the faster the diffusion (due to a larger positive stress gradient), although this is slowed by the effect of stress on mobility when negative.

A study of the stress amplitude for two sample thicknesses confirmed that the effect of the stress gradient becomes important from an order of magnitude of the gradient of the order of the GPa/mm. This study therefore led to the study of stress fields equivalent to known mechanical tests: tensile/compressive test (i.e. homogeneous stress) and bending test (i.e. stress gradient). The homogeneous stress study shows that a negative homogeneous stress has a negative impact on the evolution of the diffusion kinetics. Furthermore, that this negative impact is 20 % greater than the positive impact of a positive homogeneous stress. The study on the stress gradients shows that if considering an applied case of a nitrided sample put **under bending**, there are two possible observations allowing to conclude on the effect of the stresses on the mobility:

— Negligible mobility effect ($\beta = 0$): the compressive side ($\sigma < 0$) due to the positive gradient ($\frac{\partial \sigma}{\partial x_3} > 0$) accelerates the diffusion and vice versa for the tensile side,

— Mobility effect $\beta > 0$: side in compression slows down the diffusion and inversely for the side in tension then the parameter β will have to be quantified/identified.

These observations then help to understand and justify the results obtained in the laboratory in 2018 by B. Guillot [Guillot, 2018]. A sample subjected to a bending test was nitrided at 520 °C for 50 h with $K_N = 4.37$ $atm^{-1/2}$. Fig. 3.32 shows the nitrogen concentration profile for both sides of the sample and compares it to a reference sample. The results show an acceleration of the kinetics on the tensile side and a slowing down on the compressive side. This result shows that for this stress state, mobility predominates over the effect of the gradient.

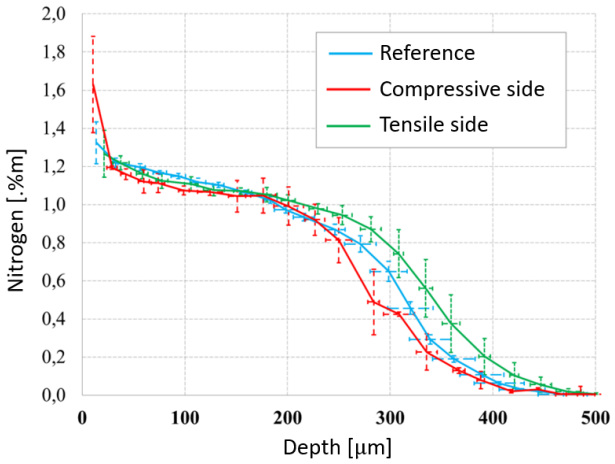

Figure 3.32 – Nitrogen composition profiles of the reference and nitrided samples under bending stress at 520 °C for 50 h and a nitriding potential $K_N = 4.37$ atm$^{-1/2}$ [Guillot, 2018].

These numerical analyses then allowed us to think about future experiments, taking into account the disadvantages linked to the limited space available in the thermogravimeter. The effect of the stress gradient and the effect of the stresses on the mobility will then be experimented, in the Chapter 4, from experiments on the effect of elastic strains (residual/applied stresses) and plastic strains (strain hardening).

Chapter 4

Experimental study

Contents

4.1 Introduction

The objective of this chapter is to study the role of elastic (residual) and plastic stresses in the nitriding process. Stress-diffusion couplings are frequently studied by combining mechanical pretreatment with thermochemical treatment. They can significantly improve the compound and diffusion layer thicknesses of a nitrided steel. However, these studies mainly conclude on the influence of grain boundaries and dislocation densities, without taking into account the residual stresses, i.e. the elastic strains. The objective of this chapter is to separate the effects of elastic and plastic strains. The experiments will be carried out on the steel grade 33CrMoV12-9, which gives a more complex industrial system than the assumptions made in the numerical simulation chapter. However, the nitriding of this grade has been known for years. The nitriding of this steel requires the consideration of carbon precipitation and co-diffusion processes. Long-range diffusion will be studied by comparing the nitrogen/carbon content, hardening and residual stress profiles of the samples. Then the impact on carbon precipitation and co-diffusion by examining the effects on compound layer thickness, distribution, nitride depth and cementite depth.

This chapter is divided into two sections. The first section focuses on the effect of elastic strains. Two experiments were set up with the aim of generating an elastic strain gradient by a direct method through the application of a load and an indirect method through mechanical rebalancing. Each sample in this section was nitrided at 520 °C, $K_N = 3.711$ atm$^{-1/2}$ for 5 h. Previous numerical (see section 3.1.3.4.2) and experimental studies [Jegou et al., 2018] have shown the value of a short time. In the case of nitriding treatment, the shorter the time, the higher the residual stress gradient. The first study consists in generating an asymmetric diffusion in order to study the effect of a stress gradient with negative values on the obtained diffusion kinetics. For this purpose, semi-infinite and thin samples with a thickness factor of ten will be compared. The stresses are influenced by two factors: a structural effect (i.e. dynamic equilibrium) and a mechanical equilibrium effect. The structural effect does not exist in the case of a semi-infinite sample. The second study involves stressing a split ring through its slot by imposing a displacement, resulting in a bending-type stress field. This experiment is intended to be carried out in the thermogravimeter and therefore involved difficulties related to the dimensions of the thermogravimeter tube and the maximum weight (max 30 g) that the beam balance can support. The objective of these two studies will be to determine the relative importance of a stress gradient (driving force) and stress on mobility. The second section deals with the effect of plastic strains. A tensile specimen was machined in order to observe the effect of a homogeneous plastic strain field on the diffusion kinetics. Each specimen was obtained from controlled tensile tests, prior to nitriding treatment, using preliminary numerical finite element studies on ABAQUS, allowing the specimens to be nitrided at different strain hardening levels. The results are compared to a reference condition, obtained from a tensile specimen not subjected to nitrided work hardening under the same conditions (at 520 °C, $K_N = 3.711$ atm$^{-1/2}$ for 24 h).

Due to the repeatability of the treatments, only one sample per set of samples will be presented in this study.

4.2 Elastic strain effect

The effect on short- and long-range, i.e. the thickness of the compound layer or the depth of diffusion of nitrogen, was observed. Two studies were established.

4.2.1 Self-stress-induced diffusion

As a nitrogen diffusion blocker, a copper solution was recommended (procedure presented in section 2.1.8). Copper is ductile and does not undergo thermal stress at high temperatures, as can be seen in the oxide layers. Furthermore, as the alloy used does not contain copper, the Kirkendall effect will not occur.

Fig. 4.1 shows the different cycles to which the samples were subjected: one sample (F1) which was copper plated on one side and then nitrided, and one sample (F2) which was decopper plated, copper plated on the other side and then nitrided. Samples undergoing simultaneous nitriding on both sides will be defined by (S).

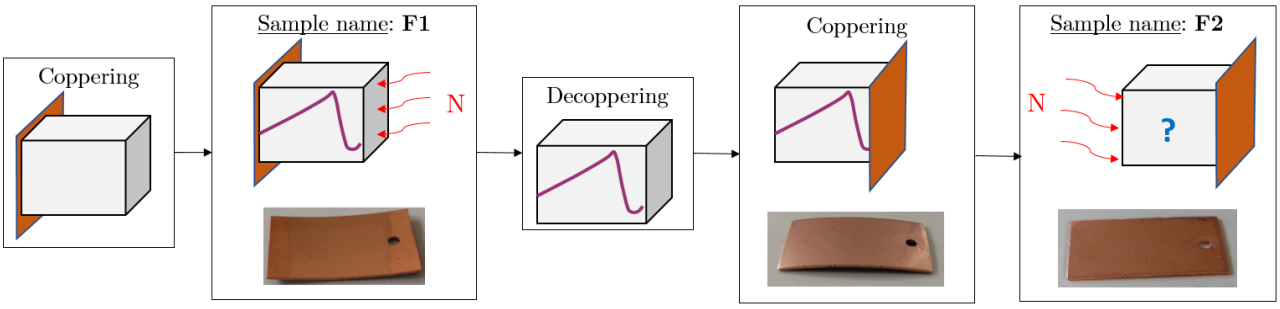

Figure 4.1 – Diagram of the experiments performed with the equivalent names.

All thermochemical nitriding treatments will be the same. A high K_N= 3.711 atm$^{-1/2}$ was chosen to create a two-phase compound layer and, therefore, to study the influence on the phase distribution. Previous laboratory work showed that during a period of 5 h at 520 °C, a diffusion layer of the order of 200 μm can be formed [Jegou et al., 2018].

Simulations with the FreeFEM++ calculation code (in section 2.1.2) and the 2D axisymmetric model (in section 2.1.3) have shown that the thinner the sample thickness, the greater the stress gradient. The influence of residual stresses on the diffusion kinetics will therefore be compared between thin samples 0.5 mm and 5 mm samples.

Then, each sample will be examined by:

— XRD to obtain residual stress profiles down to the base material and a quantitative study of the phases obtained over the first 50 μm,

— chemical analysis to obtain nitrogen and carbon profiles down to the base material,

— micro-hardness to determine the hardness profiles of the diffusion layers,

— SEM observations to produce BSE images and EBSD maps to measure different particular layers/depths (see Fig. 4.2) of a nitrided layer (i.e. compound layer thickness, nitrides (i.e. ϵ-$Fe_{2-3}N$ and γ'-Fe_4N) depth, cementite depth) and compound layer proportion (ϵ-$Fe_{2-3}N$ and γ'-Fe_4N nitrides).

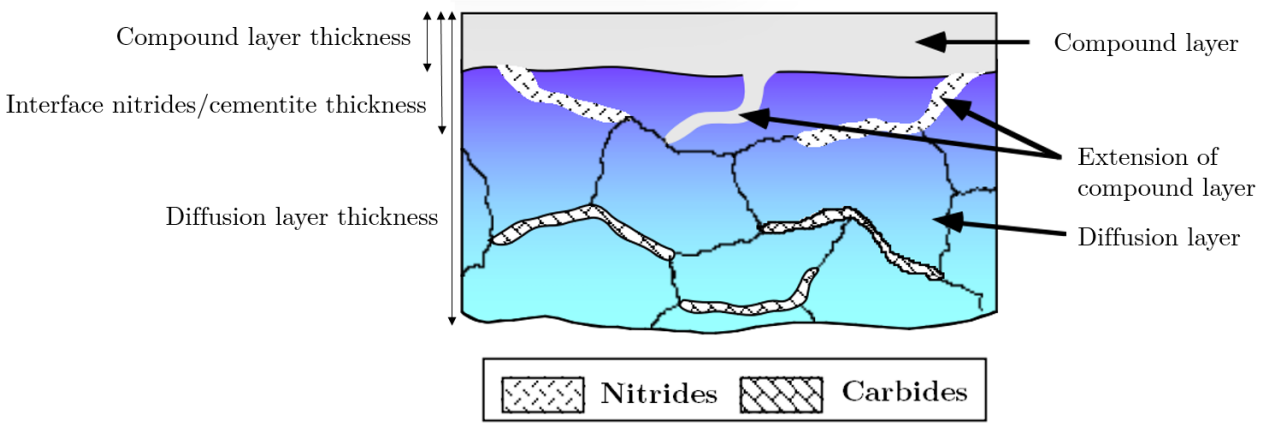

Figure 4.2 – Diagram of the different layers and depths studied in the SEM observations. Image modified from J.N. Locquet image [Locquet, 1998].

Throughout this study specific characteristics of the experimental profiles of a nitrided sample will be used to simplify the discussion. Fig. 4.3a) presents the terms for the residual stress profile: the surface stress σ_s which can be positive or negative depending on the experimental conditions, the maximum stress σ_{max} with its equivalent depth z_{max}, the stress gradient $\frac{\partial\sigma}{\partial x}$ and its range $[z_e] = z_e - z_{max}$. Fig. 4.3b) presents the terms for the hardness HV0.2 profile: surface hardness HV_s, core hardness HV_c and effective depth z_d with equivalent hardness HV_d. The latter is the most important parameter. The effective depth is defined as the depth at which the difference in Vickers hardness with the base material is +100 HV [Afnor, 1985].

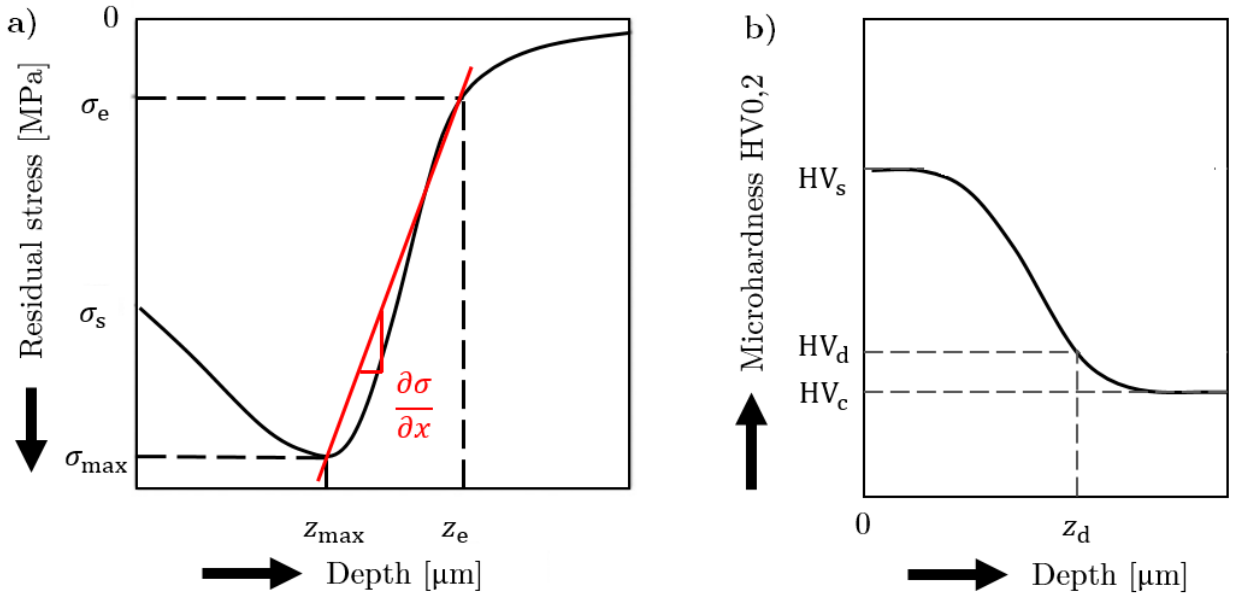

Figure 4.3 – Diagrams of the characteristic points of a) a residual stress profile, and, b) a hardness HV0.2, of a nitrided surface.

A preliminary study confirmed that the nitriding treatment is reproducible for both thicknesses, which

implies that only one result per sample from each series will be presented.

4.2.1.1 Influence of thickness sample on gas nitriding (K_N= 3.711 atm$^{-1/2}$)

2 sides (S) nitrided specimens were initially examined in order to firstly collect references for the thicknesses and secondly to determine whether the structure effect (i.e. dynamic balance) has an impact on the microstructure.

Fig. 4.4 compares the profiles of calculated stresses and integral breadths for 5 mm and 500 μm nitrided specimens on both sides (S). Figs. 4.4 shows that as the sample thickness decreases, the surface stress σ_s decreases due to the structure effect (i.e. dynamic balance), as shown in Tab. 4.1. The stress profiles show that the thin sample has a higher tensile equilibrium due to mechanical equilibrium. The 5 mm sample has a higher stress gradient $\frac{\partial\sigma}{\partial x}$ value of 2.4 GPa/mm (see section 3.1.3.4.3). The positions z_{max} of the stress maxima σ_{max} when grouped by sample thickness are equal. In the case of the 500 μm sample, a plateau corresponding to the value of the stress maxima σ_{max} has a wider range. The associated gradient describes a greater depth. This observation is consistent with the evolution of the integral breadth profiles obtained by DRX method.

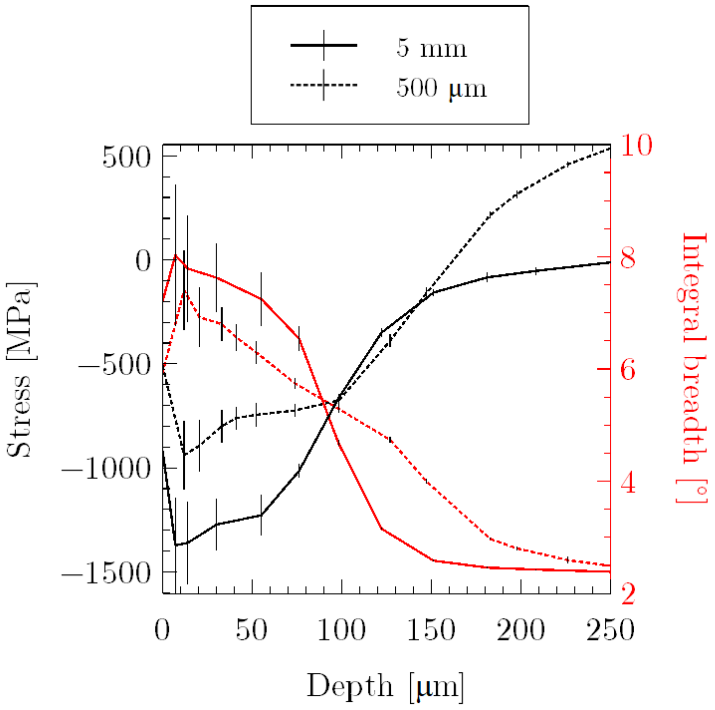

Figure 4.4 – Residual stress and integral breadth profiles, of 5 mm and 500 μm, 2 sides (S) nitrided samples at 520 °C and 3.711 atm$^{-1/2}$ during 5 h.

Thickness [mm]	Surface stress σ_s [MPa]	Stress gradient $\frac{\partial\sigma}{\partial x}$ [GPa/mm]	Gradient range [z_e] [mm]
5	- 923	11,7	55 to 151
0,5	- 514	9,3	98 to 225

Table 4.1 – Surface stress, stress gradient and gradient range of 5 mm and 500 μm 2 sides (S) nitrided samples at 520 °C and 3.711 atm$^{-1/2}$ during 5 h.

Fig. 4.4 corresponds to unbalanced residual stress profiles, i.e. where the sum of the normal stresses $\int_0^e N_x \neq 0$. They correspond to the stresses obtained directly by the XRD analysis. A mechanical balancing, presented in Fig. 4.5, must therefore be performed to correct the results. For this purpose, an equivalent profile of a semi-infinite sample is calculated from the experimental data of the 5 mm sample. This semi-infinite profile is then used in an inverse method to calculate the stress profile for a 5 mm thick specimen and then on a 0.5 mm thick specimen. It is crucial to understand that the experimental profile corresponds to the stress profile in the ferrite ($\sigma_{11} - \sigma_{33}$) with the assumption of a two-phase material, whereas the recalculated profile takes into account the average stresses σ_{mean}. These mean stress σ_{mean} calculations are a function of the stresses in the semi-infinite specimen profile $\sigma_{\text{S-I}}$, the sum of the normal forces N_x and the thickness of the selected specimen e. Moreover, this method leads to the assumption that the microstructure between the thicknesses is equivalent in terms of long-range diffusion (N%m.), short-range diffusion (precipitation phenomena) and carbon co-diffusion (C%m.).

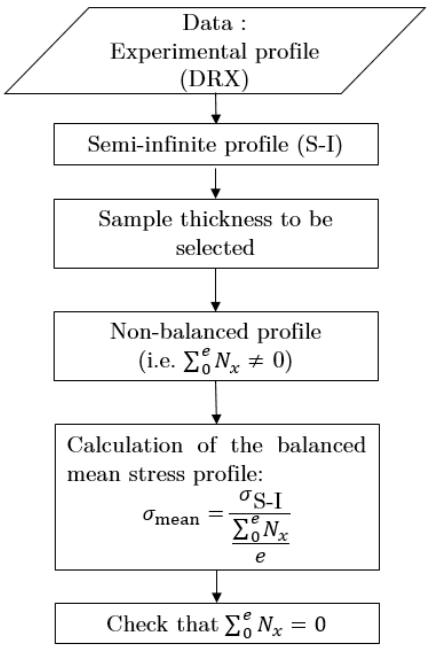

Figure 4.5 – Different steps for calculating the balanced mean stress profile for simultaneous diffusion (2 sides).

Fig. 4.6a) presents these analytically measured curves compared to the experimental profiles. It is interesting to note the difference between the analytical and experimental profiles for the 0.5 mm specimens in terms of affected depth and stress maxima. The analytical profile shows significant diffusion with a slightly larger stress maximum. This difference seems to support the fact that the microstructure between the two thicknesses is

different. L. Barrallier and V. Goret carried out studies on the discrepancies between the stresses $\sigma_{11} - \sigma_{33}$ predicted by XRD and the balanced profiles using the mean stresses σ_m [Barrallier, 1992, Goret, 2006]. They showed large differences between the profiles measured with average stresses σ_m on the balanced profiles and the experimental stress profiles $\sigma_{11} - \sigma_{33}$ in the ferrite. L. Barrallier showed that $\sigma_{11} - \sigma_{33} \simeq \frac{\sigma_m}{1.33}$ and V. Goret showed that $\sigma_{11} - \sigma_{33} \simeq \frac{\sigma_m}{1.5}$. Here in this study, so that the stress amplitudes, for the thin sample, are equivalent, it is found that $\sigma_{11} - \sigma_{33} \simeq \frac{\sigma_m}{1.1}$, as plotted in Fig. 4.6b).

A study (not presented here) was conducted to examine the impact of stress redistribution on a sample. To summarize, thin samples were implanted in a conductive resin to reduce the influence of stress relaxation by retaining the sample in its original shape and to allow electrochemical polishing for phase and stress control. The calculation revealed that, on a scale of 0 to 1, where 0 represents a rigid mount and 1 represents the sample being totally free in its stress redistribution, the mount in our situation is in the range of 0.2-0.3. This difference can therefore be added to the first conclusion that the analytical calculation of the average stresses is true under the assumption of an identical microstructure between the samples.

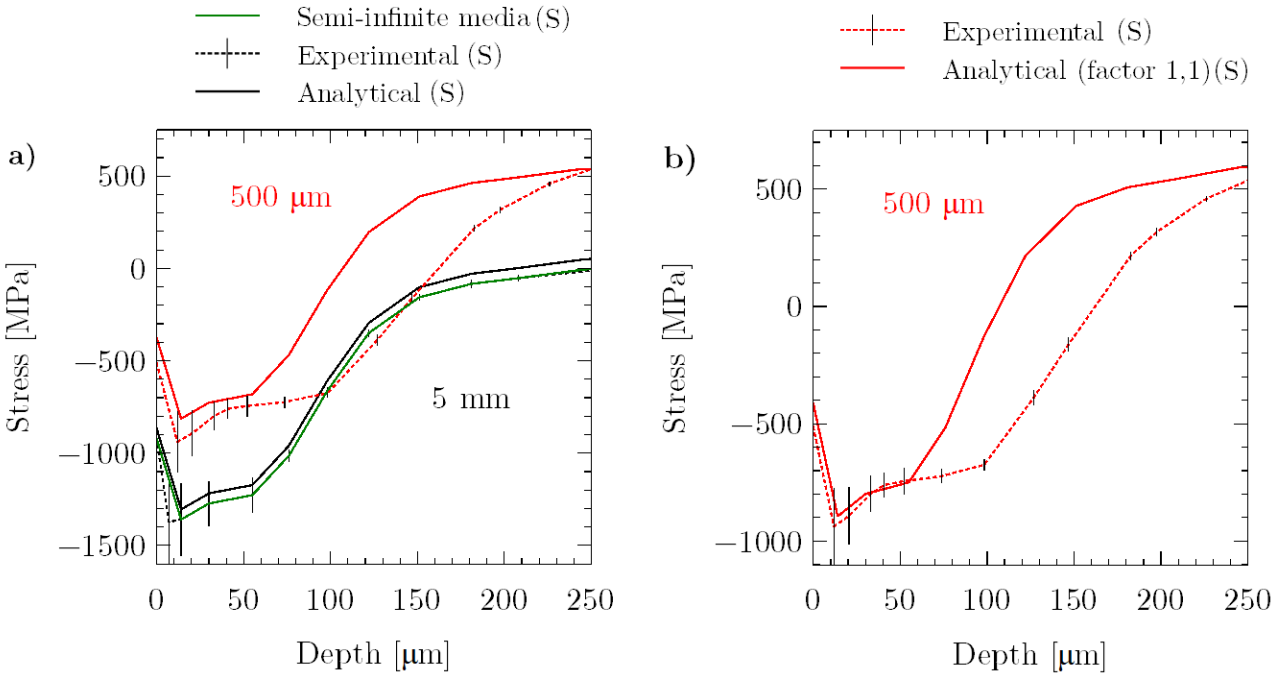

Figure 4.6 – a) Experimental and analytical residual stress profiles of 5 mm and 500 μm 2 sides (S) nitrided samples at 520 °C and 3.711 atm$^{-1/2}$ during 5 h. b) Comparison of the experimental residual stress profile and the analytical residual stress profile corrected with a multiplication factor of 1.1.

A quantitative study of the diffraction phase peaks was performed using the approach described in Section 2.1.6.1.1. Fig. 4.7 shows the superposition of two spectra for the 500 μm reference sample obtained at the surface and at 30 μm depth. These results show that the compound layer is mainly composed of nitride ϵ-$Fe_{2-3}N$ and that the depth of the nitrides is less than 30 μm because there is only α-Fe at this depth.

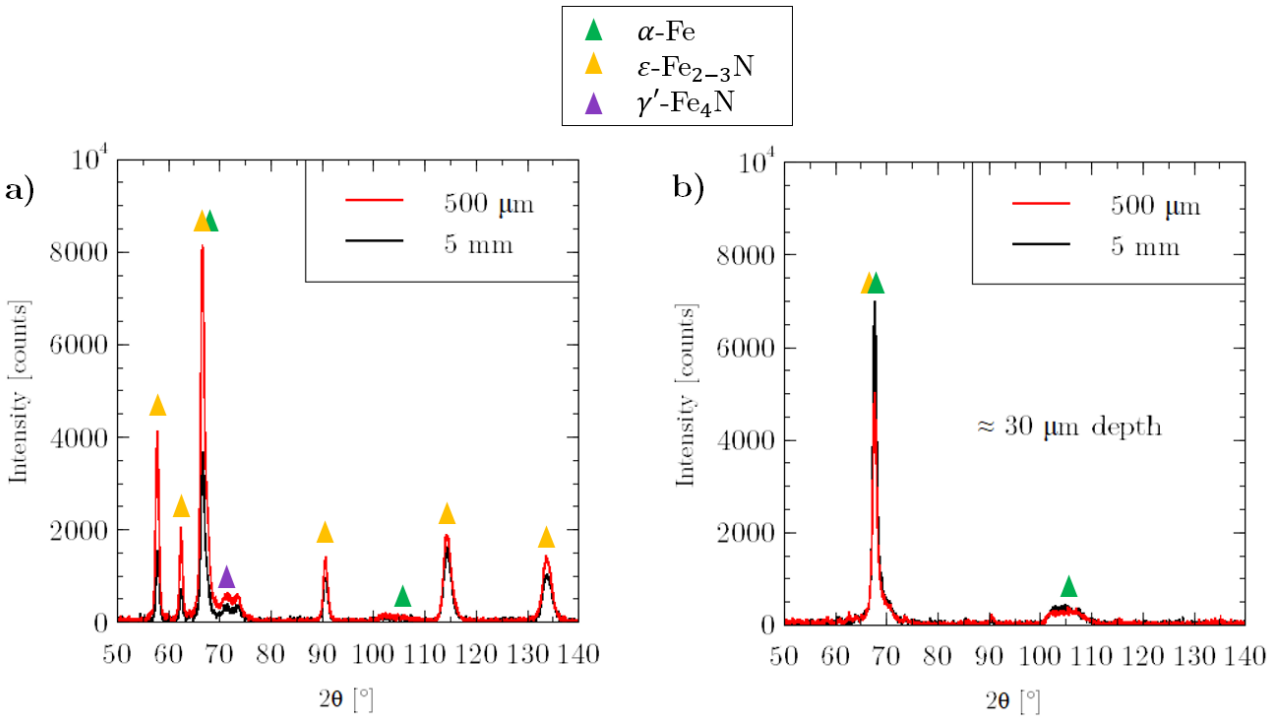

Figure 4.7 – Phase spectra of samples nitrided at 520 °C and 3.711 $atm^{-1/2}$ for 5 h at 500 μm and 5 mm thickness a) at the sample surface, b) at 30 microns depth, with an X-ray penetration depth of 7 μm.

Figs. 4.8a) and b) show the hardness profiles in depth as well as the nitrogen and carbon profiles for both thicknesses. The hardness filiations were performed on the cross-section of each sample. The profiles are fairly comparable, showing that the structural impact does not appear to have an effect on the diffusion kinetics. The core hardness HV_c is 410 HV0.2 for both samples. Their effective depths z_d are identical with a value of 136 μm. Fig. 4.8b) shows the comparison of the nitrogen and carbon profiles of the nitrided samples on both sides (S) 5 mm and 500 μm. The nitrogen content profiles show equivalence down to a depth of 120 μm. The nitrogen concentration of the 5 mm sample is zero at 160 μm depth, while the nitrogen content of the 500 μm sample is 0.08 N%.m in the centre of the sample. The carbon profile of the 500 μm (S) sample shows less surface decarburisation than the 5 mm sample up to the overburden zone. The over carburisation of the 5 mm sample is approximately 160 μm, compared to 220 μm for the 500 μm with comparable values, up to 0.37 C%.m, located at the depth of their respective nitrogen diffusion fronts. The initial carbon content (0.325 C%.m) of the 5 mm sample is reached after 250 μm, against 0.34 C%.m in the centre of the 500 μm sample.

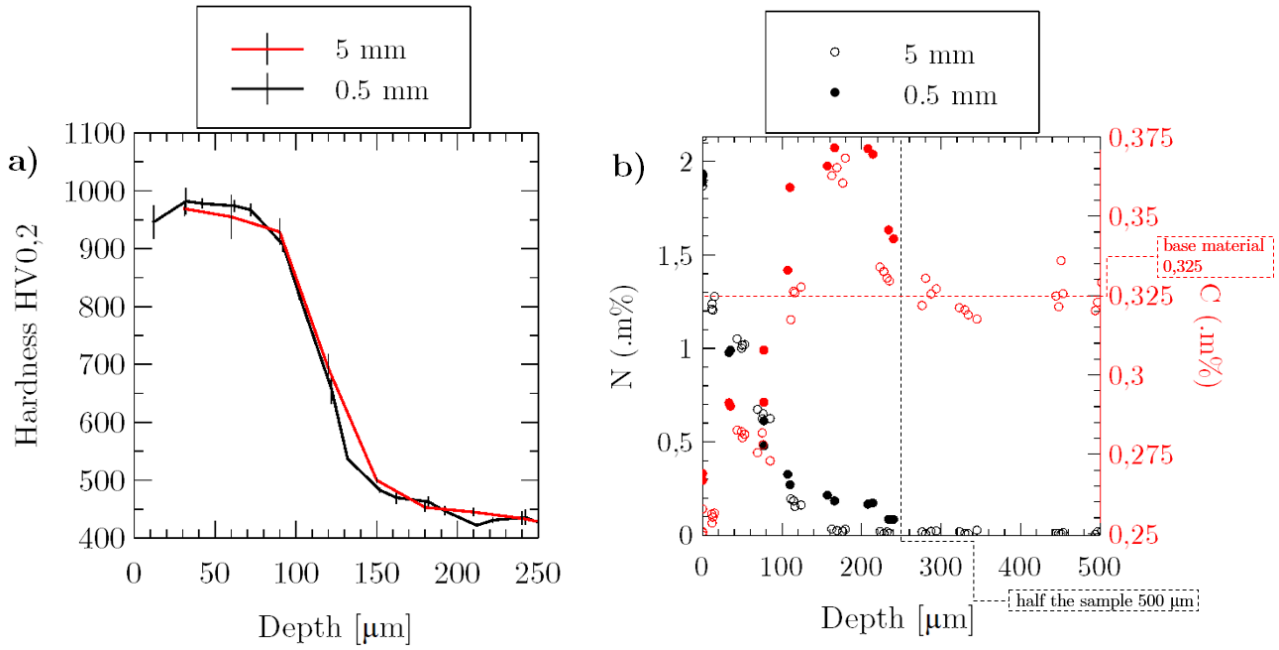

Figure 4.8 – a) Hardness profiles and b) Nitrogen and carbon profiles, of 33CrMoV12-9 specimens nitrided at 520 °C and 3.711 $atm^{-1/2}$ during 5 h.

The evolution of the mole fractions of the different precipitations for the 5 mm (S) and 500 μm (S) samples are, respectively, shown in Fig. 4.9, calculations made with Thermo-Calc from experimental chemical composition profiles. The following elements were selected for this study: C, N, Fe, Cr, V and Mo. The base material is quenched and tempered, i.e. a ferritic matrix with carbides of $M_{23}C_6$ (M=Cr,Fe), M_7C_3 (M=Cr,Fe), and/or VC depending on the steel composition. The nitrided layer forms globular nitrides of type MN (M=Cr,Fe) that are incompatible with the ferritic matrix. The initial tempering carbides are converted into globular nitrides, with the carbon diffusing at grain boundaries to create the alloyed cementite M_3C (M=Cr,Fe). This process explains nitrogen and carbon linked diffusion. Semi-coherent nitrides of the same type MN (M=Cr,V,Mo) are also generated from the addition elements present in the ferritic matrix in solid solution. In this situation, the FCC profiles correspond to the transition of VC carbides into VN semi-coherent nitrides, the substitution of Cr and V by Fe (in the event of a high N content), and the core is VC vanadium carbide. The # symbol represent distinct compositions. For the HCP profiles, they correspond to Mo_2N before the Mo is found in globular CrN nitrides.

Fig. 4.9 shows that the profiles differ greatly in the evolution of $FCC_{A1\#X}$. The profiles show that the position of the maximum carbon content corresponds to the position of the maximum carbide content M_7C_3. However, these M_7C_3 profiles show that the amplitude is greater for the thicker sample. The evolution of the $M_{23}C_6$ profiles is almost identical. The $FCC_{A1\#X}$ phase also shows strong differences due to the non-zero nitrogen content in the case of the 500 μm sample.

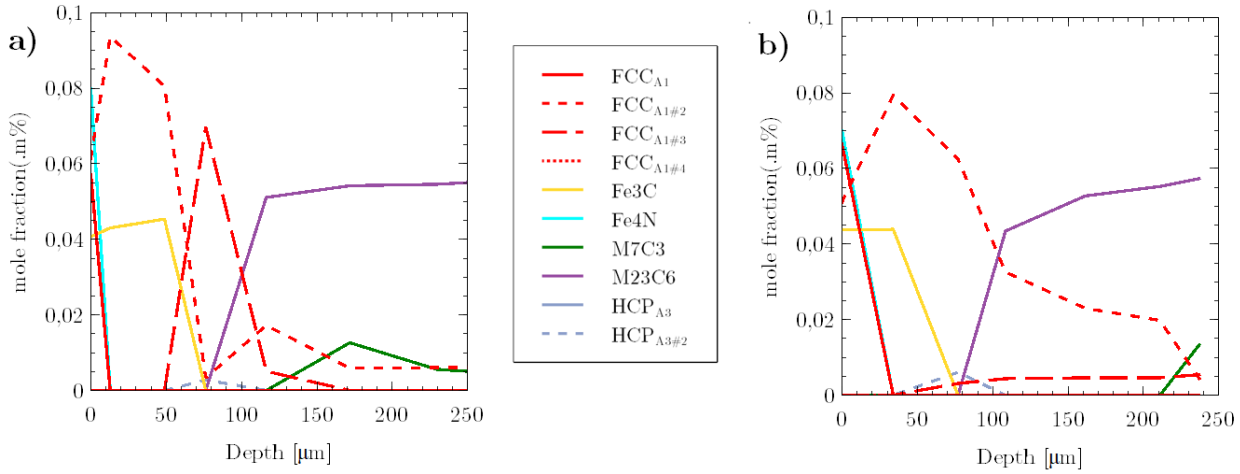

Figure 4.9 – Evolution of the mole fractions of nitrides and carbides obtained in 33CrMoV12-9 steel grade for 2 sides (S) nitrided samples with thicknesses of a) 5 mm and b) 500 μm.

Figure 4.10 shows two BackScatter Electron analysis (BSE) images and an EBSD cartography, all taken on the 500 μm sample. BSE images was used to distinguish iron carbides from iron nitrides at the anterior grain boundaries of the austenite. These observations are performed by grey contrast based on the atomic numbers of the different phases observed where nitrides (ϵ-$Fe_{2-3}N$ and γ'-Fe_4N) are darker than carbides (Fe_3C cementite). The EBSD observation allows a detailed identification of the different phases present in the compound layer and at the grain boundaries. Usually, ϵ-$Fe_{2-3}N$ nitrides are described as a porous component of the compound layer and γ'-Fe_4N nitrides as a dense component. However, the observed layer is dense but EBSD mapping shows that the compound layer is 95-98% of ϵ-$Fe_{2-3}N$. This EBSD mapping is consistent with quantitative XRD studies which show a low proportion of γ'-Fe_4N in the compound layer. The interface between the compound layer and the diffusion layer often corresponds to a decarburization, which occurs as a result of the transition from carbide to nitride. This is often explained by the low carbon solubility limit of γ'-Fe_4N iron nitride (0.2 %m.) and the decarburizing atmosphère (presence of hydrogen).

Between 7 and 23 μm depth, the compound layer extends to the grain boundaries of the diffusion layer. This is assumed to be independent of grain size. G. Fallot hypothesised that the thickness of the compound layer is not constant in the case of nitriding at 520 °C because the growth mechanism of the compound layer is different compared to a higher temperature (which shows a constant compound layer) [Fallot, 2015]. This hypothesis was found in the case of this study. G. Fallot explained that at 520 °C, the nitrogen concentration is lower and the growth of the compound layer occurs by consumption of a grain from a grain boundary where iron nitrides are already present. Grain transformation takes place along the martensite lath boundaries.

At the grain boundaries parallel to the nitrided surface, i.e. the boundary between the compound and diffusion layers, two phases (i.e. iron nitrides (dark grey) and cementite Fe_3C (light grey)) are visible in the BSE images. The iron nitride is on the side of the compound layer with the highest nitrogen flux. The change of the initial carbides ($M_7C_3/M_{23}C_6$ (M = Cr, Mo...)) into MN nitrides (M = Cr, V, Mo...) explains the near parallel precipitation of Fe_3C cementite on the nitrided surface. The grain boundaries might be linked to the grain surface depending on the nitriding circumstances. The compound layer can be attached to the grain boundaries.

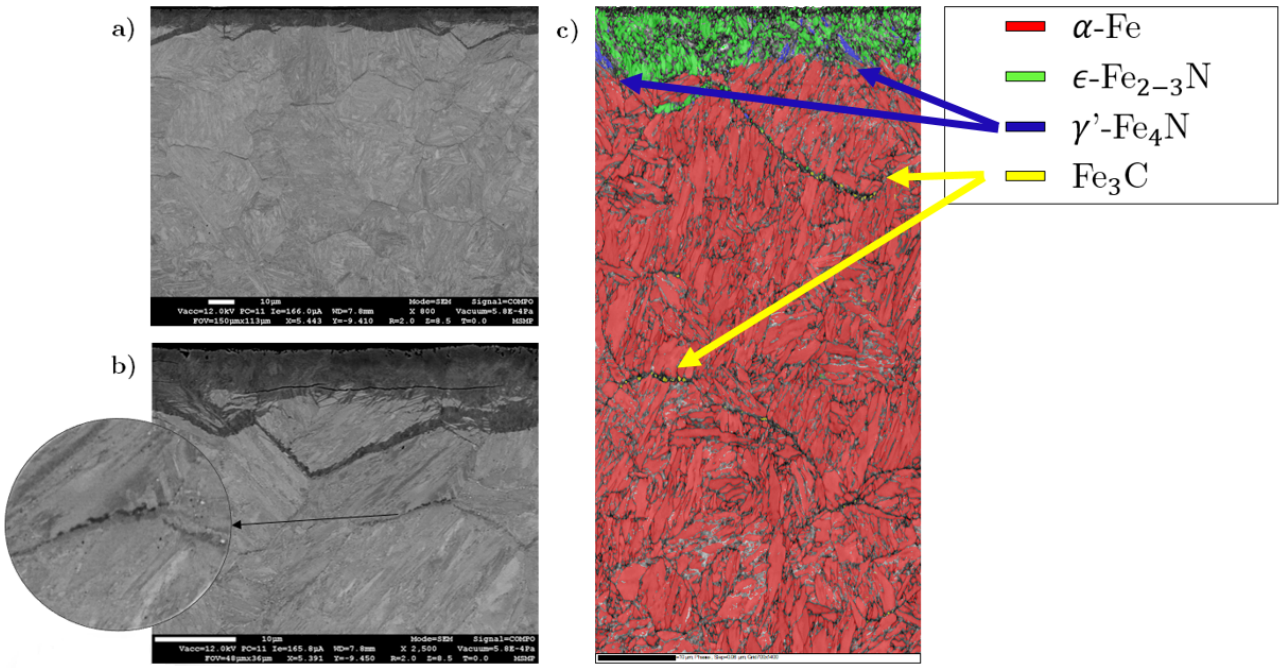

Figure 4.10 – a) BSE image ×800, b) BSE image ×2500 c) EBSD cartography, of 33CrMoV12-9 specimens nitrided simultaneously (S), of 500 μm thick, at 520 °C and 3.711 atm$^{-1/2}$ during 5 h.

Tab. 4.2 shows the average depths, obtained from BSE images, of the compound layer thickness, the depth of the nitride/cementite interface and the depth of the cementite for the two thicknesses sample. The results show a decrease in the compound layer and the nitride/cementite interface of about 20 % and 3 % for the cementite depth, as the sample thickness decreases.

Thickness sample [mm]	Compound layer [μm]	Nitrides/Fe_3C interface [μm]	Fe_3C depth [μm]
5	8,2	21,0	98,5
0,5	6,9	17,9	95,6

Table 4.2 – Average depths, obtained from BSE images, of compound layer thickness, nitride/cementite interface depth and cementite depth for simultaneously nitrided 33CrMoV12-9 samples of thicknesses 5 mm and 500 μm, at 520 °C with K_N= 3.711 atm$^{-1/2}$ for 5 h.

4.2.1.1.1 Discussion The hardness profiles showed similar evolutions, which, to a first approximation, would show that the precipitation mechanisms are comparable. This would imply that the volume percentage of nitrides and the nitrogen content are equivalent between the samples. However, this approximation does not corroborate with the nitrogen profiles which show that the 500 μm sample never returns to zero content and therefore appears to exhibit a double flow effect. Furthermore, the stress profiles showed that the gradient for the thinner sample ends at a greater depth, indicating that the diffusion is deeper, as shown by the evolution of the integral breadth profiles, despite the structural effect.

A correlation between σ_e value on the stress profiles and the overcarburisation on the carbon profiles was confirmed. Furthermore, this overcarburisation could be defined as equivalent to the maximum M_7C_3 carbide

content. Furthermore, it is known that decarburisation and surface enrichment are observable upstream of the nitrogen diffusion front, which is the case in this study.

Concerning the agreement with numerical simulations. The surface stress σ_s showed a similar trend to that observed in the simulations. This value decreases with the decrease of the sample thickness, this is due to the coupling between the mechanical equilibrium and the structural effect (i.e. the dynamic equilibrium). However, the surface point will not be studied throughout this study. The experimentally calculated stresses are those of the ferrite. However, the nitrided sample has a compound layer of about 7-8 μm, which is close to the X-ray penetration depth (5-7 μm). The value of the stress gradient $\frac{\partial \sigma}{\partial x}$ showed an inverse observation with a higher gradient in the thicker sample. This was justified by errors related to stress redistribution during material removal.

4.2.1.2 Effect of self-induced stress

Samples nitrided on one side (F1) were studied to see if the structural effect (i.e. dynamic balance) affects the characteristics (HV0.2 profiles, residual stress profiles, N.%m and C.%m profiles, etc.). Under identical processing conditions, nitrided samples (F1) undergo one-sided diffusion, resulting in asymmetric diffusion, so an asymmetric stress field, all of which causes the sample to bend as shown in Fig. 4.1. This asymmetry leads to the creation of a residual stress gradient, more or less important depending on the thickness of the sample, as shown by the numerical simulations performed in section 3.1.2.2.2.

A metrology probe was used to study the macroscopic reproducibility of the nitriding treatment (F1). The analysis revealed that the acquired curvature is, in fact, spherical. The measurements presented in Fig. 4.11 were carried out on a series between 2 and 4 samples. These results reveal that the standard deviation between each sample is modest (represented by a red standard error line; almost zero), allowing us to state that the method adopted is repeatable, thus proving the macroscopic repeatability of the treatment. Indeed, the calculations were carried out by a python code whose aim was to recover the point cloud obtained by the metrology probe and to pass a least squares function of the equation of a sphere in order to obtain the radius and to compare them. The point cloud is obtained by an affiliation in the form of a grid composed of points every 0.5 mm.

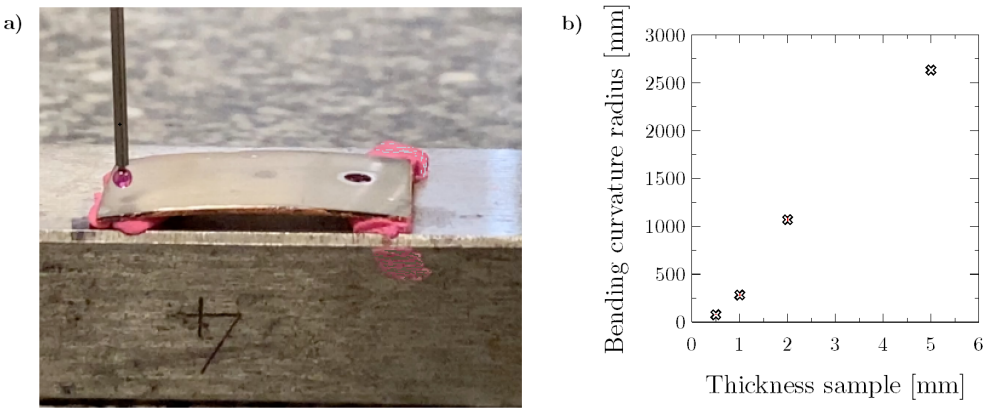

Figure 4.11 – a) Set up of a curvature measurement with a metrology probe. b) Evolution of the curvature radius as a function of the thickness of the sample.

The comparative profiles (S) and (F1) of the calculated stresses and integral breadths for the 5 mm and

500 μm thicknesses are presented in Fig. 4.12a) and b) respectively. The 5 mm sample shows larger values of $\frac{\partial\sigma}{\partial x}$ and $[z_e]$ for the sample (F1) than for the sample (S). For the thinner sample, the profiles indicate a similar progression to the previous study (S), with a deeper $[z_e]$, greater mechanical equilibrium in tensile stress and the position of the maxima z_{max} of the stress profiles comparable between samples (see Tab. 4.3). The integral breadths show that up to 120 m depth, the 500 μm profile appears to have accelerated diffusion.

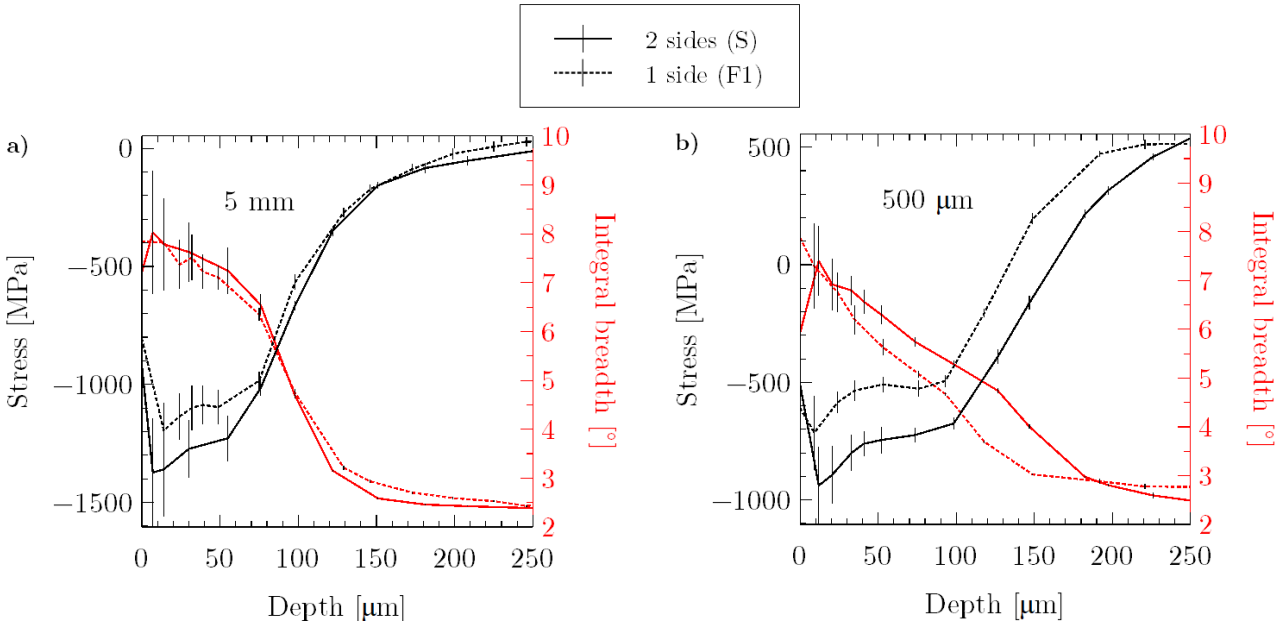

Figure 4.12 – Residual stress and integral breadth profiles of 5 mm and 500 μm one-sided (F1) nitrided samples at 520 °C and 3.711 atm$^{-1/2}$ during 5 h.

Thickness sample [mm]	Stress gradient $\frac{\partial\sigma}{\partial x}$ [GPa/mm]	Gradient range $[z_e]$ [mm]
5	11,2	75 to 146
0,5	9,9	93 to 192

Table 4.3 – Stress gradient and gradient range of 5 mm and 500 μm one-sided (F1) nitrided samples at 520 °C and 3.711 atm$^{-1/2}$ during 5 h.

The computational steps for calculating the analytical profiles of the average stresses estimated from the experimental results of the 5 mm nitrided sample not simultaneously (F1) is presented in Fig. 4.13. These mean stress σ_{mean} calculations are, as before, a function of the stresses in the semi-infinite profile of the specimen $\sigma_{S\text{-}I}$, the sum of the normal forces N_x and the thickness of the selected specimen e, but also of the depth reached z and the sum of the bending moments M_f related to the non-symmetrical profile.

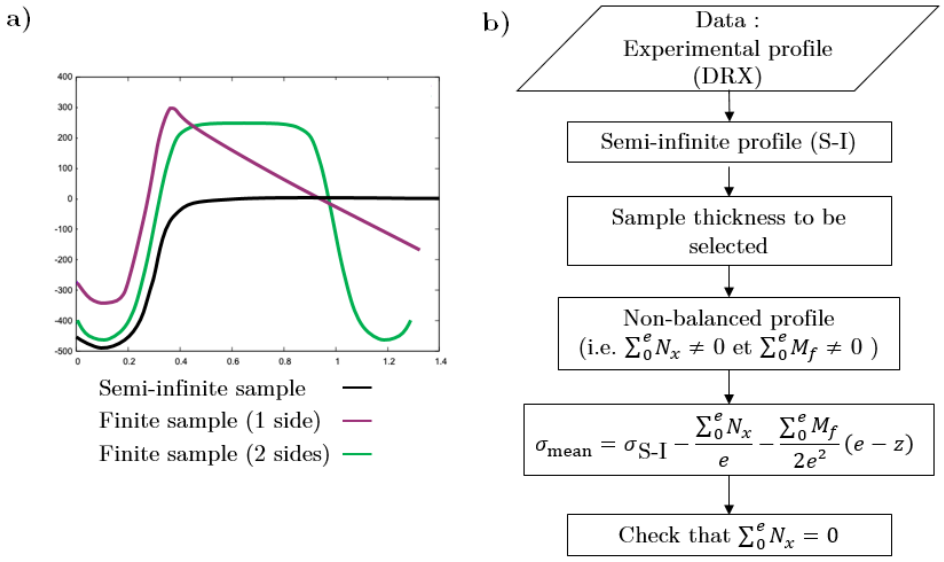

Figure 4.13 – a) Schematic representation of the evolution of balanced stress profiles for a semi-infinite sample, a finite sample undergoing simultaneous diffusion (2 sides) and a finite sample undergoing not simultaneous diffusion (1 side). b) Different steps for calculating the balanced mean stress profile for not-simultaneous diffusion (1 side).

The comparison of the experimental profiles and the analytical profiles estimated from the experimental results of the non-simultaneously nitrided 5 mm specimen (F1) is presented in Fig. 4.14b). These results indicate that the 5 mm profiles have identical $\frac{\partial \sigma}{\partial x}$ values with different peak stress levels, resulting in different mechanical tensile equilibrium.

As before, the analytical profiles in Fig. 4.14b) were multiplied by a multiplication factor to obtain stress maxima. The deviations in Fig. 4.14c) are much larger. The experimental profile shows a strong difference which takes into account two points previously presented which are that the {sample + mounting} is not considered as rigid and also that the analytical profile corresponds to the fact that the profile has the same microstructure as the 5 mm sample. The 5mm sample being considered as semi-infinite thus allows to show that the affected depth is of the order of 5-10 μm, as shown in Fig. 4.14c).

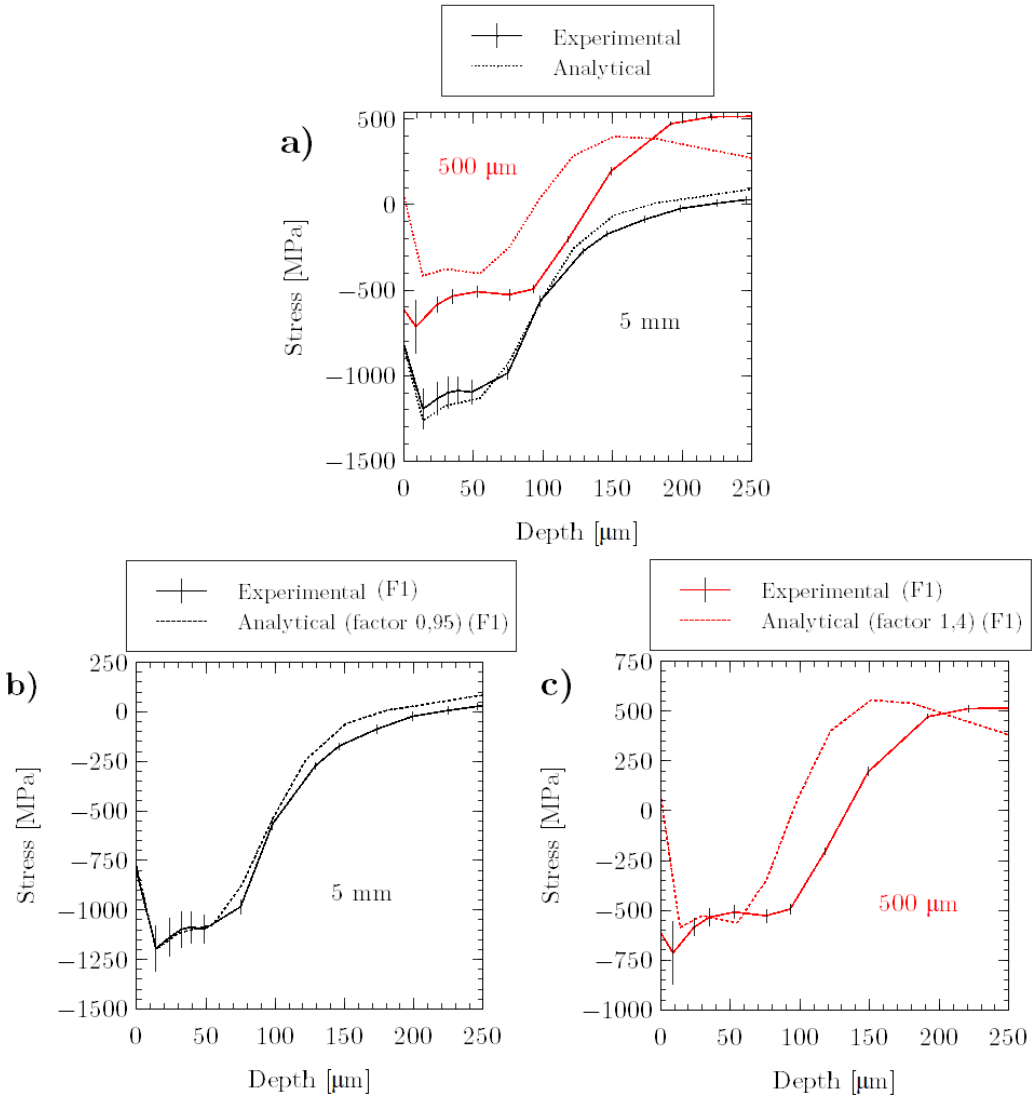

Figure 4.14 – a) Experimental and analytical residual stress profiles of (F1) sample for 5 mm and 500 μm thick sample. Experimental profiles and analytical profiles adjusted by a multiplication factor b) 5 mm (F1) sample and multiplication factor 0.95, c) 500 μm (F1) sample and multiplication factor 1.4.

Fig. 4.15a) shows the superposition of the XRD surface diffractograms for the 500 μm and 5 mm one-sided (F1) nitrided sample. These diffractograms show that the intensity of the peaks is clearly different. The intensity of the peaks of the 500 μm sample except for the γ'-Fe_4N peaks at 58° and 114° is higher than that of the 5 mm sample. These 2θ angle values, chosen by the operator, are specific to the interreticular distances d. These results show that the compound layer is still mainly composed of nitride ϵ-$Fe_{2-3}N$. Fig. 4.15b) shows the comparison of the phase proportions of samples (S) and (F1) for 500 μm thickness. The proportions near the surface are the same, but the progression is different, reaching a percentage of 100% α-Fe at roughly 40 μm of depth.

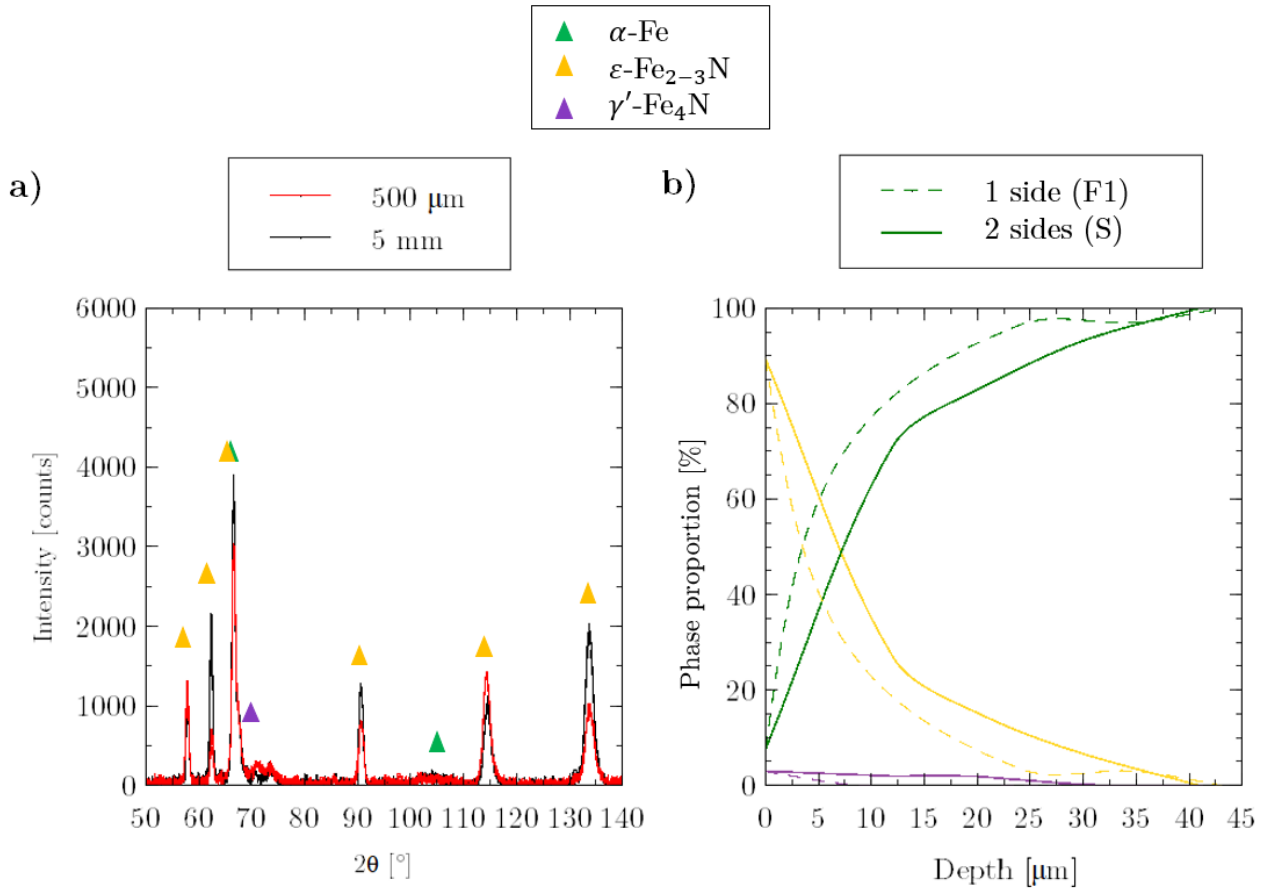

Figure 4.15 – a) Phase diffractogram of samples nitrided at 520 °C and 3.711 $atm^{-1/2}$ for 5 h at 500 μm and 5 mm thickness at the sample surface. b) Phase profiles (α-Fe, ε-$Fe_{2-3}N$ and γ'-Fe_4N) for the 500 μm samples (S) and (F1).

The residual stress gradient $\frac{\partial\sigma}{\partial x}$ and the comparable integral breadths obtained on the opposite side (F1) for the 5 mm and 500 μm specimens are shown in Figs. 4.16a) and b), respectively. The integral breadths confirm that the microstructure is identical with depth. The XRD $\frac{\partial\sigma}{\partial x}$ values reveal that the gradient for the 500 μm sample is significantly larger than the gradient for the 5 mm sample. This is to be expected given the mechanical rebalancing seen in Fig. 4.14, which indicates a rebalancing in the high tensile stresses for the 500 μm sample.

Figures 4.17a) and b) show the residual stress profiles calculated by XRD and the average stresses determined from the 5 mm experimental profile (S) (see section 4.2.1.1). The values of σ_s and $\frac{\partial\sigma}{\partial x}$, calculated experimentally by a diffractometer (i.e. stresses in the ferrite ($\sigma_{11} - \sigma_{33}$)) and analytically (i.e. average stresses σ_{mean}) from the stresses of the 5 mm (S) sample, are presented in Tab. 4.4. The analytical profiles presented correspond to profiles corrected with a multiplication factor of 0.95 for the 5 mm sample and 1.4 for the 500 μm sample. Experimentally, the 5 mm sample has a comparatively modest gradient compared to the 500 μm sample, which is 150 times larger. σ_s values have a ratio of 2.8. Comparing the deviations between the experimental and analytical results, it can be observed that the deviations for the 5 mm sample are small with 10% more for σ_s

value and 18% less for the $\frac{\partial \sigma}{\partial x}$ value. In comparison, the 500 μm sample has 77% and 12% lower values. This 77% difference was expected given the profile differences observed in the figure, where the compressive zone of the experimental sample is significantly wider with a similar stress fit.

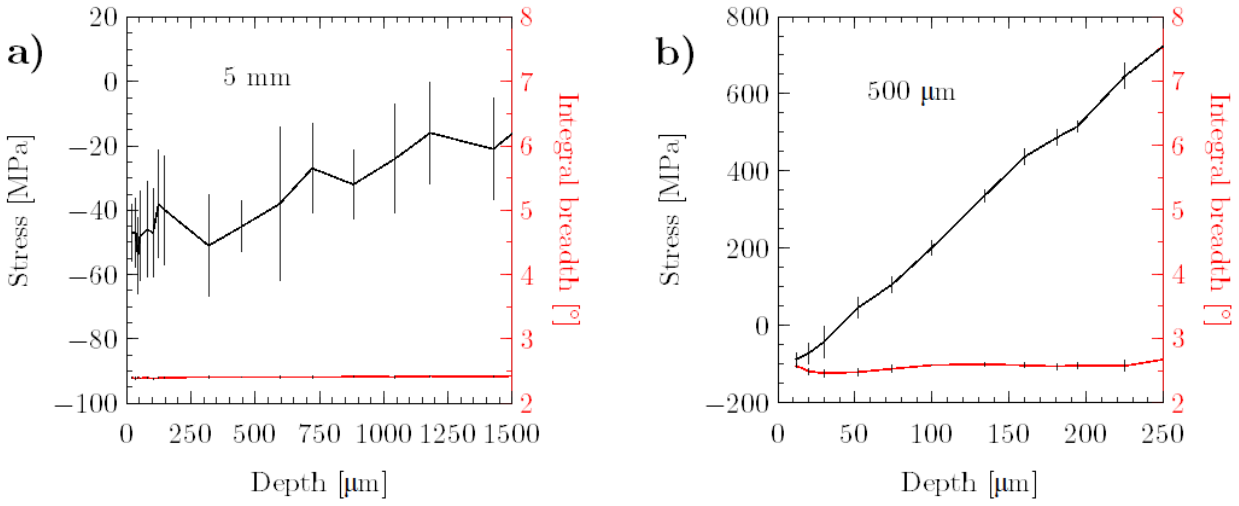

Figure 4.16 – Residual stress and integral breadth profiles of the opposite side of face (F1) a) 5 mm thick sample, b) 500 μm thick.

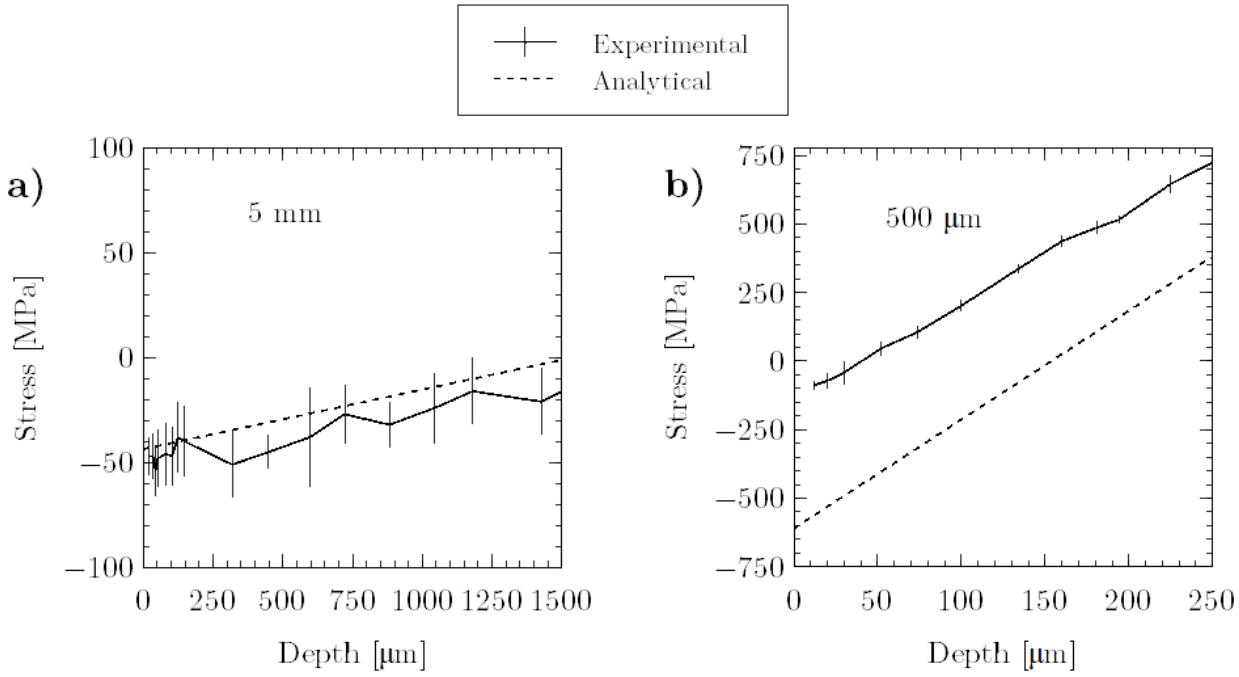

Figure 4.17 – Experimental residual stress profiles and analytical residual stress profiles adjusted by a multiplication factor on the opposite side of face (F1) a) 5 mm sample and multiplication factor 1.1, b) 500 μm sample and multiplication factor 1.4.

	In XRD ($\sigma_{11} - \sigma_{33}$)		σ_{mean}	
	σ_s [MPa]	$\nabla\sigma$ [MPa/mm]	σ_s [MPa]	$\nabla\sigma$ [MPa/mm]
5 mm	- 49	23	-44	28
500 μm	- 138	3460	-610	3953

Table 4.4 – Surface stress σ_s and stress gradient $\nabla\sigma$ values of the experimental XRD profiles ($\sigma_{11} - \sigma_{33}$) and the determined average profiles (σ_{mean}) for the two sample (F1) thicknesses: 5 mm and 500 μm.

Fig. 4.18a) shows the nitrogen and carbon profiles of the 5 mm and 500 μm thick samples. These profiles initially show different nitrogen profiles with a greater affected depth in the case of the 500 μm thick sample. This affected depth is 200 μm deeper. These results of increased long-range diffusion are also observed in the hardness profiles in Fig. 4.18b). Indeed, both results show that the nitrogen and hardness profiles of the 500 μm thick sample would be equivalent to a longer treatment for a 5 mm thick sample. For this purpose, Eq. 4.1 is used to define the time t [s] equivalent to the effective depth z [cm] in function of the coefficient diffusion D [cm^2.s^{-1}]:

$$t = \frac{z^2}{2D} \tag{4.1}$$

It is known that the diffusion coefficient $D_{33CrMoV12\text{-}9\ steel}$ of 33CrMoV12-9 steel at 520 °C is equal to $4.75.10^{-9}$ cm^2.s^{-1} [Jegou et al., 2018]. The effective depth of 500 μm is comparable to an additional treatment time of 2 h 30 min compared to a time of 5 h. To accomplish this depth of diffusion with a 5 mm sample, a nitriding period of 7 h 30 min would be necessary under the same circumstances (K_N and T). These observations compiled with the stress profiles further confirm that there is a structural effect which is directly related to the stress effect, and more specifically to the temporal influence of residual stresses on diffusion kinetics.

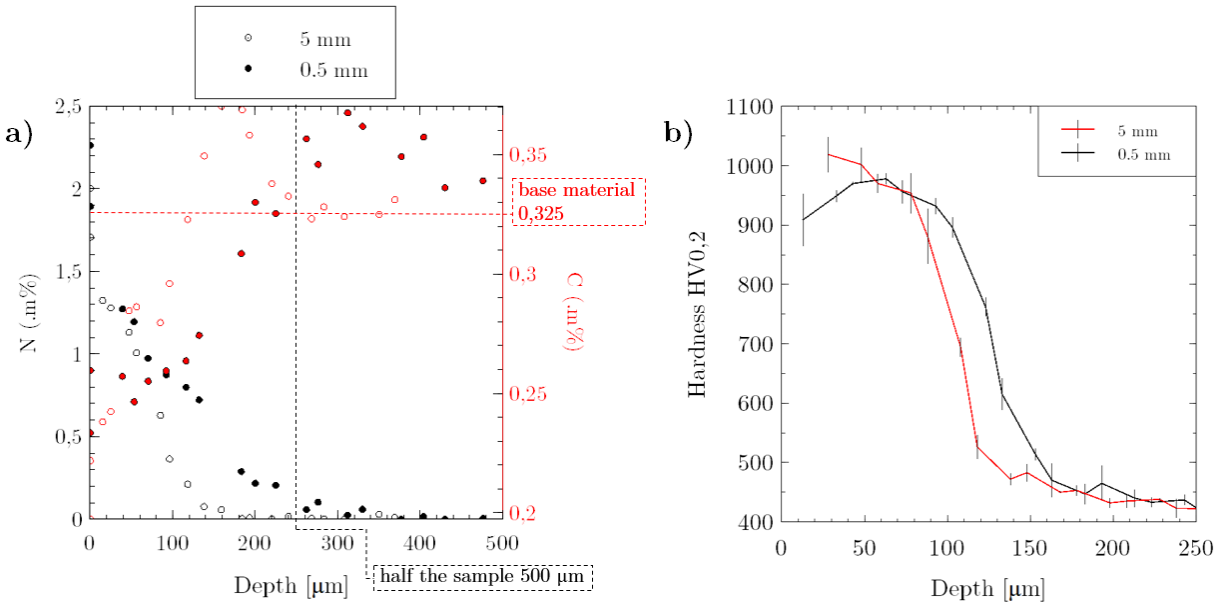

Figure 4.18 – Comparison for 5 mm and 500 μm thick samples of a) nitrogen (N%.m) and carbon (C%.m) profiles, b) Hardness HV0.2 profiles, of 33CrMoV12-9 samples nitrided at 520 °C with K_N = 3.711 atm$^{-1/2}$ during 5 h.

Figure 4.19 shows two BSE pictures and an EBSD cartography (all acquired on the same nitrided sample, 500 μm thick, for 5 hours at 520 °C and Kn = 3.711 atm$^{-1/2}$. The compound layer is dense, as previously, but the EBSD mapping indicates that it is constituted of 98% ϵ-$Fe_{2-3}N$. This EBSD mapping agrees with quantitative XRD results, which demonstrate a low fraction of γ'-$Fe_{2-3}N$ in the compound layer. Tab. 4.5 shows that the average layers (compound layer and nitride/cementite interface) are quite identical. However, the depth of the cementite layer differs by over 10 μm.

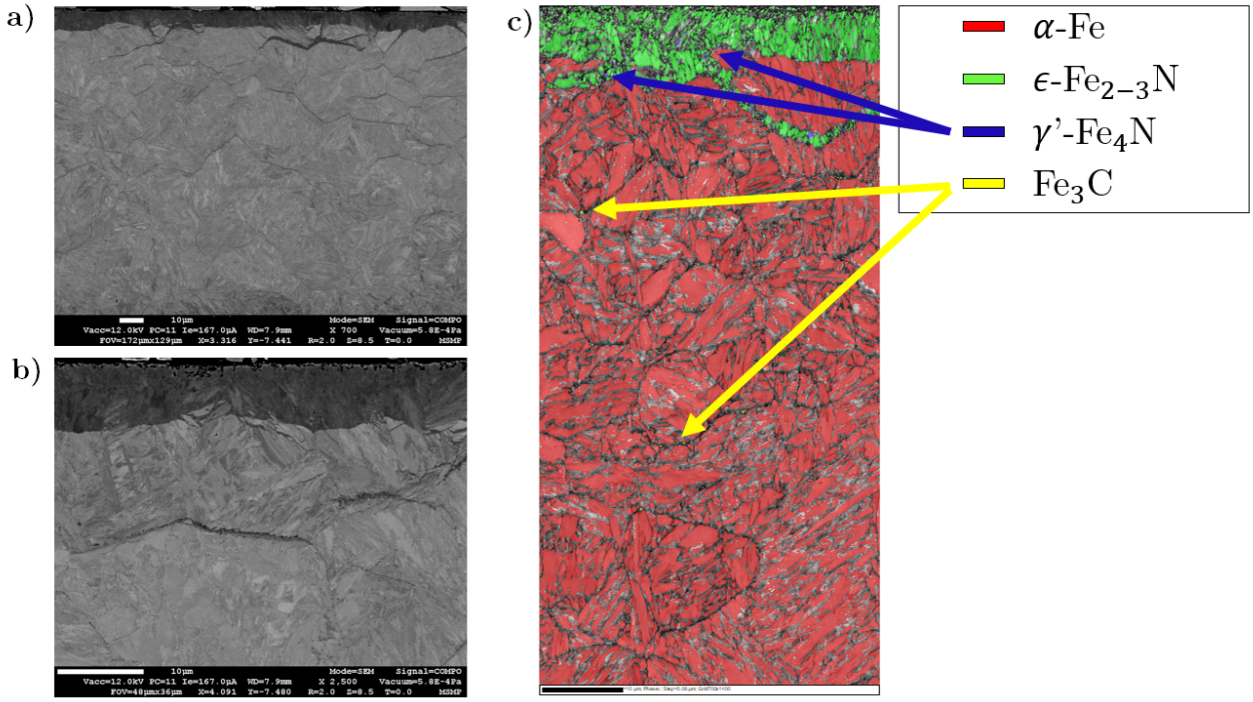

Figure 4.19 – a) BSE image ×800, b) BSE image ×2500 c) EBSD cartography, of 33CrMoV12-9 specimens one-sided (F1) nitrided, of 500 μm thick, at 520 °C with K_N = 3.711 atm$^{-1/2}$ during 5 h.

Thickness [mm]	Compound layer [μm]	Nitrides/Fe_3C interface [μm]	Fe_3C depth [μm]
5	6,9	20,8	97,6
0,5	6,9	20,3	106,6

Table 4.5 – Comparison of average layers (compound layer, the nitrides/Fe_3C interface and the Fe_3C depth) on 5 mm and 500 μm 33CrMoV12-9 steel samples of one-sided (F1) nitrided at 520 °C with K_N = 3.711 atm$^{-1/2}$ during 5 h.

4.2.1.2.1 Discussion The dynamic equilibrium effect has an effect on the long-range diffusion kinetics and the co-diffusion of carbon, according to this study on two samples that have undergone asymmetric diffusion. The temporal effect of residual stresses clearly accelerates and justifies this dynamic equilibrium effect. Indeed, at the beginning of the treatment, where the kinetics are most important, the thinner sample shows a much higher residual stress gradient than the thicker sample.

The following correlations between the hardness profiles, nitrogen/carbon profiles and stress profiles, presented in the first study, were again confirmed.

4.2.2 Stress-induced diffusion

The effects of a stress gradient $\frac{\partial \sigma}{\partial x}$ (here of a residual nature, i.e. elastic strains) on the diffusion kinetics were studied on non-simultaneously nitrided samples (F2). The hardness profiles, associated thicknesses and depths as well as the N.%m and C.%m profiles were compared to a simultaneously nitrided sample (S). The samples (F2) undergo a first one-sided diffusion, corresponding to the diffusion of the samples (F1) presented in Subsection 4.2.1.2. This first diffusion causes an asymmetry in diffusion, which results in a residual stress gradient on the opposite face, more or less important according to the thickness of the sample (see sections 3.1.2.2.2 and 4.2.1.2).

The face with the residual stress gradient acquired after nitriding (F1) is nitrided (K_N = 3,71 atm$^{-1/2}$, t = 5 h, T = 520 °C) to study the impact of this stress gradient on the diffusion kinetics. Fig. 4.20 shows a comparison of the residual stress profiles and integral breadths of the 5 mm and 500 μm thick nitrided samples: (S) and (F2) . The stress profiles show that for the 5 mm sample, the (F2) profile appears to show a minor increase in diffusion, as shown by the integrals breadth profile. For the 500 μm sample (F2), the integral breadth profiles show that the diffusion appears to increase at the beginning of the profile, decrease thereafter and then increases in the core. The stress profiles show that the gradient stress is 7 % higher for the sample (F2).

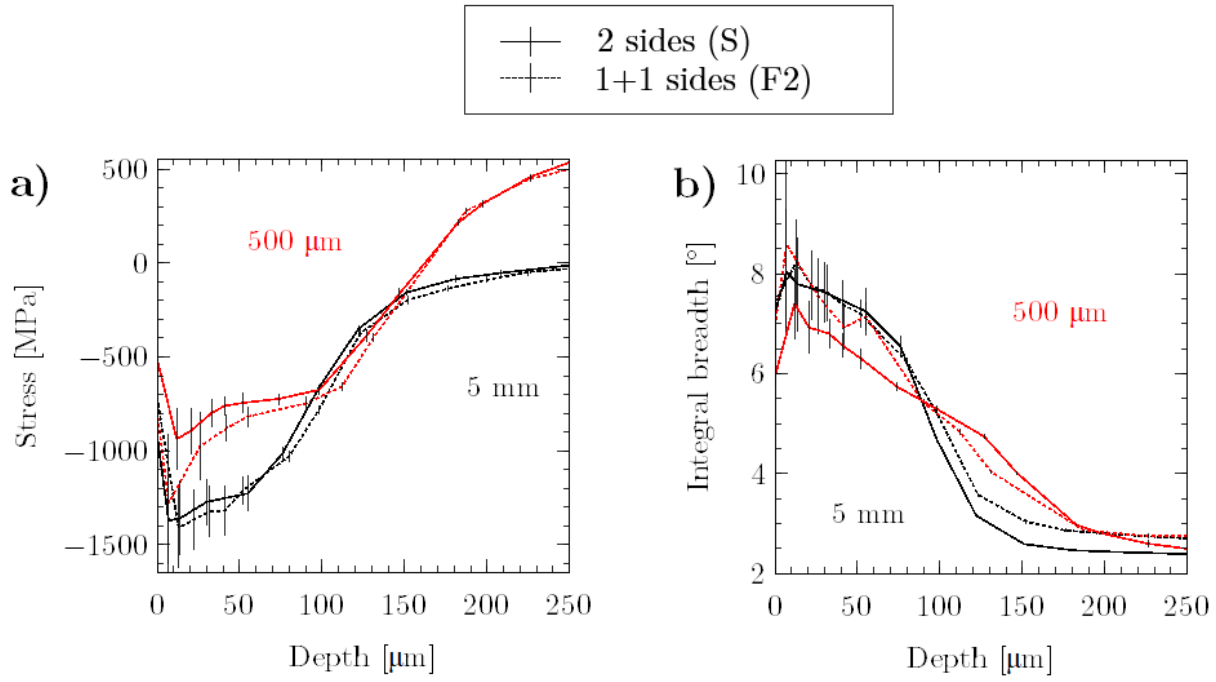

Figure 4.20 – Comparison of residual stress and integral breadth profiles between 5 mm and 500 μm (F2) to 5 mm and 500 μm (S) nitrided samples at 520 °C with K_N = 3.711 atm$^{-1/2}$ during 5 h.

The comparison of the phase diffractogram at the surface of the samples (F2) for the two thicknesses (5

mm and 500 μm) is presented in Fig. 4.21. The diffractogram shows an equivalence between the profiles, and at the surface, the compound layer is otherwise composed of the same proportions of phases. As before, the predominant phase is nitride ϵ-$Fe_{2-3}N$.

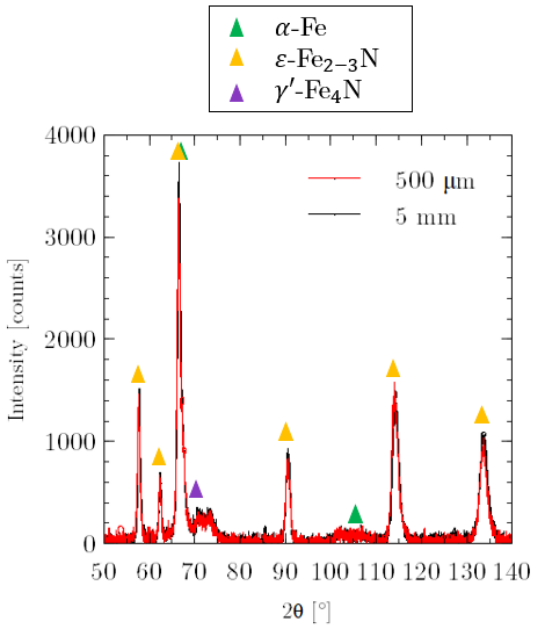

Figure 4.21 – Phase diffractogram of samples nitrided at 520 °C with $K_N = 3.711$ atm$^{-1/2}$ for 5 h at 500 μm and 5mm thickness (F2) at the sample surface.

Fig. 4.22a) and b) are the nitrogen and carbon profiles as a function of depth for the 5 mm thick samples (S) and (F2), respectively. The nitrogen profiles show comparable trends. The carbon profiles clearly show distinct differences. The (F2) profile shows a higher surface decarburisation, less overcarburisation and a lower core content than the base material.

This variation in the development of nitride and carbide depths should lead to a change in mass gain kinetics due to the lower density of nitrides and higher density of carbides compared to that of α-Fe. Fig. 4.23 shows that the evolution of mass gains and their kinetics have little impact. The mass gain kinetics reveal a peak at the beginning of the treatment that can be attributed to the development of the diffusion layer (see section 1.1.2.1) and a decrease that is mainly due to long-range diffusion. The figure shows that the sample one-sided (F1) nitrided shows a slightly higher mass gain (1.5 mg.cm^{-2}) and kinetics than the others. Furthermore, the increase in kinetics occurs after one hour of treatment, confirming the results observed in the hardness and N%m. profile, where long-range diffusion thus appears to be well accelerated. The non-simultaneously nitrided sample (F2) had a lower mass gain than the simultaneously nitrided sample (S) from the first 20 minutes to 4 h of treatment, resulting in a mass gain of the order of (1.49 mg.cm^{-2}) at the end of the treatment.

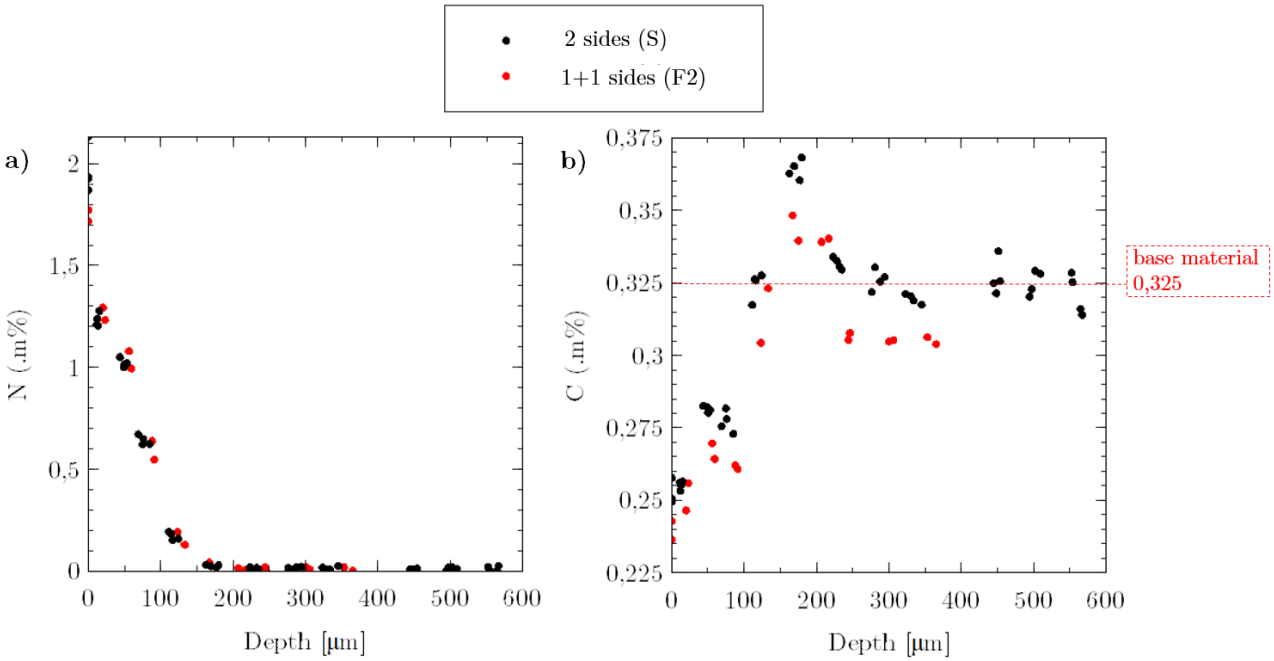

Figure 4.22 – Comparison of a) nitrogen and b) carbon profiles for samples (S) and (F2) of 5 mm thickness.

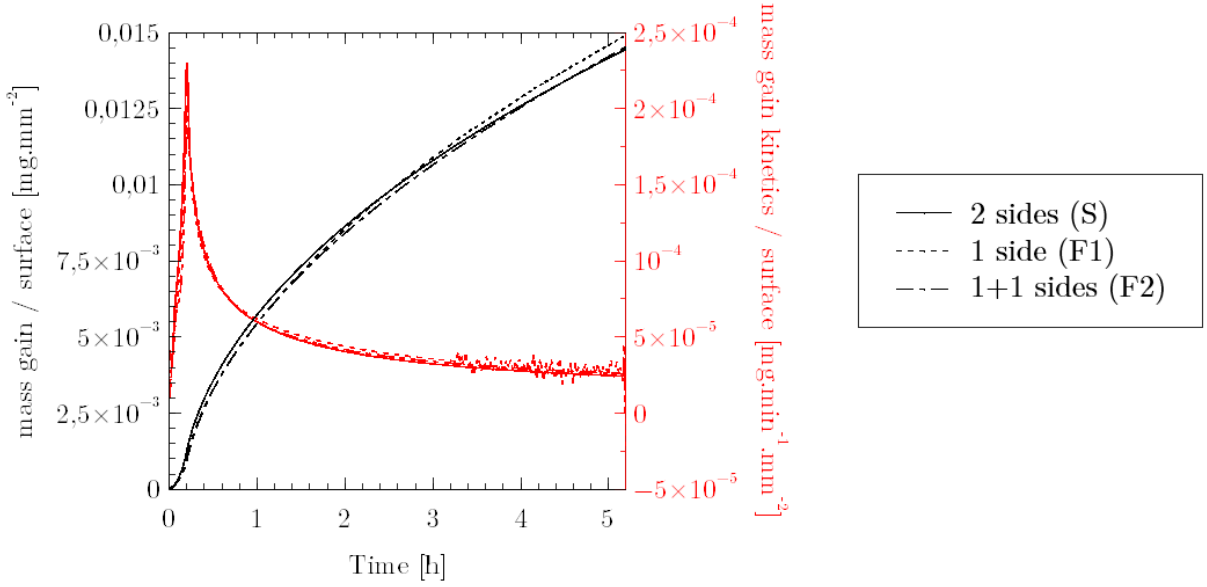

Figure 4.23 – Mass gain and kinetics both normalised to the surface of the three 500 μm samples: (S), (F1) and (F2).

Fig. 4.24 shows the evolution of the nitrogen and carbon profiles between the sample (S) and (F2) for a thickness of 500 μm. Fig. 4.24b) shows the carbon profiles. They show that the profiles are clearly different. Sample (S) shows overcarburisation after half the sample and shows that the sample never returns to its initial

value of 0.325 C.%m). Sample (F2) shows overcarburization in the centre of the sample up to about 0.40 C.%m with a decay due to decarburization during the first nitriding. The nitrogen profiles also show different profiles. Sample (S) shows a nitrogen content beyond the centre of the sample at around 300 μm. Sample (S) shows a nitrogen content of 0.05 N.%m at around 200 μm with an increase in nitrogen up to 500 μm. This increase is due to the first nitriding. This profile shows however that the profile no longer follows an erfc law and has a lower content due to the diffusion that continued without further nitriding.

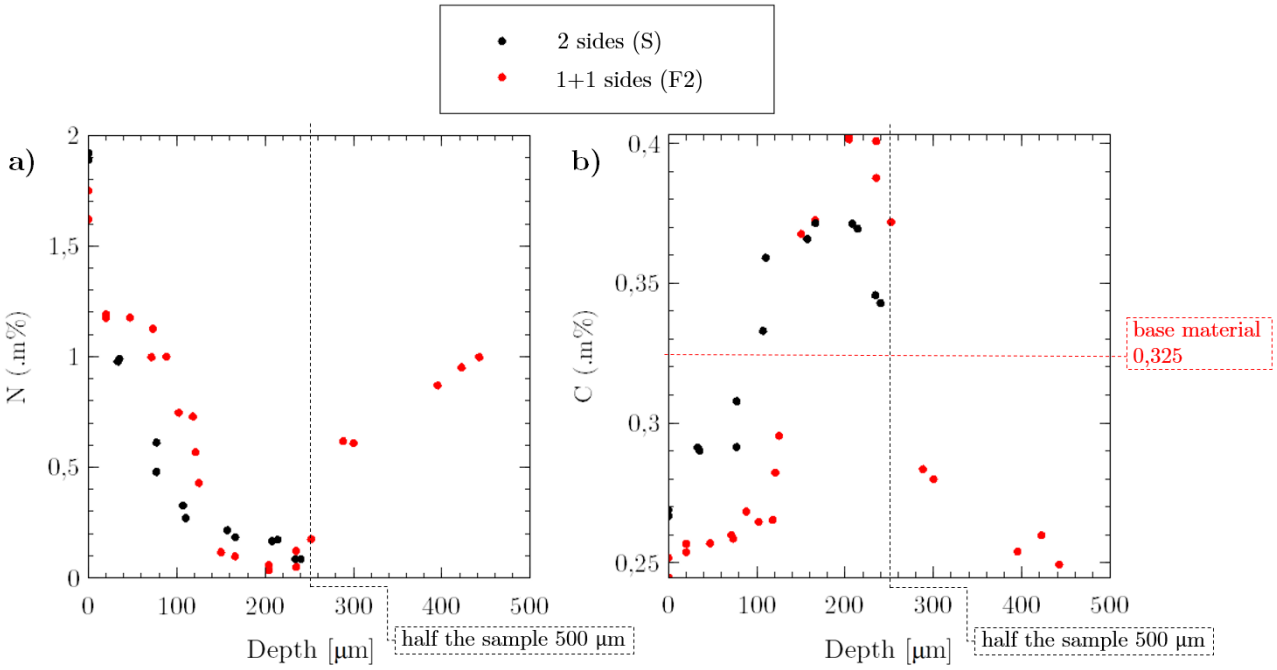

Figure 4.24 – Comparison of a) nitrogen and b) carbon profiles for samples (S) and (F2) of 500 μm thickness.

The evolution of the mole fractions of the different precipitations that can be observed in this type of nitrided steel for the 500 μm (S) and (F2) samples is, respectively, shown in Fig. 4.25. Sample (S) has the most cementite, however sample (F2) has a considerably higher cementite impact depth. It is possible to examine which events correlate with the difference in coverage between the two materials in terms of M_7C_3 and $M_{23}C_6$ precipitation. The $M_{23}C_6$ profile in (S) is significantly more spread out, with a larger maximum value in the centre of the sample. (F2) represents a much more spread out M_7C_3 profile towards the diffusion front, with a much larger maximum at the overcarburization peak.

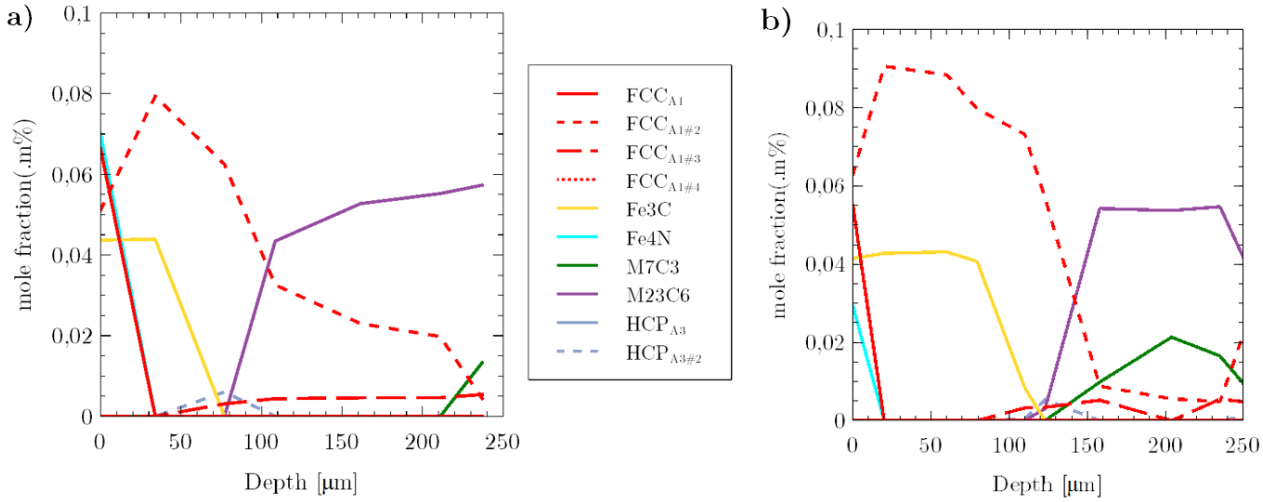

Figure 4.25 – Evolution of the mole fractions of nitrides and carbides obtained in steel grade 33CrMoV12-9 for a) a 5 mm thick (S) nitrided sample and b) a 500 μm thick (F2) nitrided sample.

Two SEM BSE images and EBSD mapping were carried out and are presented in Figs. 4.26a) to c). These results do not present different observations than those of the samples (S) presented in the section 4.2.1.1.

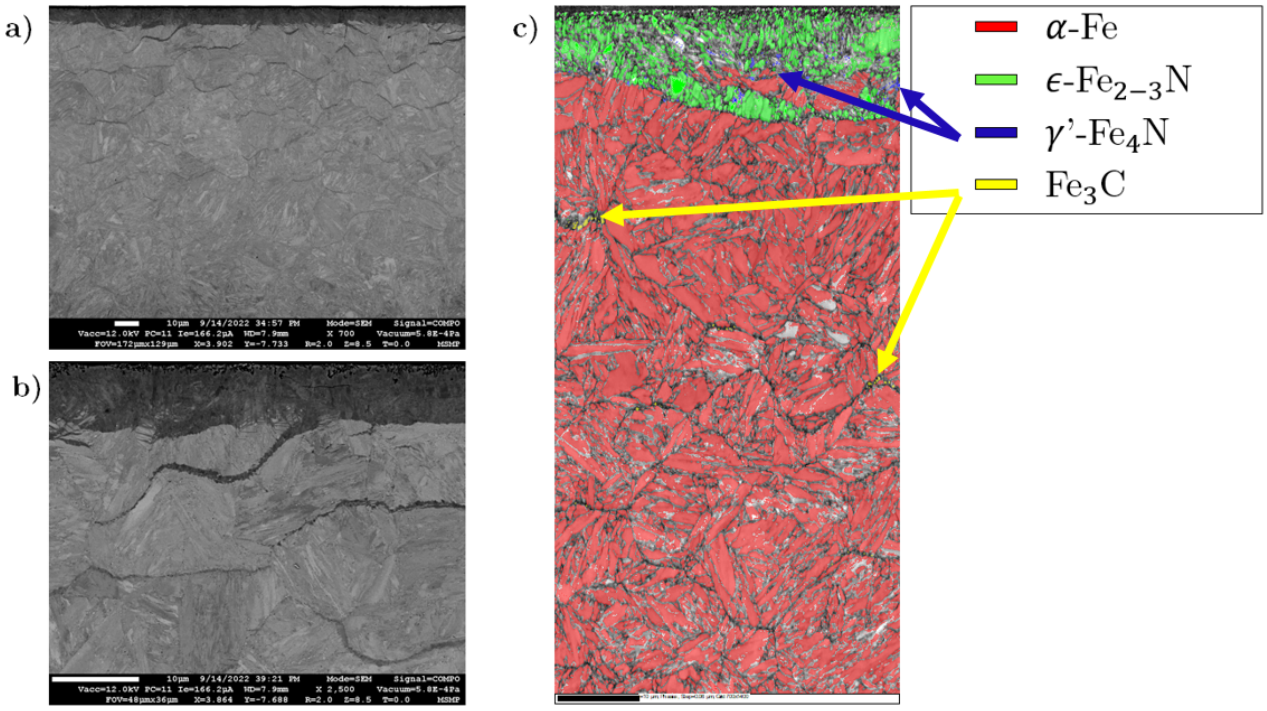

Figure 4.26 – a) BSE image ×800, b) BSE image ×2500 c) EBSD cartography, of 33CrMoV12-9 specimens 1+1 sides (F2) nitrided, of 500 μm thick, at 520 °C with $K_N = 3.711$ atm$^{-1/2}$ during 5 h.

On the other hand, the profiles reveal multiple inflection points. The evolution of the residual stress gradients with respect to space as a function of depth is presented in Fig. 4.27. The profiles have a similar evolution and can be divided into five zones:

— A strong negative gradient at the near surface of the compound layer. The XRD calculations are performed with a maximum penetration depth of 7 microns (approximate thickness of the compound layer) and the stresses calculated are those in the ferrite. Previous quantitative investigations have revealed that the percentage of surface ferrite (α-Fe) is in the order of 8 %,

— A large positive gradient for the first 30 μm, then a decrease,

— A plateau representing the highest stress and the maximum zone of cementite,

— An expansion zone with a plateau, followed by a decrease zone correspond to the surcarburisation zone,

— A decrease zone to a zero derivative.

Fig. 4.27 shows that a (small) difference exists between the two samples. A higher stress gradient is observed for the sample that has undergone "1+1 side" nitriding.

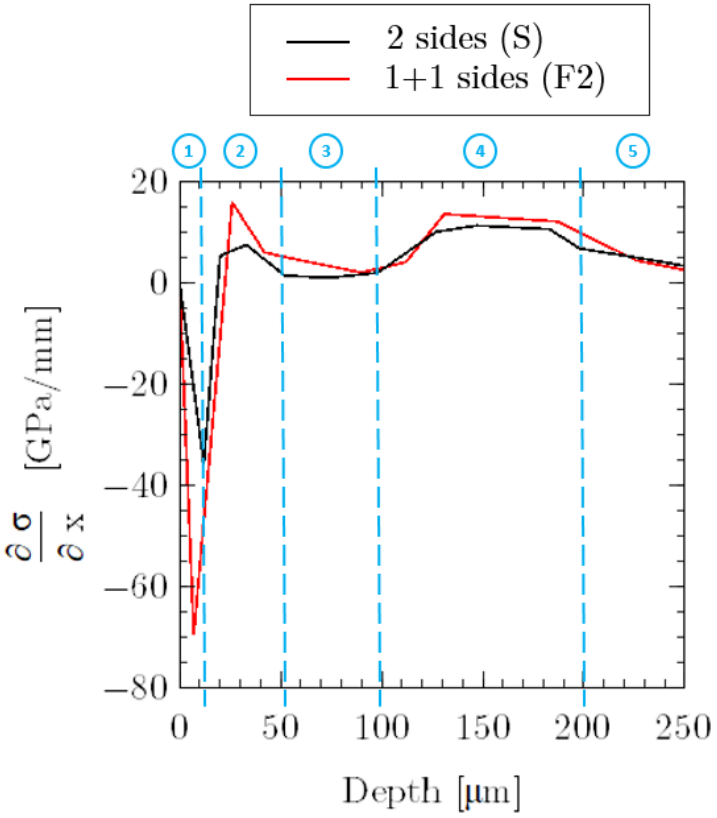

Figure 4.27 – Comparison of the evolution of the experimental residual stress gradient (data from Fig. 4.20) as a function of depth for the 500 μm samples (S) and (F2).

Fig. 4.28 shows two BSE images and an EBSD map of the opposite face of a non-simultaneously nitrided sample that has undergone nitriding and post-nitriding tempering. Comparing to Fig. 4.26, it can be seen that

the compound layer has almost completely dissociated, there is some α-Fe on the surface and the cementite has advanced to the surface. In reality, this corresponds to post-nitriding tempering at zero nitrogen flow, so the treatment continues. A decrease in surface nitrogen concentration has been linked to an increase in depth, [Barrallier, 1992, Ginter et al., 2006]. This effect is explained by the loss of iron atoms from the nitrides of the alloying elements during tempering, allowing the nitrogen atoms to diffuse.

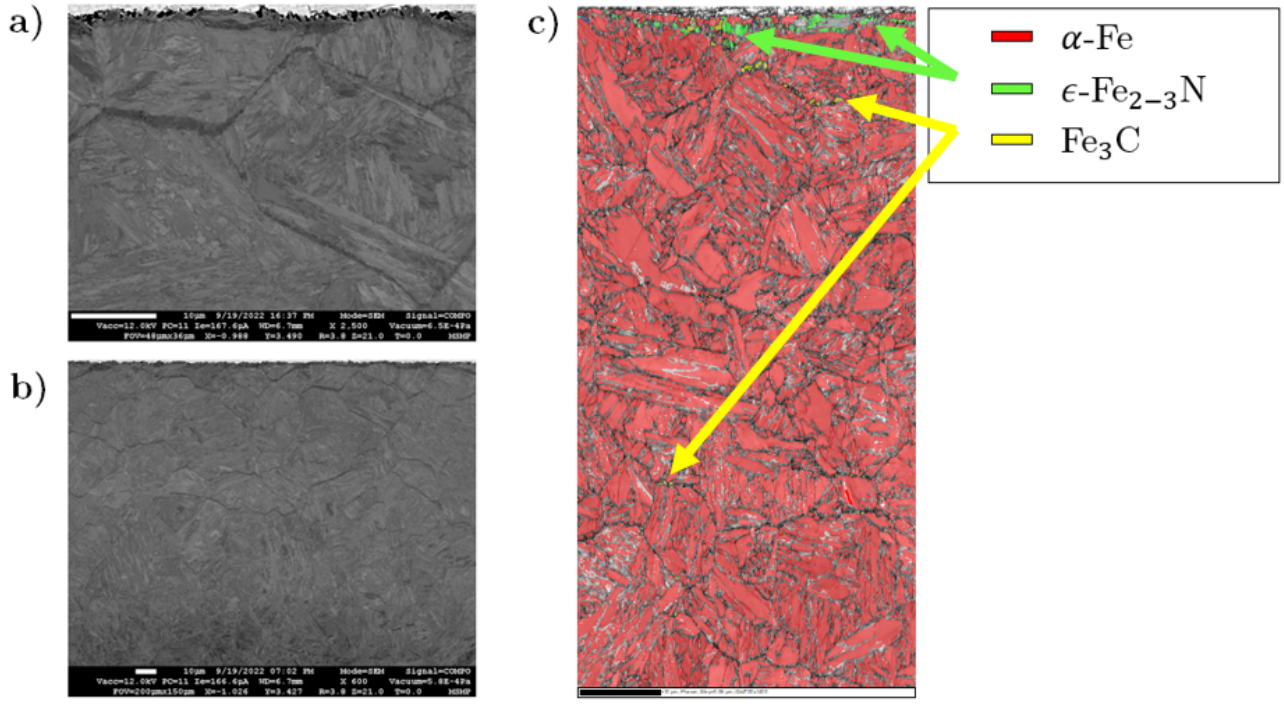

Figure 4.28 – a) BSE image ×800, b) BSE image ×2500 c) EBSD cartography, of 33CrMoV12-9 specimens, the opposite side of an 1+1 sides (F2) nitrided, of 500 μm thick, at 520 °C with $K_N = 3.711$ atm$^{-1/2}$ during 5 h.

Fig. 4.29 shows a decrease in surface hardness of the "1 side + 1 time tempering" sample. This is due to a decrease in the volume fraction of the nitrides of the alloying elements due to the loss of iron. It should be noted, however, that despite the loss of surface hardness, post-nitriding tempering results in a significantly greater effective depth. Fig. 4.29a) shows that in the case of one sample (opposite side F2) the increase in effective depth is of the order of 50 μm over an effective sample depth (S) of 130 μm. The impact of post-nitriding tempering for both sample thicknesses can be seen in Fig. 4.29b). This observation shows that the diffusion is strongly increased in the 500 μm sample.

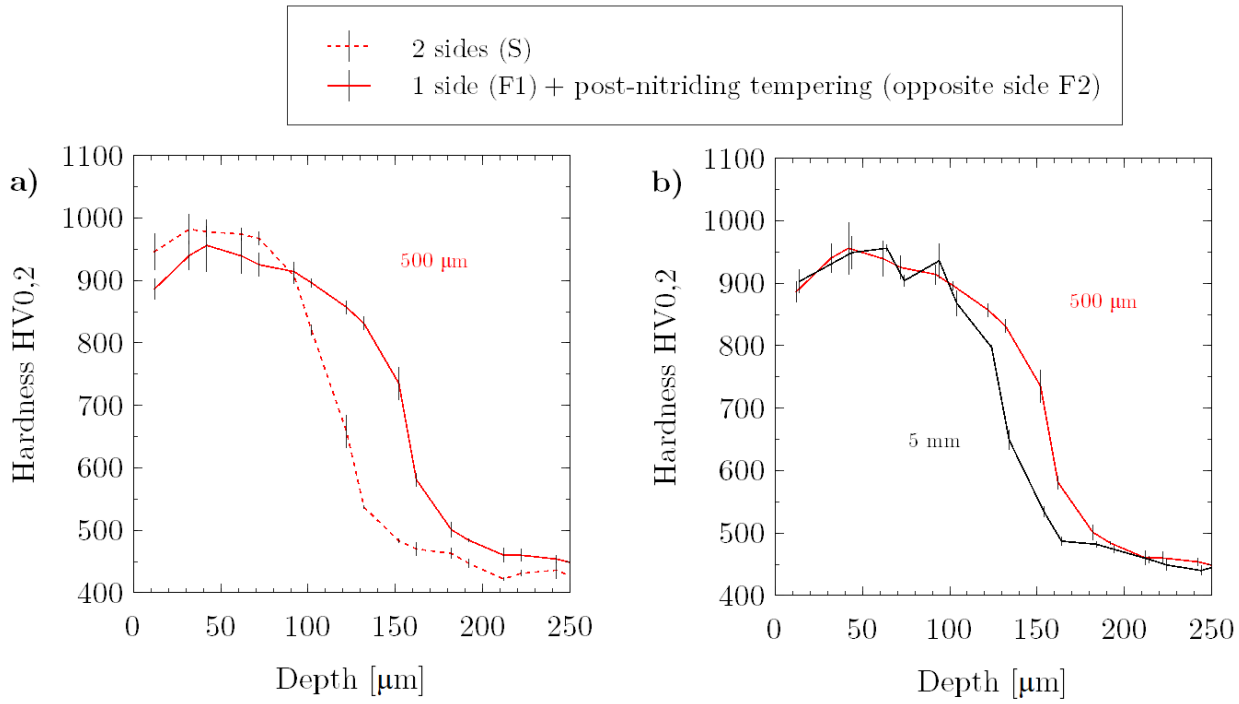

Figure 4.29 – Comparison of the HV0.2 hardness profiles of 33CrMoV12-9 samples nitrided at 520 °C and 3.711 $atm^{-1/2}$ for 5 h. a) comparison of one sample (S) and one sample (opposite side (F2)) for the 500 μm thickness. b) comparison of the profiles (opposite side (F2)) for both thicknesses (5 mm and 500 μm)

The objective of this study is to see the effect of a stress and a stress gradient on the diffusion. To do this, the aim is to observe the effect of the $\frac{\partial \sigma}{\partial x}$ value (driving force) and/or the stress amplitude (mobility) by comparing the 500 μm sample (F2) with the 5 mm sample (S). Corresponding hardness profiles are presented in Fig. 4.30a). These profiles show variations in the effective depth and a difference in core hardness, the latter leading to the assumption of a non-zero core nitrogen content. Indeed, the core nitrogen concentration for the 50 μm sample is 0.05 N%m., as illustrated in Fig. 4.30a). Thanks to Eq. 4.1, the equivalent time through the effective depth are compared. This difference in depth shows the opportunity to reduce the treatment time by 50 minutes compared to an initial time of 5 hours.

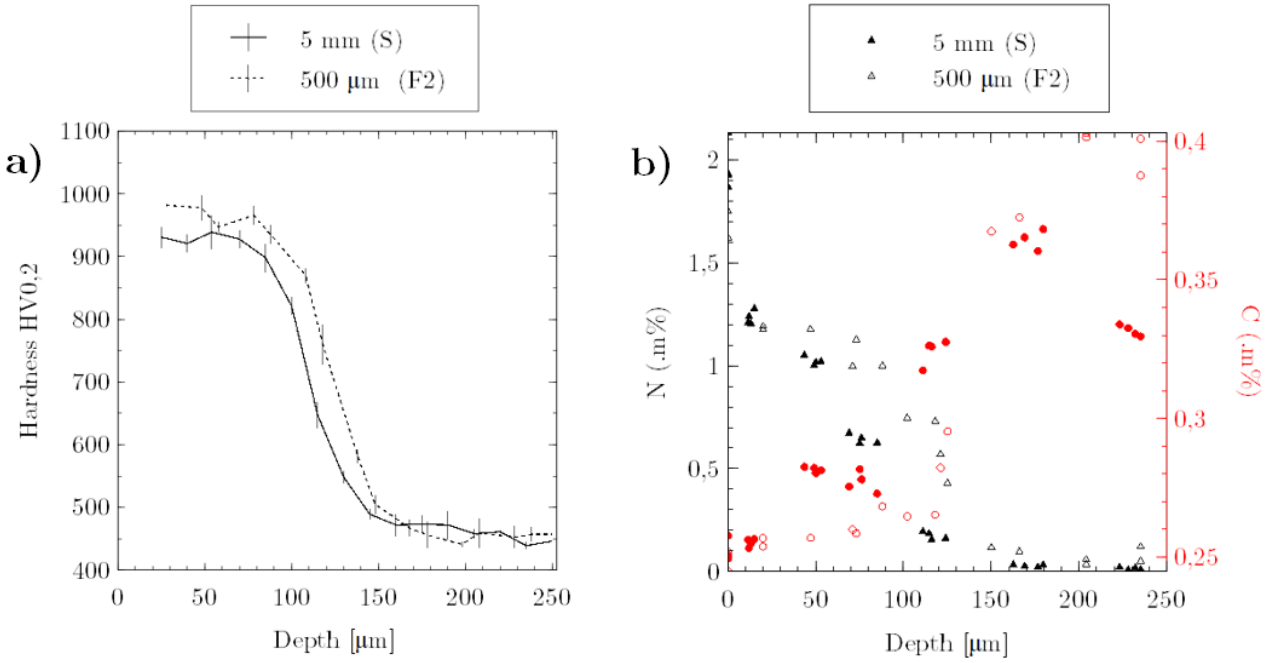

Figure 4.30 – Comparison of a) hardness and b) nitrogen and carbon profiles of 5 mm (S) and 500 μm (F2) samples.

4.2.2.1 Discussion

The objective of this research was to study the impact of a residual stress gradient obtained by asymmetric diffusion. This is a positive residual stress gradient with a negative σ_s value. The research was divided into three sub-studies, each comparing two sample thicknesses by a factor of ten: 5 mm and 500 μm.

The first study found that mechanical equilibrium of a simultaneously nitrided sample (S) showed no significant effect on hardness but did show differences at the end of the diffusion layer in the nitrogen and carbon profiles. This leads to differences in the stress profiles. However, these analyses are associated in the first approximation with a nitriding of the core due to a too long time. The EBSD mapping and SEM BSE observations revealed that the compound layer is mainly composed of 95-98% of ϵ-$Fe_{2-3}N$. It was also observed that its thickness is not constant along the sample.

A second study examined how the structural effect (i.e. dynamic equilibrium) affected an asymmetrically nitrided sample. The hardness, nitrogen and carbon profiles were found to be significantly different. The long range diffusion kinetics are significantly accelerated. In addition, the carbon profiles show significantly different profiles, with a significantly larger overcarburization zone on the thin sample side. The time effect of residual stresses clearly accelerates and justifies this dynamic equilibrium effect. This effect showed that for this grade of steel and under these treatment conditions, the treatment times could be reduced by 2.5 hours.

In a third study, several phenomena were observed:

1. The (S) and (F2) profiles were compared:

   — 5 mm samples: The hardness profiles and the nitrogen profiles have a similar profile. In contrast, the

carbon profiles reveal that sample (F2) has less core carbon and more surface decarburisation than the base material. Based on these results, the observed over-carburization corresponds to the highest carbide content M_7C_3. In addition, the cementite zone at the surface increases with decarburisation,

— 500 μm samples: The nitrogen profiles clearly demonstrate an enhancement in the long-range diffusion of nitrogen. The carbon profiles of sample (F2) show deeper overcarburization and higher surface decarburization. The carbon profiles of samples (F2) showed a considerable shift in the carbon profile with a content that did not return to the initial content of the base material, which helped to explain the overcarburization. The mass capture kinetics supported the dominance of long-range diffusion by showing that the diffusion kinetics of sample (F2) improved towards the end of the treatment.

2. The 5 mm (S) and 500 μm (F2) profiles were then compared to see how the stress gradient (here of a residual nature) affected the diffusion kinetics. In the case of two additive stress fields, the residual stress gradient (F1) added to the residual stress gradient (F2) during nitriding appears to result in a significantly larger residual stress gradient. This strong gradient would therefore seem to play an important role in the diffusion kinetics. Due to the evolution of the residual stresses at each time point, numerical simulations revealed that the shorter the diffusion period, the larger the diffusion-related residual stress gradient, as shown in Fig. 1.15. This means that, unlike a continuous load during the treatment, the residual stress gradient (F1) will not remain constant over time t. Therefore, it will play an increasingly insignificant additive role during treatment. Numerical models have shown that a larger stress gradient is required to have an effect on long-range diffusion. Furthermore, that the effects are strongest in the first few seconds after treatment. This residual stress gradient (F1) is therefore expected to be large in the early stages of the treatment, when kinetics are at their maximum. These interpretations are therefore consistent with the results obtained. The 5 mm sample through a low residual stress gradient (F1) of about 30 MPa/mm shows very little difference with the double-sided nitrided sample (S). Profiles on the 500 μm sample revealed that a residual gradient of 3.5 GPa/mm and a compressive σ_s value of - 140 MPa had a positive effect on the long-range diffusion kinetics. These orders of magnitude for this grade of steel and these treatment conditions, would therefore allow a reduction in treatment time of 50 minutes. This result indicates that the effect of the positive stress gradient (driving force) outweighs the effect of negative stresses (mobility),

3. The effect of post-nitriding tempering (treatment without nitrogen flow) was studied. According to the nitrogen and hardness profiles, the surface hardness decreased while the effective depth increased. These phenomena are known and explained by the fact that the diffusion processes are thermally activated. According to Fick's law, the flow strives to reach a thermodynamic equilibrium, i.e., the diffusion moves from more concentrated areas to less concentrated areas. This phenomenon is explained by the loss of iron atoms during the tempering of nitrided alloying elements, which allows nitrogen atoms to disperse. This loss of iron atoms was observed in SEM and EBSD mapping, which shows the dissociation of the compound layer, which is replaced by ferrite, but also by a cementite front that moves towards the surface.

4.2.3 Applied stress

An investigation into the effect of a stress gradient on diffusion kinetics was conducted. A split ring (see Fig. 4.31) was subjected to displacement, in order to obtain a stress field that could be represented as a bending test. The aim of this study is to compare the tensile side with a negative stress gradient to the compressive side

with a positive stress gradient as presented in Fig. 4.32.

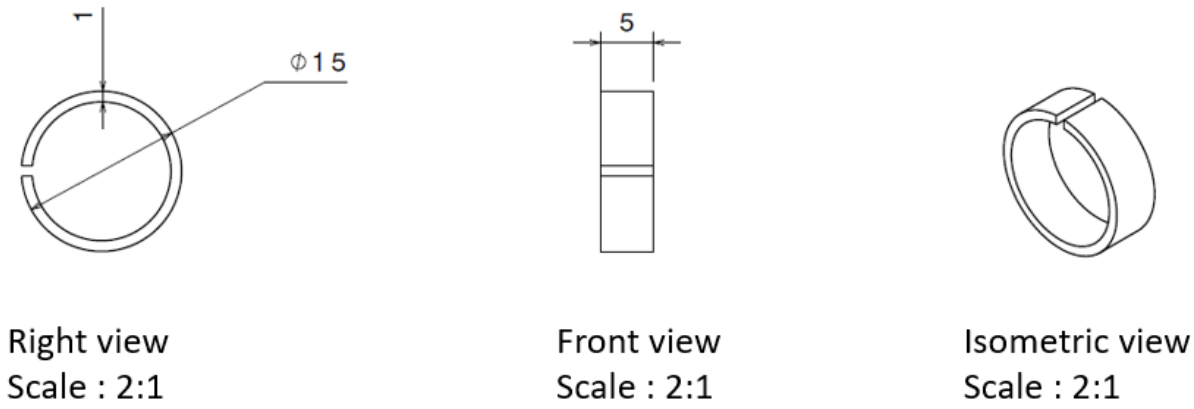

Figure 4.31 – Technical drawing of the split ring (in mm).

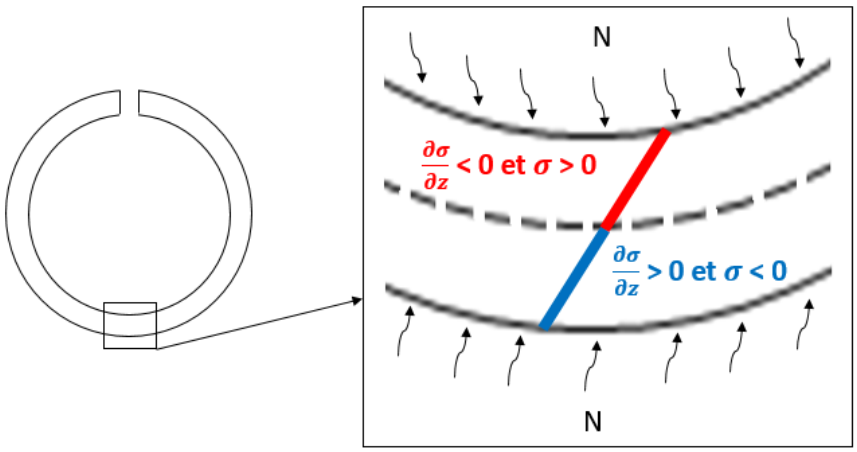

Figure 4.32 – Diagram of the stress fields seen by the diffusion on the tensile side in red and on the compressive side in blue.

The aim is to distinguish between the influence of stress on mobility and the effect of a stress gradient. The thermogravimeter has a small footprint (18 mm diameter and 30 mm length) and a maximum weight (30 g) that should not be exceeded. Due to the tiny sample size, only hardness testing, phase analysis, stress analysis and BSE images can be compared. In contrast to previous research, the stress field is an applied field that does not evolve at each time t for any neglected creep source.

Several prior investigations were conducted to ensure the experiment's validity:

— examination of the sample's surface condition post machining,

— investigation of creep,

— investigation of the stress field concomitant with the applied displacement.

4.2.3.1 Residual stress state after machining study

A first study was to analyse the rough state after machining of the accessible surface by XRD which corresponds to the external surface which will be in compressive. This study led to the creation of a particular support made in 3D printing, in order to ensure the horizontal position of the sample on the diffractometer. Fig. 4.33 shows the schematic assembly on the diffractometer. The aim of this assembly is to fix the 3D printed support to the diffractometer and to hold the ring in place with a set (screw + nut + washer) in order to ensure the flatness of the sample and its good fixation during the rotation of the sample at $\phi = 90$ °. The study focused on the calculation of circumferential and axial stresses.

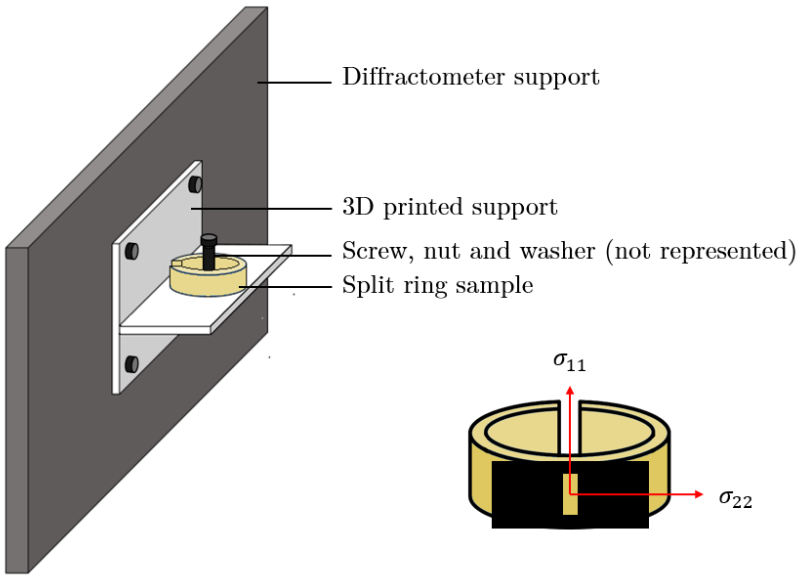

Figure 4.33 – Diagram of the setup used to hold the split ring during stress analysis by XRD.

Tab. 4.6 shows the example of stress data obtained on a raw ring after machining. These results show that machining causes significant residual stresses and plastic strains, as observed in the literature. The aim of this effort is to prevent any source of plastic strain in order to dissociate the consequences according to the type of strain. These results led to the use of electrolytic polishing to remove the impacts of machining (i.e. surface hardening). This involves immersing the sample in an A2 electrolyte liquid and transmitting a current between an anode (sample) and a cathode (metal component) for a predetermined time. The example of stress data acquired on a ring after removing 15-20 μm in each side by electropolishing is shown in Tab. 4.6. These results show an insignificant stress state compared to the expected stresses when the sample is loaded.

	σ_{11} [MPa]	± [MPa]	σ_{22} [MPa]	± [MPa]
raw state	-332	21	-19	26
electropolishing state	-15	11	-9	8

Table 4.6 – Surface stresses on the compressive side of a raw ring sample after machining and after electropolishing.

4.2.3.2 Creep study

According to the studies, this grade of steel does not show creep [Jegou et al., 2018]. However, preliminary research has been carried out to confirm or not this phenomenon on the rings. Two studies were conducted for this purpose, one at room temperature and one at elevated temperature. The temperature sample showed no difference against a lowering of 80 MPa in the case of the high temperature sample. This preliminary study allowed for an additional stress relieving tempering step under neutral gas of the sample loaded at nitriding temperature during the nitriding time in order to relieve possible machining stresses.

4.2.3.3 Mechanical-Thermal study

4.2.3.3.1 Abaqus model. A finite element model on Abaqus is carried out to determine the imposed displacement required to achieve maximum stresses of approximately ±900 MPa. This stress value is intended to remain in the elastic range of the material and thus avoid any source of macroscopic plastic strain. The model is based on the elastoplastic law identified and presented in section 2.3.2 and with a Young's modulus of 202 GPa and a Poisson's ratio of 0.29.

The finite element model takes into account a general step with a time of 1 s and 1000 time increments was performed for this purpose. The boundary conditions are an embedded edge ($U_x = U_y = U_z = UR_x = UR_y = UR_z = 0$) and a pressurised edge P (see Fig. 4.34). In order to guarantee the circular opening of the ring and not to restrict it in one direction, it was indeed impossible to apply a displacement directly. The study then used Abaqus to calculate the displacement of the nodes in order to define the displacement using the inverse approach. The ring is meshed with C3D8R i.e. an 8-node linear brick, reduced integration, hourglass control. The mesh size is 0.1 mm in order to have 10 elements along the ring thickness.

In parallel, a thermal study was carried out to determine analytically the extent of material expansion at 520°C. For this, the linear law of thermoelasticity is applied: $\varepsilon = \alpha.\Delta T$, where $\varepsilon = \frac{\Delta L}{L}$ is the strain [-], ΔL is the elongation, L is the total length of the sample, α is the thermal expansion (= 13,6. 10^{-6} [K^{-1}]) and ΔT (= 500 [°C]) is the temperature variation. The calculations are carried out assuming that the ring is unrolled, so $L = 2\ \Pi r$ where r is the radius of the ring (= 7.5 mm). The elongation is therefore $\Delta L = 0.32$ mm.

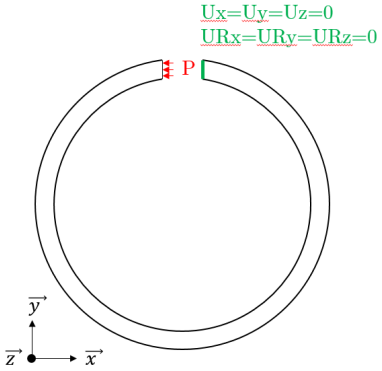

Figure 4.34 – Boundary conditions of the finite element model.

Fig. 4.35 shows the boundary conditions of the finite element model. The final and validated study is for an imposed displacement of 2.3 mm i.e. a spacer thickness of 3.0 mm. This displacement shows a stress gradient of 1.8 GPa/mm with surface stress values of 874 MPa on the tensile side (i.e. the inner circle of the ring) and -796 MPa on the compressive side (i.e. the outer circle of the ring). These gradients show that the circumferential stress is not symmetrical. This is justified by the fact that the polar coordinates are different and therefore the circumferential stresses due to the opening angle of the ring are different.

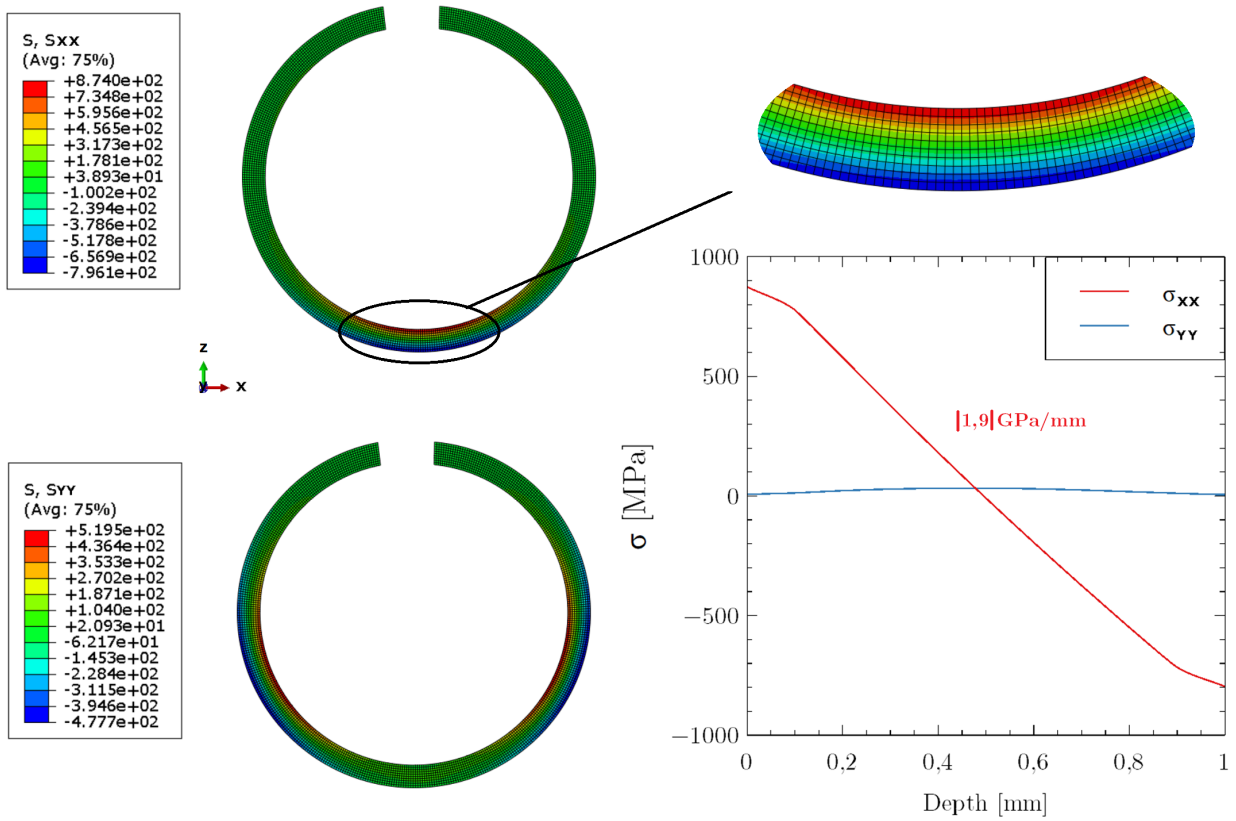

Figure 4.35 – Stress field (σ_{xx} and σ_{yy}) on the ring section obtained on ABAQUS. Stress state profiles (σ_{xx} and σ_{yy}) along the thickness of the ring.

4.2.3.3.2 Correlation between numerical and experimental results. The objective is to experimentally validate this stress state by comparing it with the results obtained by the finite element method in ABAQUS (see section 4.2.3). The applied stress gradient cannot be observed due to the complexity of the sample and the equipment available in the laboratory. Therefore, only the surface stress state σ_s value on the compressive side is studied. The split ring was subjected to a displacement of 2.3 mm from a 3.0 mm thick wedge. Tab. 4.7 summarises the data for a ring under stress. The experimental values were obtained by the DRX method as presented in subsection 4.2.3.1.

	σ_{xx} [MPa]	± [MPa]	σ_{yy} [MPa]	± [MPa]
Experimental results	- 833,9	15,2	- 60,3	- 1,9
Numerical results	- 796.1	-	5.3	-

Table 4.7 – Experimentally obtained surface stresses on the compressive face of a split ring specimen subjected to a displacement of 2.1 mm.

For σ_{xx}, the values have a deviation of 5 %. Experimentally, it is not possible to calculate the stress on the tensile face of the face. It is assumed that numerically and experimentally the ratio between the two tensile/compressive surfaces is the same. Therefore, the tensile stress value would be 915 MPa. This

value indicates that the specimen remains in its elastic range (the material's yield strength is 1082 MPa). An unloading study also confirmed that the specimen does not plastify.

4.2.3.4 Nitrided study

The rings were nitrided for 5 hours at 520 °C in a nitriding environment $K_N = 3.711$ atm$^{-1/2}$.

The complexity of the study stems from the choice of analyses to be made in order to gather as much information as possible from a single ring and thus draw conclusions. Unlike parallelepipedic samples, rings do not allow the sample to be divided into several parts with identical behaviour. A single zone allows to observe the influence at the level of the maximum gradient.

The effect on the residual stresses in the tensile and compressive faces was studied. Because stress analysis is a destructive process, the equivalent profile on both faces at the point where the specimen is most stressed could not be observed. The stress profiles were therefore taken in a less stressed area. As shown in Figure 4.36, one half of the specimen is then divided into two equal parts to examine the residual stress profile on the inner (tensile) and outer (compressive) faces of the ring. The residual stress field and microstructure are therefore assumed to be symmetrical with respect to the half. The cut sections were made large enough to eliminate the possibility of stress redistribution.

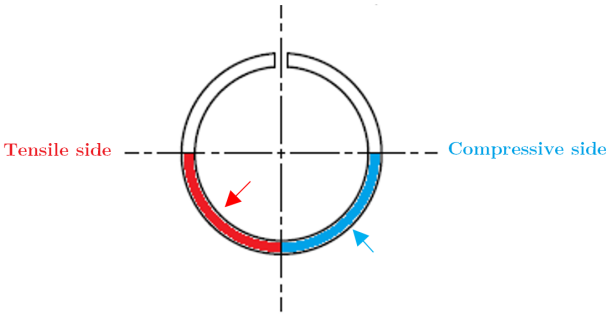

Figure 4.36 – Schematic of the sections of the ring for phase and stress analysis. In red the section for the analyses inside the ring (i.e. tensile side) and in blue the section for the analyses outside the ring (i.e. compressive side).

Before analysing the stress and hardness profiles, the stress fields relative to the analysed sections were studied from the finite element model in ABAQUS (section 4.2.3). Fig. 4.37 shows that the σ_s and stress gradients values are much lower where the residual stress study has been performed. The gradient at the stress analysis is 1.1 GPa/mm compared to 1.8 GPa/mm for the maximum area, which implies a decrease in the gradient of 40% and similarly a decrease of 43% in the σ_s values.

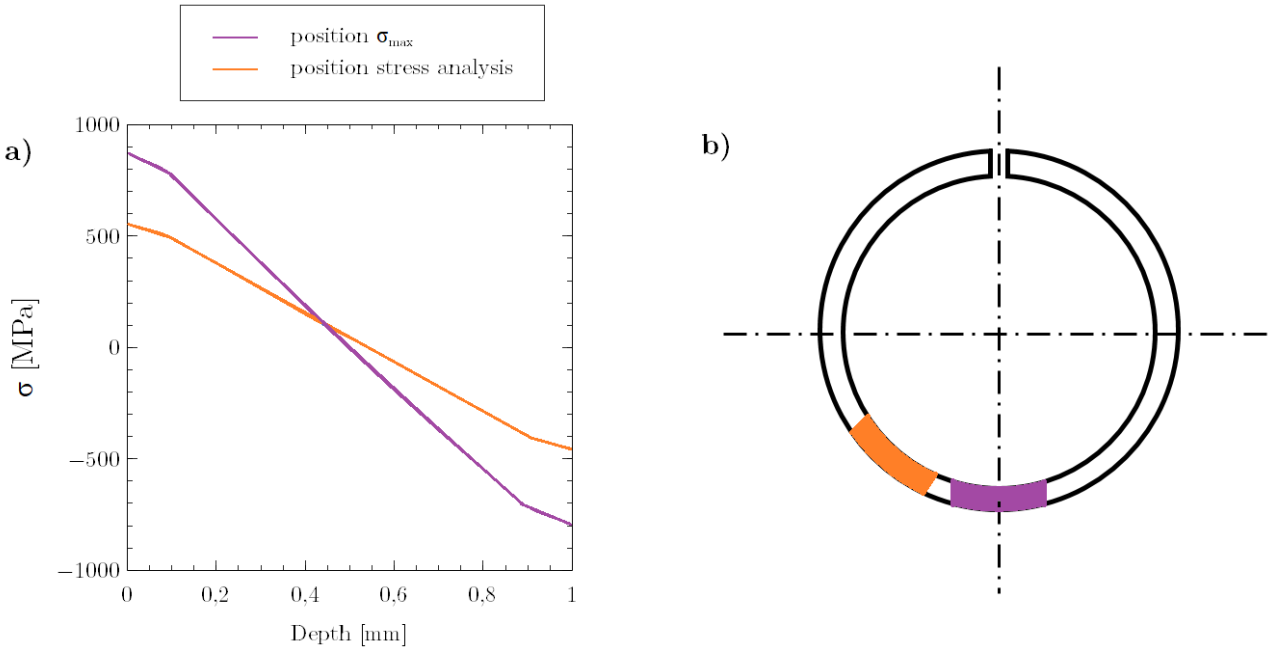

Figure 4.37 – a) Numerical residual stress profiles, obtained on ABAQUS, of the ring on the tensile and compressive sides. b) Schematisation of the positions equivalent to the profiles presented in a).

Fig. 4.38 shows the stress profiles calculated by X-ray diffraction for the two faces studied compared to a 1 mm thick reference sample. The position of the stress maximum is equivalent which suggests that gradient and/or mobility effects have no impact on the location of the precipitation maximum. The integral breadths show that the diffusion accelerates on the compressive side, which seems to suggest that the influence of the gradient predominates over the effect of mobility stresses. The tensile profile shows an evolution of the core in tension compared to a profile that remains in compressive for the compressive side. This observation is due to the superposition of the residual and applied stresses. But the gradients show similar evolutions of the order of 10 GPa/mm. The two hardnesses corresponding to the stress fields (Fig. 4.37) were compared. The tensile profiles show comparable developments along the profile. The compressive profile corresponding to the experimental stress position shows a kinetic acceleration after 150 μm depth. This is also evident in the integral breadth profiles shown in Fig. 4.38. The equivalent times between the two "position σ_{max}" samples relative to the reference sample are calculated using Eq. 4.1. The results show that diffusion on the tensile side would be equivalent to a time of 6 h 36 min compared to 3 h 17 min on the compressive side. In other words, this indicates that for one, diffusion increased by 32 % (tensile profile) and for the other, it decreased by 34 % (compressive profile). This shows that the percentages are almost similar for all the selected measurement errors.

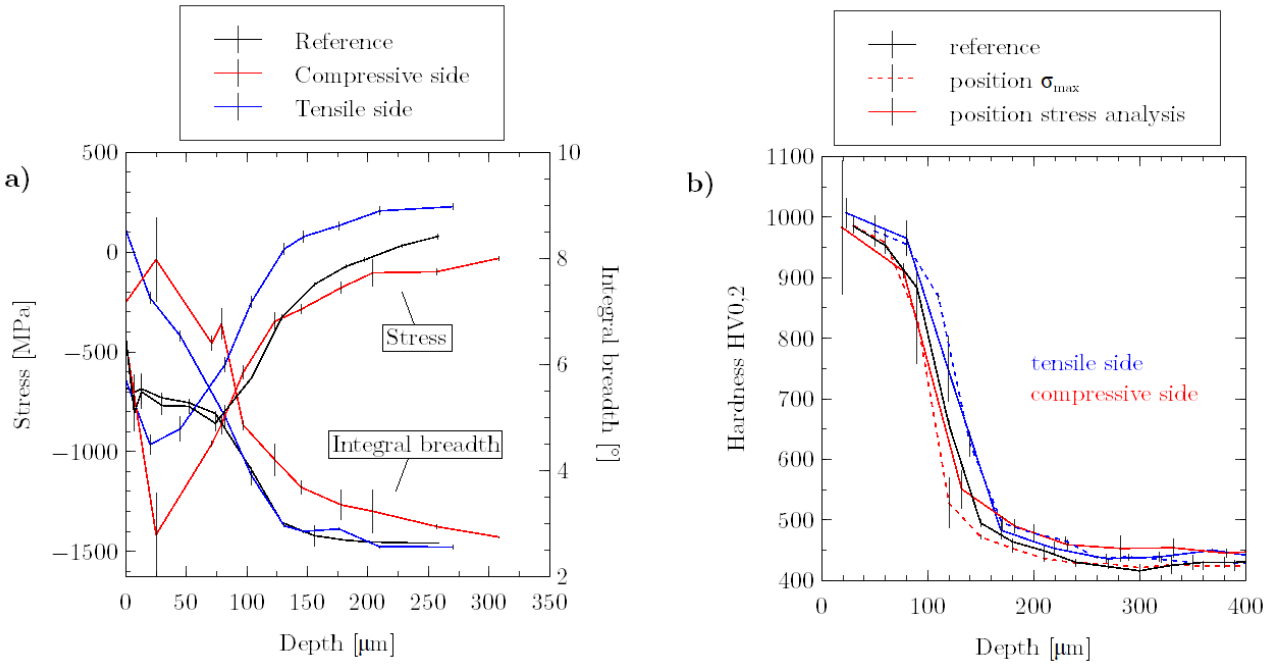

Figure 4.38 – a) Residual stress profiles of the ring on the tensile and compressive sides. b) Hardness profile of the ring on the tensile and compressive sides compared to the reference profile in two positions (see Fig. 4.37).

4.2.3.5 β coefficient identification

The parameter β is known as a strictly positive parameter, with unit $cm^2.s^{-1}.MPa^{-1}$. Numerical simulations have indicated that the effect of stress on mobility is significant when $\beta\sigma_{kk} = 0{,}1\ D_I^{\Phi}$. An inverse method study was carried out to obtain an order of magnitude of β_{mean} in the case of a change of the type: (in tension side) σ[GPa] = - 1.9 z + 0.8 and (in compression side) σ[GPa]= + 1.9 z - 0.8 where z is the depth. The calculation steps are shown in Fig. 4.39. They take into account the equivalent time t_{ref} corresponding to the reference sample, which is a function of its effective depth z_{ref} and the diffusion coefficient of the material D_I^{Φ} [Jegou et al., 2018], and the effective diffusion coefficient D_{eff}, which is a function of the effective depth z_s of the sample studied. These calculations were carried out under the strong assumption that the effect of stress on the driving forces is not taken into account. This study therefore focused on the study of the modified Einstein equation: $z^2 = 2D_{\text{eff}}t$ where $D_{\text{eff}} = D_I^{\Phi} + \beta\sigma_{kk}$.

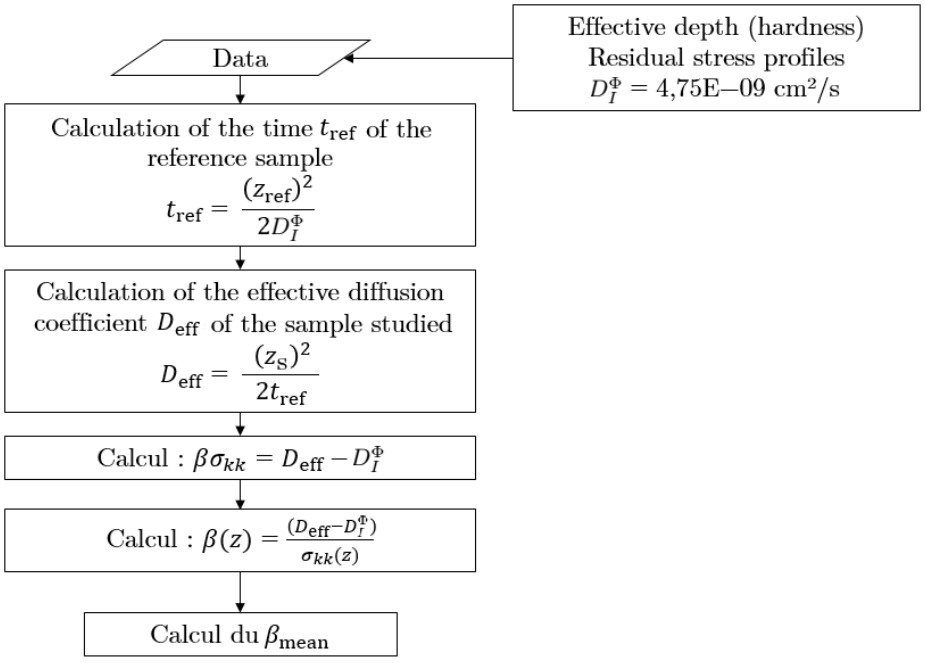

Figure 4.39 – Steps to determine the order of magnitude of the β coefficient without taking into account the effect of stress through driving forces.

Tab. 4.8 shows the values obtained from β_{mean}, those resulting from $(\beta_{\text{mean}}\sigma_{kk})_{\text{mean}}$ and D_{eff}^{mean} $(= D_I^\Phi + (\beta_{\text{mean}}\sigma_{kk})_{\text{mean}})$, for both sides (tension/compression).

	Tension side	Compression side
β_{mean} [cm^2.s^{-1}.MPa^{-1}]	2,19.10^{-12}	1,94.10^{-12}
$(\beta\sigma_{kk})_{\text{mean}}$ [cm^2.s^{-1}]	0,68.10^{-9}	-1,99.10^{-9}
$D_{\text{eff}}^{\text{mean}}$ [cm^2.s^{-1}]	5,43 .10^{-9}	2,76 .10^{-9}

Table 4.8 – Order of magnitude of the identification by the inverse method of β_{mean}, $(\beta_{\text{mean}}\sigma_{kk})_{\text{mean}}$ and $D_{\text{eff}}^{\text{mean}}$ for the split ring experiment, comparison for the compression side and the tension side.

However, it is important to understand that these averages of the values of β_{mean} and $(\beta_{\text{mean}}\sigma_{kk})_{\text{mean}}$ are averages with strong standard deviations. Indeed, Fig. 4.40 shows that the evolution of $(\beta_{\text{mean}}\sigma_{kk})$ does not evolve linearly as a function of depth.

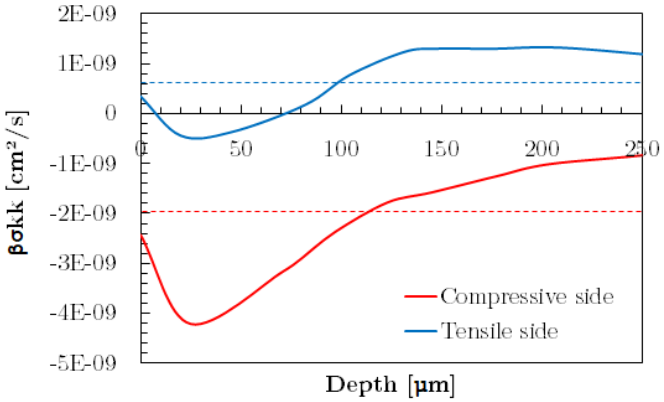

Figure 4.40 – Evolution of $(\beta_{\text{mean}}\sigma_{kk})$ (in line) as a function of the depth for the compressive side (in red) and the tensile side (in blue). The $(\beta_{\text{mean}}\sigma_{kk})_{\text{mean}}$ are represented respectively by the same dashed colours.

4.2.3.6 Discussion

The observations between the stress/integral breadth profiles and the hardnesses show phenomena that do not appear to be instinctive.

On the applied stress gradient side. The residual stress profiles are consistent with the expected results. This shows that the bending loading modified the final residual stress profiles. On the tensile side, lower stresses and high tensile stresses in the core were observed, compared to a compressive-only profile with large area values for the compressive side.

On the compressive side, the integral breadths have larger values. This result suggests a different microstructure with more defects. In other words, a microstructure that contains more nitrogen or more nitrogen with smaller precipitates. It is well known that integral breadths and hardness profiles are correlated in terms of depth evolution, but this is not the case here. Indeed, the hardness filiations for the lower gradient revealed a slowing down on the compressive side for the first 150 μm of depth and an acceleration thereafter. The results on the integral breadth profiles should reveal more significant hardness evolutions. However, the fact that the integral breadths are larger as a function of depth does not imply that deeper diffusion is observed. The combination of the residual stress/integral breadth plot and the associated hardness filiations leads to the hypothesis that greater precipitation is associated with larger or more "semi-coherent" precipitates due to the activation of diffusion on the tensile side. Due to this precipitation, total strains would increase, resulting in precipitation-induced accommodation. All this would lead to fewer defects, which is why there are lower integral breadths.

The hardness filiations for the higher gradient ("position σ_{max}") showed a symmetry between the deceleration (compressive side) and acceleration (tensile side) observed on the effective depths. These orders of magnitude for this grade of steel and these treatment conditions would therefore allow a reduction of the treatment time of 1 h 40 min. These observations are consistent with a study carried out in the laboratory in 2018 [Guillot, 2018] and the literature, where diffusion is accelerated in the case of a positive stress and conversely in the case of a negative stress, i.e. a mobility effect. The measurements show that the acceleration and deceleration are comparable in difference 33 %.

Through these two applied stress gradients and the residual stress gradient it could be observed that in the

case of the steel grade 33CrMoV12-9, there is a strong coupling between the stress gradient and mobility. In the case of the highest gradient, a predominance of the influence of the stress on the mobility seems to be observed in view of the results close to the trends observed in Fig. 3.30b). In the case of the 1.1 GPa/mm gradient, it is observed that at the beginning of the treatment the effect of mobility seems to be predominant and then a predominance of the gradient. These observations show that for the effect of the gradient to be predominant, the maximum stresses of this gradient must be sufficiently low.

The identification of the parameter β_{mean} in the case where only the effect of the stresses on the mobility is taken into account, in other words where the effect of the driving forces is neglected, made it possible to observe that its value for a stress field of σ[GPa] $= \pm 1.9\ z\ \pm 0.8$ is of the order of 2.0^{-12} cm^2.s^{-1}.MPa^{-1}. Numerical simulations have shown that the effect of stress on mobility is significant when $\beta\sigma_{kk} = 0.1\ D_I^{\Phi}$. Here, it was observed that the order of magnitude of $\beta\sigma_{kk}$ is 0.14 for the tensile side and about 0.4 for the compressive side.

4.3 Plastic strain effect

According to the literature review, plastic strain has an effect on the adsorption and diffusion of atoms during subsequent chemical surface treatments such as nitriding. A form of tensile specimen was designed to study the effect of strain hardening on gas nitriding of steels, based on controlled tensile tests. The specimens were designed to study the effect of uniform strain hardening, thus allowing nitrided specimens to be obtained at different strain hardening levels. The study of short- and long- range diffusion kinetics during a gas nitriding process is carried out. Two plastic strains were studied in this section for a nitriding time of 24 hours at 520 °C and a nitriding potential $K_N = 3.711$ atm$^{-1/2}$. The specimens are modelled to produce two samples (shown in grey in Fig. 4.41). These two samples will be compared to a so-called reference sample undergoing the same nitriding treatment and having the same dimensions.

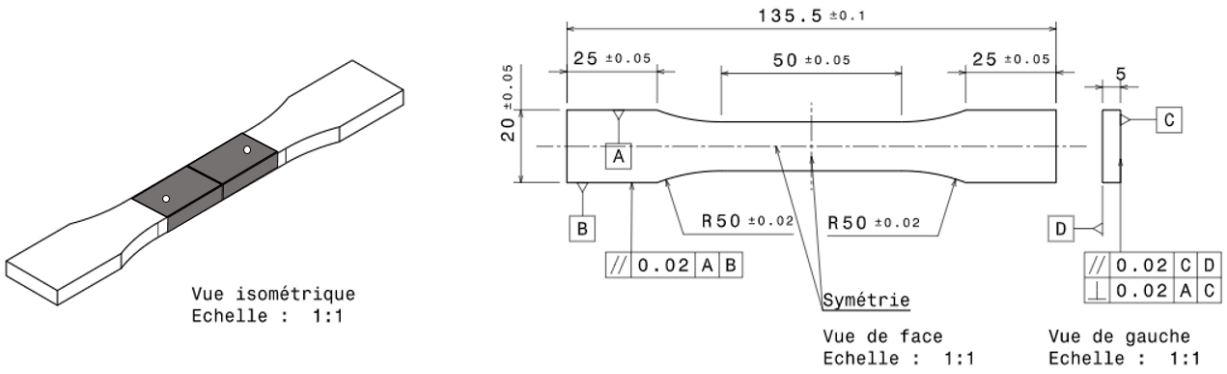

Figure 4.41 – Drawing of the constant section tensile specimen (in mm).

4.3.1 ABAQUS model

The finite element model was run on ABAQUS. A general step with a time of 1 s and 1000 time increments was performed. An embedded edge and an edge imposed in displacement constitute the boundary conditions (see Fig. 4.42). The displacement is applied to a reference point at the centre of the section. The reference point and the section where the displacement is imposed create a coupling. The objective is to immediately

extract the reaction force (N) associated with the defined plastic strain in order to perform the tensile test on the machine. The model is based on the elastoplastic law identified and presented in section 2.3.2 and with a Young's modulus of 202 GPa and a Poisson's ratio of 0.29. The specimen is meshed with C3D10 i.e. a 10-node quadratic tetrahedron on the non-rectangular parts and C3D8R i.e. an 8-node linear brick, reduced integration, hourglass control. In the useful part of the specimen, the elements are 0.1 mm.

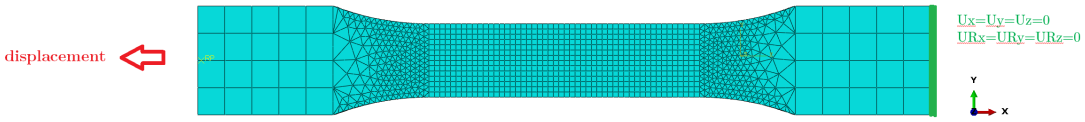

Figure 4.42 – Mesh and boundary conditions of the constant section tensile specimen.

The objective was to define the reaction forces associated with two plastic strain values: 2 % et 4 %.

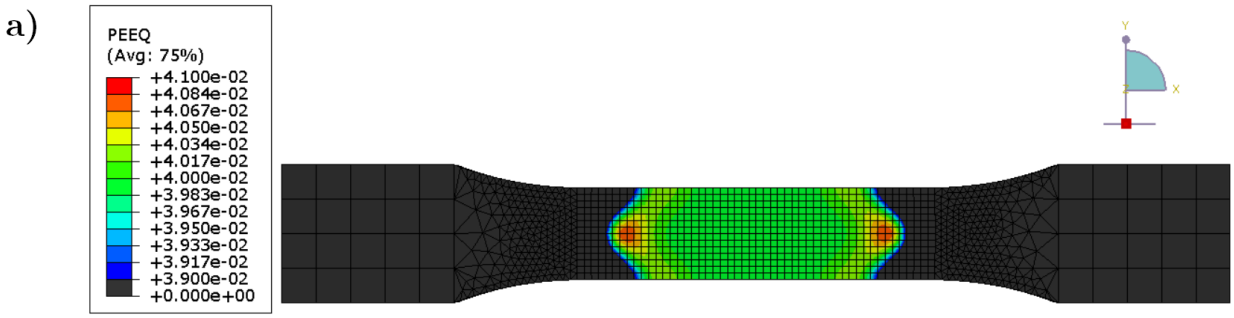

Figure 4.43 – Visualization of the Equivalent Plastic Strain (PEEQ)for the 4% strained specimen.

Thanks to the reference point, the reaction force of each test were extrated (see. Table 4.9).

	$\varepsilon^P = 2$ %	$\varepsilon^P = 4$ %
|Reaction force| [N]	-81000	- 86100

Table 4.9 – Reaction forces extracted, for the two plastic strains, on the finite element model on ABAQUS.

4.3.2 Mechanical tensile test

Figs. 4.44a) and b) show, respectively, the two conventional and rational experimental stress-strain curves for the two specimens studied. The plastic strain are 2,3% and 3,8%. The test conditions are as follows: same geometries of the specimens before the test and the test is carried out in imposed displacement with a speed of 0.1 mm/s.

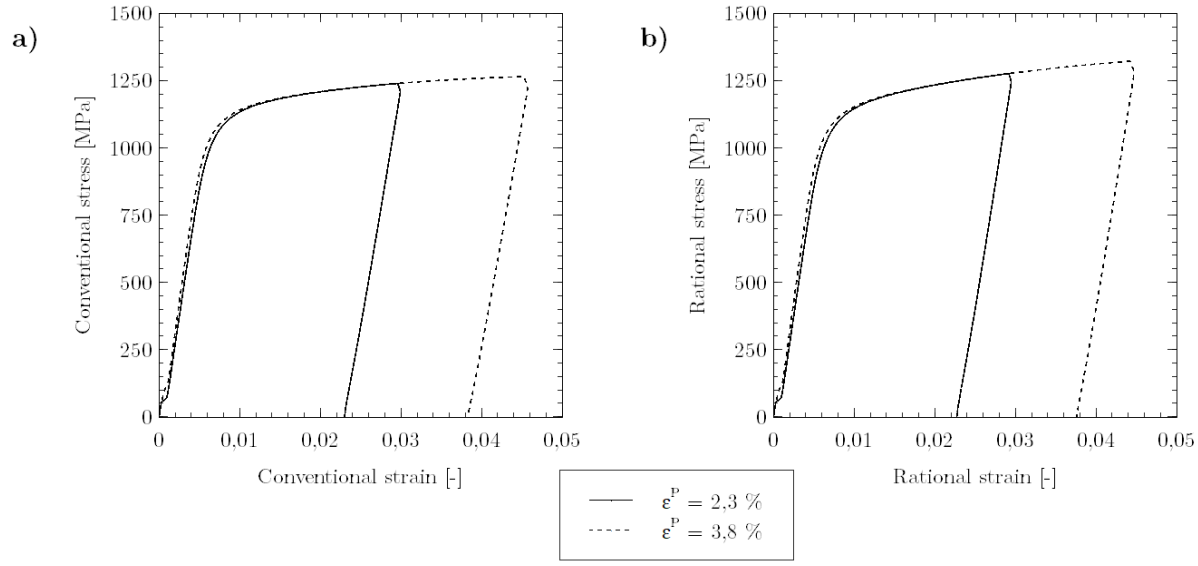

Figure 4.44 – a) Conventional stress-strain curves, b) Rational stress-strain curves, obtained for specimens subjected to 2.3 % and 3.8 % plastic strain.

4.3.3 Nitriding treatment

The samples were then nitrided (t = 24 h, T = 520 °C and K_N = 3.711 $atm^{-1/2}$). Firstly, they were cut to the same dimensions (17*13.5*5 mm). The equivalent mass gains and kinetics for the three samples, obtained by the thermogravimeter, presented in Fig. 4.46, show no difference throughout the treatment.

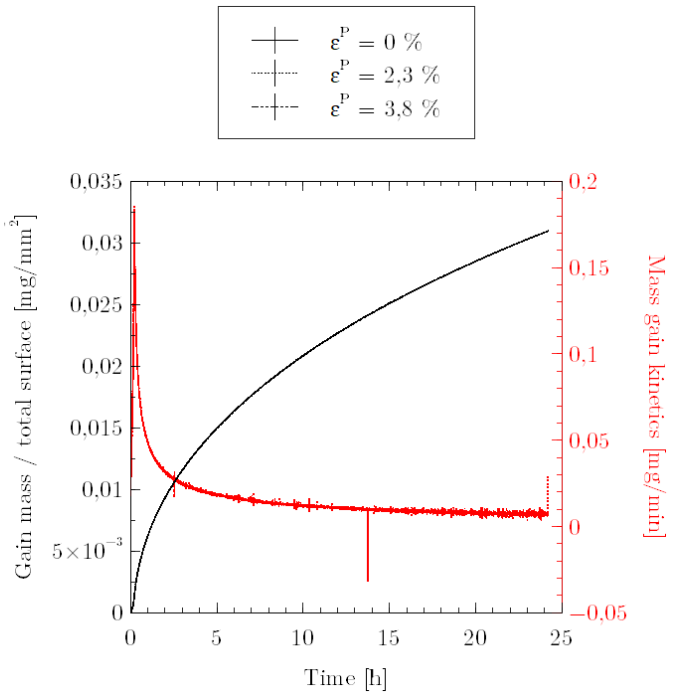

Figure 4.45 – Mass gain normalised to the total surface sample and kinetics to the three samples: ε^P = 0 %, 2.3 % and 3.8 %.

The evolution of residual stresses ($\sigma_{11} - \sigma_{33}$) and integral breadths as a function of depth is shown in Fig. 4.46a). The stress curves show comparable trends up to 180-200 μm, with stress maxima shifted by about 10 μm. The more the sample is deformed, the more the profiles move in depth. Indeed, the integral breadth curves, which are indicative of microstructure changes, reveal that the profiles are identical up to 150 μm, then the most strained sample (ε^P = 3.8 %) shows deeper diffusion but the base material profiles remains equivalent. These results are consistent with the hardness profiles observed in Fig. 4.46b). The hardness profiles reveal that the most deformed sample accelerates the diffusion kinetics from the beginning of the profile to a depth of 300 μm. However, as the effective depths (HV_core + 100 HV) are identical for all samples, the observed acceleration of kinetics cannot be expressed in terms of comparable time. However, the acceleration of kinetics shows that it is more efficient near the surface and that the difference reduces with depth.

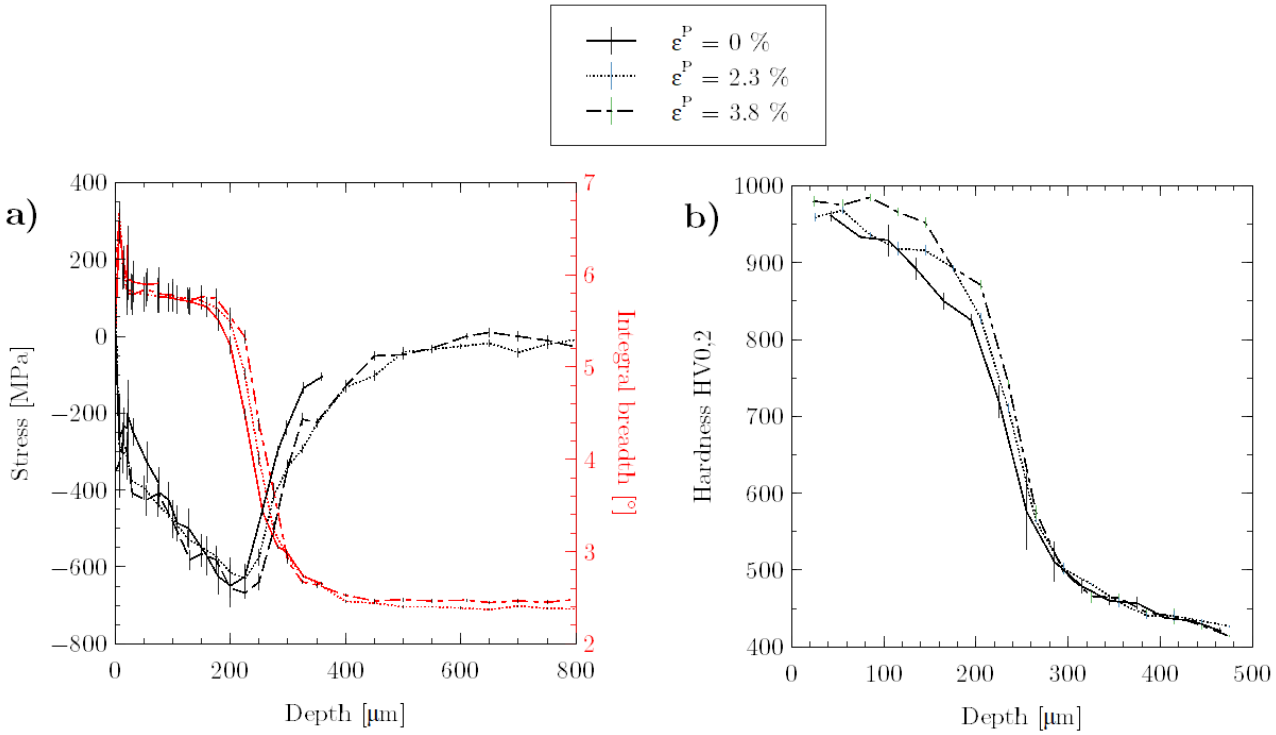

Figure 4.46 – a) Residual stress profiles; b) Hardness profiles, of plastically strained (ε^{P} = 2.3 % and 3.8 %) samples compared to a reference (ε^{P} = 0 %).

4.3.4 Discussion

This study has shown a different behaviour in terms of hardness improvement compared to previous studies. This difference seems to show that the long range diffusion kinetics do not seem to be accelerated but that the phenomena seem to play a role on the short-range kinetics (precipitation). These observations are consistent with what has been observed in the literature where it has been found that precipitation plays an important role on the kinetics. These observations therefore seem consistent with what has been observed in the literature where precipitation phenomena (e.g. the thickness of the compound layer in the case of nitrogen diffusion) are strongly influenced by incompatible strains.

Conclusion

This thesis work focused on the understanding of stress-diffusion coupling, starting with interstitial diffusion problems and progressing to the case of gas nitriding of the ferritic steel grade 33CrMoV12-9. This research was carried out through the development of 2D and 1D models and specific experiments. The first objective was to understand the effect of elastic strain (applied/residual stresses) on the diffusion kinetics by combining theoretical and experimental observations. The second objective was to decouple the effects of elastic stresses and incompatible plastic stresses on the diffusion kinetics.

For many years, a large number of studies have been carried out on the understanding of stress-diffusion coupling phenomena. From the literature review, it is clear that the studies have mainly focused on the influence of a stress gradient on the diffusion kinetics assuming an effective diffusion coefficient. However, a study by Voorhees and Larché defined analytical formulations that take into account the effect of stress on mobility and stress gradient. This equation thus includes the coupling of two effects of stress on long-range diffusion phenomena: the effect of the magnitude and sign of the stress on mobility (Fickian term) and the stress gradient as a driving force (Nersntien term). A first 2D model was used to observe the tensorial aspects of the stress on the flow vector equations. A tensorial definition of the coupling between the mechanical and diffusion problems allowed to observe that the edge effect can have a detrimental effect on, for example, stressed parts (gear teeth type by example). It was observed that a double flow phenomenon leading to a higher affected depth results in a low negative residual stress field with even positive values at the near surface. A second 1D model observed that individually, a positive stress gradient and a positive homogeneous stress both lead to accelerated diffusion kinetics; and respectively the opposite for a negative stress gradient and a negative homogeneous stress. A study of the stress amplitude confirmed that the effect of the stress gradient becomes significant from an order of magnitude of the gradient in GPa/mm. Parametric studies on specific stress fields (tension/compression and bending test type) showed that a tensile stress with a negative gradient in the case of :

— Without the effect of mobility ($\beta = 0$) leads to a slowed down diffusion,

— With the effect of mobility ($\beta > 0$) leads to an accelerated diffusion.

Moreover, the effect in the case of a positive stress gradient with negative stresses is 3 times slower than the effect in the case of a negative stress gradient with positive stresses for an equivalent value of β.

These studies have shown that the Fickian coupling factor ($\beta\sigma_{kk}$) must be about 10 times smaller than the diffusion coefficient D_I^{Φ} to have a significant impact on long-range diffusion kinetics.

Specific experimental studies on 33CrMoV12-9 nitrided steel samples were carried out to investigate the effect of elastic strains on diffusion kinetics. These experiments were based on the study of short- and long-

range diffusion kinetics. The samples were nitrided for 5 h at 520 °C with $K_N = 3.711$ atm$^{-1/2}$. These nitriding parameters were intended to influence the time aspect of the residual stresses, which show higher kinetics at the beginning of the treatment. The high K_N was used in order to obtain a two-phase compound layer. The aim of these studies was to observe and compare these results with numerical simulations (long-range diffusion), and then on the kinetics of short-range diffusion (precipitation) and carbon co-diffusion.

A first study focused on the structural effect (i.e. dynamic equilibrium) through two asymmetrically nitrided parallelepipedic samples with a thickness ratio of 10. The results showed that the long-range diffusion kinetics was significantly accelerated in the case of the thinner sample. These phenomena on the dynamic equilibrium effect could be justified by the time effect of the residual stresses. This effect showed that, for this grade of steel and under these treatment conditions, the treatment times could be reduced by 2.5 hours over a period of 5 hours.

Two studies were then conducted on the influence of a stress gradient. One was a study of a split ring undergoing a bending-type stress field. For this, two sections of the ring were studied involving two stress gradient values (±1.8 GPa/mm and ±1.1 GPa/mm) with surface stress values of approximately ±850 MPa and ±550 MPa respectively. The other was a residual stress gradient obtained by a first asymmetric diffusion of 3.5 GPa/mm with a surface stress of -140 MPa on a 500 μm thick parallelepiped sample.

The study on applied stress gradients showed similar results to those observed in the literature review. It was shown that the diffusion kinetics was accelerated when the stresses were of positive sign and vice versa for negative stresses. From the point of view of numerical simulation, it was also observed that the influence of the sign of the stresses is much more sensitive than the effect of the stress gradient. This first observation allows us to see that for a gradient of the order of ±1-2 GPa/mm at maximum stresses of the order of ±550-850 MPa, the sign of the stresses is predominant. For mechanical loading (±1.8 GPa/mm and ±850 MPa), the stress acceleration on the tensile side would result in a reduction in processing time of 1 hour and 40 minutes over an initial 5 hour period. These observations were countered by the residual stress gradient study. The results showed an acceleration of the stresses for a positive stress gradient and a negative stress sign, which could be translated into a reduction of the treatment time by 50 minutes over an initial period of 5 hours. A much larger increase was expected. This was justified by the time effect of residual stresses. The initial stress gradient was not constant over time, unlike an applied stress gradient (without creep). The temporal aspect suggests that this residual stress gradient has a major role in the early stages of the treatment, when the kinetics are more important.

These three studies thus provide strong evidence of the coupling between the effect of the stress gradient and the effect of the stress on mobility. These observations show that for the effect of the gradient to be predominant, the magnitude of the stresses (in absolute value) must be sufficiently low.

The effect of bending loading was observed on the residual stress profiles and on the evolution of the integral breadths. The profiles showed a clear difference between the tensile side (negative gradient/positive stress) and the compressive side (positive gradient/negative stress). The tensile side has lower compressive stresses and high tensile balancing, while the compression side has a fully compressive profile. The integral breadths are larger on the compression side. This difference has been justified by the assumption that it is due to the fact that the microstructure is different with more defects on the compression side. One hypothesis is that the compressive side has a higher nitrogen content or a higher nitrogen content with smaller precipitates. The fact that the integral breadths increase (compressive side) with depth does not imply that deeper diffusion is observed. Due

to the activation of diffusion on the tensile side, the combination of residual stress, integral breadth and hardness results lead to the hypothesis that higher precipitation is associated with larger or more "semi-coherent" precipitates. Total strains would increase due to precipitation, resulting in precipitation-induced accommodation.

Plastically deformed 33CrMoV12-9 nitrided steel specimens were studied in a conventional tensile test to decouple the effects of incompatible elastic and plastic stresses on diffusion kinetics. The purpose of these deformed specimens was to observe the influence of diffusion short-circuits (dislocation density), but also the density of grain boundaries, which was not quantified in this work. The results show that the long-range diffusion kinetics do not seem to be accelerated but that the phenomena seem to play a role on the short-range kinetics (precipitation). These observations are consistent with what has been observed in the literature where precipitation phenomena are strongly influenced by incompatible plastic strains [Lin et al., 2006, Tong et al., 2008, Thiriet et al., 2012, Chemkhi, 2014].

This study compared to those on elastic stresses allowed to understand that elastic stresses play a role mainly on long range diffusion by having an impact on the potential energies (jump distances of atoms) and that plastic stresses play a role on the density of grain boundaries and the density of dislocations.

This work leads to additional considerations and the opening of new perspectives, such as:

— The optimisation of short nitriding treatments in order to define the ideal thickness for an equivalent time and temperature so as not to observe any double flux phenomenon,

— Carrying out these tests for long treatments, if not for deep treatments (>300 μm),

— To extend the split ring experiment by studying :

  — Different stress fields and thus observe whether the effect is linear or non-linear and be able to conclude on the predominant effect of stresses on mobility or by driving forces,

  — The effect of stress on mobility through an experiment involving stress loading for different processing times,

  — The effect of temperature (avoiding any source of thermal relaxation) in order to define the dependence or not of temperature on mobility,

  — The profiles of a stressed ring for an initial treatment time and of an unstressed ring for a time equivalent to the effective depth of the stressed ring. Their hardness profiles are then compared and it is observed whether the influence of a stress field only accelerates the kinetics (depth of the diffusion layer) or whether other phenomena appear.

— To carry out pure shear tests in order to understand their effect and thus determine the possible importance of the term $2\gamma_I\sigma_{ij}$ in the effect of stress on mobility in the numerical simulations,

— Identify the specific parameter β for the steel grade 33CrMoV12-9 by taking into account the global equation, i.e. the effect of mobility and/or driving forces as a function of the applied stress field, through identification methods such as: inverse method or scale transition study,

— Performing experiments on, for example, a mechanically pre-treated specimen (e.g. by shot blasting) and then nitrided or a specimen subjected to an applied stress field in the plastic deformation range and then nitrided, in order to confirm the hypotheses made on the decoupling of the phenomena between the types of strain (elastic/plastic),

— Conducting experiments on real parts (i.e. with complex geometry) by studying the conditions of nitrogen adsorption (gas-solid exchange) as a function of the mechanical preparation of the surfaces (e.g. conditions and type of machining and sandblasting),

— The implementation of the coupling equation in the 1D diffusion-precipitation code developed in the laboratory by adding the incremental aspect, i.e. by taking into account the stresses at each moment, is to be considered in order to be able to predict the short and long distance diffusion according to the input parameters (t, T, surface concentration),

— Apply numerical simulations to other fields involving binary systems, such as microelectronics field involving additional gradient fields of an electrical nature.

Part II

Résumé long en français

Introduction

Depuis de nombreuses années, un un domaine majeur d'étude est celui des phénomènes de couplage entre un champ de contraintes mécaniques (appliquées ou résiduelles) et un champ chimique dans un processus de diffusion des matériaux. L'amélioration des propriétés physiques et mécaniques des surfaces des matériaux est un défi auquel s'intéressent les chercheurs universitaires et industriels. Industriellement, les profondeurs effectives sont utilisées et définies pour déterminer la profondeur d'une couche nitrurée. Ces recherches se concentrent donc principalement sur l'épaisseur de la couche de diffusion, c'est-à-dire la diffusion à longue distance. La diffusion entraîne des améliorations de dureté en surface mais également une modification locale de la microstructure et donc une modification des volumes locaux. Cette forte déformation locale conduit à une déformation élastique à longue distance, ce qui entraîne un champ de contraintes résiduelles. Ce champ résiduel permet d'améliorer les propriétés mécaniques comme, par exemple, la durée de vie en fatigue de la pièce sollicitée [Godet, 2018]. Plus la profondeur de la couche de diffusion est importante, plus le profil de contraintes résiduelles correspondant est profond.

Expérimentalement, de nombreuses études se concentrent sur le couplage entre un prétraitement mécanique et un traitement thermochimique dans le but de créer des courts-circuits de diffusion afin d'augmenter les profondeurs diffusées. Les conclusions de ces études sont basées sur des phénomènes de déformation plastique (par exemple, la nanocristallisation). Les surfaces nanostructurées induisent une augmentation de la fraction volumique des joints de grains, une forte densité de dislocation qui ont une influence significative sur la cinétique de diffusion [Lu and Lu, 2004, Tong et al., 2008, Chemkhi, 2014]. Les nanostructures fournissent aux atomes interstitiels de la surface du matériau des chemins de diffusion plus rapides mais le prétraitement mécanique provoque également des gradients de contraintes résiduelles (c'est-à-dire des déformations élastiques). L'effet des contraintes, qu'elles soient à gradient ou homogènes, a révélé que c'est le signe des contraintes qui prédomine sur les cinétiques de diffusion : une contrainte positive augmente la cinétique de diffusion, inversement pour les contraintes négatives [Kirchheim, 1986, Araki and Arai, 2010a, Guillot, 2018].

La première question pourrait donc être : quelle source de contrainte (élastique ou plastique) domine la cinétique de diffusion à courte et longue distance ? La nitruration gazeuse est le traitement thermochimique étudié dans cette thèse. Il consiste à placer une pièce en acier dans un four où l'atmosphère, notamment l'ammoniac, est contrôlée. La diffusion de l'azote améliore significativement les propriétés mécaniques de la surface (résistance à la fatigue, à l'usure, à la fissuration et à la corrosion). Le développement de contraintes résiduelles de compression et l'augmentation du durcissement de la surface entraînent une augmentation des propriétés mécaniques. La diffusion interstitielle à longue distance conduit à de grands gradients de contrainte induits par les transformations de phase (diffusion à courte distance). La formation de contraintes résiduelles pendant la nitruration est causée par le type de changement volumique associé à la précipitation de phase

pendant la diffusion de l'azote [Barrallier, 1992].

La nuance d'acier nitruré 33CrMoV12-9 étudiée dans cette thèse est couramment utilisée dans les domaines aérospatial, naval et du sport automobile et présente des propriétés mécaniques non homogènes. Une zone superficielle nitrurée est significativement plus dure que le métal de base et présente des contraintes de compression élevées en surface. Industriellement, le développement des pièces nécessite des chargements mécaniques de plus en plus élevés, avec des plages de nitruration de plus en plus profondes, ce qui entraîne des temps de traitement de plus en plus longs et donc des ressources gourmandes. La recherche de l'effet des contraintes sur la cinétique de diffusion vise à réduire les temps et/ou les températures de traitement tout en optimisant les plages de traitement. Aujourd'hui, les méthodes numériques combinées aux méthodes expérimentales sont un moyen peu coûteux et rapide de prédire les phénomènes.

Sur le plan analytique, un grand nombre d'études ont été menées sur la compréhension des phénomènes de couplage contrainte-diffusion. Ces études se sont principalement intéressées à l'influence d'un gradient de contrainte sur la cinétique de diffusion en supposant un coefficient de diffusion effectif. En 1996, Voorhees et Larché ont défini des formulations analytiques qui prennent en compte l'effet de la contrainte sur la mobilité [Larché and Voorhees, 1996]. Cette équation inclut donc le couplage de deux effets de la contrainte sur les phénomènes de diffusion à longue distance : l'effet de la magnitude et du signe de la contrainte sur la mobilité (terme Fickien) et le gradient de contrainte comme force motrice (terme Nersntien). Une deuxième question pourrait être : quel est l'effet du signe de la contrainte ? Enfin, une troisième question serait : quel terme (fickien ou nersntien) domine la cinétique de diffusion à longue distance ? Depuis de nombreuses années, le développement numérique des traitements thermochimiques (c'est-à-dire les phénomènes de diffusion de l'oxygène, de l'hydrogène ou, par exemple, de l'azote) est connu et développé. Au laboratoire, un modèle 1D a été développé, optimisé et couplé à la base de données Thermo-calc afin de prédire les profils de concentration en azote et les teneurs en nitrure/carbone en fonction des conditions aux limites d'entrée [Barrallier, 1992, Jegou, 2009, Fallot, 2015]. Cependant, ce modèle ne prend pas en compte le couplage contrainte-diffusion (effets des contraintes à chaque instant t), mais calcule uniquement le profil final de contraintes résiduelles à partir du profil final de concentration.

L'objectif de cette thèse est de mieux comprendre ce couplage, en commençant par les problèmes de diffusion interstitielle et en progressant vers le cas de la nitruration gazeuse de la nuance d'acier ferritique 33CrMoV12-9. Le premier objectif de cette recherche est de comprendre l'effet des contraintes élastiques (contraintes appliquées/résiduelles) sur la cinétique de diffusion en combinant les observations théoriques et expérimentales. Le second objectif est de découpler les effets des contraintes élastiques et des contraintes plastiques incompatibles sur la cinétique de diffusion.

Le premier chapitre se concentrera donc sur une synthèse bibliographique du traitement de nitruration gazeuse, les équations analytiques du couplage contrainte-diffusion, la modélisation sur les modèles binaires existants, et les expériences impliquant les phénomènes de diffusion par les contraintes élastiques et plastiques. Un deuxième chapitre sera consacré à l'étude numérique du couplage contrainte-diffusion dans le cas d'un modèle binaire sans précipitation et sans phénomène de co-diffusion du carbone, dans le but d'observer et de comprendre l'impact d'un gradient de contrainte et celui des contraintes de mobilité sur la cinétique à longue distance. Un troisième chapitre sera consacré à la mise en œuvre de tests spécifiques pour découpler l'effet des contraintes élastiques et des contraintes plastiques incompatibles sur la diffusion à courte et longue distance. L'analyse des propriétés mécaniques (dureté, contraintes résiduelles et microstructure) des échantillons sera étudiée et comparée à des échantillons de référence. Un quatrième chapitre sera consacré à une discussion des résultats

numériques et expérimentaux obtenus. Un dernier chapitre sera consacré aux conclusions de ce travail.

Chapitre 1

Bibliographie

1.1 Nitruration gazeuse

La nitruration est un processus thermochimique dans lequel l'azote diffuse de la surface vers le cœur du matériau [Fry, 1932, Ghiglione et al., 1996]. Il existe différents procédés de nitruration (bain de sel, ionique ou gazeux), chacun ayant ses propres avantages et inconvénients, qui permettent d'obtenir des couches ayant les caractéristiques souhaitées. Les caractéristiques mécaniques, métallurgiques et chimiques des couches dépendent fortement des procédés utilisés pour les former. La nitruration gazeuse est le traitement particulier utilisé dans cette étude. Ce traitement est étudié depuis des années au sein du laboratoire, dans le cadre de la compréhension de la genèse des contraintes résiduelles [Barrallier, 1992], de la caractérisation métallurgique et mécanique des couches nitrurées [Locquet et al., 1997], de l'influence des éléments d'alliage sur la genèse des contraintes résiduelles [Jegou, 2009], du rôle du carbone [Jegou, 2009, Fallot, 2015], de l'influence des préparations de surface avant traitement [Guillot, 2018] ou l'influence du comportement mécanique d'une couche nitrurée [Godet, 2018]. Ce traitement est souvent utilisé sur des pièces finies "surchargées" comme les roulements et les engrenages grâce à de faibles déformations de la pièce après traitement. Ce procédé présente également des points faibles, qui sont principalement le temps de traitement (souvent plusieurs heures), les températures de traitement élevées entre 400 et 590°C. Les autres points faibles sont les faibles profondeurs de diffusion atteintes (jusqu'à 1 mm selon le matériau : acier austénitique [Somers et al., 1989, Christiansen et al., 2008], acier martensitique [Barrallier, 1992, Locquet, 1998, Jegou, 2009, Guillot, 2018]), la complexité de trouver la combinaison parfaite des paramètres de traitement (temps, température, potentiel d'azote), la toxicité et le danger des produits utilisés : ammoniac, azote, hélium, hydrogène.

La diffusion est associée à un enrichissement local de la matrice en azote [KlÄumper-Westkamp et al., 1989]. Les atomes interstitiels ont une vitesse de diffusion plus élevée que les atomes des éléments d'addition qui sont substitués dans le réseau cristallin [Jack, 1975]. Lorsque la limite de solubilité de l'azote dans la ferrite est atteinte, des précipités se forment et grossissent. Schématiquement, une partie de l'azote est utilisée pour précipiter le nitrure tandis que l'autre partie diffuse vers le matériau de base. Le mécanisme s'arrête lorsque le système est en équilibre thermodynamique.

Dans l'industrie, les profondeurs de nitruration effectives sont utilisées et définies pour déterminer la profondeur d'une couche nitrurée. Elle est définie comme l'épaisseur de la couche nitrurée avec une différence de dureté entre le matériau central et la couche de surface qui est spécifiée arbitrairement. L'effet initial de la nitruration

est une augmentation considérable de la dureté de la surface de la pièce. La nitruration se produit dans le cas d'un durcissement structurel causé par une précipitation de seconde phase, à savoir par la petite taille des nitrures dans l'alliage MN. Les précipités sont la principale source de l'augmentation de la dureté superficielle de l'acier dans le cas de la nitruration. Plus précisément, le contournement des précipités incohérents implique un mécanisme de contournement de type Orowan avec la formation de boucles de dislocation résultant d'un processus de Frank-Read [Locquet, 1998]. Le processus de cisaillement des précipités est impliqué dans le cas des précipités semi-cohérents MN [Locquet, 1998].

La diffusion interstitielle est le mouvement des atomes entre les sites cristallins. La diffusion implique une modification locale de la microstructure et donc une modification des volumes locaux. L'expansion du réseau cristallin introduit des contraintes mécaniques en réponse à cette déformation. Cet effet local introduit la notion de déformations libres de contrainte, également appelées "eigenstrain". Les déformations libres de contrainte correspondent à des déformations inélastiques telles que la dilatation thermique, la transformation de phase et les déformations plastiques. Ces fortes déformations locales conduisent à des déformations élastiques à longue distance et donc à un champ de contraintes résiduelles.

Les contraintes résiduelles sont définies comme les contraintes qui existent dans un échantillon sans sollicitation extérieure [Totten et al., 2002]. Pour concevoir correctement les pièces, les bureaux d'études doivent comprendre et quantifier les champs de contraintes générés par les forces mécaniques afin de les contrebalancer par des contraintes résiduelles, souvent de compression. Les contraintes résiduelles de compression s'opposeront par exemple à l'ouverture de fissures, augmentant ainsi la résistance à la traction et à la fatigue. Les contraintes de compression induites par la nitruration ont été évaluées pour la première fois par R.B. Waterhouse par comparaison avec les contraintes de compression obtenues dans les revêtements sulfurés à partir de la déflexion de l'éprouvette [Waterhouse, 1965].

L'origine des contraintes résiduelles dans le cas de la nitruration est due à la précipitation et à la transformation de phase induite par la diffusion de l'azote (contraintes d'ordre II) et au gradient de microstructure qui en résulte (contraintes d'ordre I). D'un point de vue macroscopique, la surface nitrurée se dilate et le matériau de base s'y oppose. L'état de contrainte de compression est donc dû aux valeurs positives de changement de volume de la couche nitrurée. D'un point de vue microscopique, la couche nitrurée peut être divisée en sous-couches selon la profondeur, chacune d'entre elles se distinguant par des déformations volumétriques spécifiques à sa microstructure. Le gradient chimique lié à la diffusion des atomes d'azote génère un gradient de microstructure et donc un gradient de déformation volumique le long de l'axe de diffusion. Dans le cas de la nitruration d'une éprouvette à géométrie unique, il peut être supposé que le gradient de déformation conduit à des déformations incompatibles dans la direction du gradient [Mittemeijer, 1984, Somers and Mittemeijer, 1990, Barrallier and Barralis, 1994]. Ces contraintes étant incompatibles, des contraintes supplémentaires d'accommodation vont se créer entre les différentes profondeurs, ce qui, par équilibrage, conduit à un état plan de contrainte résiduelle de compression en surface. L'équilibre mécanique macroscopique est exprimé par la divergence du tenseur des contraintes.

D'un point de vue de la mécanique des milieux continus, les contraintes résiduelles sont décrites par un certain nombre d'équations. Un champ tensoriel de contraintes compatibles dans une plaque est un champ tensoriel unique qui est obtenu lorsque le corps est soumis à un champ de déplacement continu à valeur unique afin de garantir l'unicité de la solution [Noyan and Cohen, 1987, François et al., 2012b]. Le champ de contraintes résiduelles est statiquement admissible, les déformations totales $\varepsilon_{ij}^{\text{tot}}$ doivent satisfaire les six équations de compatibilité de Saint-Venant :

$$\varepsilon^{\text{tot}}_{ik,jl} - \varepsilon^{\text{tot}}_{jk,il} - \varepsilon^{\text{tot}}_{il,jk} + \varepsilon^{\text{tot}}_{jl,ik} = 0 \tag{1.1}$$

La déformation totale est la somme des déformations élastiques ε^{e}, qui sont des déformations compatibles, et des déformations sans contrainte (eingenstrains) ε^{F}, qui sont des déformations incompatibles [Mura, 1987] :

$$\varepsilon^{\text{tot}}_{ij} = \varepsilon^{\text{e}}_{ij} + \varepsilon^{\text{F}}_{ij} \tag{1.2}$$

Dans le cas de petites déformations, de petits déplacements et d'un matériau isotrope, les déformations élastiques $\varepsilon^{\text{e}}_{ij}$ sont décrites comme suit :

$$\varepsilon^{\text{e}}_{ij} = \frac{1+\nu}{E}\sigma_{ij} - \frac{\nu}{E}\,\sigma_{kk}.\delta_{ij} \tag{1.3}$$

Où ν est le coefficient de Poisson, E est le module d'Young et δ_{ij} est le symbole de Kronecker.

Les déformations libres de contrainte, $\varepsilon^{\text{F}}_{ij}$, sont la somme des déformations plastiques, thermiques, volumiques et de transformation. Dans le présent travail, les déformations thermiques et plastiques sont négligées parce qu'aucune hétérogénéité de déformation plastique post-mortem n'est observée, et que les effets de la température sont négligeables, surtout pendant le refroidissement. Seules les déformations volumétriques qui sont associées aux transformations de phase et à la solution solide pendant le processus de diffusion sont prises en compte [Cahn, 1961].

Dans le cas où un réseau cristallin se trouve dans un milieu homogène avec des propriétés élastiques anisotropes, la déformation libre de contrainte $\varepsilon^{\text{F}}_{ij}$, fonction de la concentraion c^{ϕ}_{I}, est définie par [Larché and Cahn, 1973, Larché and Cahn, 1982, Cahn, 1961] :

$$\varepsilon^{\text{F}}_{ij}\left(c^{\phi}_{I}\right) = \eta_{ij}.c^{\phi}_{I} \tag{1.4}$$

Où c^{ϕ}_{I} est la concentration [mol/m^3] de l'élément I de la phase ϕ et η_{ij} est le tenseur de dilatation chimique défini comme $\left(\eta^{\phi}_{I}\right)_{ij} = \frac{\partial \varepsilon^{F}_{ij}}{\partial c^{\phi}_{I}}$. Dans le cas isotrope, le tenseur de déformation de composition prend la forme :

$$\left(\eta^{\phi}_{I}\right)_{ij} = \eta^{\phi}_{I}\delta_{ij} = \frac{\triangle V_I}{3V_a}\delta_{ij} \tag{1.5}$$

Où $\triangle V_I$ est le volume molaire partiel de l'élément I et V_a est le volume molaire du réseau hôte.

1.2 Couplage contrainte-diffusion

La description de la microstructure d'une surface nitrurée a permis d'inclure plusieurs préoccupations thermochimiques. Par conséquent, le traitement de nitruration est un sujet difficile à étudier en termes de processus physiques. L'effet principal du traitement est la diffusion de l'azote. La diffusion dans les aciers alliés est effectuée par des processus physiques tels que la diffusion à courte distance (précipitation), la diffusion à longue distance (diffusion de l'azote) et la co-diffusion (carbone), qui présentent un certain nombre de défis de simulation. La diffusion de l'azote se produit dans un régime forcé, avec un flux ou une concentration constante à la surface du matériau. Le facteur clé de la diffusion est le gradient de potentiel chimique avec la profondeur. Le flux d'azote au cours de la transformation a une influence significative sur la diffusion du carbone [Jegou, 2009]. Les

facteurs mécaniques (contraintes, déformations plastiques, etc.) provoqués par les effets métallurgiques (précipitation) affectent les mécanismes de diffusion macroscopiques impliqués dans les processus de précipitation (diffusion microscopique). En 1855, Fick propose deux équations en analogie avec l'équation de la chaleur de Fourier [Fourier and Darboux, 1822]. Les lois de diffusion classiques de Fick décrivent la diffusion de l'azote [Fick, 1855]. Eq.1.6 décrit la diffusion de la matière dans un milieu binaire en supposant que la diffusion est isotrope dans l'hypothèse d'un état stable. La diffusion se produit alors des régions de forte concentration vers les régions de faible concentration, avec une magnitude proportionnelle au gradient de concentration (dérivée spatiale).

$$\left(J_I^\phi\right)_z = -D_I^\phi \frac{\partial c_I^\phi}{\partial z} \tag{1.6}$$

Où $\left(J_I^\phi\right)_z$ est le flux dans la direction z, c_I^ϕ est la concentration de l'élément I, $\frac{\partial c_I^\phi}{\partial z}$ est le gradient de concentration en fonction de la direction z et D_I^ϕ est le coefficient de diffusion de l'élément I dans la phase ϕ décrite par une loi d'Arrhenius [Logan, 1982, Arrhenius, 1889].

La deuxième loi de Fick (Eq. 1.7), connue sous le nom de loi de conservation de la masse, est une équation non permanente. Cette équation ne s'applique qu'aux espèces (ou particules) strictement conservatrices [Philibert, 1990]. Eq. 1.7 prédit les changements de concentration par rapport au temps sous la forme d'une équation différentielle partielle également présente avec la condition aux limites :

$$\left\{ \begin{array}{rcll} \frac{\partial c_I^\phi}{\partial t} & = & -\frac{\partial \left(J_I^\phi\right)_z}{\partial z} & \text{sur} \quad \text{V} \\ J_I^\phi & = & \left(J_I^\phi\right)_z n_z & \text{sur} \quad \partial\text{V} \end{array} \right. \tag{1.7}$$

Où $\frac{\partial c_I^\phi}{\partial t}$ est le gradient de concentration en fonction du temps et ∂V est la surface du volume V

Cette loi ne considère que la diffusion à longue distance, autrement dit la diffusion sans précipitation. Cette loi ne s'applique pas à la nitruration gazeuse (ou dans d'autres cas de diffusion, par insertion ou substitution). Ceci est dû au fait que la diffusion à courte et longue distance crée des déformations libres de contrainte ε^F, et la loi de Fick ne tient pas compte du couplage contrainte-diffusion. Les couplages contrainte-diffusion entraîne deux types de problèmes : vectoriel (flux) et tensoriel (contraintes). Cela signifie que les équations sont un problème d'espace. En d'autres termes, la diffusion est un problème d'échelle, à la fois locale et globale. De ce fait, seule la diffusion à longue distance (c'est-à-dire l'effet global) est prise en compte. En réalité, les profondeurs de diffusion efficaces (c'est-à-dire la diffusion à longue distance) sont cruciales dans l'industrie comme il a été dit précédement. L'objectif est de les améliorer continuellement et d'augmenter leur épaisseur. Par conséquent, l'analyse du couplage contrainte-diffusion ne peut se faire que dans le cas d'un système binaire avec une solution solide infiniment diluée (pas de précipitation). Plusieurs chercheurs se sont intéressés aux équations de couplage entre diffusion et contrainte depuis le milieu du 20$^{\text{ème}}$ siècle. L'objectif des chercheurs a été de construire des modèles physiques capables de gérer l'équilibre mécanique et chimique d'un système ouvert (comme les traitements de surface thermochimiques) au moyen de coefficients élastiques. L'objectif ici était de retravailler les méthodes nécessaires au développement de formulations analytiques pour le couplage contrainte-diffusion en utilisant la thermodynamique irréversible. Cahn et Larché ont utilisé l'équation de Li pour étudier l'influence

des contraintes locales sur la diffusion dans un milieu solide présentant des inhomogénéités de composition [Chen-Min Li, 1978, Larche and Cahn, 1978a, Larché and Cahn, 1982]. Ils ont développé un modèle basé sur la thermodynamique d'un solide multicomposant qui trouve l'équilibre sous contrainte (non hydrostatique) [Larché and Cahn, 1973, Larche and Cahn, 1978a, Larché and Cahn, 1982, Larché and Cahn, 1985]. Ils se sont placés dans un cas purement élastique, afin d'estimer que l'équilibre est possible puisque tout mouvement relatif des atomes, soit par glissement, soit par diffusion, est ignoré.

1.2.1 Equations de couplage du flux avec les champs mécaniques

Cahn et Larché ont utilisé un formalisme basé sur l'équation définie par Einstein [Einstein, 1905] et Darken [Sridhar, 2010], montrant que le flux est proportionnel au gradient du potentiel de diffusion tel que présenté dans l'équation 1.8 [Larché and Cahn, 1973, Larche and Cahn, 1978a, Larché and Cahn, 1982].

$$\left(J_I^\phi\right)_{ij} = -B_{ij}^\phi \frac{\partial M_I^\phi}{\partial x_i} \tag{1.8}$$

Où M_I^ϕ est le potentiel de diffusion sur l'équilibre thermochimique des solides multiphases sous contrainte introduit par Cahn et Larché [Larche and Cahn, 1978a, Larché and Cahn, 1982, Larché and Cahn, 1985] où dans le cas insterstitiel : $M_I^\phi\left(P, \sigma_{ij}, c_I^\phi\right) = \mu_I^\phi\left(P, \sigma_{ij}, c_I^\phi\right)$. μ_I^ϕ est le potentiel chimique connu de l'élément I et $P = -\frac{1}{3}\sigma_{kk}$ est la pression hydrostatique d'un fluide [Pa]. Il est important de comprendre que dans le cas de la diffusion de l'azote, la force principale est le gradient de potentiel chimique $\frac{\partial \mu_N\left(P,\sigma_{ij},c_N^\phi\right)}{\partial x_i}$ de l'azote N dans la matrice ferritique, où la diffusion a lieu. Plus on s'éloigne de la surface, plus le potentiel chimique de l'azote est faible. Voorhees et Larché ont proposé un développement concernant le coefficient B [Larché and Cahn, 1985] :

$$B_{ij}^\phi = \frac{c_I^\phi}{\Phi RT}\left(D_I^\phi \delta_{ij} + \beta\sigma_{kk}\delta_{ij} + 2\gamma_I\sigma_{ij}\right) \tag{1.9}$$

Où $\Phi\left(= 1 + \left(\frac{\partial \ln \gamma_I}{\partial \ln c_I^\phi}\right)\right)$ est le facteur thermodynamique. Larche et Voorhees défini les coefficients β et γ comme étant des scalaires [Larché and Voorhees, 1996].

L'ajout des termes $(\beta\sigma_{kk}\delta_{ij} + 2\gamma\sigma_{ij})$ montre l'influence des contraintes sur la mobilité au moyen des contraintes hydrostatiques σ_{kk} et des contraintes normales σ_{ij}. Les auteurs suggèrent et montrent, par des expériences, que le terme $2\gamma_I\sigma_{ij}$ équivalent à l'effet du cisaillement ne semble pas avoir d'influence sur la mobilité [Kirchheim, 1986, Philibert, 1996b, Larché and Voorhees, 1996]. De plus, si les trois composantes σ_{kk} sont égales, l'effet bien connu de la pression hydrostatique est présent [Mehrer, 1996]. A l'heure actuelle, il n'est donc pas possible de définir réellement ces deux coefficients (β et γ). Ils seront donc utilisés sans leur donner un sens physique.

Sur la base de la théorie thermodynamique, lorsqu'un soluté mobile dans une solution solide idéale et diluée est soumis à des contraintes, le potentiel de diffusion devient :

$$M_I^\phi\left(T, \sigma_{ij}, c_I^\phi\right) = M_I^\phi\left(T, 0, c_I^\phi\right) - V_a\eta_I^\phi\sigma_{kk} \tag{1.10}$$

Dans le cas d'une solution diluée c'est-à-dire $c << 1$ et d'un matériau isotrope, le gradient du potentiel de diffusion devient [Larché and Cahn, 1985] :

$$\frac{\partial M_I^\phi}{\partial x_i} = \frac{RT}{c_I^\phi}\frac{\partial c_I^\phi}{\partial x_i} - V_a \eta_I^\phi \frac{\partial \sigma_{kk}}{\partial x_i} \tag{1.11}$$

Le flux (Eq. 1.8) dans le cas général, en cas de matériau isotrope, est égal à :

$$\left(J_I^\phi\right)_{ij} = -\frac{c_I^\phi}{RT}\left(D_I^\phi \delta_{ij} + \beta \sigma_{kk}.\delta_{ij} + 2\gamma\sigma_{ij}\right)\left(\frac{RT}{c_I^\phi}\frac{\partial c_I^\phi}{\partial x_i} - V_a \eta_I^\phi \frac{\partial \sigma_{kk}}{\partial x_i}\right) \tag{1.12}$$

1.2.2 Equations de couplage du tenseur des contraintes avec les champs de compositions

Il est nécessaire de déterminer le couplage d'un point de vue mécanique en fonction des champs de composition. Comme expliqué précédemment, à l'équilibre, le potentiel de diffusion M est constant et satisfait l'équation du bilan de masse (Eq. 1.7). L'expression de la concentration chimique d'équilibre est obtenue en fonction du potentiel de diffusion correspondant, $\left(M_I^\phi\right)_{eq}$, en supposant que $c_I^\phi \ll 1$.

$$\left(c_I^\phi\right)_{eq} = \exp\left(\frac{V_a}{RT}\left(M_I^\phi\right)_{eq} - \frac{E_f}{RT}\right)\exp\left(\frac{V_a}{RT}\left(\eta_I^\phi\right)_{ij}\sigma_{ij}\right) \tag{1.13}$$

La concentration d'équilibre chimique, peut être simplifiée comme suit :

$$\left(c_I^\phi\right)_{eq} = \chi_I^\phi \left(\eta_I^\phi\right)_{ij}\sigma_{ij} \tag{1.14}$$

Où $\chi_I^\phi = \frac{V_a}{RT}c_I^\phi$ est une notion introduite par Cahn et Larché, dans le cas d'un système ouvert élastique constant [Larché and Cahn, 1985]. Donc à l'équilibre :

$$\varepsilon_{ij}^F(c) = \left(\eta_I^\phi\right)_{ij} c_I^\phi + \chi\left(\eta_I^\phi\right)_{ij}\left(\eta_I^\phi\right)_{kl}\sigma_{ij} \tag{1.15}$$

Le problème de diffusion/équilibre mécanique est équivalent à la résolution du problème purement élastique pour un coefficient "fictif" $\mathcal{S}_{ijkl}^0$ connu. Les constantes d'élasticité pour un système ouvert sont définies comme suit :

$$\nu_0 = \frac{\nu - \chi_I^\phi\left(\eta_I^\phi\right)^2 E}{1 + \chi_I^\phi\left(\eta_I^\phi\right)^2 E} \quad ; \quad E_0 = \frac{E}{1 + \chi_I^\phi\left(\eta_I^\phi\right)^2 E} \tag{1.16}$$

Où ν_0 est le coefficient de Poisson "fictif" et E_0 est le module d'Young "fictif". Les équations 1.16 montrent que si la concentration, c_I^ϕ, ou le paramètre de couplage, η_I^ϕ, sont petits, alors, les constantes du système ouvert se réduisent aux constantes élastiques standard.

Dans le cas de l'isotropie, la loi de Hooke généralisée Eq. 1.2 et les équations 1.3 à 1.4 sont utilisées pour définir la déformation totale $\varepsilon_{ij}^{\text{tot}}$ comme :

$$\varepsilon_{ij}^{\text{tot}} = \frac{1+\nu}{E}\sigma_{ij} - \frac{\nu}{E}\sigma_{kk}\delta_{ij} + c_I^\phi \eta_I^\phi \delta_{ij} \tag{1.17}$$

Le tenseur des contraintes prend la forme :

$$\sigma_{ij} = 2\mu\left(\varepsilon_{ij}^{\text{tot}} - c_I^{\phi}\eta_I^{\phi}\delta_{ij}\right) + \lambda\left[\varepsilon_{kk}^{\text{tot}} - 3c_I^{\phi}\eta_I^{\phi}\right]\delta_{ij} \tag{1.18}$$

Dans le cas isotrope, les coefficients de Lamé μ et λ sont une fonction de E_0 et ν_0 (constantes d'élasticité pour un système ouvert) :

$$\lambda = \frac{E_0\left(\nu_0 + \chi_I^{\phi}\left(\eta_I^{\phi}\right)^2 E_0\right)}{(1+\nu_0)\left(1 - 2\nu_0 - 3\chi_I^{\phi}\left(\eta_I^{\phi}\right)^2 E_0\right)} \tag{1.19}$$

$$\mu = \frac{E_0}{2\,(1+\nu_0)} \tag{1.20}$$

L'équation d'équilibre mécanique (div = 0) appliquée à cette étude dans le cas d'un matériau isotrope est :

$$\text{div}\left[2\mu\left(\varepsilon_{ij}^{\text{tot}} - c_I^{\phi}\eta_I^{\phi}\delta_{ij}\right) + \lambda\left[\varepsilon_{kk}^{\text{tot}} - 3c_I^{\phi}\eta_I^{\phi}\right]\delta_{ij}\right] = 0 \tag{1.21}$$

1.2.3 Simulations numériques réalisées sur le couplage contrainte-diffusion

Les champs de contraintes auto-induits sont à l'origine du phénomène de diffusion induit par les contraintes, c'est pourquoi des recherches ont été menées sur le couplage. L'objectif de ces recherches numériques est, par exemple, de prévoir les fissures dans les problèmes de diffusion de l'hydrogène ou de l'oxygène, afin d'améliorer la cinétique de diffusion et donc de créer des couches de diffusion plus épaisses. Dans le cas de la diffusion de l'azote, par exemple, il est souhaitable de pouvoir minimiser le temps ou la température de traitement.

Le tableau 1.1 présente une liste non exhaustive des articles publiés dans la littérature sur les simulations numériques du couplage entre contrainte et diffusion. L'étude se concentre sur le couplage contrainte-diffusion appliqué à la diffusion interstitielle, comme indiqué précédemment dans les hypothèses des formulations analytiques. L'étude s'est principalement concentrée sur celui-ci. D'autres articles, en revanche, se sont concentrés sur la diffusion des atomes en substitution avec les lacunes (liste succincte présentée dans ce travail). La première colonne du tableau résume les formulations analytiques générales de la diffusion interstitielle et substitutive. Le tableau présente cinq exemples d'applications de la diffusion interstitielle : azote $N_2\,(N^+)$, hydrogène $H_2\,(H^+)$, oxygène $O_2\,(O^-)$, carbone C et lithium (Li^+). Le tableau montre les résultats de trois hypothèses de comportement des matériaux : élastique, élasto-plastique et visco-élastoplastique.

		Considérations générales	Interstitielle					Lacunes / Substitution
			$N_2\,(N^+)$	$H_2\,(H^+)$	$O_2\,(O^-)$	C	Li (Li^+)	
Comportement du matériau	Elastique	[Larché and Cahn, 1973] [Larche and Cahn, 1978b] [Larche and Cahn, 1978a] [Li, 1981] [Larché and Cahn, 1982] [Larché and Cahn, 1985] [Larche, 1988] [Larché and Voorhees, 1996] [Philibert, 1996a] [Voorhees and Johnson, 2004] [Nazarov and Mikheev, 2005] [Ko et al., 2007] [Gururajan and Lahiri, 2016]	[Galdikas and Moskalioviene, 2010] [Christiansen and Somers, 2010] [Moskalioviene and Galdikas, 2019] [Galdikas and Moskalioviene, 2020]	[Simon and Grzywna, 1992] [Xuan et al., 2009] [Haftbaradaran et al., 2011] [Dejardin et al., 2013] [Creton et al., 2014] [li Lin et al., 2017]	[Sallès-Desvignes et al., 2000] [Araki and Arai, 2010b] [Araki and Arai, 2010a] [Dong et al., 2013] [Zhang et al., 2014] [Liu and Shen, 2018] [Ramsay et al., 2019]	[Li et al., 2017]	[Gao et al., 2015] [Zuo and Zhao, 2014] [Baker et al., 2016] [Li et al., 2016]	
	Elastoplastique		[Jespersen et al., 2016] [Kücükyildiz et al., 2020]	[Di Leo and Anand, 2013] [Barrera et al., 2016]	[Creton et al., 2009] [Wang et al., 2015]		[Zhao et al., 2011]	
	Visco-élasto-plastique		[Depouhon et al., 2014]	[Anand, 2011]	[Loeffel and Anand, 2011]			[Villani et al., 2014]

TABLE 1.1 – Liste non exaustive des simulations numériques du couplage contrainte-diffusion.

1.2.4 Expériences du couplage entre un prétraitement et un traitement thermochimique

Les effets des contraintes auto-induites sur la diffusion ont été reconnus et étudiés depuis quelques années [Li et al., 1966, Larché and Cahn, 1973, Larche and Cahn, 1978a, Li, 1981, Larché and Cahn, 1982, Larché and Cahn, 1985, Larché and Voorhees, 1996, Philibert, 1996b]. Les effets des contraintes (appliquées/résiduelles) sont maintenant étudiés dans une variété d'applications de recherche afin d'améliorer les propriétés mécaniques des matériaux ou de minimiser le temps de traitement. Cette section se concentre sur les effets des contraintes sur la diffusion, comme l'influence des déformations élastiques ou plastiques, ainsi que l'effet des pré-contraintes résiduelles ou des taux de déformation plastique différents subis par le matériau avant le traitement. En raison de leurs qualités physiques et mécaniques distinctives, les métaux sont fréquemment utilisés comme matériaux structurels dans l'industrie moderne. La diffusion interstitielle se produit dans une variété d'applications, notamment la nitruration gazeuse (diffusion d'atomes d'azote), l'oxydation des métaux (diffusion d'atomes d'oxygène), la fragilisation structurelle par l'hydrogène (diffusion d'atomes d'hydrogène), etc. La nitruration gazeuse est un procédé thermochimique qui améliore les propriétés de surface d'un matériau, telles que la résistance à l'usure, à la fatigue et à la corrosion [Barrallier and Jégou, 2017]. Dans le cas de la nitruration gazeuse, l'objectif des chercheurs est de découvrir un moyen de réduire le processus et d'abaisser la température autant que possible. De longues périodes et des températures élevées ont généralement été employées, ce qui entraîne des coûts de fabrication élevés. Ces traitements longs et ces températures élevées sont principalement dus à la faible diffusivité de l'azote dans l'acier et au transfert de masse limité entre la réaction gazeuse et l'acier.

L'effet des contraintes sur la cinétique de diffusion est connu sous différents angles, notamment une contrainte homogène, un gradient de contrainte (souvent soumis par flexion), une déformation plastique (via les mécanismes de fluage et de fatigue), un état de contrainte résiduel (déformation élastique) subi précédemment par le matériau, et une vitesse de déformation plastique (densité de dislocation, courts-circuits de diffusion).

Les tableaux 1.2, 1.3 et 1.4 présentent une liste non exhaustive des articles publiés dans la littérature sur le couplage entre contrainte et diffusion. Le tableau 1.2 est à deux entrées montrant la relation entre l'expérience physique (contrainte appliquée ou contrainte résiduelle) et le phénomène physique (comme la transformation de phase (ϕ), les joints de grains (GB), la dislocation de densité (ρ_D), les lacunes ($\overline{V}$). Les tableaux 1.3 et 1.4 représentent une liste de références coïncidant entre le prétraitement thermique présenté dans le tableau 1.2 et les systèmes de diffusion (interstitiel ou substitution/vacances).

Le tableau 1.2 montre qu'un certain nombre d'études expérimentales ont pu mettre en évidence une amélioration du coefficient de diffusion (c'est-à-dire de la mobilité) grâce aux différents phénomènes physiques présentés (transformation de phase ϕ, joints de grains GB, dislocation de densité ρ_D et lacunes ($\overline{V}$). Le tableau comprend également une colonne qui décrit comment une contrainte homogène affecte la mobilité. En fait, les coefficients sont inclus dans le travail de Voorhees en 1996 (voir l'équation 1.9). Des exemples sont présentés dans ces colonnes.

		Coefficient diffusion D				σ		$\partial\sigma$
		ϕ	GB	ρ_D	$\overline{V}$	β	γ	
Contraintes appliquées σ	sans σ	Effet de Kirkendall	Taille des grains					
	$\sigma < \sigma_E$		Fluage	Fluage	Fluage	*Traction*	*Cisaillement*	Flexion Polissage Sablage
	$\sigma > \sigma_E$		Fluage Laminage à froid Traction	Fluage Laminage à froid Traction	Fluage			
Contraintes résiduelles σ_R à partir du gradient spatial	Thermique $\partial\varepsilon_{th}$							
	Plasticité $\partial\varepsilon_p$	Broyage à billes LHT [1]	SMAT [2] SANCT [3] USP [4] UCFT IB	SMAT SANCT UCFT Fluage SP [5]	SANCT			
	Transf. phase $\partial\varepsilon_T$	HPT [6] Broyage à billes Traitement thermique LHT		HPT				Flexion Sablage
	Lacunes $\partial\varepsilon\overline{V}$				IB			

TABLE 1.2 – Liste non exhaustive des phénomènes physiques obtenus par des traitements mécaniques.

1. Traitement thermique au laser
2. Traitement mécanique de surface par attrition -> formation de nanocristallites dans la couche de surface (nanostructuration) = amélioration des propriétés mécaniques des matériaux métalliques.
3. Traitement nanocristallin à courant alternatif de surface -> rupture et reformation des liaisons chimiques dues à la transgression ionique = grain affiné.
4. Grenaillage de précontrainte par ultrasons -> traitement de surface par travail à froid via un milieu qui impacte la surface d'une pièce mécanique : déformation plastique importante à la surface de la pièce (nanocristallisation) + couche de contraintes résiduelles de compression = amélioration des propriétés mécaniques du matériau.
5. Grenaillage de précontrainte -> (similaire au procédé USP) traitement de surface par travail à froid via un milieu qui impacte la surface d'une pièce mécanique : déformation plastique importante à la surface de la pièce (nanocristallisation) + couche de contraintes résiduelles de compression = amélioration des propriétés mécaniques du matériau.
6. torsion froide à haute pression -> transformation de phase (par exemple austénite en martensite)

Traitements	Interstitiel			Lacunes / Substitution	Observations	
	$N_2\,(N^+)$	$H_2\,(H^+)$	$O_2\,(O^-)$		Couche de surface	Couche de diffusion
Effet de Kirkendall				[Smigelskas and Kirkendall, 1947]		
Taille de grains						(grains plus gros) ↙
Fluage	[Limarga and Wilkinson, 2006]		[Moulin et al., 1996] [Krupp et al., 2008]		traction ↗ compression ↙	traction ↗ compression ↙
Essai de traction ou de compression	[Guillot et al., 2016]	[Beck et al., 1966] [Bockris et al., 1971] [Kirchheim, 1986] [Hwang and Perng, 1994] [Frappart et al., 2012]	[Calvarin et al., 2000] [Yen and Hwu, 2000] [Calvarin-Amiri et al., 2001] [Gauthier et al., 2009] [Araki and Arai, 2010b] [Araki and Arai, 2010a] [Zhou et al., 2010] [Ramsay et al., 2019]	[Li et al., 2017]	traction ↗ compression ↙	traction ↗ compression ↙
Essai de cisaillement		[Kirchheim, 1986]			pas d'effet	no effect
Essai de flexion	[Hirsch et al., 2004] [Guillot, 2018]				traction ↗ compression ↙	traction ↗ compression ↙
Polissage	[Hirsch et al., 2004]					↗
Sablage	[Hirsch et al., 2004]					↗
Laminage à froid	[Lecis et al., 2012] [Lu et al., 2021] [Biehler et al., 2017]				↙	↙
Broyage à billes	[Cemin et al., 2010]				↗	↗
Traitement thermique	[Manova et al., 2007] [Kochmanski and Nowacki, 2008]	[Vizcaíno et al., 2014]				$T_{annealing}$ augmente -> grains plus gros : ↙
Traitement thermique au laser	[Panfil et al., 2017]					

TABLE 1.3 – Liste non exaustive de références de traitements mécaniques (inclus dans le tableau 1.2), classées selon leur type de diffusion (insterstitielle, lacunes ou substitutions), et description des observations faites sur le comportement de la cinétique de diffusion en couplage avec un traitement thermochimique. (partie n°1)

Traitements	Interstitielle			Lacunes / Substitution	Observations	
	$N_2\,(N^+)$	$H_2\,(H^+)$	$O_2\,(O^-)$		Couche en surface	Couche de diffusion
SMAT	[Tong et al., 2003] [Tong et al., 2006] [Lin et al., 2006] [Tong et al., 2007] [Chemkhi et al., 2013] [Balusamy et al., 2013] [Samih et al., 2014] [Sun et al., 2016] [Chemkhi et al., 2017]			[Wang et al., 2003] [Wang et al., 2005] [Lu et al., 2010]	↗	↗
SANCT	[Wang et al., 2006]				↗	
USP	[Gu et al., 2002] [Thiriet et al., 2012]					↗
SP	[Kikuchi et al., 2010] [Jayalakshmi et al., 2016] [Biehler et al., 2017]				↗	↗
UCFT	[She et al., 2013]				↗	↗
IB : Bombardement ionique	[Ochoa et al., 2006] [Abrasonis et al., 2006]					↗
Diffusion de carbone	[Stewart et al., 1994]					compression ↙
HPT	[Ferkel et al., 2002] [Ferkel et al., 2003b] [Ferkel et al., 2003a] [Shabashov et al., 2009] [Ramazanov et al., 2016]				↗	↗
Attrition atomique (plasma d'argon)	[Cemin et al., 2010]					↗

TABLE 1.4 – Liste non exaustive de références de traitements mécaniques (inclus dans le tableau 1.2), classées selon leur type de diffusion (insterstitielle, Lacunes ou substitutions), et description des observations faites sur le comportement de la cinétique de diffusion en couplage avec un traitement thermochimique. (partie n°2)

1.2.5 Conclusion

Ce chapitre bibliographique a permis de :

— Définir les formulations analytiques du couplage contrainte-diffusion dans la situation de diffusion interstitielle, en commençant par la formulation générale et en progressant vers la formulation simplifiée. Ces simulations permettent de réaliser des simulations macroscopiques proches des contextes réels des expériences, même si elles n'incluent pas encore tous les systèmes actifs,

— Regrouper un certain nombre d'articles sur les simulations numériques de matériaux élastiques, élastoplastiques et viscoélastoplastiques,

— Regrouper un certain nombre d'articles expérimentaux sur l'influence de la contrainte sur la cinétique de diffusion. L'influence des contraintes a été principalement observée par les contraintes appliquées (essai de traction/compression/cisaillement, essai de fluage) et les contraintes résiduelles impliquant des gradients de déformation : thermique, plastique ou transformations de phase.

Ces études ont permis de comprendre l'intérêt de ses prétraitements sur la cinétique de diffusion via les différentes mécaniques que sont celles jouant sur le coefficient de diffusion, c'est-à-dire les transformations de phase, les joints de grains, les densités de dislocation, l'effet des contraintes homogènes, puis jouant sur les forces de transport via un gradient de contrainte. L'effet des contraintes appliquées, qu'elles soient à gradient ou homogènes, a révélé que la contrainte de traction augmente la cinétique de diffusion alors que la contrainte de compression la diminue. La contrainte de torsion semble avoir peu d'effet sur la diffusion ; néanmoins, peu d'essais semblent avoir été réalisés. Les essais de charge de flexion donnent les mêmes résultats que les essais de base en traction/compression, l'épaisseur de la surface traitée augmentant du côté de la traction et diminuant du côté de la compression. Ils peuvent absorber les contraintes résiduelles et renforcer la profondeur du processus de nitruration, selon des tests incluant des mécanismes de fatigue et de fluage. Le gradient de contrainte externe a un impact considérable sur le développement de la contrainte chimique lorsque le temps de diffusion augmente. Les traitements impliquant des surfaces nanostructurées qui augmentent la fraction volumique des joints de grains ont une influence significative sur la cinétique de diffusion. Ceci est dû au fait que ces nanostructures fournissent aux atomes interstitiels de la surface du matériau des chemins de diffusion rapides. Les matériaux nanostructurés présentant une forte densité de dislocation ont une influence significative sur la dynamique de diffusion.

Cette revue de la littérature a montré que la simulation numérique et les études expérimentales se concentrent principalement sur la prise en compte d'un coefficient de diffusion effectif en ne considérant que le terme de Nernstian (force motrice ou gradient de contrainte) et en ignorant l'impact de la contrainte sur la mobilité (facteur $\beta\sigma_{kk}$). Cependant, de nombreux traitements mécaniques ont démontré la relation entre les contraintes résiduelles et les phénomènes de microstructure. Le premier travail clé de cette thèse sera d'étudier par simulations numériques la prédominance entre la force motrice et l'effet de la contrainte sur la mobilité. Le deuxième travail clé de cette thèse sera de mettre en place des expériences basées sur les observations expérimentales et de corréler les compréhensions numériques avec les observations expérimentales.

Cette revue de la littérature a également montré que de nombreuses études s'intéressent au couplage entre le prétraitement mécanique et le traitement thermochimique afin d'améliorer les épaisseurs des couches de diffusion. Elles fondent leurs résultats sur des aspects de déformation plastique incompatibles (densité de joints de grains, densité de dislocation, etc.) en oubliant les aspects de déformation élastique à travers par exemple la

contrainte résiduelle. Le troisième travail clé de cette thèse sera donc de découpler les effets des déformations élastiques compatibles et des déformations plastiques incompatibles par le biais d'expériences.

Chapitre 2

Mise en évidence du couplage contrainte-diffusion

2.1 Simulations du couplage contrainte-diffusion

De nombreuses situations nécessitent aujourd'hui l'utilisation de technologies numériques afin de mener à bien les études (qui sont coûteuses, longues, etc.). Ainsi, le but de ces simulations numériques du couplage contrainte-diffusion est d'abord de comprendre le phénomène en faisant varier des facteurs tels que le temps, l'épaisseur de l'échantillon, les conditions aux limites, le paramètre β ou l'amplitude de la contrainte. L'objectif est de comprendre l'effet sur la cinétique de diffusion, en particulier la diffusion à longue distance de l'azote. Ces résultats de calcul représenteront des valeurs numériques de paramètres phénoménologiques, qui seront ensuite analysés et interprétés afin de concevoir des études appropriées pour tenter de valider ces phénomènes et ainsi conclure sur la dominance des effets de contrainte (force motrice et mobilité). Il est important de noter que les simulations numériques (réalisées dans ce travail) sont une représentation mathématique du comportement d'un système réel sous certaines conditions (solution infiniment diluée, pas de phénomènes de précipitation, pas de co-diffusion, etc).

Dans cette section, deux modèles seront présentés. Un premier modèle 2D implémenté sur le logiciel libre FreeFEM++ [Hecht, 2020] dans le but de visualiser et de comprendre les champs de concentration et de contrainte 2D. Les équations de couplage ont mis en évidence un couplage entre un aspect vectoriel par les composantes flux et concentration et surtout un aspect tensoriel par les composantes déformation et contrainte. Le but de ce modèle est de mettre en évidence l'équilibre mécanique à travers la section transversale d'un échantillon pour différents cas d'étude : diffusion symétrique, diffusion dissymétrique, variation de l'épaisseur de l'échantillon. Aucune étude paramétrique ne sera présentée dans ce modèle. Un second modèle 1D (2D axisymétrique) sera présenté, utilisant cette fois un code de calcul développé au laboratoire. Le but de ce modèle est de réaliser des études paramétriques sur l'effet du gradient de contrainte et des contraintes sur la mobilité en prenant en compte, d'une part, l'aspect temporel des contraintes résiduelles et, d'autre part, l'aspect constant des contraintes appliquées (pour toutes les sources de fluage négligées).

La figure 2.1 illustre schématiquement l'algorithme utilisé dans ce travail.

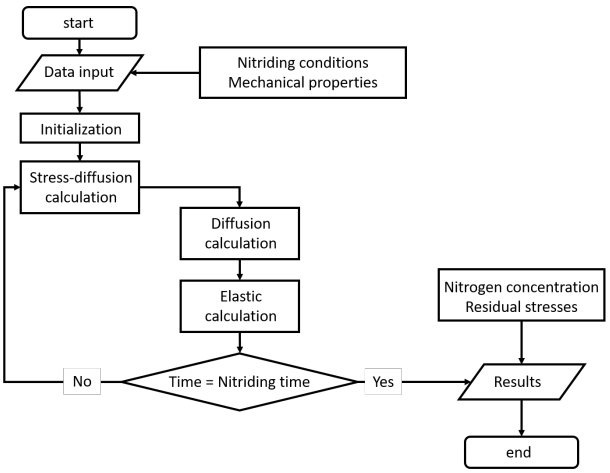

FIGURE 2.1 – Algorithme du couplage contrainte/diffusion.

2.1.1 Hypothèses

Cette partie traite des simulations numériques basées sur le code de calcul FreeFEM++, et son objectif principal est de se placer dans un cas avec des hypothèses fortes :

— Système binaire fer-azote (α-Fe-N) ;

— Cas de diffusion interstitielle ;

— Milieu infiniment dilué ($c \ll 1$) avec un seul élément diffuseur (sans co-diffusion de carbone ni précipitation associée) ;

— Un matériau élastique supposé isotrope (E = 200 [GPa] et ν = 0,29 [-] [Fallot, 2015]) ;

— Processus isotherme : 520 °C.

Tout au long de ces études numériques, la concentration en azote sera considérée comme constante, c'est-à-dire que des conditions de Dirichlet seront utilisées.

2.1.2 Implémentation dans FreeFEM++ (modèle 2D)

Un modèle 2D a été construit à l'aide du logiciel libre FreeFEM++ [Hecht, 2020]. A partir d'une formulation variationnelle, ce langage permet de résoudre facilement un problème linéaire, non linéaire, dépendant du temps ou couplé. Les équations du couplage contrainte-diffusion présentent un aspect vectoriel par l'aspect flux et concentration mais aussi un aspect tensoriel par la prise en compte des déformations et des contraintes. L'intérêt principal de ce modèle est d'observer à partir d'une maille fine ($\Delta z = 5$ μm), les champs de concentration et de contrainte hydrostatique sur la section transversale d'un échantillon. Ces champs seront présentés comme des images symétriques et aussi comme des profils en fonction de la profondeur.

L'aspect tensoriel de la contrainte sur la cinétique de diffusion en utilisant un modèle de couplage contrainte-diffusion 2D sera ensuite étudié. L'hypothèse de contraintes planes est utilisée dans ce modèle, permettant de réduire un modèle 3D à un modèle 2D.

L'aspect variationnel du problème mécanique prenant en compte la déformation libre de contrainte de type déviateur, sous forme simplifiée, est donné par l'équation 2.1 :

$$\int_{\partial V} v_i.g_i dS - \int_V \frac{\partial v_i}{\partial z} \left(2\mu \left(\varepsilon_{ij}^{tot} - c\eta_{ij}\right) + \lambda \left[\varepsilon_{kk}^{tot} - c\eta_{kk}\right] \delta_{ij}\right) dV = 0 \tag{2.1}$$

L'aspect variationnel du problème de diffusion, sous une forme simplifiée, est résumé par l'équation 2.2 :

$$\int_V c^* \frac{\partial c}{\partial t} dV + \int_{\partial V} c^*.\mathrm{j} dS - \int_V \frac{\partial c^*}{\partial z} \left[-D\frac{\partial c}{\partial z} + \frac{1}{3}\frac{D\Delta v}{RT} c.\frac{\partial \left(\sigma_{kk}\delta_{ij}\right)}{\partial z}\right] dV = 0 \tag{2.2}$$

Une analyse a été menée dans la situation de l'équation 2.2, c'est-à-dire en considérant uniquement l'influence de la contrainte sur les forces motrices ($\nabla\sigma \neq 0$ et $\beta = 0$).

La figure 2.2 montre les champs de concentration c et de contrainte hydrostatique σ^{H} (= - $\frac{1}{3}\sigma_{kk}$) 2D d'un échantillon carré de 1×1 mm soumis à une concentration de surface fixe de $c_0 = 0,001$ [-] avec les paramètres d'étude présentés dans le tableau 2.1. Le coefficient de diffusion est beaucoup plus élevé que dans la réalité car l'objectif est uniquement d'étudier l'effet et l'influence des contraintes sur la cinétique sans réaliser d'études paramètriques.

D [cm^2.s^{-1}]	T [°C]	E [GPa]	ν [-]	t [s]	η [-]
5.10^{-5}	520	200	0.29	1	$2{,}4.10^{-3}$

TABLE 2.1 – Paramètres utilisés : le coefficient de diffusion D_0, la température de traitement T, le module de Young E, le coefficient de Poisson ν et le temps t.

Ce modèle 2D vise à comprendre les aspects tensoriels en visualisant la symétrie des champs ainsi que les effets de bord. Les champs de concentration montrent une concentration maximale à la surface suivie d'une décroissance. Les champs de contrainte hydrostatique montrent une contrainte négative à la surface avec une augmentation de la contrainte jusqu'à une contrainte positive. Les calculs de contrainte sont mécaniquement valides car l'équilibre mécanique est respecté immédiatement à partir de l'équation 2.1 mentionnée ci-dessus.

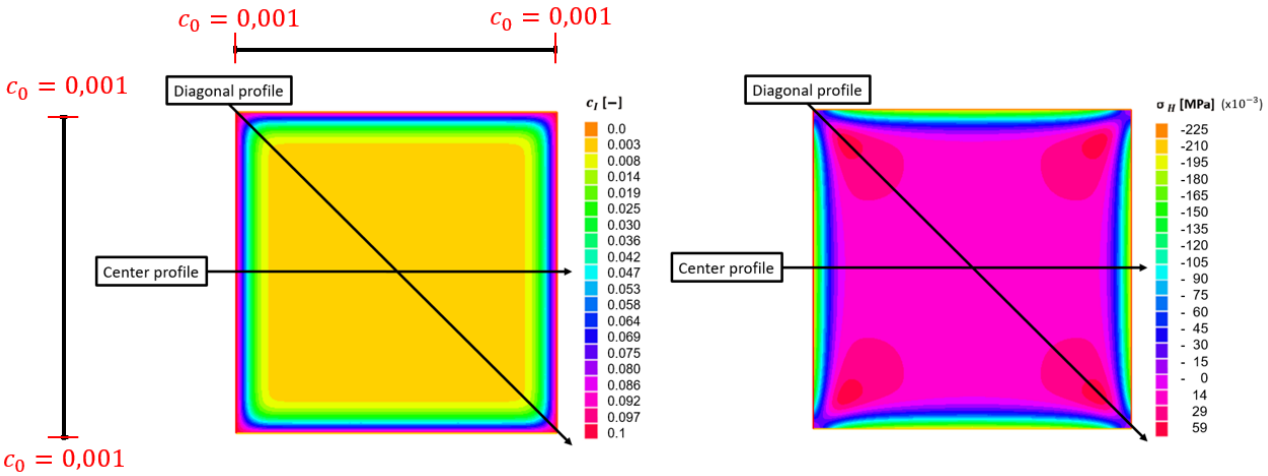

FIGURE 2.2 – a) Champ de concentration et b) champ de contrainte hydrostatique, d'une diffusion prenant en compte uniquement la force de transport ($\nabla\sigma \neq 0$ et $\beta = 0$), d'un échantillon carré 1×1 mm.

Les évolutions de la concentration et de la contrainte hydrostatique du profil central et du profil diagonal sont, respectivement, présentées dans les figures 2.3a) et b). Le profils centraux présentent les évolutions typiques. Une loi de type erfc est observée pour le profil de concentration, c'est-à-dire une concentration maximale à la surface et une diminution rapide jusqu'à zéro dans le matériau de base. C'est la solution classique de la loi de Fick avec ces conditions aux limites et initiales. Le profil de contrainte hydrostatique montre un maximum des contraintes (de compression) en surface et une forte croissance des contraintes jusqu'à des valeurs plus ou moins élevées en traction suivant l'épaisseur de l'échantillon. Le profil diagonal montre une évolution qui ne suit pas une loi de type erfc et démontre une nette augmentation de la concentration en profondeur. Le profil diagonal en contrainte hydrostatique montre un profil particulier avec une valeur nulle à la surface, un gradient négatif avec une faible contrainte de compression, un gradient positif avec une contrainte de traction beaucoup plus élevée que le profil central, et enfin un gradient négatif vers le matériau de base. L'équation utilisée semble avoir un effet inverse sur l'accélération des contraintes (équation 2.2). En contrainte hydrostatique, le profil diagonal présente un gradient de contrainte plus faible, des contraintes de compression très faibles, puis des contraintes de traction. L'équation utilisée ne considère que l'effet du gradient de contrainte ($\nabla\sigma \neq 0$) en termes de couplage et ne prend donc pas en compte l'effet du signe de la contrainte mais uniquement le signe du gradient de contrainte. L'accélération de la concentration est simplement le produit d'un double effet de flux (l'addition des flux latéraux et perpendiculaires) et de l'effet de gradient. Cette première simulation a été validée en utilisant le profil de concentration analytique de Fick (non présenté ici).

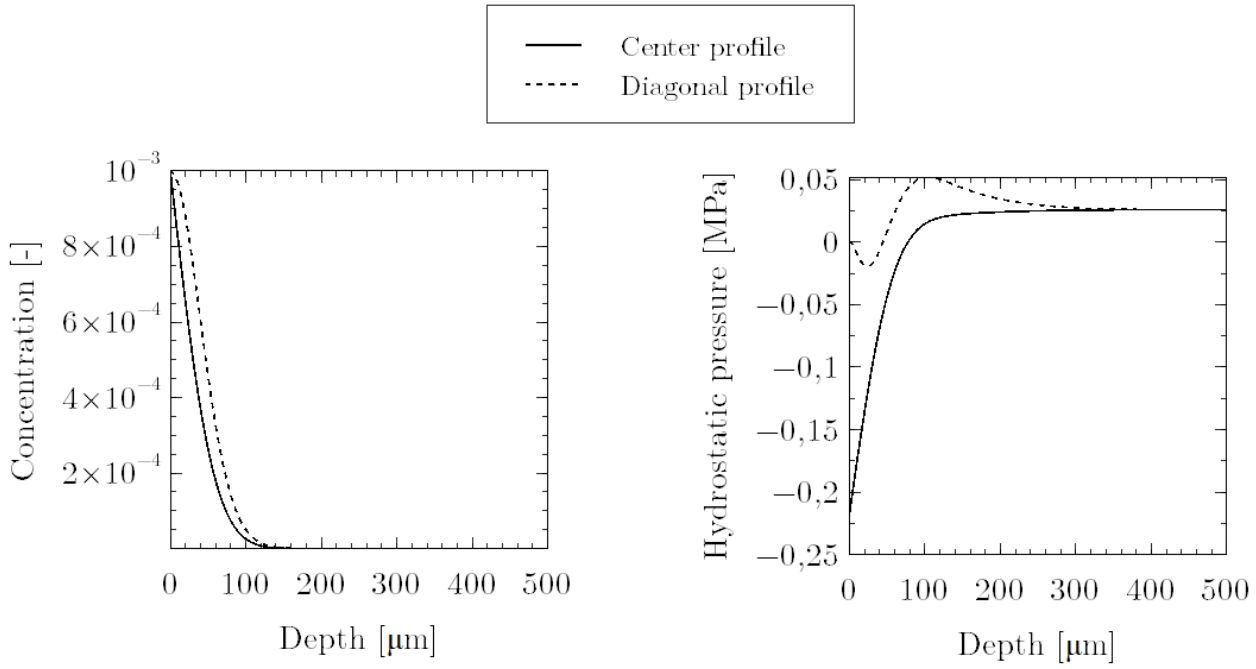

FIGURE 2.3 – Évolution de la concentration et de la contrainte hydrostatique en fonction de la profondeur, pour une diffusion prenant en compte uniquement la force de transport ($\nabla\sigma \neq 0$ et $\beta = 0$), pour un échantillon carré 1×1 mm pour les profils diagonal et central.

Le facteur de triaxialité est représenté sur la figure 2.4a) pour mieux comprendre l'aspect tensoriel sur la cinétique. Le rapport entre la contrainte hydrostatique σ^{H} et la contrainte de von Mises équivalente σ^{VM}

détermine la triaxialité Tx des contraintes : $Tx = \frac{\sigma^{\mathrm{H}}}{\sigma^{\mathrm{VM}}}$. La figure 2.4a) montre que le profil central est en compression unixiale ($Tx = -0.33$) pour les 80 premiers μm, puis tend vers une contrainte d'équi-bitraction ($Tx = 0.66$) au cœur. Le profil diagonal décrit un profil de compression uniaxiale ($Tx = -0.33$) à la surface, suivi d'un état de traction uniaxiale ($Tx = 0.33$) et d'un état de contrainte d'équi-bitraction ($Tx = 0.66$) au cœur.

La figure 2.4b) illustre l'évolution du module d'Young E_0 défini pour un système ouvert, décrit par l'équation 1.16. Ce profil montre une évolution inverse de la concentration, plus la concentration est élevée, plus le module de Young E_0 est faible. Bien que les traitements thermochimiques soient destinés à améliorer les propriétés de surface telles que la dureté et la résistance à la fatigue, ce graphique montre que l'échantillon perd de son élasticité (faible perte dans cette application) le long de la couche de diffusion.

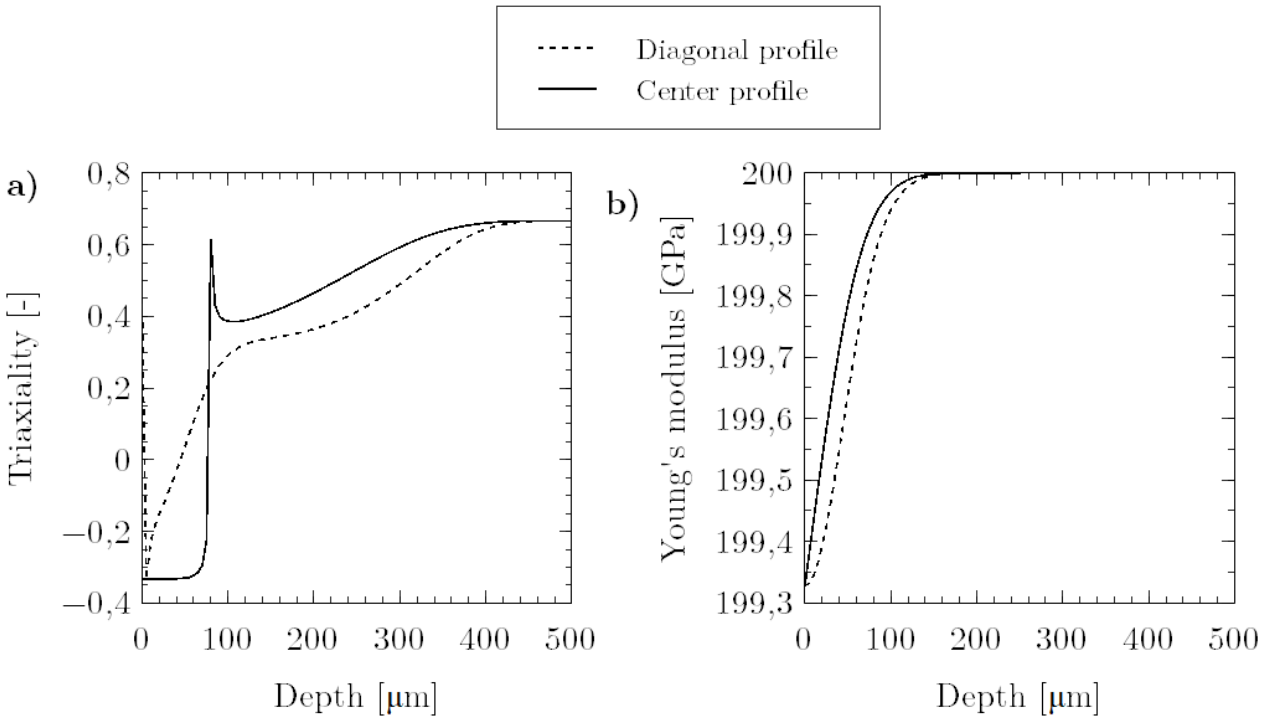

FIGURE 2.4 – Évolution a) de la triaxialité et b) du module d'Young, en fonction de la profondeur pour une éprouvette carrée 1×1 mm pour les profils diagonal et central.

Les profils central et diagonal de la concentration, de la contrainte hydrostatique, du facteur de triaxialité et du module d'Young dans un système ouvert ont été observés. Ces résultats ont permis de comprendre l'intérêt expérimental de disposer d'échantillons de dimensions suffisamment grandes pour éviter tout effet de bord. Les observations montrent que le comportement dans les coins semble être uniquement un problème causé par un double flux, avec un profil de contrainte hydrostatique très spécifique qui ne présente pas un profil standard. Cette observation montre l'intention de comprendre les aspects tensoriels afin d'observer ces phénomènes qui, dans des cas industriels spécifiques tels que les dents d'engrenages, peuvent provoquer des défaillances prématurées en modifiant les caractéristiques de durée de vie en fatigue des pièces subissant des phénomènes de double flux.

2.1.3 Implémentation en langage C (modèle axisymétrique 2D)

Un modèle axisymétrique 2D (1D) a été développé dans le but de réaliser des études paramétriques et ainsi observer la prédominance de l'effet des contraintes entre la force de transport et la mobilité. La méthode des différences finies est utilisée. Ce modèle 1D conduit à l'utilisation de nouvelles hypothèses. Les déformations et les contraintes macroscopiques peuvent être exprimées en utilisant les relations de la mécanique des milieux continus. Les contraintes résiduelles déterminent un champ statiquement admissible (S.A.) et satisfont les équations d'équilibre $\sigma_{ij,j} = 0$ et $\sigma_{ij} n_j = g_i$ sur ∂V où n_j est le vecteur unitaire dans la direction $\vec{j}$ sur la frontière et g_i est la force appliquée dans la direction $\vec{i}$, en d'autres termes, la densité de force de surface en ∂V. Donc pour $z = 0$, $\sigma_{ij} n_j = 0$ avec $n_j = \begin{pmatrix} 0 \\ 0 \\ 1 \end{pmatrix}$: $\left\{ \begin{array}{rcl} \sigma_{12} & = & 0 \\ \sigma_{23} & = & 0 \\ \sigma_{33} & = & 0 \end{array} \right.$.

La solution analytique de l'équilibre est directement adaptée au problème à partir de l'équation 1.12 et de l'équation 1.21. Le fait de considérer un corps semi-infini implique que $\left(J_I^\phi\right)_i = \left(J_I^\phi\right)_z$ et $2\gamma_I \sigma_{ij} = 0$ pour toute valeur de γ_I (seul le flux le long de z n'est pas égal à zéro). Il s'ensuit que le flux (voir l'équation 1.12) devient :

$$\begin{aligned} \left(J_I^\phi\right)_z &= -\frac{c_I^\phi}{\Phi RT}\left(D_I^\phi + \beta\sigma_{kk}\right)\left(\frac{RT\Phi}{c_I^\phi}\frac{\partial c_I^\phi}{\partial z} - V_a\eta_I^\phi\frac{\partial \sigma_{kk}}{\partial z}\right) \\ &= -\left(D_I^\phi + \beta\sigma_{kk}\right)\frac{\partial c_I^\phi}{\partial z} + \frac{V_a\eta_I^\phi}{\Phi RT}\left(D_I^\phi + \beta\sigma_{kk}\right)c_I^\phi\frac{\partial \sigma_{kk}}{\partial z} \end{aligned} \tag{2.3}$$

L'équation 2.3 montre que la somme $(D\delta_{ij} + \beta\sigma_{kk}\delta_{ij})$ ralentira la diffusion lorsque $\beta\sigma_{kk}\delta_{ij}$ est négatif, où D est indépendant de la concentration.

2.1.3.1 Étude des contraintes résiduelles

L'effet des contraintes chimiques sur la diffusion a été largement étudié dans la littérature, cependant, l'objectif est d'avoir des informations sur la prédominance entre l'effet des contraintes sur la partie mobilité (voir l'équation 2.3) avec le $(D\delta_{ij} + \beta\sigma_{kk}\delta_{ij})$ et le gradient de contrainte [Larche and Cahn, 1978a, Chen-Min Li, 1978].

2.1.3.1.1 Influence du paramètre β. Le paramètre β établi par Voorhees et Larché permet d'observer l'influence de la contrainte sur la mobilité en faisant varier l'amplitude de la contrainte. L'ampleur des contraintes impliquerait qu'elles jouent un rôle important dans la cinétique de diffusion d'un point de vue empirique. La première étude porte donc sur l'effet du paramètre β sur la cinétique de diffusion d'une plaque semi-infinie (10 mm d'épaisseur) traitée pendant 1 heure à 520 °C avec une concentration en surface constante. Dans cette étude, trois valeurs de β $\mathrm{cm^2.s^{-1}.MPa^{-1}}$ sont analysées : 0, 10^{-11} et 10^{-10}, toutes comparées à l'équation de Fick où le coefficient de diffusion est égal à $D = 4.9.10^{-8}$ $\mathrm{cm^2.s^{-1}}$. Ces valeurs choisies de β ont été définies après plusieurs simulations numériques afin de ne comparer que certaines valeurs intéressantes.

La figure 2.5 montre uniquement l'effet d'un gradient de contrainte résiduelle ($\nabla\sigma \neq 0$) en utilisant l'équation 1.12 dans le cas de $\beta = 0$. Une influence positive est observée grâce au gradient de contrainte positif.

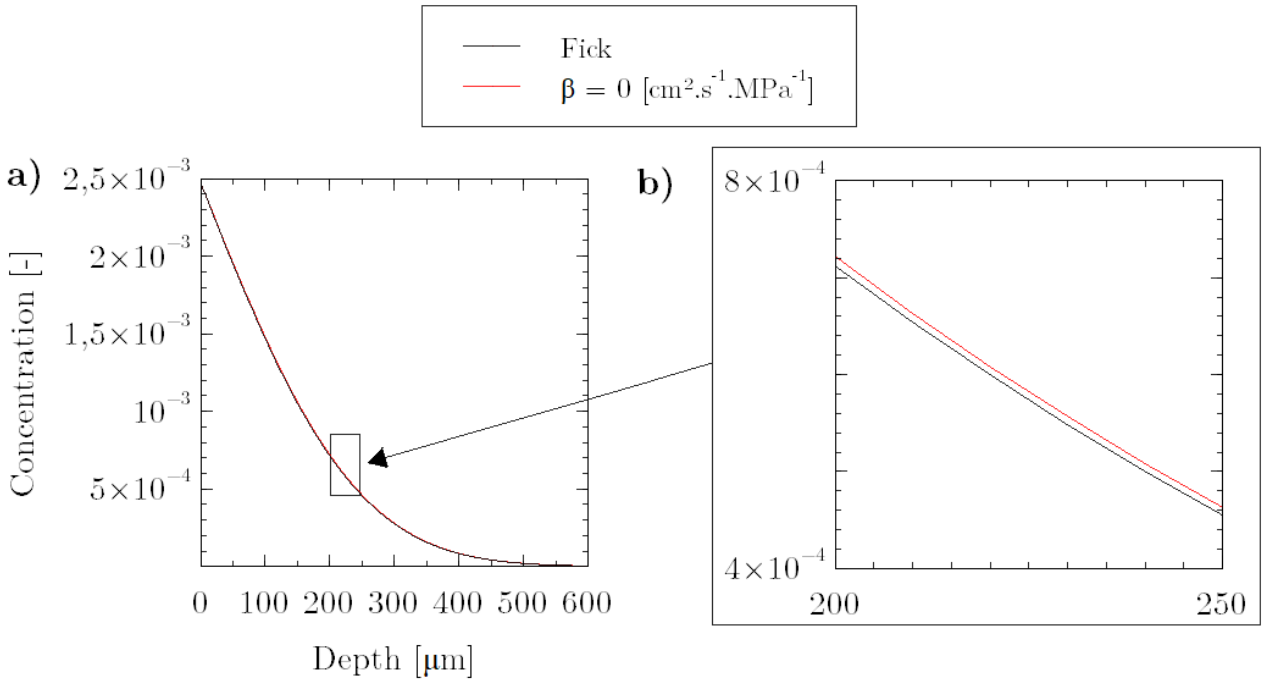

FIGURE 2.5 – Évolution des profils a) de concentration et b) de contraintes résiduelles, en fonction de la profondeur pour un échantillon de 10 mm d'épaisseur à 520 °C pendant 1 h. Comparaison du profil de Fick et de $\beta = 0$.

La figure 2.6 a) montre que lorsque la valeur de β augmente, la diffusion ralentit. Plus précisément, il est intéressant de noter qu'à partir d'une certaine valeur de β, la diffusion est ralentie par rapport au profil analytique de Fick. La courbe de $\beta = 10^{-11}\text{cm}^2.\text{s}^{-1}.\text{MPa}^{-1}$ montre une diffusion qui reste accélérée par rapport à la courbe de Fick mais qui est ralentie par rapport à la courbe prenant en compte uniquement le gradient de contrainte. Sur la courbe de $\beta = 10^{-10}\text{cm}^2.\text{s}^{-1}.\text{MPa}^{-1}$, la diffusion est considérablement ralentie par rapport à la courbe de Fick. De plus, le gradient de contrainte [MPa/mm] augmente lorsque β augmente, comme le montre le tableau 2.2). L'évolution positive du gradient de contrainte conduit à une diminution significative de la cinétique de diffusion. En général, l'étude montre la compétition entre le gradient de mobilité et la force motrice mécanique (gradient de contrainte seul sans effet sur la mobilité). La figure 2.6 b) correspond au zoom représenté par un rectangle dans la figure 2.6 a) et illustre le fait que lorsque β atteint une valeur particulière, la mobilité prend le dessus sur l'influence du gradient de contrainte. Le tableau 2.2 rassemble également les ordres de grandeur F entre le coefficient de diffusion de Fick D_0 et le facteur $(\sigma_{kk}.\beta)$ où $\sigma_{kk}.\beta = F \times D$. Le signe des contraintes résiduelles est à l'origine de cette influence négative sur la cinétique.

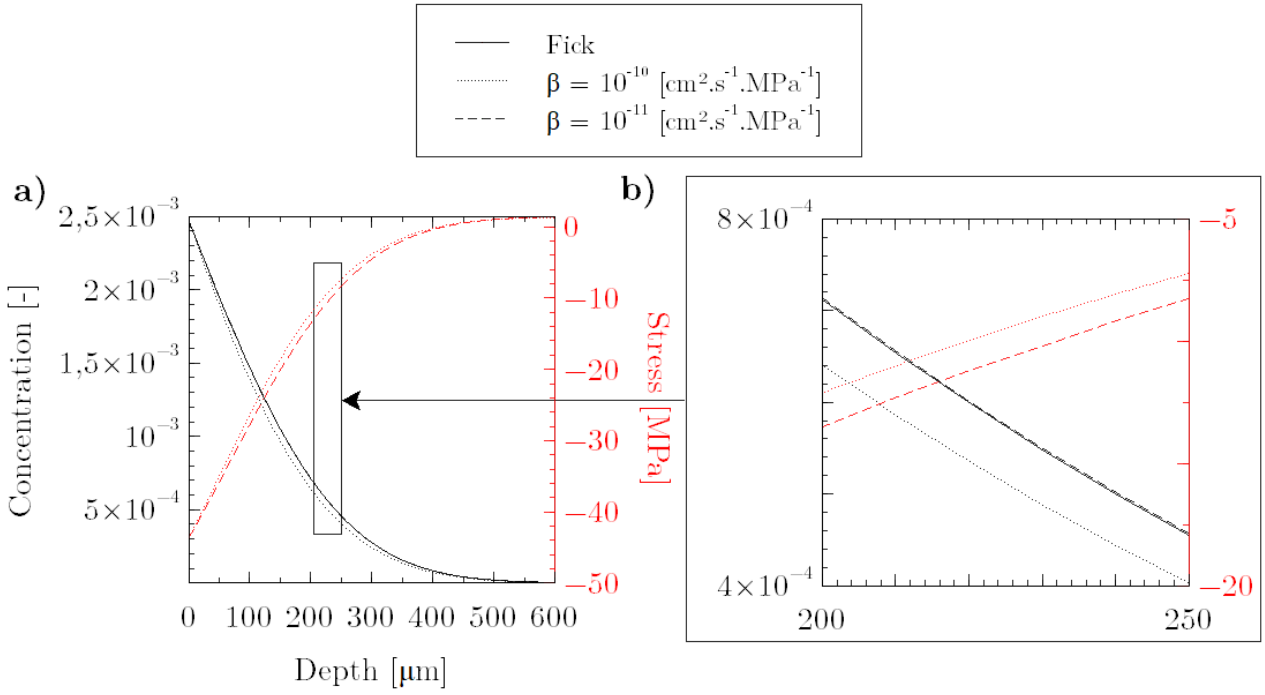

FIGURE 2.6 – a) Évolution des profils de concentration et de contraintes résiduelles en fonction de la profondeur pour un échantillon de 10 mm d'épaisseur à 520 °C pendant 1 h. Comparaison du profil de Fick et de 2 valeurs β du coefficient : 10^{-11} et 10^{-10} cm^2.s^{-1}.MPa^{-1}. b) Zoom de la figure a).

β	$\frac{\partial\sigma}{\partial z}$ [MPa/mm]	F [-]
0	139,3	0
10^{-11}	139,5	0,01
10^{-10}	141,2	0,1

TABLE 2.2 – Évolution du gradient de contrainte résiduelle et évolution du facteur F entre le coefficient de diffusion de Fick D_0 et le terme de mobilité de la contrainte ($\sigma_{kk}.\beta$) obtenus pour 3 valeurs de β.

La figure 2.7 montre l'influence des contraintes sur la mobilité ($\beta \neq 0$ et $\nabla\sigma = 0$). Cette observation montre que pour toutes les valeurs de β la cinétique de diffusion est ralentie. La figure 2.8 compare les profils de concentration et de contrainte résiduelle en fonction de la profondeur pour le cas ($\beta \neq 0$ et $\nabla\sigma = 0$) et le cas ($\beta \neq 0$ et $\nabla\sigma \neq 0$) pour $\beta = 10^{-10}$ cm^2.s^{-1}.MPa^{-1}. Cette comparaison révèle que le couplage du gradient de contrainte avec la mobilité entraîne un ralentissement 3 fois plus important que le profil qui ne prend en compte que la mobilité.

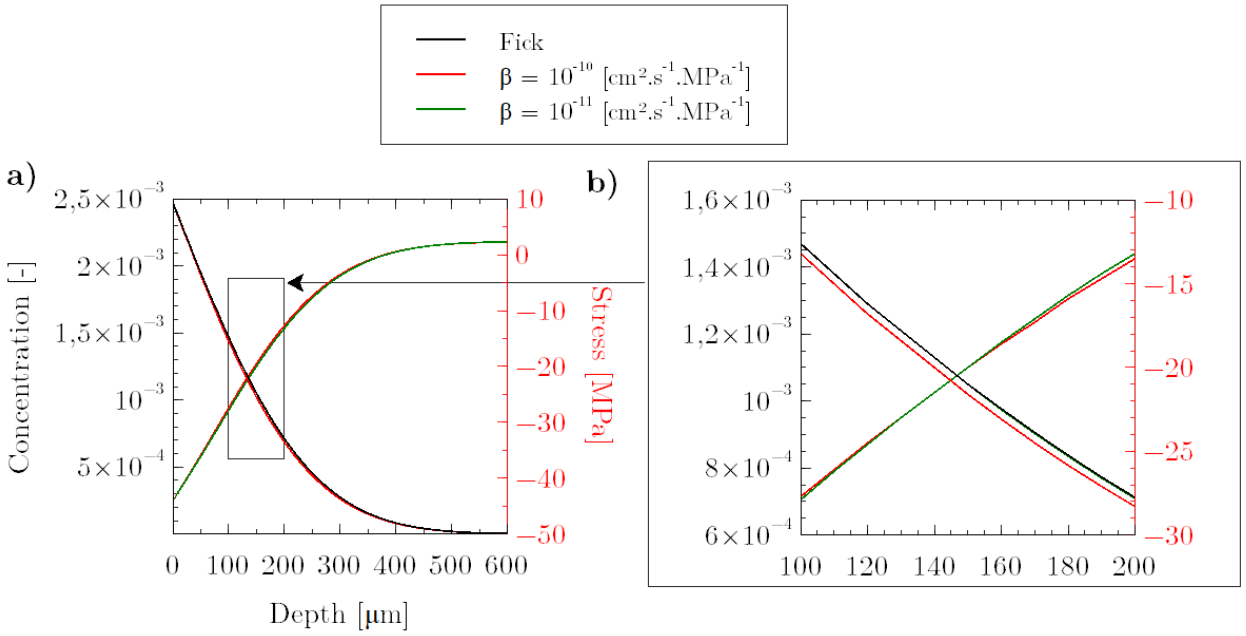

FIGURE 2.7 – a) Évolution des profils de concentration et de contrainte résiduelle en fonction de la profondeur pour le cas de l'effet de la contrainte sur la mobilité ($\beta > 0$ et $\nabla\sigma = 0$) pour un échantillon de 10 mm d'épaisseur à 520 °C pendant 1 h. Comparaison du profil de Fick et des 2 valeurs du coefficient : 10^{-11} et 10^{-10} $cm^2.s^{-1}.MPa^{-1}$. b) Zoom de la figure a).

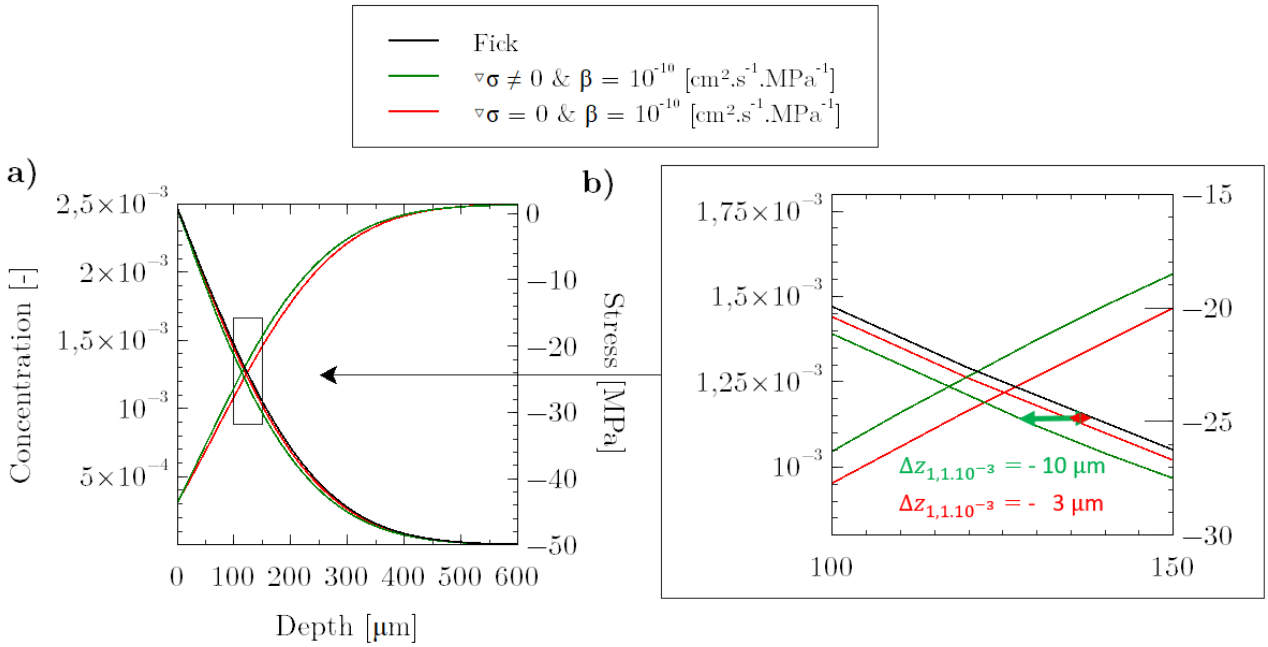

FIGURE 2.8 – a) Comparaison des profils de concentration (par rapport au profil de Fick) et de la contrainte résiduelle en fonction de la profondeur pour le cas ($\beta > 0$ et $\nabla\sigma = 0$) et le cas ($\beta > 0$ et $\nabla\sigma \neq 0$) pour un échantillon de 10 mm d'épaisseur à 520 °C pendant 1 h pour $\beta = 10^{-10}$ $cm^2.s^{-1}.MPa^{-1}$. b) Zoom de la figure a).

2.1.3.1.2 Evolution de l'épaisseur. Une deuxième étude porte sur l'influence de la contrainte sur la mobilité en fonction de l'épaisseur (1 mm, 5 mm et 10 mm), en concurrence avec le gradient de contrainte résiduelle. L'étude s'est concentrée sur un facteur multiplicateur de contrainte CC = 1 et deux valeurs de β (0 et 10^{-10} $cm^2.s^{-1}.MPa^{-1}$) afin d'observer l'effet de structure (autrement dit, l'équilibrage dynamique).

Les courbes de concentration ne présentent aucun changement discernable pour $\beta = 0$, comme le montre la figure 2.9. Cependant, dans le cas de $\beta = 10^{-10}$ $cm^2.s^{-1}.MPa^{-1}$, une petite différence positive peut être remarquée lorsque l'épaisseur diminue, malgré le fait que l'influence sur la mobilité a un effet négatif sur la cinétique de diffusion. La diffusion est en effet moins ralentie pour le matériau le plus fin (1 mm). Ceci est dû à la compétition entre la valeur de la contrainte $|\sigma|$ et le gradient de contrainte $\frac{\partial \sigma}{\partial z}$.

Un cas particulier concerne ici l'échantillon de 1 mm d'épaisseur, qui ne sera pas étudié dans ce paragraphe. En effet, le graphique montre le phénomène de double flux, démontrant qu'à partir d'une certaine valeur de profondeur, la concentration change et ne suit plus l'évolution des champs de concentration des autres épaisseurs. Ceci montre l'intérêt d'étudier des échantillons ayant des évolutions similaires afin de déduire quel effet de contrainte est prédominant.

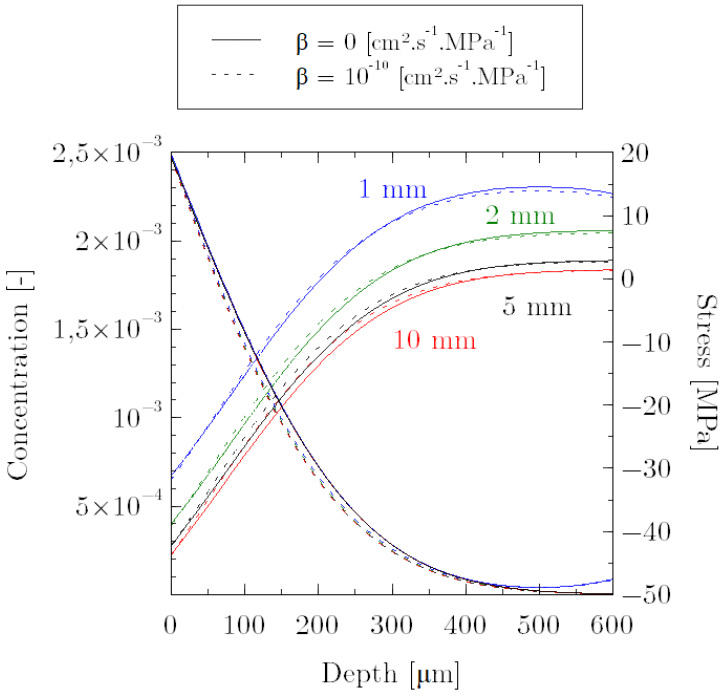

FIGURE 2.9 – Évolution des profils de concentration et de contrainte résiduelle pour quatre épaisseurs d'échantillon (1 mm, 2 mm, 5 mm et 10 mm) en fonction de deux valeurs de β (0 et 10^{-10} $cm^2.s^{-1}.MPa^{-1}$).

2.1.3.2 Étude de chargements spécifiques

Afin d'obtenir une influence significative sur le gradient de contrainte (dans le cas de contraintes résiduelles uniquement, c'est-à-dire un gradient positif et des contraintes négatives), il est nécessaire d'utiliser un échantillon mince avec un temps de traitement court et une grande amplitude de contrainte. Il est essentiel de se rappeler qu'un acier nitruré donne lieu à un champ de contraintes résiduelles beaucoup plus important (en raison des

énormes changements de volume dus aux phénomènes de précipitation) que le fer pur, avec des contraintes de surface allant de -500 à -1000 MPa. De plus, en raison de la co-diffusion du carbone et des phénomènes de précipitation, l'acier nitruré présente une diffusion à longue distance beaucoup plus lente, où à 520 °C $D_{\text{azote}} =$ 4,9. 10^{-8} cm^2.s^{-1} et $D_{\text{33CrMoV12-9 steel}} = 4{,}7.10^{-9}$ cm^2.s^{-1} [Jegou et al., 2018].

La recherche s'est concentrée sur l'impact des champs de contraintes qui peuvent être facilement obtenus expérimentalement, comme un essai de traction/compression ou un essai de flexion sans prendre en compte l'influence des contraintes résiduelles (aspect temporel). Une constante arbitraire de concentration en surface $c_0 = 0,001$ a donc pu être prise. L'objectif sera d'émettre des conclusions sur l'influence d'une contrainte dite homogène (effet de mobilité) avec/sans l'influence du paramètre β (effet de mobilité) et ensuite l'influence d'un gradient de contrainte (effet de force motrice) avec/sans l'influence du paramètre β (effet de mobilité). Dans le cas d'une contrainte homogène, la contrainte n'aura d'effet que sur la mobilité, les forces motrices mécaniques étant nulles (gradient de contrainte). Inversement, dans le cas d'un gradient de contrainte avec $\beta = 0$, la contrainte n'a aucun effet sur la mobilité. Un échantillon de 1 mm d'épaisseur traité pendant 1 heure à 520 °C est étudié.

La figure 2.10a) montre l'évolution du profil de concentration pour une contrainte positive de 1 GPa avec différentes valeurs de β (0, 10^{-13}, 10^{-12}, 10^{-11} et 10^{-10} cm^2.s^{-1}.MPa^{-1}). La figure 2.10a) montre qu'une contrainte homogène positive accélère la cinétique de diffusion. Lorsque $\beta = 10^{-12}$ cm^2.s^{-1}.MPa^{-1}, l'accélération devient considérable et perceptible, c'est-à-dire lorsque les ordres de grandeur sont : $\sigma\beta = 0,1D$. La figure 2.10b) montre l'influence d'une contrainte positive et négative ($|1|$ GPa) pour $\beta = 10^{-11}$ cm^2.s^{-1}.MPa^{-1}. Une contrainte négative induit plus d'impact sur la cinétique de diffusion en ralentissant fortement la diffusion. La cinétique de diffusion est donc accélérée ou ralentie selon le signe des contraintes. La figure 2.11a), montre les profils en fonction de deux gradients de contraintes pour deux valeurs de β. Lorsque $\beta = 0$, alors plus le gradient positif est important, plus la cinétique de diffusion est rapide et inversement pour un gradient négatif. Lorsque β augmente, plus l'amplitude des contraintes négatives est importante plus la diffusion est ralentie et inversement pour des contraintes positives. La figure 2.11b) montre les profils obtenus d'un échantillon soumis a un essai de flexion de gradient 4 GPa.mm^{-1} pour $\beta = 10^{-13}$ cm^2.s^{-1}.MPa^{-1}.

Cette étude a permis d'illustrer le fait qu'un même niveau de contrainte positive ou négative n'entraîne pas une diffusion symétrique. En utilisant les profondeurs des trois points de concentration, une contrainte négative produit une cinétique inférieure de 20 % à celle d'une contrainte positive. De plus, la prise en compte d'un gradient de contrainte positif ou négatif avec l'effet des contraintes sur la mobilité ($\beta > 0$) n'entraîne pas une diffusion symétrique. En utilisant les profondeurs des trois points de concentration, un gradient de contrainte négative montre une décélération 3 fois plus importante par rapport à l'accélération d'un gradient de contrainte positive. Ce résultat montre une tendance similaire à celle observée dans le cas d'une contrainte homogène. Cependant, cette étude a montré que pour un gradient positif avec des contraintes négatives, l'effet de ralentissement est accentué. Ceci est causé par le gradient de mobilité, c'est-à-dire le couplage mobilité-contrainte. Une fois encore, la relation d'Einstein ($z^2 = 2Dt$) démontre que ces observations sont cohérentes.

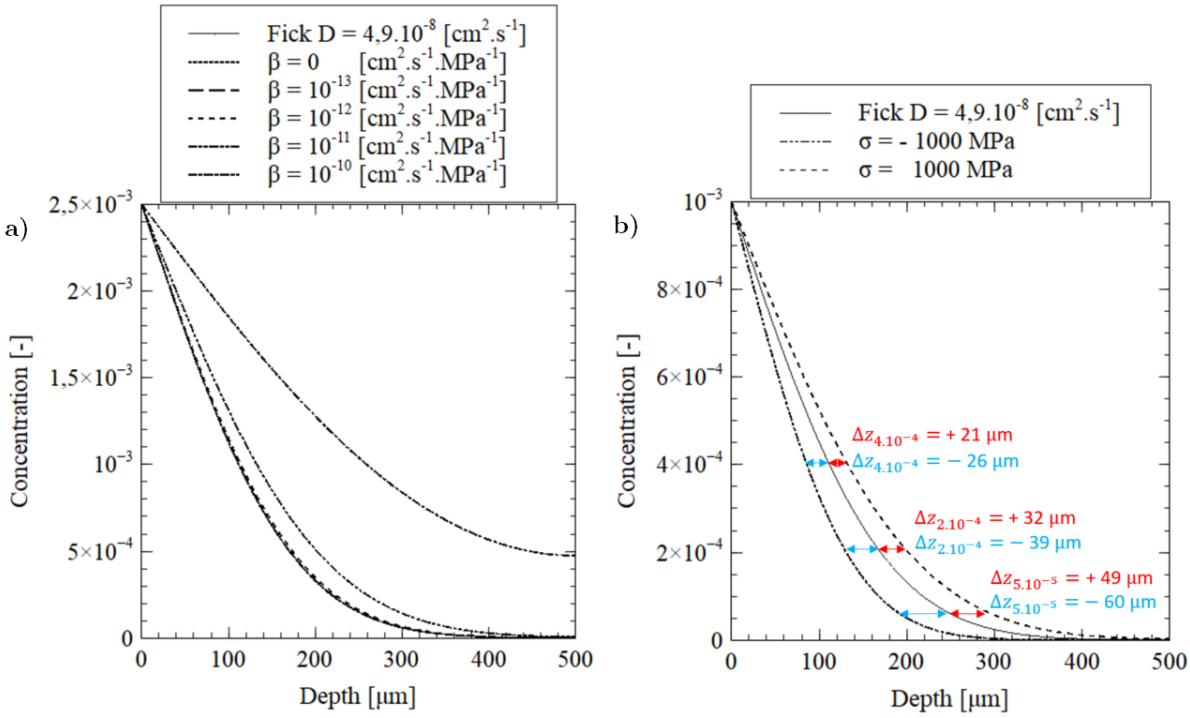

FIGURE 2.10 – a) Evolution des profils de concentration en fonction de cinq valeurs de β (0, 10^{-13}, 10^{-12}, 10^{-11} et 10^{-10} $cm^2.s^{-1}.MPa^{-1}$) soumis à un essai de traction homogène (1 GPa) ; b) Evolution des profils de concentration pour deux essais mécaniques (traction pure à 1 GPa et compression pure à -1 GPa en fonction de $\beta = 10^{-11}$ $cm^2.s^{-1}.MPa^{-1}$; pour un échantillon de 1 mm d'épaisseur, à 520 °C pendant un traitement de 1 h.

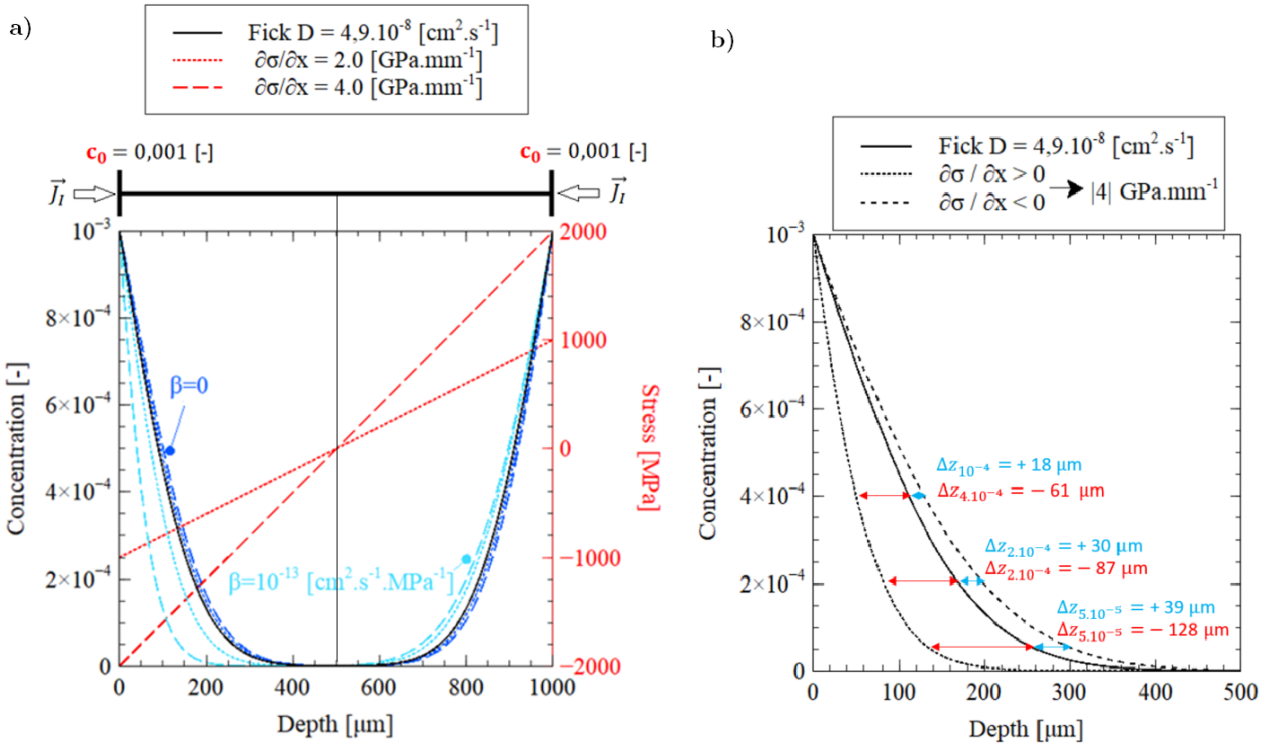

FIGURE 2.11 – a) Évolution des profils de concentration en fonction de cinq valeurs de β (0, 10^{-13}, 10^{-12}, 10^{-11} et 10^{-10} $cm^2.s^{-1}.MPa^{-1}$) soumis à deux essais de flexion (2 GPa.mm^{-1} et 4 GPa. mm^{-1}) ; b) Évolution des profils de concentration pour un essai de flexion (4 GPa.mm^{-1}) en fonction de $\beta = 10^{-13}$ $cm^2.s^{-1}.MPa^{-1}$; pour un échantillon de 1 mm d'épaisseur, à 520 °C pendant un traitement de 1 h.

Chapitre 3

Étude expérimentale

3.1 Introduction

L'objectif de ce chapitre est d'apporter des éléments de réponses à la question du rôle des contraintes élastiques (résiduelles) et des déformations plastiques dans le processus de nitruration. Ce chapitre est divisé en deux sections. La première section se concentre sur l'effet des déformations élastiques. Deux expériences ont été mises en place. Chaque échantillon de cette section a été nitruré à 520 °C, $K_N = 3.711$ atm$^{-1/2}$ pendant 5 h. La première expérience consiste à créer une diffusion asymétrique afin d'étudier l'effet de ce gradient de contrainte positif à valeurs négatives sur la cinétique de diffusion. Pour cela, des échantillons semi-infinis et finis avec un facteur d'épaisseur de dix seront comparés. Les contraintes sont influencées par deux facteurs : un effet structurel (c'est-à-dire un équilibrage dynamique) et un effet d'équilibrage mécanique. L'effet structurel n'existe pas dans le cas d'un échantillon semi-infini. La seconde expérience consiste à ouvrir un anneau fendu en imposant un déplacement, ce qui entraîne un champ de contraintes de type flexion. L'objectif de ces deux études sera de déterminer l'importance relative d'un gradient de contrainte (force motrice) et de la contrainte sur la mobilité. La deuxième section traite de l'effet des déformations plastiques homogènes sur la cinétique de diffusion. Chaque éprouvette a été obtenue à partir d'essais de traction contrôlés en utilisant des études numériques préliminaires par éléments finis sur ABAQUS, permettant de nitrurer les échantillons à différents niveaux d'écrouissage. Les résultats sont comparés à une condition de référence, obtenue à partir d'une éprouvette de traction non soumise à un écrouissage et nitrurée dans les mêmes conditions.

Les conditions de recherche sont différentes ; en effet, le matériau analysé est le 33CrMoV12-9, ce qui suggère la prise en compte des processus de précipitation et de co-diffusion du carbone. La diffusion à longue distance sera d'abord étudiée, puis l'influence des déformations (élastiques/plastiques) sur la précipitation du carbone et la co-diffusion en examinant les impacts sur l'épaisseur de la couche de diffusion, la distribution, la profondeur de nitrure et la profondeur de cémentite.

En raison de la répétabilité des traitements, un seul échantillon par série d'échantillons sera présenté dans cette étude.

3.2 Effet des déformations élastiques

L'effet sur le court et le long terme, c'est-à-dire l'épaisseur de la couche de composé ou la profondeur de diffusion de l'azote, a été observé. Deux études ont été établies.

Tous les traitements de nitruration thermochimique seront les mêmes. Des travaux antérieurs en laboratoire ont montré que pendant une période de 5 h à 520 °C, une couche de diffusion de l'ordre de 200 μm peut être formée [Jegou et al., 2018]. Un potentiel de nitruration elevé K_N= 3,711 atm$^{-1/2}$ a été choisi pour créer une couche de combinaison biphasée et, par conséquent, pour étudier l'influence sur la distribution des phases.

3.2.1 Effet des contraintes résiduelles et du gradient des contraintes résiduelles

Un dépôt de cuivre a été utilisé comme bloqueur de diffusion. Le cuivre est ductile et ne subit pas de contrainte thermique à haute température, comme en témoignent les couches d'oxyde. De plus, comme l'alliage utilisé ne contient pas de cuivre, l'effet Kirkendall ne se produira pas.

La figure 3.1 montre les différents cycles auxquels les échantillons ont été soumis : un échantillon (F1) qui a été cuivré sur une face puis nitruré, et un échantillon (F2) qui a été décuivré, cuivré sur l'autre face puis nitruré. Les échantillons subissant une nitruration simultanée sur les deux faces seront définis par (S).

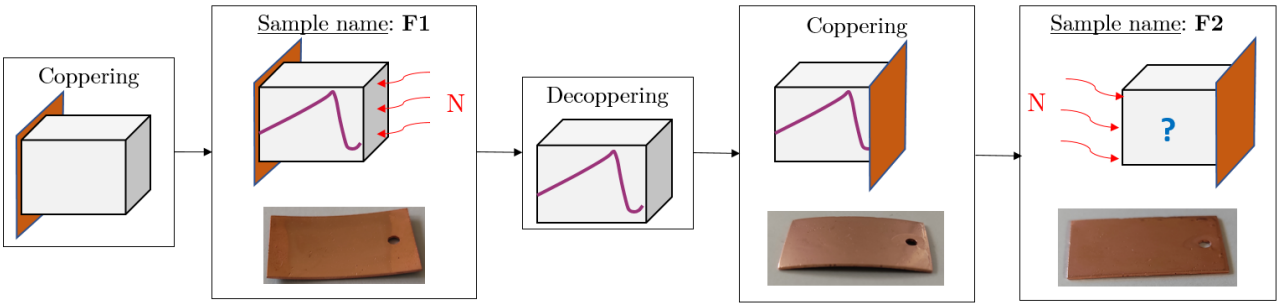

FIGURE 3.1 – Schématisation des expériences sur l'effet des contraintes résiduelles et du gradient des contraintes résiduelles.

3.2.1.1 Effet des contraintes auto-induites

Des échantillons nitrurés d'un côté (F1) ont été étudiés pour voir si l'effet structurel (c'est-à-dire l'équilibrage dynamique) affecte leurs caractéristiques (profils HV0,2, profils de contraintes résiduelles, profils N.%m et C.%m, etc). Les échantillons nitrurés (F1) subissent une diffusion sur un côté, ce qui entraîne une diffusion asymétrique, donc un champ de contraintes asymétrique, le tout provoquant une flexion de l'échantillon comme le montre la figure 3.1. Cette asymétrie conduit à la création d'un gradient de contrainte résiduelle, plus ou moins important selon l'épaisseur de l'échantillon.

Les profils comparatifs (S) et (F1) des contraintes et des largeurs intégrales calculées pour les épaisseurs de 5 mm et 500 μm sont présentés dans les figures 3.2a) et b) respectivement. L'échantillon de 5 mm présente une valeur maximale des contraintes moins importante pour l'échantillon (F1) que (S) et un profil équivalent par la suite. L'échantillon 500 μm) (F1) présente un décalage vers la surface du profil, un maximum des contraintes plus faible et une position des maximums des contraintes équivalents. Une étude des graphiques montrent que

le gradient de contrainte de l'échantillon 5 mm (F2) est de 11,2 GPa/mm contre 9,9 GPa/mm pour l'échantillon 500 μm (F1).

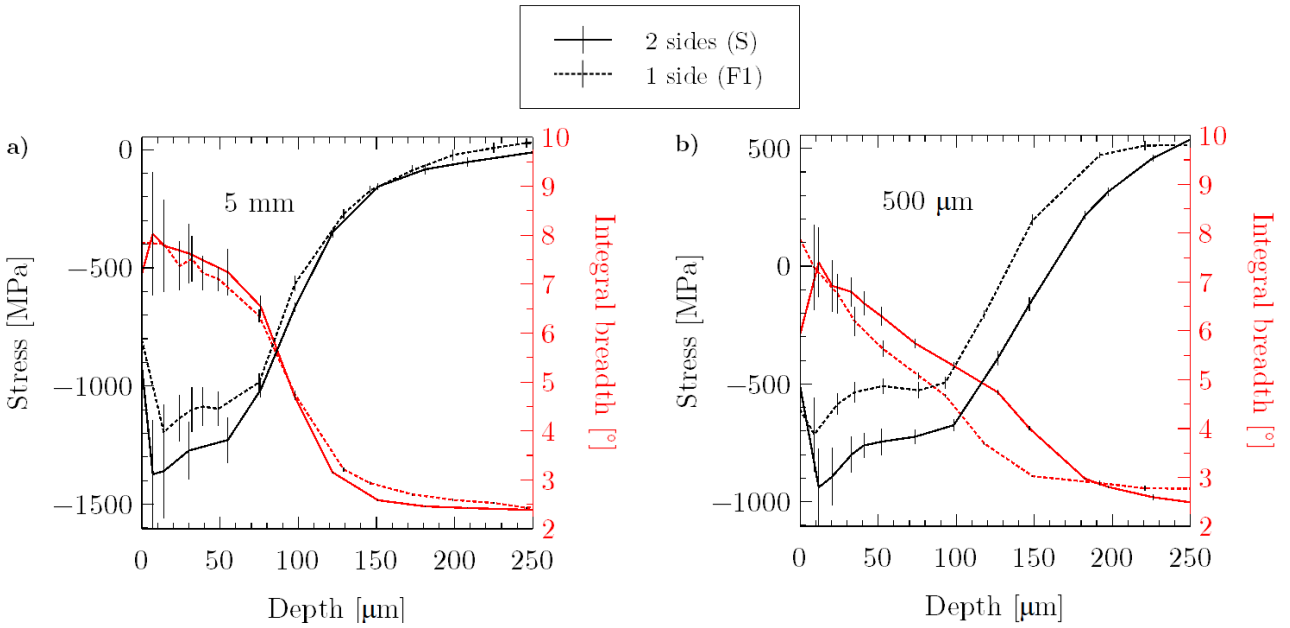

FIGURE 3.2 – Profils de contrainte résiduelle et de largeur intégrale d'échantillons nitrurés d'un côté (F1) de 5 mm et 500 μm à 520 °C et 3,711 atm$^{-1/2}$ pendant 5 h.

La figure 3.3a) montre une profondeur affectée en azote plus importante dans le cas de l'échantillon de 500 μm d'épaisseur ce qui corrèle avec les profils de dureté (sur la figure 3.3b)). Cette profondeur affectée est de 200 μm plus profonde. Les deux résultats montrent que les profils de l'échantillon de 500 μm d'épaisseur seraient équivalents à un traitement plus long pour un échantillon de 5 mm d'épaisseur. À cet effet, l'équation 3.1 est utilisée pour définir le temps t [s] équivalent à la profondeur effective z [cm] en fonction du coefficient de diffusion D [cm^2.s^{-1}] :

$$t = \frac{z^2}{2D} \tag{3.1}$$

Une étude au laboratoire a montré que le coefficient de diffusion $D_{33\text{CrMoV12-9 steel}}$ de l'acier 33CrMoV12-9 à 520 °C est égal à 4,75.10^{-9} cm^2.s^{-1}. La profondeur effective de 500 μm est comparable à une durée de traitement supplémentaire de 2 h 30 min. Pour atteindre cette profondeur de diffusion avec un échantillon de 5 mm, une période de nitruration de 7 h 30 min serait nécessaire dans les mêmes circonstances (K_N et T). Ces observations, compilées avec les profils de contrainte, confirment l'existence d'un effet structurel directement lié à l'effet de contrainte, et plus particulièrement à l'influence temporelle des contraintes résiduelles sur la cinétique de diffusion.

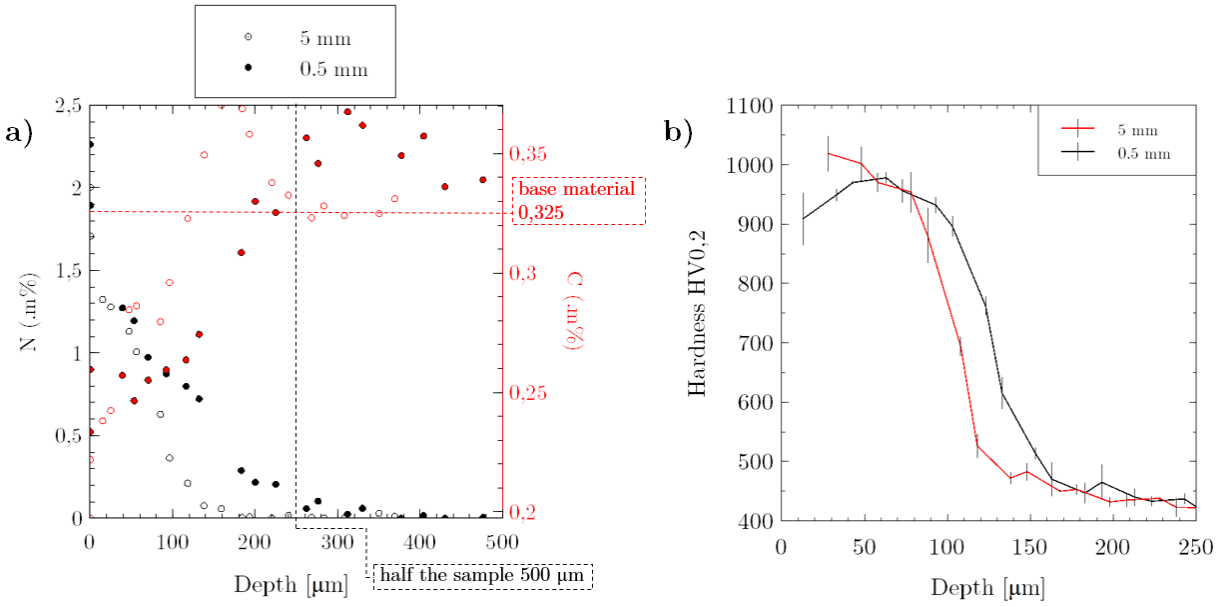

FIGURE 3.3 – Comparaison pour des échantillons de 5 mm et 500 μm d'épaisseur des a) profils d'azote (N%.m) et de carbone (C%.m), b) profils de dureté HV0.2, des échantillons 33CrMoV12-9 nitrurés à 520 °C et 3,711 atm$^{-1/2}$ pendant 5 h.

3.2.1.2 Effet des contraintes induites

Les effets d'un gradient de contrainte (ici de nature résiduelle, c'est-à-dire des déformations élastiques) sur la cinétique de diffusion ont été étudiés. Les échantillons (F2) subissent une première diffusion unilatérale, correspondant à la diffusion des échantillons (F1) présentée dans la sous-section 3.2.1.1. Cette première diffusion provoque une asymétrie de diffusion, qui se traduit par un gradient de contrainte résiduelle sur la face opposée, plus ou moins important selon l'épaisseur de l'échantillon. Cette face opposée est ensuite nitrurée dans les mêmes conditions de traitement.

Le gradient de contrainte résiduelle et les largeurs intégrales comparables obtenues sur la face opposée (F1) pour les échantillons de 5 mm et de 500 μm sont présentés sur les figures 3.4a) et b), respectivement. Les largeurs intégrales confirment que la microstructure est identique en profondeur. Les gradients de contrainte résiduelle calculés révèlent que le gradient pour l'échantillon de 500 μm est significativement plus grand que le gradient pour l'échantillon de 5 mm. Une étude des graphiques montrent que la contrainte en surface et le gradient de surface pour l'échantillon 5 mm et 500 μm sont, respectivement, -49 MPa / 23 MPa/mm et -138 MPa / 3460 MPa/mm. La figure 3.5 montre une comparaison des profils de contraintes résiduelles et des largeurs intégrales des échantillons nitrurés de 5 mm et 500 μm d'épaisseur : (S) et (F2) . Les profils de contrainte montrent que l'échantillon de 5 mm présente une augmentation mineure de la diffusion. Les profils de largeur intégrale (500 μm (F2)) montrent que la diffusion semble augmenter au début du profil, diminuer par la suite, puis augmenter au cœur. Les profils de contrainte montrent que la contrainte de gradient est supérieure de 7 % pour l'échantillon (F2).

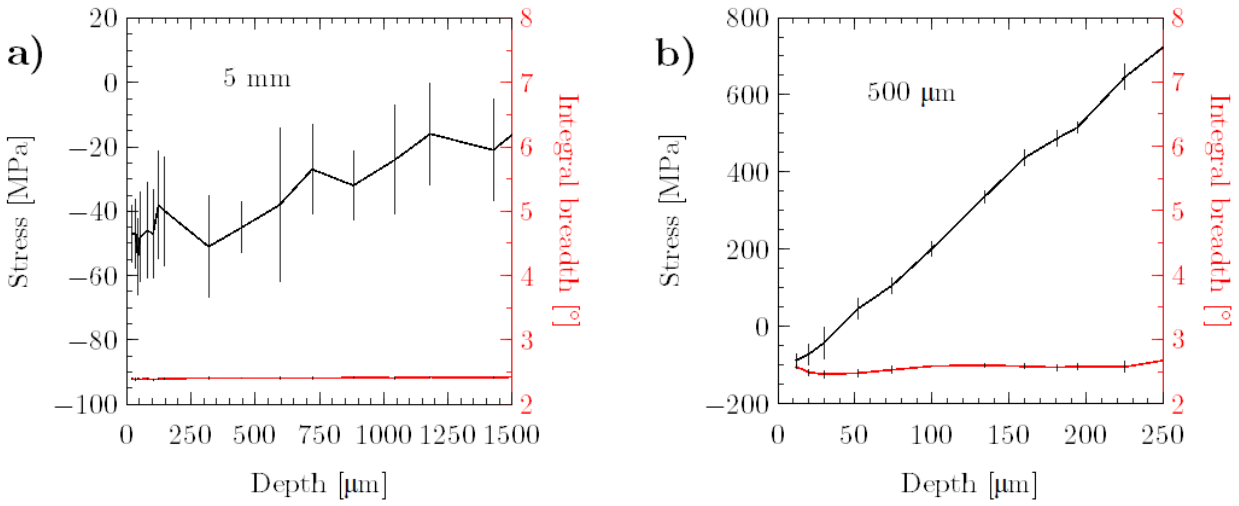

FIGURE 3.4 – Profils de contrainte résiduelle et de largeur intégrale du côté opposé de la face (F1) : a) échantillon de 5 mm d'épaisseur, b) échantillon de 500 μm d'épaisseur.

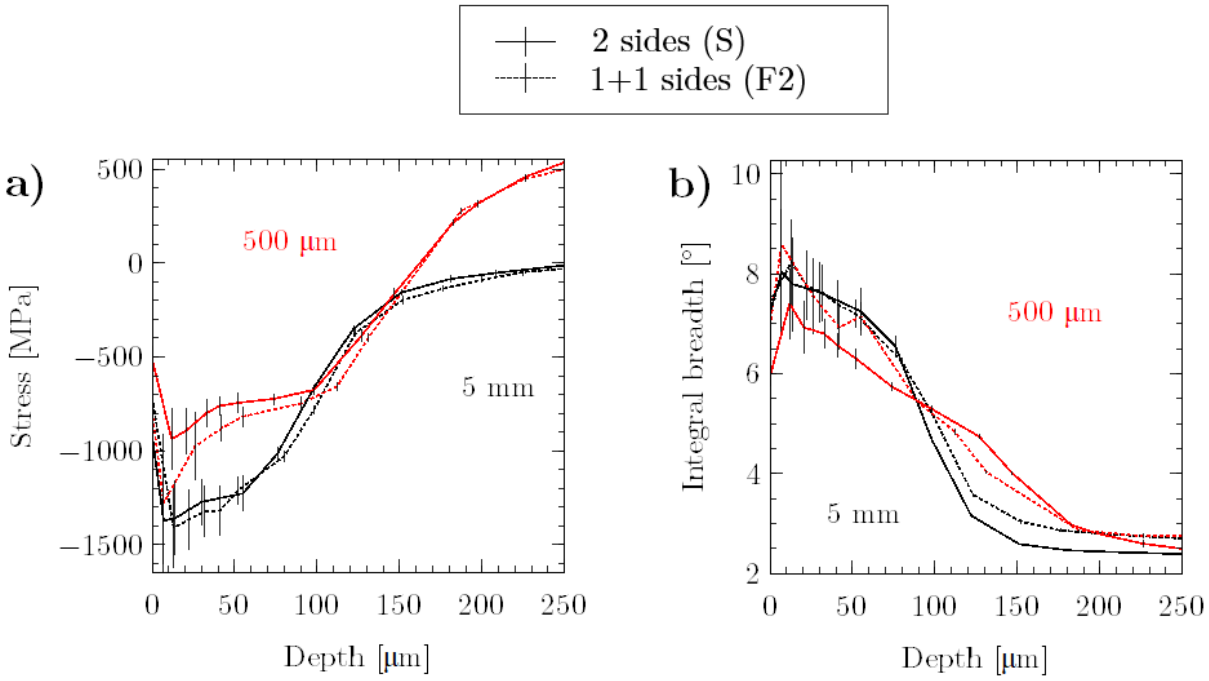

FIGURE 3.5 – Comparaison a) des profils de contrainte résiduelle et b) des largeurs intégrales entre des échantillons nitrurés de 5 mm et 500 μm (F2) à 520 °C et 3,711 atm$^{-1/2}$ pendant 5 h.

Les profils de dureté sont présentés dans la figure 3.6a). Ces profils montrent des variations de la profondeur effective et une différence de dureté du noyau, cette dernière conduisant à l'hypothèse d'une teneur en azote du coeur non nulle. En effet, la concentration en azote du noyau pour l'échantillon de 500 μm est de 0,05 N%m., comme l'illustre la figure 3.6a). Grâce à l'équation 3.1, le temps équivalent en fonction de la profondeur effective est comparé au temps initial. Cette différence de profondeur montre l'opportunité de réduire le temps

de traitement de 50 minutes par rapport à un temprs de traitement de 5 heures.

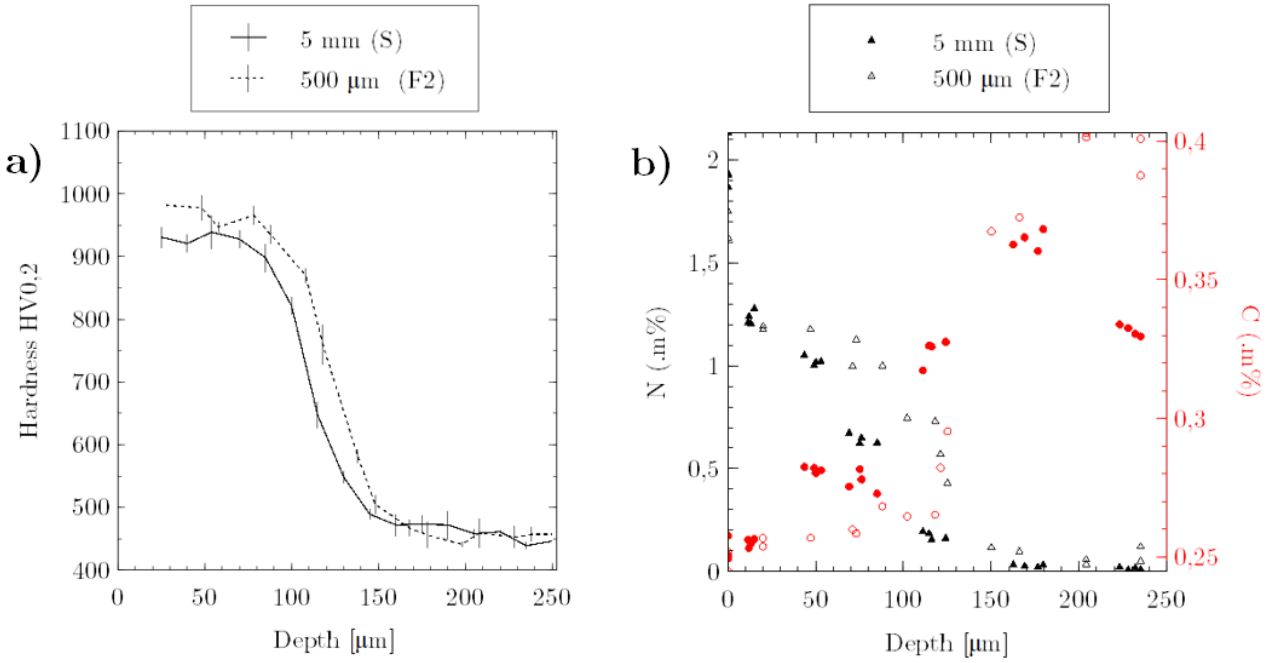

FIGURE 3.6 – Comparaison a) de la dureté et b) des profils d'azote et de carbone d'échantillons de 5 mm (S) et de 500 μm (F2).

3.2.2 Effet des contraintes appliquées

Une étude de l'effet d'un gradient de contrainte sur la cinétique de diffusion a été menée. Un anneau fendu a été soumis à un déplacement, afin d'obtenir un champ de contrainte pouvant être représenté comme un essai de flexion. L'objectif de cette étude est de comparer le côté traction avec un gradient de contrainte négatif au côté compression avec un gradient de contrainte positif. Le but est de distinguer l'influence de la contrainte sur la mobilité et l'effet d'un gradient de contrainte. La thermobalance, utilisée pour les traitements de nitruration, a un faible encombrement (18 mm de diamètre et 30 mm de longueur) et un poids maximal (30 g) qui ne doivent pas être dépassés. Contrairement aux recherches précédentes, le champ de contrainte est un champ appliqué qui n'évolue pas à chaque temps t pour toute source de fluage négligée.

Les anneaux ont été préalablement étudiés par la méthode des éléments finis sous abaqus afin de définir le déplacement nécessaire pour obtenir des contraintes maximales de l'ordre de ±800 MPa, tout en s'assurant de rester dans le domaine élastique (c'est-à-dire en évitant toute source de déformation plastique macroscopique) à la température de nitruration. La figure 3.7 illustre le champ de contraintes obtenu pour un déplacement de 2,3 mm. Les valeurs de surface sont de 874 MPa sur la face interne de l'anneau (côté traction) et de -796 MPa sur la face interne (côté compression). Le gradient de contrainte est de 1,8 GPa/mm.

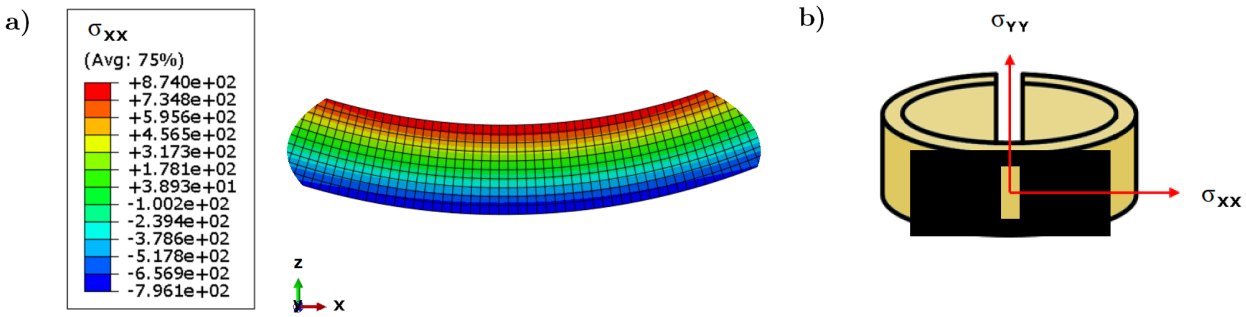

FIGURE 3.7 – a) Représentation du champ de contraintes σ_{xx} de la zone en flexion de l'anneau. b) Représentation schématique des contraintes σ_{xx} et σ_{yy} et de la zone étudiée par XRD.

Expérimentalement, le champ mécanique avant le traitement de nitruration ne peut être défini. Seule la contrainte de surface sur la face externe de l'échantillon (côté compression) est calculée. Les analyses des contraintes par DRX ont porté sur le calcul des contraintes circonférentielles et axiales de l'anneau, de dimensions 15×5×1 mm. Les valeurs obtenues expérimentallement par DRX des contraintes de la face en compression sont de $\sigma_{xx} = -833,9$ MPa ±15,2 MPa et $\sigma_{yy} = -60,3$ MPa ±-1,9 MPa. σ_{xx} montre un écart de 5%. Une étude de déchargement a également confirmé que l'anneau ne se plastifie pas.

Les anneaux ont ensuite pu être nitrurés pendant 5 heures à 520 °C dans un environnement de nitruration avec $K_N = 3{,}711$ atm$^{-1/2}$. L'analyse des contraintes étant un processus destructif, le profil équivalent sur les deux faces au point où le gradient est maximal n'a pas pu être observé. Les profils de contrainte ont donc été calculés sur une zone moins sollicitée, représentée par la zone orange sur la figure 3.8. Avant d'analyser les profils de contrainte et de dureté, les champs de contrainte relatifs aux sections analysées ont été étudiés à partir du modèle d'éléments finis dans ABAQUS (section 3.2.2). La figure 3.8 montre que les valeurs du σ_s et des gradients de contrainte sont beaucoup plus faibles là où l'étude des contraintes résiduelles a été effectuée. Le gradient au niveau de l'analyse des contraintes est de 1,1 GPa/mm contre 1,8 GPa/mm pour la zone maximale, ce qui implique une diminution du gradient de 40% et de même une diminution de 43% des valeurs de σ_s.

La figure 3.9 montre les profils de contrainte calculés par diffraction des rayons X pour les deux faces étudiées par rapport à un échantillon de référence de 1 mm d'épaisseur. Les largeurs intégrales montrent que la diffusion s'accélère du côté de la compression, ce qui semble suggérer que l'influence du gradient prédomine sur l'effet des contraintes de mobilité. Le profil en traction montre une évolution du coeur en traction par rapport à un profil qui reste en compression pour le côté compression. Cette observation est due à la superposition des contraintes résiduelles et appliquées mais aussi à une redistribution des contraintes lors du déchargement de l'échantillon (hypothèse non quantifiée dans cette étude). Les gradients montrent des évolutions similaires de l'ordre de 10 GPa/mm. Les deux duretés correspondant aux champs de contraintes (sur la figure 3.8) ont été comparées. Les profils de traction montrent des évolutions comparables le long du profil. Le profil de compression correspondant à la position de contrainte expérimentale montre une accélération cinétique après 150 μm de profondeur. Ceci est également évident dans les profils de largeur intégrale présentés dans la figure 3.9. Les temps équivalents entre les deux échantillons "position σ_{max}" par rapport à l'échantillon de référence sont calculés en utilisant l'équation 3.1. Les résultats montrent que la diffusion du côté de la traction serait équivalente à un temps de 6 h 36 min contre 3 h 17 min du côté de la compression. En d'autres termes, cela indique que pour l'un, la diffusion a augmenté de 32 % (profil en traction) et pour l'autre, elle a diminué de 34 % (profil en compression). Cela

montre que les pourcentages sont presque similaires à toutes erreurs de mesure gardées.

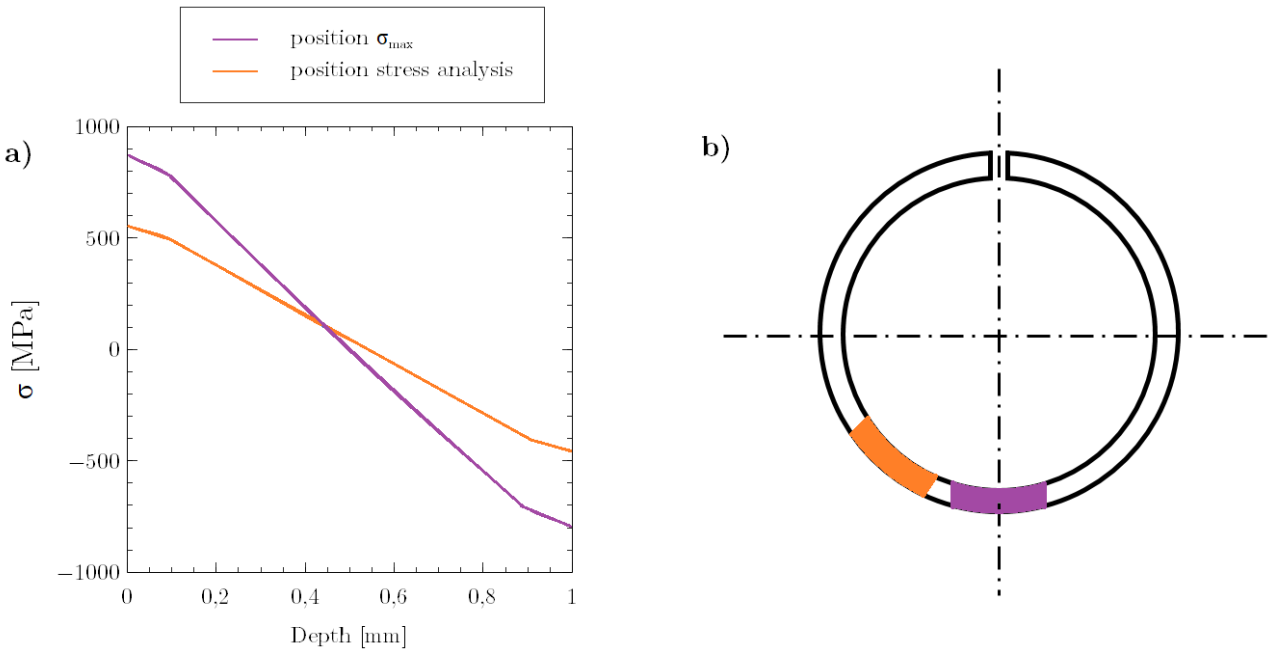

FIGURE 3.8 – a) Profils numériques de contraintes résiduelles, obtenus sur ABAQUS, de l'anneau du côté de la traction et de la compression. b) Schématisation des positions équivalentes aux profils présentés en a).

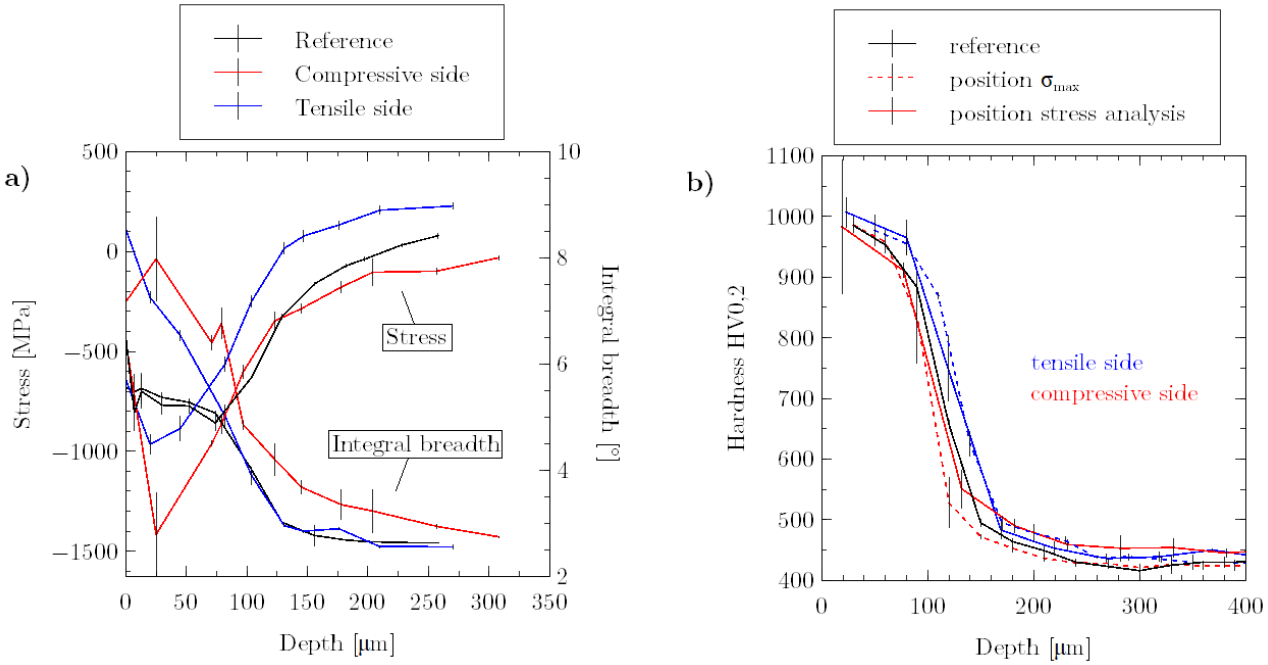

FIGURE 3.9 – a) Profils de contrainte résiduelle de l'anneau sur les côtés traction et compression. b) Profil de dureté de l'anneau sur les côtés traction et compression comparé au profil de référence dans deux positions (voir la figure 3.8).

3.3 Effet de la déformation plastique

Selon la revue bibliographique, l'influence de la déformation plastique ε^P a un effet sur l'adsorption et la diffusion des atomes lors des traitements chimiques de surface ultérieurs tels que la nitruration. Une éprouvette de traction a été conçue pour étudier l'effet de l'écrouissage sur la nitruration gazeuse des aciers, sur la base d'essais de traction contrôlés. Les éprouvettes ont été conçues pour étudier l'effet d'un écrouissage uniforme, permettant ainsi d'obtenir des échantillons nitrurés à différents niveaux d'écrouissage. Les résultats sont comparés à une condition de référence dérivée d'une éprouvette de traction qui n'a pas été exposée à l'écrouissage. Des mesures de dureté, des profils de profondeur de carbone et d'azote seront effectués pour caractériser le comportement des échantillons nitrurés.

Des éprouvettes à section constante sont déformées plastiquement à l'aide de la machine d'essai de traction conventionnelle INSTRON 100kN. Les échantillons ont préalablement été modélisés sur Abaqus afin d'y extraire la force de réaction [N] équivalente aux valeurs de ε^P étudiés. Chaque éprouvette de traction produit deux échantillons de dimensions 17×13×5 mm. Ces échantillons ont été par la suite, nitruré pendant 24 heures à 520 °C sous un potentiel nitrurant $K_N = 3.711$ atm$^{-1/2}$. Chaque échantillon a été comparé à un échantillon dit de référence ($\varepsilon^P = 0$ %) subissant le même cycle de nitruration.

Deux valeurs de déformations plastiques sont étudiés : $\varepsilon^P = 2$ % et $\varepsilon^P = 4$ %. Les forces de réactions associées, obtenues à partir du modèle par élements finis, sont respectivement -81000 N et - 86100 N.

L'évolution des contraintes résiduelles ($\sigma_{11} - \sigma_{33}$) et des largeurs intégrales en fonction de la profondeur est présentée dans la figure 3.10a). Les courbes de contrainte présentent des tendances comparables jusqu'à 180-200 μm, avec des maxima de contrainte décalés d'environ 10 μm. Plus l'échantillon est déformé, plus les profils se déplacent en profondeur. En effet, les courbes de largeur intégrale, qui sont indicatives des changements de microstructure, révèlent que les profils sont identiques jusqu'à 150 μm, puis l'échantillon le plus sollicité ($\varepsilon^P = 3{,}8$ %) montre une diffusion plus profonde mais les profils du matériau de base restent équivalents. Ces résultats sont cohérents avec les profils de dureté observés sur la figure 3.10b). Les profils de dureté révèlent que l'échantillon le plus déformé accélère la cinétique de diffusion en début de profil jusqu'à une profondeur de 300 μm. En effet, les déformations plastiques aident à une précipitation cohérente, ce qui conduit à suggérer que la dureté de la surface est plus importante car la cinétique de précipitation est plus rapide, et qu'il y aurait donc plus de germination que de croissance.

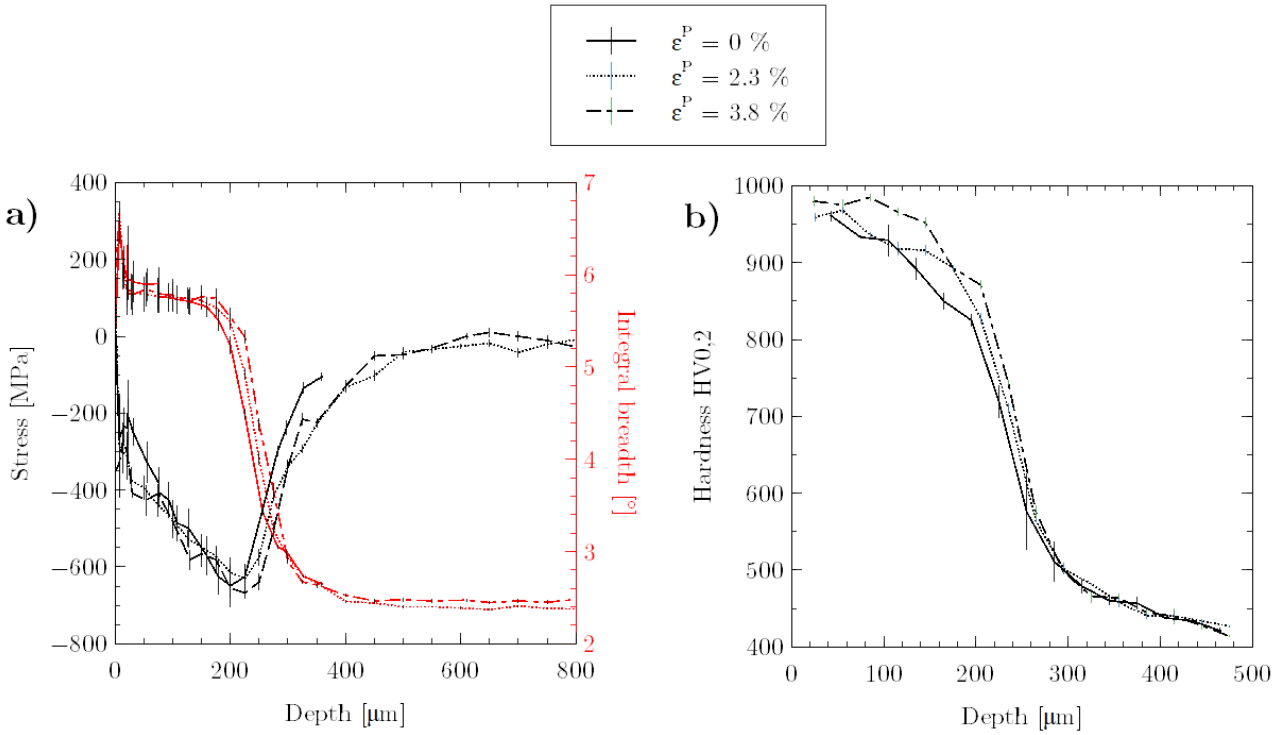

FIGURE 3.10 – a) Profils de contrainte résiduelle ; b) Profils de dureté, d'échantillons soumis à une déformation plastique (ε^P = 2,3 % et 3,8 %) comparés à une référence (ε^P = 0 %).

Cette étude permet donc d'observer que, compte tenu des profils de dureté, la cinétique de diffusion à longue distance ne semble pas être accélérée mais que les phénomènes semble jouer un rôle sur la cinétique à courte distance (précipitation). Ces observations sont cohérentes avec ce qui a été observé dans la littérature où les phénomènes de précipitation sont fortement influencés par les déformations incompatibles.

Discussion

Des simulations numériques 2D et 1D ont permises d'apporter des éléments de compréhension et de visualisation de l'influence des contraintes sur la cinétique de diffusion à longue distance. Cette investigation sur l'évolution de la cinétique dans le cas de l'évolution temporelle des contraintes (i.e. les contraintes résiduelles), a permis d'observer plus précisément les effets connus depuis des années, et de tirer des conclusions sur la prédominance entre l'influence d'un gradient de contrainte $\frac{\partial \sigma}{\partial z}$ et celle de la contrainte sur la mobilité $(D + \beta\sigma_{kk})$. Une première étude a permis de visualiser les aspects tensoriels des contraintes face aux aspects vectoriels du flux. Une étude de l'amplitude de la contrainte pour deux épaisseurs d'échantillon a confirmé que l'effet du gradient de contrainte devient significatif pour une valeur de l'ordre du GPa/mm. Elle a également permis de comprendre les effets néfastes, pour des pièces sollicités (type dent d'engrenage), que peuvent entraîner les effets de bord en observant qu'un double flux couplé à l'équilibrage mécanique induit un champ de contrainte résiduel faible en compression.

Le tableau 3.1 résume l'évolution des contraintes de surface, des gradients de contrainte (en surface et en profondeur) et des gradients de concentration (en surface et en profondeur) en fonction de quatre facteurs (temps t, épaisseur de l'échantillon e, amplitude de la contrainte CC et paramètre β). Pour une meilleure compréhension, la figure 3.12 schématise les termes utilisés en termes de contrainte de surface, gradient de surface et gradient de profondeur.

Evolution des paramètres		$\lvert\sigma_{\text{surface}}\rvert$	$\frac{\partial \sigma}{\partial z}$ surface	$\frac{\partial \sigma}{\partial z}$ en profondeur	$\frac{\partial c}{\partial z}$ surface	$\frac{\partial c}{\partial z}$ en profondeur
Temps t	$\downarrow$	$\uparrow$	$\uparrow$	$\downarrow$	$\uparrow$	$\downarrow$
Epaisseur e	$\downarrow$	$\downarrow$	$\uparrow$	$\downarrow$	$\downarrow$	$\downarrow$
Amplitude des contraintes	$\uparrow$	$\uparrow$	$\uparrow$	$\uparrow$	$\uparrow$	$\uparrow$
β	$\uparrow$	$\uparrow$	$\uparrow$	$\downarrow$	$\uparrow$	$\downarrow$

TABLE 3.1 – Tableau récapitulatif de l'évolution observée en fonction de quatre facteurs (temps t, épaisseur de l'échantillon e, amplitude de la contrainte CC et paramètre β).

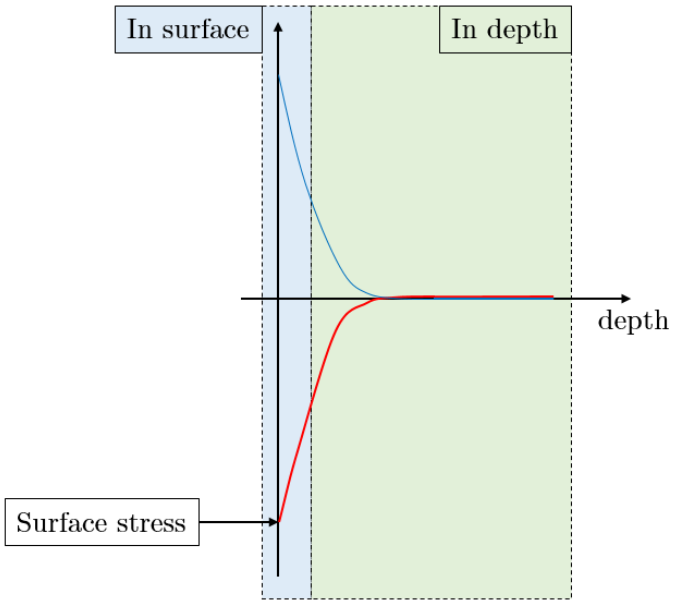

FIGURE 3.11 – Schématisation des termes : contrainte de surface, gradient de surface et gradient de profondeur.

En outre, quelques observations individuelles ont été faites. Dans le cas de :

— l'augmentation de l'amplitude des contraintes CC : un déplacement en profondeur du maximum $\frac{\partial \sigma}{\partial z}$ et un effet structurel dû à l'augmentation $\frac{\partial \sigma}{\partial z}_{\text{surface}}$ sont observés. En outre, il est observé une augmentation générale de $\frac{\partial \sigma}{\partial z}$;

— la diminution de l'épaisseur e entraine une augmentation moyenne globale du gradient de contrainte $\frac{\partial \sigma}{\partial z}$;

— une augmentation du champ de concentration à la surface conduit à une augmentation du champ de concentration le long du profil entier.

Des études paramétriques sur des champs de contraintes spécifiques (type essai traction/compression et de flexion) ont permis d'observer que :

— Une contrainte de traction homogène conduit à une diffusion accélérée, et inversement pour une contrainte de compression homogène ;

— Une contrainte de traction avec un gradient négatif dans le cas :

  — Sans l'effet de la mobilité ($\beta = 0$) conduit à une diffusion ralentie ;

  — Avec l'effet de la mobilité ($\beta > 0$) entraîne une diffusion accélérée.

— L'effet dans le cas d'un $\frac{\partial \sigma}{\partial z} > 0 + \sigma < 0$ est 3 fois plus lent que l'effet dans le cas d'un $\frac{\partial \sigma}{\partial z} < 0 + \sigma > 0$ pour une valeur équivalente β.

Des études expérimentales sur des échantillons de nuance d'acier 33CrMoV12-9 nitrurés ont été menés afin d'observer l'influence des contraintes sur les cinétiques de diffusion. Ces cinétiques observées seront dans un premier temps celles de la diffusion à longue distance afin d'observer et de comparer ces résultats avec les simulations numériques et dans un second temps sur les cinétiques de diffusion à courte distance (précipitation)

et sur la co-diffusion du carbone. L'étude de l'influence des contraintes élastiques sur la cinétique de diffusion a permis de faire plusieurs observations et de mieux comprendre les différents phénomènes.

Une étude a permis d'observer l'effet structurel (c'est-à-dire l'équilibre dynamique) à travers deux échantillons ayant un rapport 10 en épaisseur, nitrurés de manière asymétrique. Les profils de dureté, d'azote et de carbone présentaient des différences significatives, montrant que la cinétique de diffusion à longue distance est considérablement accélérée dans le cas de l'échantillon le plus fin. L'effet structurel a également montré de nettes différences dans les profils de carbone, avec une zone de surcharge significativement plus importante du côté de l'échantillon mince. Ces phénomènes sur l'effet d'équilibre dynamique pourraient être justifiés par l'effet temps des contraintes résiduelles. Cet effet a montré que pour cette nuance d'acier et dans ces conditions de traitement, les temps de traitement pouvaient être réduits de 2 heures 30 minutes par rapport à un temps de 5 heures.

Deux études ont ensuite été réalisées sur l'influence d'un gradient de contrainte. L'une portait sur un gradient de contrainte résiduelle de 3,5 GPa/mm avec une contrainte en surface de -140 MPa. L'autre portait sur deux gradients de contrainte appliqués négatif /positif de $|1,8|$ et $|1,1|$ GPa/mm avec respectivement des valeurs de contraintes en surface de l'ordre de $\pm$850 MPa et $\pm$550 MPa.

Contrairement au gradient de contrainte appliqué, le gradient de contrainte résiduelle évolue à chaque instant, il aura donc un rôle additif de moins en moins significatif au cours du traitement. L'influence de ce gradient de contraintes résiduelles aura donc un rôle majeur dans les premiers instant du traitement lorsque les cinétiques sont les plus grandes. Les profils de dureté ont montré un effet positif sur la cinétique de diffusion à longue distance. Ces ordres de grandeur pour cette nuance d'acier et ces conditions de traitement, permettraient donc une réduction du temps de traitement de 50 minutes par rapport à un temps de 5 heures.

Du côté du gradient de contrainte appliqué, les profils de contrainte résiduelle sont conformes aux résultats attendus. Cela montre que la charge de flexion a modifié les profils de contraintes résiduelles finaux. Du côté en traction, des contraintes de compression plus faibles et des contraintes de traction élevées dans le matériau de base ont été observées. Contrairement au profil en compression qui montre un profil de contraintes résiduelles uniquement en compression.

Du côté en compression, les largeurs intégrales ont des valeurs plus importantes. Ce résultat suggère une microstructure différente avec plus de défauts. En d'autres termes, une microstructure qui contient plus d'azote ou plus d'azote avec des précipités plus petits. Il est bien connu que les largeurs intégrales et les profils de dureté sont corrélés en termes d'évolution de la profondeur, mais ce n'est pas le cas ici. En effet, les filiations de dureté pour le gradient inférieur ont révélé un ralentissement du côté de la compression pour les premiers 150 μm de profondeur et une accélération par la suite. Les résultats sur les profils de largeur intégrale devraient révéler des évolutions de dureté plus significatives. Cependant, le fait que les largeurs intégrales soient plus grandes en fonction de la profondeur n'implique pas qu'une diffusion plus profonde soit observée. La combinaison du graphique contrainte résiduelle / largeur intégrale et des filiations de dureté associées conduit à l'hypothèse qu'une précipitation plus importante est associée à des précipités plus grands ou plus "semi-cohérents" en raison de l'activation de la diffusion du côté de la traction. En raison de cette précipitation, les déformations totales augmenteraient, ce qui entraînerait une accommodation induite par la précipitation. Tout ceci entraînerait moins de défauts, expliquant pourquoi les largeurs intégrales sont plus faibles.

Les filiations de dureté pour le gradient supérieur ont montré une symétrie entre la décélération (côté en compression) et l'accélération (côté en traction) observées sur les profondeurs effectives. Ces ordres de grandeur

pour cette nuance d'acier et ces conditions de traitement, permettraient donc une réduction du temps de traitement de 1 heure 40 minutes par rapport à un temps de 5 heures. Ces observations ont permis de montrer, dans le cas de la nuance d'acier 33CrMoV12-9, le fort couplage qui existe entre le gradient de contrainte et la mobilité. Dans le cas du gradient le plus élevé, une prédominance de l'influence de la contrainte sur la mobilité semble observée avec un comportement proche des simulations numériques présentées sur la figure 2.10. Dans le cas du gradient de 1,1 GPa/mm, il est observé qu'au début du traitement l'effet de la mobilité est prédominant puis à partir de 150 μm la prédominance du gradient apparaît. Ces observations montrent que pour que l'effet du gradient soit prédominant, les contraintes maximales de ce gradient doivent être suffisamment faibles.

Ces observations permettent alors de comprendre et de justifier les résultats obtenus au laboratoire en 2018 par B. Guillot [Guillot, 2018]. Un échantillon soumis à un essai de flexion a été nitruré à 520 °C pendant 50 h avec un K_N = 4,37 atm $^{-1/2}$. La figure 3.12 montre le profil de concentration en azote pour les deux faces de l'échantillon et comparé à un échantillon de référence. Les résultats montrent une accélération de la cinétique du côté de la traction et un ralentissement du côté de la compression. Ce résultat montre que pour cet état de contrainte, la mobilité prédomine sur l'effet du gradient.

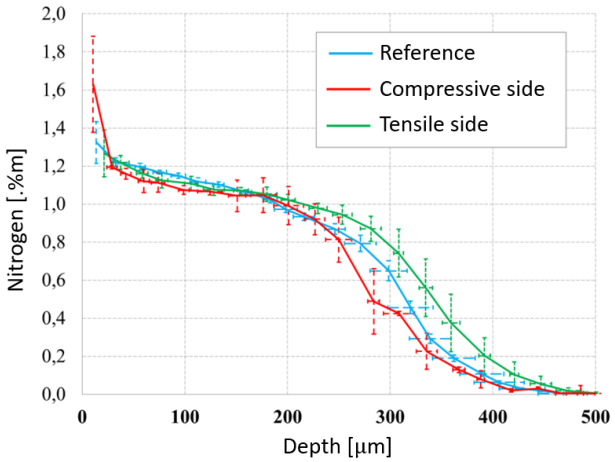

FIGURE 3.12 – Profils de teneur en azote d'échantillons de référence et d'échantillons nitrurés sous contrainte de flexion à 520 °C pendant 50 h avec un K_N = 4,37 atm $^{-1/2}$ [Guillot, 2018].

Une étude expérimentale a été réalisée sur des éprouvettes d'acier nitruré 33CrMoV12-9 afin d'observer l'influence des déformations plastiques incompatibles sur la cinétique de diffusion, autrement dit l'étude de l'influence des court-circuits de diffusion (densité de dislocation), mais aussi la densité des joints de grains, qui n'a pas été quantifiée dans ce travail. Les résultats ont permis d'observer que la cinétique de diffusion à longue distance ne semble pas être accélérée mais que les phénomènes semblent jouer un rôle sur la cinétique à courte distance (précipitation). Ces observations sont cohérentes avec ce qui a été observé dans la littérature où les phénomènes de précipitation sont fortement influencés par les déformations incompatibles [Lin et al., 2006, Tong et al., 2008, Thiriet et al., 2012, Chemkhi, 2014].

Conclusion

Ce travail de thèse a porté sur la compréhension du couplage contrainte-diffusion, en commençant par les problèmes de diffusion interstitielle et en progressant vers le cas de la nitruration gazeuse de la nuance d'acier ferritique 33CrMoV12-9. Ces recherches ont été menées grâce au développement de modèle 2D et 1D et la mise en place d'expériences particulières. Le premier objectif était de comprendre l'effet des contraintes élastiques (contraintes appliquées/résiduelles) sur la cinétique de diffusion en combinant les observations théoriques et expérimentales. Le second objectif était de découpler les effets des contraintes élastiques et des contraintes plastiques incompatibles sur la cinétique de diffusion.

Le premier objectif était de visualiser le fort couplage entre l'effet d'une force de transport (gradient de contrainte) et l'effet de la mobilité (facteur β). Il a pu être observé qu'individuellement, un gradient positif et une contrainte homogène positive conduisent tous deux à une cinétique de diffusion accélérée ; et respectivement l'inverse pour un gradient de contrainte négatif et une contrainte homogène négative.

Le second objectif était de découpler les effets des contraintes élastiques et des contraintes plastiques incompatibles sur la cinétique de diffusion. Les observations semblent montrer que les déformations élastiques jouent principalement un rôle sur la cinétique de diffusion à longue distance contre celle à courte distance dans le cas des déformations plastiques. Cela est expliqué par le fait que les déformations élastiques jouent un rôle sur les énergies potentielles et que les déformations plastiques jouent un rôle sur la densité des joints de grains et la densité de dislocations. La figure 3.13 représente schématiquement, à partir d'articles sur la dynamique moléculaire [Araki and Arai, 2010a], la façon dont les énergies potentielles sont affectées par des contraintes homogènes.

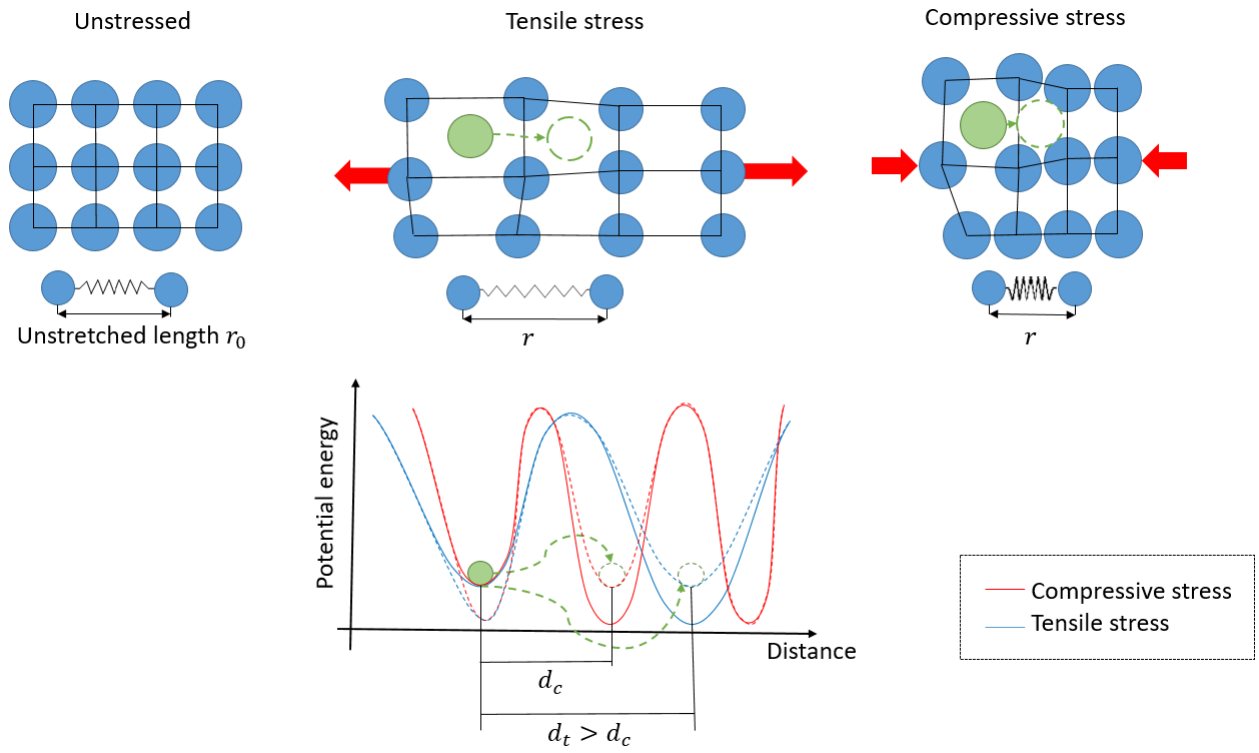

FIGURE 3.13 – Représentation schématique de l'effet des contraintes homogènes (traction/compression) sur les distances de saut et les énergies potentielles, inspirée d'études en dynamique moléculaire [Araki and Arai, 2010b, Araki and Arai, 2010a].

Ces études ont ainsi permis de comprendre d'un point de vue analytique les phénomènes (force de transport vs. mobilité) et également permis de découpler les phénomènes entre les déformations élastiques compatibles et les déformations plastiques incompatibles. Afin d'approfondir cette étude, il serait intéressant de :

- L'optimisation des traitements courts de nitruration afin de définir l'épaisseur idéale pour un temps et une température équivalents afin de ne pas observer de phénomène de double flux,
- Réaliser ces tests pour des traitements longs, c'est-à-dire des couches de diffusion dîtes profondes (> 300 μm),
- Approfondir l'expérience de l'anneau fendu en étudiant :
  - Différents champs de contraintes et ainsi observer si l'effet est linéaire ou non linéaire et pouvoir conclure sur l'effet prédominant des contraintes à travers l'effet sur la mobilité ou celle des forces motrices,
  - L'effet de la contrainte sur la mobilité à travers une expérience impliquant un champ de contrainte fixe pour différents temps de traitement,
  - L'effet de la température (en évitant toute source de fluage) afin de définir la dépendance ou non de la température sur la mobilité,
  - Les profils d'un anneau sous contrainte pour un temps de traitement initial et d'un anneau non contraint avec le temps équivalent à la profondeur effective de l'anneau sous contrainte. Leurs profils

de dureté seraient ensuite comparés et permettraient d'observer si l'influence d'un champ de contrainte accélère seulement la cinétique (profondeur de la couche de diffusion) ou si d'autres phénomènes apparaissent.

— Réaliser des essais de cisaillement pur et ainsi déterminer l'importance éventuelle du terme $2\gamma_I\sigma_{ij}$ dans l'effet de la contrainte sur la mobilité dans les simulations numériques,

— Identifier le paramètre spécifique β pour la nuance d'acier 33CrMoV12-9 en prenant en compte l'équation globale, c'est-à-dire l'effet de la mobilité et/ou des forces motrices en fonction du champ de contrainte appliqué, par des méthodes d'identification telles que : la méthode inverse ou l'étude de la transition d'échelle,

— Réaliser des expériences sur, par exemple, une éprouvette prétraitée mécaniquement (par exemple par grenaillage) puis nitrurée ou une éprouvette soumise à un champ de contraintes appliquées dans le domaine de la déformation plastique puis nitrurée, afin de confirmer les hypothèses faites sur le découplage des phénomènes entre les types de déformation (élastique/plastique),

— La réalisation d'expériences sur des pièces réelles (c'est-à-dire à géométrie complexe) en étudiant les conditions d'adsorption de l'azote (échange gaz-solide) en fonction de la préparation mécanique des surfaces (par exemple, conditions et type d'usinage et de sablage),

— L'implémentation de l'équation de couplage dans le code de diffusion-précipitation 1D développé au laboratoire en ajoutant l'aspect incrémental, c'est-à-dire en prenant en compte les contraintes à chaque instant, est à considérer afin de pouvoir prédire la diffusion à courte et longue distance en fonction des paramètres d'entrée (t, T, concentration de surface),

— Appliquer les simulations numériques à d'autres domaines impliquant des systèmes binaires, tels que le domaine de la microélectronique impliquant des champs de gradient supplémentaires de nature électrique.

Bibliography

[6507-1:2018, 2018] 6507-1:2018, N. I. (2018). Matériaux métalliques - Essai de dureté Vickers - Partie 1 : Méthode d'essai.

[AB, 2012] AB, T.-C. S. (2012). Fe-Alloys Database Version 7.0. Technical report, Sweden.

[Abrasonis et al., 2006] Abrasonis, G., Möller, W., and Ma, X. X. (2006). Anomalous ion accelerated bulk diffusion of interstitial nitrogen. *Physical Review Letters*, 96(6):15–18.

[Afnor, 1985] Afnor, n. A.-. (1985). Determination de l'épaisseur totale ou conventionnelle des couches minces durcies superficielles. Technical report.

[Alanou et al., 2004] Alanou, M. P., Evans, H. P., and Snidle, R. W. (2004). Effect of different surface treatments and coatings on the scuffing performance of hardened steel discs at very high sliding speeds. *Tribology International*, 37(2):93–102.

[Anand, 2011] Anand, L. (2011). A thermo-mechanically-coupled theory accounting for hydrogen diffusion and large elastic-viscoplastic deformations of metals. *International Journal of Solids and Structures*, 48(6):962–971.

[Andersson et al., 2002] Andersson, J.-O., Helander, T., Hdghmd, L., Shi, P., and Sundman, B. (2002). THERMO-CALC DICTRA, Computational Tools For Materials Science. *ThermoCalc*, 26(2):273–312.

[Appolaire and Gouné, 2006] Appolaire, B. and Gouné, M. (2006). Linear stability analysis of a γ-Fe4N nitride layer growing in pure iron. *Computational Materials Science*, 38(1):126–135.

[Araki and Arai, 2010a] Araki, W. and Arai, Y. (2010a). Molecular dynamics study on oxygen diffusion in yttria-stabilized zirconia subjected to uniaxial stress in terms of yttria concentration and stress direction. *Solid State Ionics*, 181(33-34):1534–1541.

[Araki and Arai, 2010b] Araki, W. and Arai, Y. (2010b). Oxygen diffusion in yttria-stabilized zirconia subjected to uniaxial stress. *Solid State Ionics*, 181(8-10):441–446.

[Arrhenius, 1889] Arrhenius, S. (1889). Über die Reaktionsgeschwindigkeit bei der Inversion von Rohrzucker durch Säuren. *Zeitschrift für Physikalische Chemie*, 4:226–248.

[ASTM International, 2013] ASTM International, W. C. (2013). ASTM E975-13, Standard Practice for X-Ray Determination of Retained Austenite in Steel with Near Random Crystallographic Orientation.

[AubertDuval,] AubertDuval. Acier GKH 33CrM0V12-9. Technical report.

[Baker et al., 2016] Baker, D. R., Verbrugge, M. W., and Bower, A. F. (2016). Thermodynamics, stress, and Stefan-Maxwell diffusion in solids: application to small-strain materials used in commercial lithium-ion batteries. *Journal of Solid State Electrochemistry*, 20(1):163–181.

[Balusamy et al., 2013] Balusamy, T., Narayanan, T. S., Ravichandran, K., Park, I. S., and Lee, M. H. (2013). Plasma nitriding of AISI 304 stainless steel: Role of surface mechanical attrition treatment. *Materials Characterization*, 85:38–47.

[Barralis et al., 1986] Barralis, J., Castex, L., and Chaize, J. (1986). Influence des conditions de traitement sur la distribution des phases et des contraintes résiduelles dans les couches nitrurées. *Mémoires et Etudes Scientifiques Revue de Métallugie*, 43(6):629–642.

[Barralis et al., 1999] Barralis, J., Castex, L., and Meader, G. (1999). *Précontraintes et traitements superficiels*, volume M1180.

[Barrallier, 1992] Barrallier, L. (1992). *Genèse des contraintes résiduelles - Etude expérimentale et modélisation.* PhD thesis.

[Barrallier, 2014] Barrallier, L. (2014). Thermochemical Surface Engineering of Steels. In *Metals and Surface Engineering*, chapter 10, pages 392–411.

[Barrallier and Barralis, 1994] Barrallier, L. and Barralis, J. (1994). On Origin of Residual Stresses Generated by Nitriding Treatment on Alloy Steels. *ICRS4, Baltimore, USA*, (June 1994):498—-505.

[Barrallier and Jégou, 2015] Barrallier, L. and Jégou, S. (2015). Traitement de nitruration et durabilité des pièces mécaniques. *CPI, Rabat, Maroc.*

[Barrallier and Jégou, 2016] Barrallier, L. and Jégou, S. (2016). Traitement de nitruration et durabilité des pièces mécaniques. In *Conception et Production Intégrées*, Tanger, Maroc.

[Barrallier and Jégou, 2017] Barrallier, L. and Jégou, S. (2017). Nitruration des aciers de construction : génération des contraintes résiduelles. In *Contraintes résiduelles, A3TS, SafranTech, Paris-Saclay.*

[Barrera et al., 2016] Barrera, O., Tarleton, E., Tang, H. W., and Cocks, A. C. (2016). Modelling the coupling between hydrogen diffusion and the mechanical behaviour of metals. *Computational Materials Science*, 122:219–228.

[Beck et al., 1966] Beck, W., Bockris, J. O., Mcbreen, J., and Nanis, L. (1966). Hydrogen permeation in metals as a function of stress, temperature and dissolved hydrogen concentration. *Proceedings of the Royal Society of London. Series A. Mathematical and Physical Sciences*, 290(1421):220–235.

[Belahssen et al., 2014] Belahssen, O., Chala, A., Temam, H., and Benramache, S. (2014). Corrosion and wear resistance of 32CrMoV13 steel nitrided by plasma. *The Royal Society of Chemistry*, pages 1–18.

[Belmonte et al., 2001] Belmonte, T., Gouné, M., and Michel, H. (2001). Numerical modeling of interstitial diffusion in binary systems. Application to iron nitriding. *Materials Science and Engineering A*, 302(2):246–257.

[Biehler et al., 2017] Biehler, J., Hoche, H., and Oechsner, M. (2017). Surface Coatings Technology Nitriding behavior and corrosion properties of AISI 304L and 316L austenitic stainless steel with deformation-induced martensite. *Surface Coatings Technology*, 324:121–128.

[Bockel et al., 1998] Bockel, S., Hess, E., Belmonte, T., Ablitzer, D., and Michel, H. (1998). Modélisation de la croissance des couches de nitrures de fer au cours de la nitruration de substrats en fer pur. *Revue de Metallurgie. Cahiers D'Informations Techniques*, 95(5):651–658.

[Bockel-Macal, 1997] Bockel-Macal, S. (1997). *Étude d'un procède de nitruration assistée par une post-décharge micro-ondes Ar-N-H en écoulement : diagnostics de la phase gazeuse et modélisation du réacteurNo Title.* PhD thesis.

[Bockris et al., 1971] Bockris, J. O., Beck, W., Genshaw, M. A., Subramanyan, P. K., and Williams, F. S. (1971). The effect of stress on the chemical potential of hydrogen in iron and steel. *Acta Metallurgica*, 19(11):1209–1218.

[Brossard et al., 2007] Brossard, J. M., Panicaud, B., Balmain, J., and Bonnet, G. (2007). Modelling of aluminized coating growth on nickel. *Acta Materialia*, 55(19):6586–6595.

[Cahn, 1961] Cahn, J. W. (1961). On spinodal decomposition. *Acta Metallurgica*, 9(9):795–801.

[Calliari et al., 2006] Calliari, I., Dabalà, M., Ramous, E., Zanesco, M., and Gianotti, E. (2006). Microstructure of a nitrided steel previously decarburized. *Journal of Materials Engineering and Performance*, 15(6):693–698.

[Calvarin et al., 2000] Calvarin, G., Huntz, A. M., and Molins, R. (2000). Oxidation mechanism of Ni-20Cr thin strips and effect of a mechanical loading. *Materials at High Temperatures*, 17(2):257–264.

[Calvarin-Amiri et al., 2001] Calvarin-Amiri, G., Huntz, A. M., and Molins, R. (2001). Effect of an applied stress on the growth kinetics of oxide scales formed on Ni-20Cr alloys. *Materials at High Temperatures*, 18(2):91–99.

[Castex, 1984] Castex, L. (1984). Redistribution des contraintes dans une plaque après enlèvement de matière. Technical report.

[Castex et al., 1987] Castex, L., Barralis, J., and Chaize, J. (1987). Etude de la tenue en fatigue de l'acier 32CDV13 nitruré. *Mémoires et Etudes Scientifiques Revue de Métallurgie*, (168):13–23.

[Castex et al., 1981] Castex, L., Lebrun, J. L., Maeder, G., and Sprauel, J. M. (1981). *Détermination des contraintes residuelles par diffraction des rayons X*. Paris.

[Cavaliere et al., 2009] Cavaliere, P., Zavarise, G., and Perillo, M. (2009). Modeling of the carburizing and nitriding processes. *Computational Materials Science*, 46(1):26–35.

[Cemin et al., 2010] Cemin, F., Echeverrigaray, F. G., Rovani, A. C., Amorim, C. L., Basso, R. L., Baumvol, I. J., and Figueroa, C. A. (2010). Influence of atomic and mechanical attrition on low temperature plasma nitriding of ferrous alloys. *Materials Science and Engineering A*, 527(13-14):3206–3209.

[Chaussumier, 1999] Chaussumier, M. (1999). *Un modèle statistique de calcul en fatigue multiaxiale pour les pièces mécaniques en acier nitruré*. PhD thesis, Paris, ENSAM.

[Chechenin et al., 2000] Chechenin, N. G., Bronsveld, P. M., Chezan, A., Craus, C. B., Boerma, D. O., De Hosson, J. T. M., and Niesen, L. (2000). TEM study of Ti-N and Cr-N precipitate formation in iron alloys. *Physica Status Solidi (A) Applied Research*, 177(1):117–125.

[Chemkhi, 2014] Chemkhi, M. (2014). *Nanocristallisation superficielle couplée à la nitruration plasma pour augmenter les propriétés de fatigue et d'usure d'alliages métalliques Systèmes Mécanique et Matériaux*. PhD thesis, Université de technologie de Troyes.

[Chemkhi et al., 2017] Chemkhi, M., Retraint, D., Roos, A., and Demangel, C. (2017). Role and effect of mechanical polishing on the enhancement of the duplex mechanical attrition/plasma nitriding treatment of AISI 316L steel. *Surface and Coatings Technology*, 325:454–461.

[Chemkhi et al., 2013] Chemkhi, M., Retraint, D., Roos, A., Garnier, C., Waltz, L., Demangel, C., and Proust, G. (2013). The effect of surface mechanical attrition treatment on low temperature plasma nitriding of an austenitic stainless steel. *Surface and Coatings Technology*, 221:191–195.

[Chen-Min Li, 1978] Chen-Min Li, J. (1978). Physical chemistry of some microstructural phenomena. *Metallurgical Transactions A*, 9(10):1353–1380.

[Christiansen et al., 2008] Christiansen, T., Dahl, K. V., and Somers, M. A. (2008). Nitrogen diffusion and nitrogen depth profiles in expanded austenite: Experimental assessment, numerical simulation and role of stress. *Materials Science and Technology*, 24(2):159–167.

[Christiansen and Somers, 2005] Christiansen, T. and Somers, M. A. (2005). Low temperature gaseous nitriding and carburising of stainless steel. *Surface Engineering*, 21(5-6):445–455.

[Christiansen and Somers, 2010] Christiansen, T. L. and Somers, M. A. (2010). The influence of stress on interstitial diffusion- Carbon diffusion data in austenite revisited. *Defect and Diffusion Forum*, 297-301(April):1408–1413.

[Chu and Lee, 1994] Chu, J. L. and Lee, S. (1994). The effect of chemical stresses on diffusion. *Journal of Applied Physics*, 75(6):2823–2829.

[Clauss et al., 2008] Clauss, A., Bischoff, E., Hosmani, S., Schacherl, R., and Mittemeijer, E. (2008). Crystal structure and morphology of mixed cr1-xalxn nitride precipitates Gaseous nitriding of fe-1.5 wt pct cr-1.5 wt pct al alloy. *Metallurgical and materials transactions A*, page 31.

[Colijn et al., 1983] Colijn, P. F., Mittemeijer, E. J., and Rozendaal, H. C. F. (1983). Light-microscopical analysis of nitrided or nitrocarburized iron and steels. *International Journal of Materials Research*, (74):620–627.

[Crank, 1979] Crank, J. (1979). *The mathematics of diffusion.* Oxford uni edition.

[Creton et al., 2014] Creton, N., Dejardin, S., Grysakowski, B., Optasanu, V., and Montésin, T. (2014). A mechano-chemical coupling for hydrogen diffusion in metals based on a thermodynamic approach. *Defect and Diffusion Forum*, 353:286–291.

[Creton et al., 2009] Creton, N., Optasanu, V., Montesin, T., Garruchet, S., and Desgranges, L. (2009). A thermodynamic approach of the mechano-chemical coupling during the oxidation of uranium dioxide. *Defect and Diffusion Forum*, 289-292:447–454.

[de Saint and de Saint-Venant, 1864] de Saint, A. J. C. B. and de Saint-Venant, M. (1864). Résumé des leçons données à École des ponts et chaussées sur l'application de la mécanique à l'établissement des constructions et des machines. *Dunod*, 1.

[Dejardin et al., 2013] Dejardin, S., Creton, N., Optasanu, V., Montesin, T., and Gruenenwald, T. (2013). Approche thermodynamique d'un modèle de diffusion de l'hydrogène dans un métal reposant sur un couplage mécano-chimique. pages 1–6, Courbevoie.

[Depouhon et al., 2014] Depouhon, P., Sprauel, J. M., Mailhé, M., and Mermoz, E. (2014). Mathematical modeling of residual stresses and distortions induced by gas nitriding of 32CrMoV13 steel. *Computational Materials Science*, 82:178–190.

[Di Leo and Anand, 2013] Di Leo, C. V. and Anand, L. (2013). Hydrogen in metals: A coupled theory for species diffusion and large elastic-plastic deformations. *International Journal of Plasticity*, 43:42–69.

[Djeghlal and Barrallier, 2003] Djeghlal, M. and Barrallier, L. (2003). Influence of alloying elements (Cr,Mo,V) on nitrides residual stresses generated during the nitriding of synthetic iron alloys. *Annales de Chimie Science des Matériaux*, 28(1):43–52.

[Dong et al., 2013] Dong, X., Fang, X., Feng, X., and Hwang, K. C. (2013). Diffusion and stress coupling effect during oxidation at high temperature. *Journal of the American Ceramic Society*, 96(1):44–46.

[Du and Ägren, 1995] Du, H. and Ägren, J. (1995). Gaseous Nitriding Iron -— Evaluation of Diffusion Data of N ın γ' and ϵ Phases. *International Journal of Materials Research*, 86(8):522–529.

[Du and Ågren, 1996] Du, H. and Ågren, J. (1996). Theoretical treatment of nitriding and nitrocarburizing of iron. *Metallurgical and Materials Transactions A: Physical Metallurgy and Materials Science*, 27(4):1073–1080.

[Dulcy and Gantois, 2005] Dulcy, J. and Gantois, M. (2005). Mécanismes de transfert appliqués aux traitements thermochimiques. *Traitement thermique*, 360:25–31.

[Dulcy and Gantois, 2012] Dulcy, J. and Gantois, M. (2012). *Formation et durcissement de la couche de diffusion en nitruration et nitrocarburation - Systèmes fer-chrome-azote et fer-chrome-azote-carbone*, volume 33.

[Dulcy et al., 2002] Dulcy, J., Torchane, L., and Gantois, M. (2002). Nitruration-Mecanismes de formation et cinetique de croissance des couches nitrurees. Traitement thermique. 341:19–25.

[Dupuy, 1930] Dupuy, E. L. (1930). Le système fer-carbone. *Rev. Met. Paris*, 27(12):686–692.

[Einstein, 1905] Einstein, A. (1905). Uber die von der molekularkinetischen Theorie der Wärme geforderte Bewegung von in ruhenden Flüssigkeiten suspensierten Teilchen. *Ann. d. Phys.*, 17:549–560.

[Fallot, 2015] Fallot, G. (2015). *Rôle du carbone lors de la nitruration d'aciers de construction et influence sur les propriétés mécaniques*. PhD thesis, Arts et Métiers.

[Ferkel et al., 2003a] Ferkel, H., Estrin, Y., Blawert, C., and Valiev, R. Z. (2003a). RF nitriding of severely deformed Armco iron and St2K50. *Surface and Coatings Technology*, 174-175:1164–1170.

[Ferkel et al., 2002] Ferkel, H., Glatzer, M., Estrin, Y., and Valiev, R. Z. (2002). RF plasma nitriding of a severely deformed high alloyed steel. *Scripta Materialia*, 46(9):623–628.

[Ferkel et al., 2003b] Ferkel, H., Glatzer, M., Estrin, Y., Valiev, R. Z., Blawert, C., and Mordike, B. L. (2003b). RF plasma nitriding of severely deformed iron-based alloys. *Materials Science and Engineering A*, 348(1-2):100–110.

[Fick, 1855] Fick, A. (1855). Ueber Diffusion. *Annalen der Physik*, 170(1):59–86.

[Fourier and Darboux, 1822] Fourier, J. B. J. and Darboux, G. (1822). *G. Théorie analytique de la chaleur, (Vol. 504). Paris: Didot.*

[François et al., 2012a] François, D., Pineau, A., and Zaoui, A. (2012a). *Mechanical Behaviour of Materials - Volume 1: Micro- and Macroscopic Constitutive Behaviour*, volume 180. Springer.

[François et al., 2012b] François, D., Pineau, A., and Zaoui, A. (2012b). *Mechanical Behaviour of Materials: Volume II: Fracture Mechanics and Damage*.

[Frappart et al., 2012] Frappart, S., Feaugas, X., Creus, J., Thebault, F., Delattre, L., and Marchebois, H. (2012). Hydrogen solubility, diffusivity and trapping in a tempered Fe-C-Cr martensitic steel under various mechanical stress states. *Materials Science and Engineering A*, 534:384–393.

[Fry, 1932] Fry, A. (1932). The theory and pratice of nitrogen case-hardening. *Iron and Steel Institute*, 1:191–213.

[Galdikas and Moskalioviene, 2010] Galdikas, A. and Moskalioviene, T. (2010). Stress induced nitrogen diffusion during nitriding of austenitic stainless steel. *Computational Materials Science*, 50(2):796–799.

[Galdikas and Moskalioviene, 2020] Galdikas, A. and Moskalioviene, T. (2020). The anisotropic stress-induced diffusion and trapping of nitrogen in austenitic stainless steel during nitriding. *Metals*, 10(10):1–13.

[Gao et al., 2015] Gao, X., Fang, D., and Qu, J. (2015). A chemo-mechanics framework for elastic solids with surface stress. *Proceedings of the Royal Society A: Mathematical, Physical and Engineering Sciences*, 471(2182).

[Garcke et al., 2004] Garcke, H., Nestler, B., and Stinner, B. (2004). A diffuse interface model for alloys with multiple components and phases. *SIAM Journal on Applied Mathematics*, 64(3):775–799.

[Gauthier et al., 2009] Gauthier, W., Pailler, F., Lamon, J., and Pailler, R. (2009). Oxidation of silicon carbide fibers during static fatigue in air at intermediate temperatures. *Journal of the American Ceramic Society*, 92(9):2067–2073.

[Gerardin and JP, 1977] Gerardin, D. and JP, M. (1977). Etude microstructurale des couches nitrurees du fer pur obtenues par bombardement ionique.

[Germain et al., 2020] Germain, L., Jégou, S., and Barrallier, L. (2020). Couplage contraintes-diffusion dans les traitements thermochimiques. *Aussois 2020 - Contraintes résiduelles : de nouveaux outils pour de nouveaux défis*, (1):1–5.

[Ghiglione et al., 1996] Ghiglione, D., Leroux, C., and Leroux, C. (1996). Nitruration, nitrocarburation et dérivés. *Techniques de l'ingénieur*, (M1227).

[Ginter, 2006] Ginter, C. (2006). *Influence des éléments d'addition sur l'enrichissement d'azote et le durcissement d'aciers nitrurés*. PhD thesis.

[Ginter et al., 2006] Ginter, C., Torchane, L., Dulcy, J., Gantois, M., Malchère, A., Esnouf, C., and Turpin, T. (2006). A new approach to hardening mechanisms in the diffusion layer of gas nitrided α-alloyed steels. Effects of chromium and aluminium: Experimental and simulation studies. *Metallurgia Italiana*, 98(7-8):29–35.

[Girodin and Moraux, 2002] Girodin, D. and Moraux, J. (2002). L'acier 32crmov13 nitrurés profond pour applications aéronautiques. *Traitement Thermique*, (341).

[Godet, 2018] Godet, F. (2018). *Influence de la microstructure sur le comportement mécanique d'une couche nitrurée de l'acier de nuance 33CrMoV12-9 en vue de l'optimisation des propriétés en fatigue*. PhD thesis, École Nationale Supérieure d'Arts et Métiers.

[Goldschmidt, 1967] Goldschmidt, H. J. (1967). *Interstitial Alloys*, volume 20.

[Goret, 2006] Goret, V. (2006). *Modélisation de la nitruration: prise en compte de la géométrie des pièces traitées*. PhD thesis, Paris, ENSAM.

[Gouné et al., 2000] Gouné, M., Belmonte, T., Fiorani, J. M., Chomer, S., and Michel, H. (2000). Modelling of diffusion-precipitation in nitrided alloyed iron. *Thin Solid Films*, 377-378:543–549.

[Gouné et al., 2003] Gouné, M., Belmonte, T., Redjämia, A., Weisbecker, P., Fiorani, J. M., and Michel, H. (2003). Thermodynamic and structural studies on nitrided Fe-1.62Fe-0.56 *Materials Science and Engineering A*, 351(1-2):23–30.

[Grabke, 1968] Grabke, H. (1968). Reaktionen von Ammoniak, Stickstoff und Wasserstoff and der Öberfläche von Eisen. *Berichte der Bunsengesellchaft*, 4(72).

[Gressmann et al., 2008] Gressmann, T., Leineweber, A., and Mittemeijer, E. J. (2008). X-ray diffraction line-profile analysis of hexagonal -iron nitride compound layers: Composition-and stress-depth profiles. *Philosophical Magazine*, 88(2):145–169.

[Gu et al., 2002] Gu, J. F., Bei, D. H., Pan, J. S., Lu, J., and Lu, K. (2002). Improved nitrogen transport in surface nanocrystallized low-carbon steels during gaseous nitridation. *Materials Letters*, 55(5):340–343.

[Guillot, 2018] Guillot, B. (2018). *Etude de procédés de préparation de surface avant nitruration - fiabilité du procédé*. PhD thesis, École Nationale Supérieure d'Arts et Métiers.

[Guillot et al., 2016] Guillot, B., Jégou, S., and Barrallier, L. (2016). Influence of strain hardening on gaseous nitriding of steels. *23rd International Federation of Heat Treatment and Surface Engineering Congress 2016, IFHTSE 2016*, pages 46–50.

[Gunther et al., 2004] Gunther, D., Hoffmann, F., and Hirsch, T. (2004). Formation and origin of residual stresses during nitriding of chromium-alloyed steels. *Harterei-Technische Mitteilungen*, 59(1):18–27.

[Gururajan and Lahiri, 2016] Gururajan, M. P. and Lahiri, A. (2016). Elastic stress effects on microstructural instabilities. *Journal of the Indian Institute of Science*, 96(3):199–234.

[Haftbaradaran et al., 2011] Haftbaradaran, H., Song, J., Curtin, W. A., and Gao, H. (2011). Continuum and atomistic models of strongly coupled diffusion, stress, and solute concentration. *Journal of Power Sources*, 196(1):361–370.

[Hecht, 2020] Hecht, F. (2020). FreeFem++ Documentation. *Documentation*, page 671.

[Hirsch et al., 2004] Hirsch, T. K., Rocha, A. D. S., Ramos, F. D., and Strohaecker, T. R. (2004). Residual stress-affected diffusion during plasma nitriding of tool steels. *Metallurgical and Materials Transactions A: Physical Metallurgy and Materials Science*, 35 A(11):3523–3530.

[Honig, 2007] Honig, J. M. (2007). Chapter 6 - Irreversible Thermodynamics. chapter Chapter 6, pages 347–396. Academic Press, Amsterdam.

[Hosmani, 2005] Hosmani, S. (2005). The kinetics of the nitriding of fe-7cr alloys the role of the nitriding potential. *Materials Science and Technology*, 21(173-174):113–124.

[HOSMANI, 2006] HOSMANI, S. (2006). Nitrogen uptake by an fe-v alloy Quantitative analysis of excess nitrogen. *Acta Materialia*, 54:2738–2792.

[Hosmani et al., 2007] Hosmani, S., Schacherl, R., and Mittemeijer, E. (2007). Kinetics of nitriding fe-2 wt pct v alloy Mobile and immobile excess nitrogen. *Metallurgical and Materials Transactions A*, 38A:7–16.

[Hosmani et al., 2008] Hosmani, S., Schacherl, R., and Mittemeijer, E. (2008). Compound layer formation on iron-based alloys upon nitriding ; phase constitution and pore formation. *HTM Journal of Heat Treatment and Materials*, (63):139–146.

[Hosmani et al., 2009] Hosmani, S. S., Schacherl, R. E., and Mittemeijer, E. J. (2009). Morphology and constitution of the compound layer formed on nitrided Fe-4wt. *Journal of Materials Science*, 44(2):520–527.

[Hwang and Perng, 1994] Hwang, L. C. and Perng, T. P. (1994). Hydrogen transport in ferritic stainless steel under elastic stress. *Materials Chemistry and Physics*, 36(3-4):231–235.

[Jack and Winnik, 1979] Jack, D. H. and Winnik, S. (1979). The Effect of Process Variables on the Fatigue Resistance of Nitrided Steel. *Heat Treatment 79*, page 30.

[Jack, 1975] Jack, K. (1975). . *Heat Treatment ´73 Proc. The Metals Society*, (21):39–50.

[Jack, 1948a] Jack, K. . H. . (1948a). Binary and Ternary Interstitial Alloys III . The Iron-Carbon System : The Characterization of a New Iron Carbide. *Proceedings of the Royal Society of London . Series A , Mathematical and Physical*, 195(1040):56–61.

[Jack, 1948b] Jack, K. H. (1948b). Binary and ternary interstitial alloys II . The iron-carbon-nitrogen system. *Proceedings of the Royal Society of London. Series A. Mathematical and Physical Sciences*, 10(195):41–55.

[Jayalakshmi et al., 2016] Jayalakshmi, M., Huilgol, P., Bhat, B. R., and Bhat, K. U. (2016). Microstructural characterization of low temperature plasma-nitrided 316L stainless steel surface with prior severe shot peening. *Materials and Design*, 108:448–454.

[Jegou, 2009] Jegou, S. (2009). Influence des éléments d'alliage sur la genèse des contraintes résiduelles d'aciers nitrurés.

[Jegou et al., 2016] Jegou, S., Barrallier, L., and Fallot, G. (2016). Science Arts Métiers (SAM). In *International Federation of Heat Treatment and Surface Engineering Congress (23; 2016; Savannah), Etats-Unis, 2016-04-18 - Conference Proceedings of the 23rd IFHTSE Congress*.

[Jegou et al., 2018] Jegou, S., Barrallier, L., and Fallot, G. (2018). Gaseous nitriding behaviour of 33CrMoV12-9 steel: Evolution of the grain boundaries precipitation and influence on residual stress development. *Surface and Coatings Technology*, 339(January):78–90.

[Jegou et al., 2010] Jegou, S., Barrallier, L., and Kubler, R. (2010). Phase transformations and induced volume changes in a nitrided ternary Fe-3 *Acta Materialia*, 58(7):2666–2676.

[Jégou et al., 2011] Jégou, S., Barrallier, L., and Somers, M. A. J. (2011). Évolution des contraintes résiduelles dans la couche de diffusion d'un acier modèle Fe-Cr-C nitruré. *Traitements et matériaux*, (411).

[Jespersen et al., 2016] Jespersen, F. N., Hattel, J. H., and Somers, M. A. (2016). Modelling the evolution of composition-and stress-depth profiles in austenitic stainless steels during low-temperature nitriding. *Modelling and Simulation in Materials Science and Engineering*, 24(2):25003.

[Jessner et al., 2009] Jessner, P., Danoix, R., Hannoyer, B., and Danoix, F. (2009). Investigations of the nitrided subsurface layers of an Fe-Cr-model alloy. *Ultramicroscopy*, 109(5):530–534.

[Jung et al., 2011] Jung, K. S., Schacherl, R., Bischoff, E., and Mittemeijer, E. J. (2011). Normal and excess nitrogen uptake by iron-based Fe-Cr-Al alloys; the role of the CrAl atomic ratio. *Philosophical Magazine, Taylor Francis*, page 1.

[Keddam et al., 2004a] Keddam, M., Djeghlal, M. E., and Barrallier, L. (2004a). A diffusion model for simulation of bilayer growth of nitrided pure iron. 378:475–478.

[Keddam et al., 2005] Keddam, M., Djeghlal, M. E., and Barrallier, L. (2005). A simple diffusion model for the growth kinetics of γ iron nitride on the pure iron substrate. *Applied Surface Science*, 242(3-4):369–374.

[Keddam et al., 2004b] Keddam, M., Djeghlal, M. E., Barrallier, L., and Salhi, E. (2004b). Computer simulation of nitrided layers growth for pure iron. *Computational Materials Science*, 29(1):43–48.

[Kikuchi et al., 2010] Kikuchi, S., Nakahara, Y., and Komotori, J. (2010). Fatigue properties of gas nitrided austenitic stainless steel pre-treated with fine particle peening. *International Journal of Fatigue*, 32(2):403–410.

[Kirchheim, 1986] Kirchheim, R. (1986). Interaction of hydrogen with external stress fields. *Acta Metallurgica*, 34(1):37–42.

[KlÄumper-Westkamp et al., 1989] KlÄumper-Westkamp, H., Hoffmann, F., and Mayr, P. (1989). Nitrierschichtbildung und kohlen stoffdiffusion in abhÄangigkeit von der nitrierkkennzahl. *HÄarterei-Technische Mitteilungen*, 44(6):346–355.

[Ko et al., 2007] Ko, S. C., Zhang, T. Y., and Lee, S. (2007). Influence of chemical stresses in the permeation, one-side and two-side charging processes. *Journal of Applied Physics*, 101(11).

[Kochmanski and Nowacki, 2008] Kochmanski, P. and Nowacki, J. (2008). Surface Coatings Technology In fl uence of initial heat treatment of 17-4 PH stainless steel on gas nitriding kinetics. 202:4834–4838.

[Kozeschnik, 2007] Kozeschnik, E. (2007). 5 - Modeling Solid-State Diffusion. pages 151–177. Academic Press, Burlington.

[Kreft et al., 1992] Kreft, U., Hoffmann, F., Hirsch, T., and Mayr, P. (1992). Investigation of the formation of residual stress in the compound layer during gas nitriding. In *3 rd European Conference on Residual Stresses*, pages 115–122.

[Kreft et al., 1995] Kreft, U., Hoffmann, F., Hirsch, T., and Mayr, P. (1995). Formation of residual stresses in compound layer during gas nitriding measured by in situ technique. *Surface Engineering*, 11(1):61–65.

[Krupp et al., 2008] Krupp, U., Orosz, R., Christ, H. J., and Monceau, D. (2008). On the mutual interaction between mechanical stresses and internal corrosion during isothermal and cyclic oxidation of nickel-base superalloys. *Materials Science Forum*, 595-598 PA:1023–1031.

[Kücükyildiz et al., 2020] Kücükyildiz, Ö. C., Sonne, M. R., Thorborg, J., Somers, M. A., and Hattel, J. H. (2020). Thermo-chemical-mechanical simulation of low temperature nitriding of austenitic stainless steel; inverse modelling of surface reaction rates. *Surface and Coatings Technology*, 381(October 2019):125145.

[Larche, 1988] Larche, F. (1988). Thermodynamics of Stressed Solids. *Solid State Phenomena*, 3-4:205–214.

[Larché and Cahn, 1978] Larché, F. and Cahn, J. W. (1978). A nonlinear theory of thermochemical equilibrium of solids under stress. *Acta Metallurgica*, 26(1):53–60.

[Larché and Cahn, 1973] Larché, F. C. and Cahn, J. W. (1973). A linear theory of thermochemical equilibrium of solids under stress. *Acta Metallurgica*, 21(8):1051–1063.

[Larche and Cahn, 1978a] Larche, F. C. and Cahn, J. W. (1978a). Thermochemical equilibrium of multiphase solids under stress. *Acta Metallurgica*, 26(10):1579–1589.

[Larche and Cahn, 1978b] Larche, F. C. and Cahn, J. W. (1978b). Thermochemical equilibrium of multiphase solids under stress. *Acta Metallurgica*, 26(10):1579–1589.

[Larché and Cahn, 1982] Larché, F. C. and Cahn, J. W. (1982). The effect of self-stress on diffusion in solids. *Acta Metallurgica*, 30(10):1835–1845.

[Larché and Cahn, 1985] Larché, F. C. and Cahn, J. W. (1985). The interactions of composition and stress in crystalline solids. *Acta Metallurgica*, 33(3):331–357.

[Larché and Voorhees, 1996] Larché, F. C. and Voorhees, P. W. (1996). Diffusion and stresses: Basic thermodynamics. *Defect and Diffusion Forum*, 129-130:31–36.

[Larsson and Ågren, 2004] Larsson, H. and Ågren, J. (2004). Gas nitriding of high vanadium steels-experiments and simulations. *Metallurgical and Materials Transactions A: Physical Metallurgy and Materials Science*, 35 A(9):2799–2802.

[Lecis et al., 2012] Lecis, N., Vedani, M., and Farè, S. (2012). Effect of substrate structure on properties of nitrided layers formed on pure iron. *International Journal of Structural Integrity*, 3(4):476–487.

[Lehrer, 1930] Lehrer, E. (1930). Uber das eisen wasserstoff-ammoniak gleichgewicht. *Z. Elektrochemie.*, 36(6):383–392.

[Lemaitre and Chaboche, 1990] Lemaitre, J. and Chaboche, J. L. (1990). *Mechanics of solid materials*. Cambridge University Press.

[Leroy et al., 1982] Leroy, C., Michel, H., and Gantois, M. (1982). Etude des transformations de phases associées à la nitruration des aciers alliés au chrome. *Associazione Italiana*.

[Leroy et al., 1986] Leroy, C., Michel, H., and Gantois, M. (1986). Transformation of (Cr, M)7C3-type carbides during nitriding of chromium alloyed steels. *Journal of Materials Science*, 21(10):3467–3474.

[Lewis et al., 1993] Lewis, F. . A. ., Tong, X. . Q. ., Kandasamy, K., Bucur, R. V., and Sakamoto, Y. (1993). Gorsky Effect Consequences of Lattice Expansive Strain Gradients in Diffusion of Hydrogen in Metals. *Thermochimica Acta*, 218:57–69.

[Lewis and Randall, 1923] Lewis, G. N. and Randall, M. (1923). Thermodynamics and the free energy of chemical substances. *McGraw-Hill*.

[Li et al., 1999] Li, C. X., Sun, Y., and Bell, T. (1999). Consideration of fretting fatigue properties of plasma nitrided En19 steel. *Surface Engineering*, 15(2):149–153.

[Li, 1981] Li, J. C. (1981). Chemical potential for diffusion in a stressed solid. *Scripta Metallurgica*, 15(1):21–28.

[Li et al., 1966] Li, J. C., Oriani, R. A., and Darken, L. S. (1966). The thermodynamics of stressed solids. *Zeitschrift für Physikalische Chemie Neue Folge*, 49:271–290.

[Li et al., 2017] Li, W., Guo, W., Zhu, X., Jin, X., Li, X., and Dong, H. (2017). The effect of applied compressive stress on the diffusion of carbon in carbon supersaturated S-phase layer. *Surface and Coatings Technology*, 331(April):1–6.

[Li et al., 2016] Li, Y., Zhang, K., Zheng, B., and Yang, F. (2016). Effect of local deformation on the coupling between diffusion and stress in lithium-ion battery. *International Journal of Solids and Structures*, 87:81–89.

[li Lin et al., 2017] li Lin, J., An, K., Stoica, A. D., and Heuser, B. J. (2017). Effect of external stress on deuteride (hydride) precipitation in Zircaloy-4 using in situ neutron diffraction. *Journal of Nuclear Materials*, 487:396–405.

[Liapina et al., 2006] Liapina, T., Leineweber, A., and Mittemeijer, E. J. (2006). Phase transformations in iron-nitride compound layers upon low-temperature annealing: Diffusion kinetics of nitrogen in ϵ- and γ-iron nitrides. *Metallurgical and Materials Transactions A: Physical Metallurgy and Materials Science*, 37(2):319–330.

[Lightfoot and Jack, 1975] Lightfoot, B. J. and Jack, D. H. (1975). Kinetics of nitriding with and without white-layer formation. *Heat Treatment'73*, page 30.

[Limarga and Wilkinson, 2006] Limarga, A. M. and Wilkinson, D. S. (2006). A model for the effect of creep deformation and intrinsic growth stress on oxide/nitride scale growth rates with application to the nitridation of γ-TiAl. *Materials Science and Engineering A*, 415(1-2):94–103.

[Lin et al., 2006] Lin, Y., Lu, J., and Wang, L. (2006). Surface nanocrystallization by surface mechanical attrition treatment and its effect on structure and properties of plasma nitrided AISI 321 stainless steel. 54:5599–5605.

[Liu and Shen, 2018] Liu, W. and Shen, S. (2018). Coupled chemomechanical theory with strain gradient and surface effects. *Acta Mechanica*, 229(1):133–147.

[Locquet, 1998] Locquet, J.-N. (1998). *Caracterisations metallurgiques et mecaniques de couches nitrurees relation microstructure comportement*. PhD thesis.

[Locquet et al., 1997] Locquet, J. N., Soto, R., Barrallier, L., and Charaï, A. (1997). Complete TEM investigation of a nitrided layer for a Cr alloy steel. *Microscopy Microanalysis Microstructures*, 8(4-5):335–352.

[Loeffel and Anand, 2011] Loeffel, K. and Anand, L. (2011). A chemo-thermo-mechanically coupled theory for elastic-viscoplastic deformation, diffusion, and volumetric swelling due to a chemical reaction. *International Journal of Plasticity*, 27(9):1409–1431.

[Logan, 1982] Logan, S. R. (1982). The origin and status of the arrhenius equation. *Journal of Chemical Education*, 59(4):279–281.

[Lu and Lu, 2004] Lu, K. and Lu, J. (2004). Nanostructured surface layer on metallic materials induced by surface mechanical attrition treatment. *Materials Science and Engineering A*, 375-377(1-2 SPEC. ISS.):38–45.

[Lu et al., 2010] Lu, S. D., Wang, Z. B., and Lu, K. (2010). Enhanced chromizing kinetics of tool steel by means of surface mechanical attrition treatment. *Materials Science and Engineering A*, 527(4-5):995–1002.

[Lu et al., 2021] Lu, Y., Li, D., Ma, H., Liu, X., Wu, M., and Hu, J. (2021). Enhanced plasma nitriding efficiency and properties by severe plastic deformation pretreatment for 316L austenitic stainless steel. *Journal of Materials Research and Technology*, 15:1742–1746.

[Macherauch, 1987] Macherauch, E. (1987). *Introduction To Residual Stress.*, volume 4. Pergamon Books Ltd.

[Macherauch and Hauk, 1987] Macherauch, E. and Hauk, V. (1987). *Residual stresses in science and technology*, volume 1.

[Manova et al., 2007] Manova, D., Mändl, S., Neumann, H., and Rauschenbach, B. (2007). Influence of grain size on nitrogen diffusivity in austenitic stainless steel. *Surface and Coatings Technology*, 201(15):6686–6689.

[Mehrer, 1996] Mehrer, H. (1996). The effect of pressure on diffusion. *Defect and Diffusion Forum*, 129-130:57–74.

[Meka et al., 2014] Meka, S. R., Bischoff, E., Hosmani, S. S., and Mittemeijer, E. J. (2014). Interrelationships of defects, nitride modification and excess nitrogen in nitrided Fe-4.75 at. *International Journal of Materials Research*, 105(11):1057–1066.

[Michalski et al., 2005] Michalski, J., Tacikowski, J., Wach, P., Lunarska, E., and Baum, H. (2005). Formation of single-phase layer of γ'-nitride in controlled gas nitriding. Metal Science and Heat Treatment. *Metals and Materials International*, (47):516–519.

[Mittemeijer, 1984] Mittemeijer, E. (1984). Proceedings of the symposium sponsored by the heat treatment committee of the metallurgical society of AIME held at the 112th AIME annual meeting. *The Metallurgical Society of AIME.Proceedings of the symposium sponsored by the heat treatment committee of the metallurgical society of AIME held at the 112th AIME annual meeting.*

[Mittemeijer et al., 1981] Mittemeijer, E. J., Rozendaal, H. C. F., Colijn, P. F., Van der Schaaf, P. J., and Furnee, R. H. (1981). Microstructure of nitrocarburized steels. Heat Treatment. (81):107–115.

[Mittemeijer and Somers, 1988] Mittemeijer, E. J. and Somers, M. (1988). A Model for Excess Nitrogen Uptake in Nitrided Binary Iron-Base Alloys. *High Nitrogen Steels–HNS*, 88:333–337.

[Mittemeijer and Somers, 1997] Mittemeijer, E. J. and Somers, M. A. (1997). Thermodynamics, kinetics, and process control of nitriding. *Surface Engineering*, 13(6):483–497.

[Moore and Evans, 1958] Moore, M. G. and Evans, W. P. (1958). Residual stress measurement by x-ray diffraction. *SAE Transactions*, (66):340–395.

[Moskalioviene and Galdikas, 2019] Moskalioviene, T. and Galdikas, A. (2019). Kinetic model of anisotropic stress assisted diffusion of nitrogen in nitrided austenitic stainless steel. *Surface and Coatings Technology*, 366(March):277–285.

[Moulin et al., 1996] Moulin, G., Arevalo, P., and Salko, A. (1996). Influence of external mechanical loadings (creep, fatigue) on oxygen diffusion during nickel oxidation. *Oxidation of Metals*, 45(1-2):153–181.

[Mura, 1987] Mura, T. (1987). *Micromechanics of defects in solids*. Springer, Dordrecht.

[Nakata et al., 2003] Nakata, K., Yamauchi, W., Akamatsu, K., and Ushio, M. (2003). Plasma nitriding behavior of low carbon binary alloy steels. *Surface and Coatings Technology*, 174-175:1206–1210.

[Nazarov and Mikheev, 2005] Nazarov, A. V. and Mikheev, A. a. (2005). Theory of Diffusion under Stress. *Diffusion Fundamentals*, 2:32.1–32.2.

[Noll, 1974] Noll, W. (1974). *The Foundations of Mechanics and Thermodynamics*.

[Noyan and Cohen, 1987] Noyan, I. C. and Cohen, J. B. (1987). *Residual Stress - Measurement by Diffraction and Interpretation*.

[Ochoa et al., 2006] Ochoa, E. A., Figueroa, C. A., Czerwiec, T., and Alvarez, F. (2006). Enhanced nitrogen diffusion induced by atomic attrition. *Applied Physics Letters*, 88(25):2004–2007.

[Ozbaysal et al., 1986] Ozbaysal, K., Inal, O. T., and Romig, A. D. (1986). Ion-nitriding behavior of several tool steels. *Materials Science and Engineering*, 78(2):179–191.

[Panfil et al., 2017] Panfil, D., Kulka, M., Wach, P., Michalski, J., and Przestacki, D. (2017). Nanomechanical properties of iron nitrides produced on 42CrMo4 steel by controlled gas nitriding and laser heat treatment. *Journal of Alloys and Compounds*, 706:63–75.

[Panicaud et al., 2012] Panicaud, B., Chemkhi, M., Roos, A., and Retraint, D. (2012). Theoretical modelling of iron nitriding coupled with a nanocrystallisation treatment. Application to numerical predictions for ferritic stainless steels. *Applied Surface Science*, 258(17):6611–6620.

[Philibert, 1990] Philibert, J. (1990). *Diffusion et transport de matière dans les solides*. les éditio edition.

[Philibert, 1996a] Philibert, J. (1996a). Diffusion and Stresses. *Defect and Diffusion Forum*, 129-130:3–8.

[Philibert, 1996b] Philibert, J. (1996b). Diffusion dans un champ de contraintes.

[Pickering, 1978] Pickering, F. (1978). Physical metallurgy and the design of steels. *Applied Science Publishers Ltd*.

[Raghavan, 1987] Raghavan, V. (1987). Phase diagrams of ternary iron alloys. *ASM International*, (226).

[Ramazanov et al., 2016] Ramazanov, K. N., Esipov, R. S., Vardanyan, E. L., and Agzamov, R. D. (2016). Influence of martensitic steel ultrafine-grained structure on diffusion processes at low-temperature ion nitriding. *Journal of Physics: Conference Series*, (1):2–4.

[Ramsay et al., 2019] Ramsay, J. D., Evans, H. E., Child, D. J., Taylor, M. P., and Hardy, M. C. (2019). The influence of stress on the oxidation of a Ni-based superalloy. *Corrosion Science*, 154(February):277–285.

[Ratajski, 2009] Ratajski, J. (2009). Relation between phase composition of compound zone and growth kinetics of diffusion zone during nitriding of steel. *Surface and Coatings Technology*, 203(16):2300–2306.

[Revel et al., 1984] Revel, J., Pomian, K., and Levy, M. (1984). *Œuvres de Pierre Curie*. Gordon and Breach Science Publishers S.A., Paris.

[Richmond et al., 1964] Richmond, O., Leslie, W., and Wriedt, H. (1964). Theory of residual stresses due to chemical concentration gradients. *Transactions of the ASM*, 57:295– 301.

[Rickerby et al., 1986] Rickerby, D. S., Henderson, S., Hendry, A., and Jack, K. H. (1986). Overview no. 51 Structure and thermochemistry of nitrided iron-titanium alloys. *Acta Metallurgica*, 34(9):1687–1699.

[Rizk, 1979] Rizk, A. S. (1979). The effects of treating inconel 625 in an N2 + H2 glow discharge. *Surface Technology*, 9(1):77–81.

[Rozendaal et al., 1985] Rozendaal, H. C., Colijn, P. F., and Mittemeijer, E. J. (1985). Morphology, composition, and residua1 stresses of compoundiayers of nitrocarburizediron and steels. *Surface Engineering*, 1(1):30–42.

[Rozendaal et al., 1983] Rozendaal, H. C., Mittemeijer, E. J., Colijn, P. F., and Van Der Schaaf, P. J. (1983). Development of Nitrogen Concentration Profiles on Nitriding Iron. *Metallurgical transactions. A, Physical metallurgy and materials science*, 14 A(2):395–399.

[Saliya et al., 2019] Saliya, K., Panicaud, B., and Labergère, C. (2019). Advanced modeling and numerical simulations for the thermo-chemico-mechanical behaviour of materials with damage and hydrogen, based on the thermodynamics of irreversible processes. *Finite Elements in Analysis and Design*, 164(July):79–97.

[Sallès-Desvignes et al., 2000] Sallès-Desvignes, I., Bertrand, G., Montesin, T., and Favergeon, J. (2000). Coupling between diffusion, stress field and chemical reaction in a metal-gas oxidation. *Solid State Phenomena*, 72:9–16.

[Samih et al., 2014] Samih, Y., Novelli, M., Thiriet, T., Bolle, B., Allain, N., Fundenberger, J. J., Marcos, G., Czerwiec, T., and Grosdidier, T. (2014). Plastic deformation to enhance plasma-assisted nitriding: On surface contamination induced by Surface Mechanical Attrition Treatment. In *IOP Conference Series: Materials Science and Engineering*, volume 63.

[Schacherl et al., 2004] Schacherl, R. E., Graat, P. C., and Mittemeijer, E. J. (2004). The nitriding kinetics of iron-chromium alloys; The role of excess nitrogen: Experiments and modelling. *Metallurgical and Materials Transactions A: Physical Metallurgy and Materials Science*, 35 A(11):3387–3398.

[Sennour, 2002] Sennour, M. (2002). *Apport de la microscopie électronique en transmission et de la spectroscopie EELS à la caractérisation de nitrures (AIN, CrN) dans le fer et l'alliage Fe-Cr (Doctoral dissertation, Lyon, INSA).* PhD thesis.

[Sennour et al., 2004] Sennour, M., Jacq, C., and Esnouf, C. (2004). Mechanical and microstructural investigations of nitrided Fe-Cr layers. *Journal of Materials Science*, 39(14):4533–4541.

[Seybolt, 1969] Seybolt, A. (1969). Some observations on the metallurgy of iron nitriding. *Transactions of the Metallurgical Society of AIME*, 245:769–778.

[Shabashov et al., 2009] Shabashov, V. A., Borisov, S. V., Litvinov, A. V., Zamatovskii, A. E., Vil'Danova, N. F., Voronin, V. I., and Shepatkovskii, O. P. (2009). Nanostructure formation and phase transformations in nitrided stainless steel Kh18N8 during severe cold deformation. *Physics of Metals and Metallography*, 107(6):601–612.

[She et al., 2013] She, D., Yue, W., Fu, Z., Gu, Y., Wang, C., and Liu, J. (2013). The effect of nitriding temperature on hardness and microstructure of die steel pre-treated by ultrasonic cold forging technology. *Materials and Design*, 49:392–399.

[Simon and Grzywna, 1992] Simon, A. M. and Grzywna, Z. J. (1992). On the Larché-Cahn theory for stress-induced diffusion. *Acta Metallurgica Et Materialia*, 40(12):3465–3473.

[Smigelskas and Kirkendall, 1947] Smigelskas, A. D. and Kirkendall, E. O. (1947). Zinc Diffusion in Alpha Brass. *Trans. AIME.*, 171:130–142.

[Somers, 1989] Somers, M. (1989). Internal and external nitriding and nitrocarburizing of iron and iron-based alloys.

[Somers, 2004] Somers, M. A. (2004). Modelling nitriding of iron: FRom thermodynamics to residual stress. *J. Phys. IV France*, 120:21–33.

[Somers et al., 1989] Somers, M. A., Lankreijer, R. M., Mittemeijer, E. J., and Lankreijer, R. M. (1989). Excess nitrogen in the ferrite matrix of nitrided binary iron-based alloys. *Philosophical Magazine A: Physics of Condensed Matter, Structure, Defects and Mechanical Properties*, 59(2):353–378.

[Somers and Mittemeijer, 1990] Somers, M. A. and Mittemeijer, E. J. (1990). Development and relaxation of stress in surface layers; Composition and residual stress profiles in γ-Fe4N1-x layers on α-Fe substrates. *Metallurgical Transactions A*, 21(1):189–204.

[Somers and Mittemeijer, 1995] Somers, M. A. and Mittemeijer, E. J. (1995). Layer-growth kinetics on gaseous nitriding of pure iron: Evaluation of diffusion coefficients for nitrogen in iron nitrides. *Metallurgical and Materials Transactions A*, 26(1):57–74.

[Sridhar, 2010] Sridhar, S. (2010). A commentary on "diffusion, mobility and their interrelation through free energy in binary metallic systems," L.S. Darken: Trans. AIME, 1948, vol. 175, p. 184ff. *Metallurgical and Materials Transactions A: Physical Metallurgy and Materials Science*, 41(3):543–562.

[Stewart et al., 1994] Stewart, J. W., Thomson, R. C., and Bhadeshia, H. K. (1994). Cementite precipitation during tempering of martensite under the influence of an externally applied stress. *Journal of Materials Science*, 29(23):6079–6084.

[Sun et al., 2016] Sun, J., Tong, W. P., Zhang, H., Du, X. D., and Wu, Y. C. (2016). Enhanced strength and plasticity of gas nitrided iron by surface mechanical attrition pretreatment. *Surface and Coatings Technology*, 286:279–284.

[Sun and Bell, 1997] Sun, Y. and Bell, T. (1997). A numerical model of plasma nitriding of low alloy steels. *Materials Science and Engineering A*, 224(1-2):33–47.

[Swartzendruber, 1998] Swartzendruber, L. J. (1998). *ASM handbook volume 3: Alloy phase diagrams.*

[Thiriet et al., 2012] Thiriet, T., Czerwiec, T., Hertz, D., Marcos, G., Toll-Duchanoy, T., Migot, S., Brugier, B., Foucault, M., and Belmonte, T. (2012). Nitrogen diffusion at low temperature in fcc materials deformed by attrition peening. *Defect and Diffusion Forum*, 323-325:471–476.

[Tong et al., 2008] Tong, W. P., Han, Z., Wang, L. M., Lu, J., and Lu, K. (2008). Low-temperature nitriding of 38CrMoAl steel with a nanostructured surface layer induced by surface mechanical attrition treatment. *Surface and Coatings Technology*, 202(20):4957–4963.

[Tong et al., 2006] Tong, W. P., He, C. S., He, J. C., Zuo, L., Tao, N. R., and Wang, Z. B. (2006). Strongly enhanced nitriding kinetics by means of grain refinement. *Applied Physics Letters*, 89(2):2–5.

[Tong et al., 2007] Tong, W. P., Liu, C. Z., Wang, W., Tao, N. R., Wang, Z. B., Zuo, L., and He, J. C. (2007). Gaseous nitriding of iron with a nanostructured surface layer. *Scripta Materialia*, 57(6):533–536.

[Tong et al., 2003] Tong, W. P., Tao, N. R., Wang, Z. B., Lu, J., and Lu, K. (2003). Nitriding iron at lower temperatures. *Science*, 299(5607):686–688.

[Torchane, 2014] Torchane, L. (2014). Gas-Solid Nitrocarburizing of Steels : Kinetic Modeling and Experimental Validation. 8(12):1458–1463.

[Torchane et al., 1994] Torchane, L., Bilger, P., Dulcy, J., and Gantois, M. (1994). Application of a mathematical model of iron-nitride layer growth during gas phase nitriding. *Materials Science Forum*, 163-6(pt 2):707–712.

[Torchane et al., 1996] Torchane, L., Bilger, P., Dulcy, J., and Gantois, M. (1996). Control of iron nitride layers growth kinetics in the binary Fe-N system. *Metallurgical and Materials Transactions A: Physical Metallurgy and Materials Science*, 27(7):1823–1835.

[Totten et al., 2002] Totten, G., Howes, M., and Inoue., T. (2002). Hanbook of Residual Stress and Deformation of Steel. *ASM International*.

[Tsujikawa et al., 2005] Tsujikawa, M., Yamauchi, N., Ueda, N., Sone, T., and Hirose, Y. (2005). Behavior of carbon in low temperature plasma nitriding layer of austenitic stainless steel. *Surface and Coatings Technology*, 193(1-3 SPEC. ISS.):309–313.

[Villani et al., 2014] Villani, A., Busso, E. P., Ammar, K., Forest, S., and Geers, M. G. (2014). A fully coupled diffusional-mechanical formulation: numerical implementation, analytical validation, and effects of plasticity on equilibrium. *Archive of Applied Mechanics*, 84(9-11):1647–1664.

[Vizcaíno et al., 2014] Vizcaíno, P., Santisteban, J. R., Vicente Alvarez, M. A., Banchik, A. D., and Almer, J. (2014). Effect of crystallite orientation and external stress on hydride precipitation and dissolution in Zr2.5 *Journal of Nuclear Materials*, 447(1-3):82–93.

[Volkl, 1965] Volkl, B. J. (1965). The Gorsky Effect. (8):797–805.

[Voorhees and Johnson, 2004] Voorhees, P. W. and Johnson, W. C. (2004). *The thermodynamics of elastically stressed crystals*, volume 59. Elsevier Masson SAS.

[Wang et al., 2015] Wang, H., Suo, Y., and Shen, S. (2015). Reaction–Diffusion–Stress Coupling Effect in Inelastic Oxide Scale During Oxidation. *Oxidation of Metals*, 83(5-6):507–519.

[Wang et al., 2006] Wang, J., Zhang, G., Sun, J., Bao, Y., Zhuang, L., and Ning, H. (2006). Low temperature nitriding of iron by alternating current pretreatment. *Surface and Coatings Technology*, 200(24):6666–6670.

[Wang et al., 2005] Wang, Z. B., Lu, J., and Lu, K. (2005). Chromizing behaviors of a low carbon steel processed by means of surface mechanical attrition treatment. *Acta Materialia*, 53(7):2081–2089.

[Wang et al., 2003] Wang, Z. B., Tao, N. R., Tong, W. P., Lu, J., and Lu, K. (2003). Diffusion of chromium in nanocrystalline iron produced by means of surface mechanical attrition treatment. *Acta Materialia*, 51(14):4319–4329.

[Waterhouse, 1965] Waterhouse, R. B. (1965). The formation, structure, and wear properties of certain non-metallic coatings on metals. *Wear*, 8(6):421–447.

[Weil, 2017] Weil, H. (2017). *Modélisation du besoin fonctionnel pour la nitruration gazeuse (Doctoral dissertation, Paris, ENSAM).* PhD thesis.

[Wipf, 1976] Wipf, H. (1976). The gorsky effect, electrotransport and thermotransport of hydrogen in metals. *Journal of the Less-Common Metals*, 49:291–307.

[Wriedt et al., 1987] Wriedt, H. A., Gokcen, N. A., and Nafziger, R. H. (1987). The Fe-N (Iron-Nitrogen) system. *Bulletin of Alloy Phase Diagrams*, 8(4):355–377.

[Xuan et al., 2009] Xuan, F. Z., Shao, S. S., Wang, Z., and Tu, S. T. (2009). Coupling effects of chemical stresses and external mechanical stresses on diffusion. *Journal of Physics D: Applied Physics*, 42(1).

[Yen and Hwu, 2000] Yen, J. Y. and Hwu, J. G. (2000). Enhancement of silicon oxidation rate due to tensile mechanical stress. *Applied Physics Letters*, 76(14):1834–1835.

[Zhang et al., 2014] Zhang, Y., Zhang, X., Tu, S. T., and Xuan, F. (2014). Analytical Modeling on Stress Assisted Oxidation and its Effect on Creep Response of Metals. *Oxidation of Metals*, 82(3-4):311–330.

[Zhao et al., 2011] Zhao, K., Pharr, M., Cai, S., Vlassak, J. J., and Suo, Z. (2011). Large plastic deformation in high-capacity lithium-ion batteries caused by charge and discharge. *Journal of the American Ceramic Society*, 94(SUPPL. 1):s226–s235.

[Zhou et al., 2010] Zhou, C. H., Ma, H. T., and Wang, L. (2010). Comparative study of oxidation kinetics for pure nickel oxidized under tensile and compressive stress. *Corrosion Science*, 52(1):210–215.

[Zuo and Zhao, 2014] Zuo, P. and Zhao, Y.-P. (2014). A phase field model coupling lithium diffusion and stress evolution with crack propagation and application in lithium ion batteries. *Physical chemistry chemical physics : PCCP*, 17.

Appendix A

Poster presented at the winter conference in Aussois

COUPLAGE CONTRAINTES-DIFFUSION DANS LES TRAITEMENTS THERMOCHIMIQUES

L. Germain [a], S. Jégou[b], L. Barrallier [c]

Laboratoire MSMP, Arts et Métiers, [a] lisa.germain@ensam.eu [b] sebastien.jegou@ensam.eu [c] laurent.barrallier@ensam.eu

Etude: Apporter des éléments de compréhension sur les couplages entre les contraintes résiduelles et/ou appliquées et plus généralement les déformations élastiques du réseau cristallin et les phénomènes de diffusion [1], [2], [3]. Réalisation d'une modélisation 2D et 3D du couplage contraintes-diffusion à partir du code de calcul FreeFEM++ [4]. FreeFEM++ est un solveur d'équations aux dérivées partielles pour les systèmes multiphysiques non linéaires en 2D et 3D qui utilise le language C++. Ce langage permet, de résoudre rapidement un problème linéaire, non linéaire, dépendant du temps ou également couplé tout cela à partir de formulation variationnelle.

Hypothèses de l'étude : Cas de la diffusion interstitielle (atome étranger en insertion) dans un milieu infiniment dilué ($c \ll 1$) avec uniquement un seul élément diffusant (sans co-diffusion de carbone, ni de précipitation associée). Cas où le matériau est supposé élastique isotrope et le coefficient de diffusion D ne dépend ni de la concentration ni des contraintes.

Equations d'équilibre

Equations de l'équilibre mécanique: $\mathrm{div}\ \sigma_{ij} = 0$ dans V

$\sigma_{ij} n_j = g_i$ sur ∂V

Equations constitutives :

$$\varepsilon_{ij}^{tot} = \varepsilon_{ij}^{e} + \varepsilon_{ij}^{l}$$

$$\varepsilon_{ij}^{tot} = \frac{1+\nu}{E}\sigma_{ij} - \frac{\nu}{E}\sigma_{kk}.\delta_{ij} + c\eta_{ij}.\delta_{ij}$$

Loi de Hooke généralisée :

$$\sigma_{ij} = 2\mu\left(\varepsilon_{ij}^{tot} - c\eta_{ij}\right) + \lambda[\varepsilon_{kk}^{tot} - c\eta_{kk}].\delta_{ij}$$

Les constantes d'élasticité :

$$\nu_0 = \frac{\nu - \chi\eta^2 E}{1+\chi\eta^2 E},\ E_0 = \frac{E}{1+\chi\eta^2 E}$$

avec $\chi = \frac{v_a}{RT}c$

Les coefficients de Lamé :

$$\lambda = \frac{E_0\nu_0}{(1+\nu_0)(1-2\nu_0)}\ ;\ \mu = \frac{E_0}{2(1+\nu_0)}$$

Conservation de la matière :

$$\frac{\partial c}{\partial t} = -\mathrm{div}\vec{j} \text{ dans } V$$

$$j = \vec{j}.\vec{n} \text{ sur } \partial V$$

Couplage contraintes-diffusion en fonction des champs de compositions

$$\mathbf{j} = -\mathbf{D}\nabla\mathbf{c} + \frac{1}{3}\frac{\mathbf{D}\Delta v}{RT}\mathbf{c}.\nabla(\mathrm{tr}\,(\boldsymbol{\sigma}))$$

Formulation variationnelle après une discrétisation temporelle (Euler implicite):

$$\int_V c^* \frac{\mathbf{c^{n+1}} - \mathbf{c^n}}{\Delta t^n}\mathbf{dV} + \int_{\partial V} c^*.\mathbf{j}\,\boldsymbol{dS} + \int_V \mathbf{D}.\nabla\mathbf{c}^*.\nabla\mathbf{c^{n+1}}\,\mathbf{dV} - \int_V \frac{1}{3}\frac{\mathbf{D}\Delta v}{RT}.\mathbf{c^{n+1}}.\nabla\mathbf{c}^*.\nabla\mathrm{tr}\,(\boldsymbol{\sigma})\,\boldsymbol{dV} = \mathbf{0}$$

Couplage contraintes-diffusion en fonction des champs mécaniques

$$\mathbf{div}\left[2\mu(\varepsilon_{ij}^{tot} - c\boldsymbol{\eta}_{ij}) + \lambda[\boldsymbol{\varepsilon}_{kk}^{tot} - c\boldsymbol{\eta}_{kk}].\boldsymbol{\delta}_{ij}\right] = \mathbf{0}$$

Formulation variationnelle :

$$\int_{\partial V} \boldsymbol{v_i}.\boldsymbol{g_i}\,\boldsymbol{dS} - \int_V \boldsymbol{\nabla v_i}.\left(2\mu(\boldsymbol{\varepsilon}_{ij}^{tot} - c\boldsymbol{\eta}_{ij}) + \lambda[\boldsymbol{\varepsilon}_{kk}^{tot} - c\boldsymbol{\eta}_{kk}].\boldsymbol{\delta}_{ij}\right)\boldsymbol{dV} = \mathbf{0}$$

Codage couplage contraintes-diffusion (cas 2D) sous FreeFEM++ [4]

```
problem diffusion(c1,c2,solver=GMRES) =
    int2d(Sh)(c2*c1/dt) - int2d(Sh)(c2*c/dt) + int2d(Sh)(D*(dx(c1)*dx(c2)+dy(c1)*dy(c2)))  - int2d(Sh)(D*delta*c1*grad(c2)'*grad(trsig))
    + on(1,c1=C0) + on(2,c1=C0) + on(3,c1=C0) + on(4,c1=C0) ;
problem elasticite([Ux, Uy],[Vx, Vy]) =
    -int2d(Sh)(2*mu*epsilon(Ux, Uy)'*epsilon(Vx, Vy)+lambda*div(Vx, Vy)*div(Ux, Uy))+ int2d(Sh)((3*lambda+2*mu)*c1*eta*div(Vx, Vy)) ;
```

Exemple : on(**label**,c1=C0)
Cas 2D **label : 1, 2, 3 ou 4**

Loi de Vegard [5], [6]

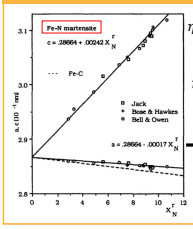

$$\eta = \frac{1}{3}\frac{\Delta v}{v_a} \text{ avec: } \Delta v = \frac{\text{Nb Avogadro}}{\text{Nb at. par mole}} * \textbf{pente}$$

$\Delta v = 51{,}2$ mm³/mol

$\eta = 0{,}002$ $\quad v_a = 7091$ mm³/mol

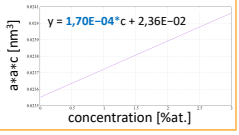

Concentration atomes interstitiels c (Cas 2D)

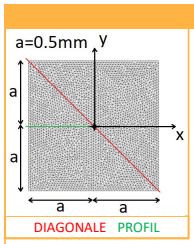

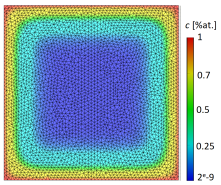

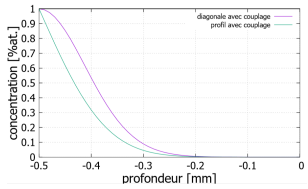

$$a^r[\%] = \frac{c_{\text{sans couplage}} - c_{\text{avec couplage}}}{c_{\text{sans couplage}}}$$

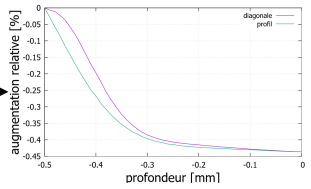

- Effet de bords
- Loi de erfc sur les profils et les diagonales
- Faible augmentation relative (effet des contraintes) de la concentration lors du couplage contraintes-diffusion

Contraintes $\sigma_{xx} = \sigma_{yy}$, σ_{xy} et σ^H (cas 2D)

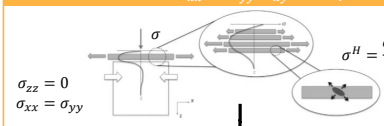

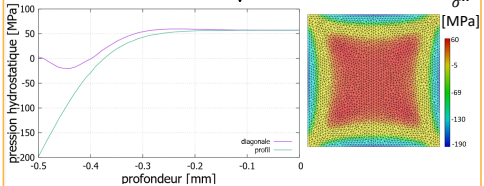

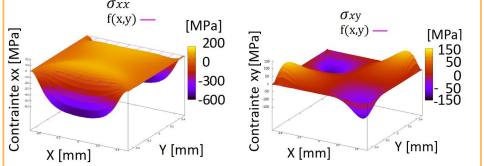

- Etat de contrainte : Compression en surface / traction à cœur
- Diminution de $\boldsymbol{\sigma^H}$ sur les diagonales

Module d'Young fictif E_0 (cas 2D)

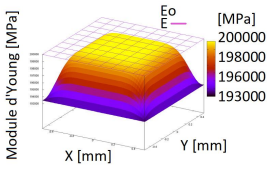

- Diminution du module en surface

Programmation FreeFEM ++ (cas 3D)

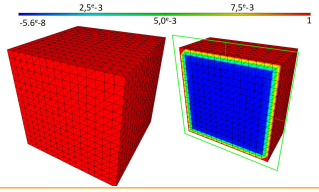

Notations utilisées :

σ_{ij}	Tenseur des contraintes	k	Constante de Boltzmann	E_0	Module d'Young (fictif)
ε_{ij}^{tot}	Déf. totale [-]	$v_i; c^*$	Fonctions tests	ν_0	Coefficient de Poisson (fictif)
ε_{ij}^{e}	Déf. élastique [-]	δ_{ij}	Symbole de Kronecker	W	nbr de chemin (at. interstitiel)
ε_{ij}^{l}	Déf. libre de contrainte [-]	D	Coeff. de diffusion	c_{eq}	Concentration à l'équilibre
c	Concentration (at. Interstitiel)	u_i	Déplacement [mm]	σ^H	Pression Hydrostatique [Mpa]

Conclusion : Cette étude a permis d'écrire un modèle numérique sur le couplage contraintes-diffusion en 2D et 3D appliqué à la diffusion interstitielle et de visualiser l'effet des contraintes résiduelles sur les cinétiques de diffusion dans le cas d'un matériau élastique isotrope et dans un milieu infiniment dilué avec uniquement un seul élément diffusant.

Perspectives :
- Comprendre l'influence du couplage sur les mobilités,
- Prendre en compte la co-diffusion du carbone et la précipitation associée aux éléments diffusant de la nitruration gazeuse,
- Applications possible sur la diffusion d'hydrogène ou le domaine de la microélectronique (diffusion interstitielle).

Références:
[1] F. Larche and J. Cahn, Acta metal, vol. 33, no. 3, pp. 331-357, 1985.
[2] A. Villani et al., Arch Appl Mech, Volume 84, Issue 9–11, pp 1647–1664, 2014.
[3] J. Lemaitre et J.L. Chaboche, Mechanics of solid materials; Cambridge university press, 1990.
[4] F. Hecht, FreeFEM Documentation, Release 4.2.1, 2019.
[5] L. Vegard, Zeitschrift für Physik. 5 (1): 17–26, 1921.
[6] L. Cheng, Larche and J. Cahn, Metal. Et Mat., vol. 24, pp. 509-514, 1905.

Lisa GERMAIN

Stress-diffusion coupling. From interstitial problems to the gas nitriding of steel

Résumé : Depuis de nombreuses années, la compréhension du couplage entre un champ de contraintes mécaniques (appliquées ou résiduelles) et un champ chimique dans un processus de diffusion de la matière est un domaine majeur d'étude. La diffusion interstitielle à longue distance, dans le cas par exemple de la nitruration gazeuse provoque de forts gradients de contraintes associés à des transformations de phase (diffusion à courte distance). Les phénomènes de diffusion-précipitation sont connus et simulés au sein du laboratoire. Le couplage contrainte-diffusion reste cependant un problème important. Deux phénomènes sur la diffusion à longue distance ont été soulignés : l'effet d'une contrainte homogène (terme Fickien) et le gradient de contraintes (terme Nersntien). De plus, un prétraitement mécanique est fréquemment couplé à un traitement thermochimique, ce qui entraîne des phénomènes rarement découplés de déformations plastiques incompatibles et de contraintes résiduelles. Des approches numériques limitées à la diffusion à longue distance et des approches expérimentales ont alors été réalisées pour aborder ces questions. Le couplage contrainte-diffusion fait l'objet de simulations numériques (1D et 2D), appliqué à un système binaire (Fe-N), utilisant la thermodynamique des processus irréversibles. Les effets d'une contrainte homogène et d'un gradient de contraintes ont été mis en évidence par des simulations numériques. Les résultats ont révélé que le facteur de couplage fickien ($\sigma_{kk}\beta$) doit être environ 10 fois inférieur au coefficient de diffusion D pour avoir un impact significatif sur la cinétique. Afin de confronter ces résultats théoriques à la réalité, des expériences de nitruration sur la nuance d'acier 33CrMoV12-9 ont été effectuées.

Mots clés : Couplage contrainte-diffusion, nitruration gazeuse, contrainte résiduelle, déformation élastique, déformation plastique.

Abstract : For many years, the understanding of the coupling between a mechanical (applied or residual) stress field and a chemical field in a material diffusion process has been an important area of study. Long-range interstitial diffusion, for example in the case of gas nitriding, causes strong stress gradients associated with phase transformations (short-range diffusion). The phenomena of diffusion-precipitation are known and simulated in the laboratory. However, the stress-diffusion coupling (short or long range) remains an important problem. Two significant phenomena on long-range diffusion have been highlighted: the effect of a homogeneous stress (Fickian term) and the stress gradient (Nersntien term). In addition, mechanical pretreatment is frequently used with thermochemical treatments, resulting in rarely decoupled phenomena of incompatible plastic strains and residual stresses. In this study numerical approaches limited to long-range diffusion and experimental approaches were carried out to investigate these issues. The stress-diffusion coupling is the subject of numerical simulations (1D and 2D) using the thermodynamics of irreversible processes. The effects of a homogeneous stress and a stress gradient were demonstrated by numerical simulations that were applied to a binary system (Fe-N). The results revealed that the Fickian coupling factor ($\sigma_{kk}\beta$) must be about 10 times lower than the diffusion coefficient D to have a significant impact on the kinetics. In order to compare these theoretical results with reality, nitriding experiments on the steel grade 33CrMoV12-9 were carried out.

Keywords: Stress-diffusion coupling, gas nitriding, residual stress, elastic strain, plastic strain.